

NASA Contractor Report 205205

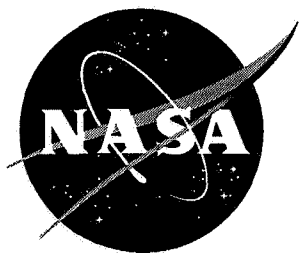
# Research Reports – 1996 NASA / ASEE Summer Faculty Fellowship Program

---

*L.M. Freeman, C.R. Chappell, F. Six, G.R. Karr, Editors*

Contract NGT8-52819  
Prepared for Marshall Space Flight Center

October 1996



# Research Reports – 1996 NASA / ASEE Summer Faculty Fellowship Program

---

*Editors:*

*Dr. L.M. Freeman*

*The University of Alabama • Tuscaloosa, Alabama*

*Dr. C.R. Chappell*

*Marshall Space Flight Center • MSFC, Alabama*

*Dr. F. Six*

*Marshall Space Flight Center • MSFC, Alabama*

*Dr. G.R. Karr*

*The University of Alabama • Huntsville, Alabama*





## TABLE OF CONTENTS

- I. Adams, Glynn  
University of Arkansas  
Process Model for Friction Stir Welding
- II. Bales, John W.  
Tuskegee University  
Hardware/Software Issues for Video Guidance Systems: The Coreco  
Frame Grabber
- III. Bucinell, Ronald B.  
Union College  
Finite Element Modeling of the Thermographic Inspection for Composite  
Materials
- IV. Carlisle, W. H.  
Auburn University  
New Interfaces to Web Documents and Services
- V. Cuttino, James F.  
Todd, Michael W., Masters Student  
The University of Alabama  
A Flexible Alignment Fixture for the Fabrication of Replication Mandrels
- VI. Dumas, Joseph D., II.  
University of Tennessee in Chattanooga  
Integration of the Shuttle RMS/CBM Positioning Virtual Environment  
Simulation
- VII. Etter, Brad  
Texas A&M University in College Station  
Evaluation of an Anthropometric Human Body Model for Simulated EVA  
Task Assessment
- VIII. Fragomeni, James M.  
The University of Alabama  
An Assessment of Molten Metal Detachment Hazards During Electron  
Beam Welding in the Space Shuttle Bay at LEO for the International  
Space Welding Experiment
- IX. Garcia, Thomas R.  
Purdue University in South Bend  
BPSK Demodulation Using Digital Signal Processing
- X. Hartfield, Roy, Jr.  
Auburn University  
Development of a Technique for Separating Raman Scattering Signals  
from Background Emission with Single-Shot Measurement Potential
- XI. Heard, Pamela D.  
Langston University  
"The Interpretation and Effective Implementation of the Stevenson-  
Wylder Technology Innovation Act of 1996"

- XII. Hochstein, John I.  
The University of Memphis  
Computational Modeling of Magnetically Actuated Propellant Orientation
- XIII. Holmes, Leonard D.  
The University of North Carolina in Pembroke  
Preliminary Work in Obtaining Site-Directed Mutants of Hen Egg White  
Lysozyme
- XIV. Hopkins, Randall  
Benzing, Daniel, Masters Student  
The University of Alabama  
SSME Condition Monitoring Using Neural Networks and Plume Spectral  
Signatures
- XV. Hung, John Y.  
Auburn University  
Pointing and Scanning Control of Instruments Using Rotating Unbalanced  
Masses
- XVI. Isaac, Kakkattukuzhy M.  
The University of Missouri in Rolla  
Spray Diagnostics in Rocket Engines Using Phase Doppler Analyzer
- XVII. Johnson, Jacqueline U.  
Alabama A&M University  
Adaptation of a Motility Analysis Apparatus for Space Science and  
Microgravity Ground-Based Experiments
- XVIII. Jones, Peter D.  
Auburn University  
Thermal Model of the Promoted Combustion Test
- XIX. Katsinis, Constantine  
The University of Alabama in Huntsville  
Development of a Computer Architecture to Support the Optical Plume  
Anomaly Detection (OPAD) System
- XX. Laird, C. E.  
Eastern Kentucky University  
The Response of the BATSE Lads to Radiation from the Crab Nebula and  
Plans for Radioactivity Studies on Space Station
- XXI. Lebo, George R.  
University of Florida  
Development of an Outreach Program for NASA: "NASA Ambassadors"
- XXII. Losure, Nancy S.  
Mississippi State University  
Testing Protocol Proposal to Identify and Evaluate Candidate Materials to  
Substitute for Silverized Teflon in Thermal Control Applications

- XXIII. Lundberg, John B.  
Auburn University  
Application of Consider Covariance to the Extended Kalman Filter
- XXIV. Maier, Mark W.  
The University of Alabama in Huntsville  
SEDSAT 1 Technologies
- XXV. McDonald, Malcolm W.  
Berry College  
Planning an Effective Speakers Outreach Program
- XXVI. Micklow, Gerald J.  
The University of Alabama  
Cooling Duct Analysis for Transpiration/Film Cooled Liquid Propellant  
Rocket Engines
- XXVII. Nadarajah, Arunan  
The University of Alabama in Huntsville  
Relationship between Equilibrium Forms of Lysozyme Crystals and  
Precipitant Anions
- XXVIII. Navaz, Homayun K.  
GMI  
Computational Modeling of Multi-Phase/Multi-Species Flows with  
Applications to Liquid Rocket Engines
- XXIX. Nordin, Gregory P.  
The University of Alabama in Huntsville  
Diffractive Optical Elements for Lidar Beam Scanning
- XXX. Olivier, Philip D.  
Mercer University  
Strehl Ratio Meter for Focusing Segmented Mirrors I
- XXXI. Pearson, Earl F.  
Western Kentucky University  
The Effect of Gravity Axis Orientation on the Growth of Phthalocyanine  
Thin Films
- XXXII. Phillips, James A.  
California Institute of Technology  
Virtual Reality Simulation of the International Space Welding Experiment
- XXXIII. Prasthofer, Thomas  
Albany College of Pharmacy  
Synthesis and Characterization of a Chitosan Derivative for Electro-  
Optical Applications
- XXXIV. Ray, Paul S.  
The University of Alabama  
An Independent Evaluation of the FMEA/CIL Hazard Analysis  
Alternative Study

- XXXV. Romine, Peter L.  
Alabama A&M University  
Investigation of Machine Design for Friction Stir Welding
- XXXVI. Rosmait, Russell L.  
Pittsburg State University  
What Drives Spacecraft Cost: A Look into How Material Characteristics  
Relate to the Material Complexity Multipliers
- XXXVII. Schreur, Julian J.  
Texas A&M University in Kingsville  
Scattering and the Point Spread Function of the New Generation Space  
Telescope
- XXXVIII. Olsen, Eugene A.  
University of Alabama in Huntsville  
Management of Technology
- XXXIX. Sheldon, John W.  
Florida International University  
Electron Flow to a Satellite at High Positive Potential
- XL. Sherif, S. A.  
University of Florida  
Analysis and Modeling of a Two-Phase Jet Pump of a Flow Boiling Test  
Facility for Aerospace Applications
- XLI. Smalley, Larry L.  
The University of Alabama in Huntsville  
Comments on SEE: Comparative Advantages and Experimental  
Consequences
- XLII. Smeyak, Gerald P.  
University of Florida  
An Analysis of MSFC Public Affairs Television and Target Audiences  
with Suggestions for Future Growth and Directions
- XLIII. Spencer, Dwight C.  
Mississippi Delta Community College  
Design, Fabrication, and Testing of Multilayer Coated X-Ray Optics for  
the Water Window Imaging X-Ray Microscope
- XLIV. Talia, George E.  
Widener, Christian A., Masters Student  
Wichita State University  
High Temperature Analysis of Aluminum-Lithium 2195 Alloy to Aid in  
the Design of Improved Welding Techniques
- XLV. Taylor, Charles R.  
Western Oregon State University  
Augmentation of Rocket Propulsion: Physical Limits

- XLVI. Taylor, Jaime R.  
Austin Peay State University  
A Real-Time Position-Locating Algorithm for CCD-Based Sunspot Tracking
- XLVII. Trivoli, George W.  
Jacksonville State University  
Technology Transfer External Metrics, Research, Success Stories, and Participation on Evaluation Team for the Reusable Launch Vehicle (RLV)
- XLVIII. Wang, Peter H.  
Alabama A&M University  
The Infrastructure of an Integrated Virtual Reality Environment for International Space Welding Experiment (ISWE)
- XLIX. Wells, B. Earl  
The University of Alabama in Huntsville  
Applying Parallel Processing Techniques to a Tether Dynamics Simulation
- L. Wilson, Gordon R.  
The University of Alabama in Huntsville  
Visualization of High Latitude Ion Upflow in Support of the Image Mission
- LI. Woodbury, Keith A.  
The University of Alabama  
Solidification Interface Shape and Location During Processing in High Gradient Furnace with Quench
- LII. Young, Ronald B.  
The University of Alabama in Huntsville  
Receptor Expression in Rat Skeletal Muscle Cell Cultures

1996

**NASA/ASEE SUMMER FACULTY FELLOWSHIP PROGRAM**

**MARSHALL SPACE FLIGHT CENTER  
THE UNIVERSITY OF ALABAMA**

**PROCESS MODEL FOR FRICTION STIR WELDING**

Prepared By:	Glynn Adams
Academic Rank:	Assistant Professor
Institution and Department:	University of Arkansas Department of Mechanical Engineering
NASA/MSFC:	
Laboratory:	Materials and Processes Laboratory
Division:	Metallic Materials and Processes
Branch:	Metallurgical Research & Development
MSFC Colleagues:	R. Jeff Ding, Art Nunes

## INTRODUCTION

Friction stir welding (FSW) is a relatively new process being applied for joining of metal alloys. The process was initially developed by The Welding Institute (TWI) in Cambridge, UK, (Dawes, 1995). The FSW process is being investigated at NASA/MSFC as a repair/initial weld procedure for fabrication of the super-light-weight aluminum-lithium shuttle external tank.

The FSW investigations at MSFC were conducted on a horizontal mill to produce butt welds of flat plate material, Figure ???. The weldment plates are butted together and fixed to a backing plate on the mill bed. A pin tool is placed into the tool holder of the mill spindle and rotated at approximately 400 rpm. The pin tool is then plunged into the plates such that the center of the probe lies at one end of the line of contact between the plates and the shoulder of the pin tool penetrates the top surface of the weldment. The weld is produced by traversing the tool along the line of contact between the plates. A lead angle allows the leading edge of the shoulder to remain above the top surface of the plate.

Dawes and Thomas (1996) list the major advantages and disadvantages of friction stir welding. When properly conducted, friction stir welding is a solid state process. The material in the weld region is plasticized but remains below its melting temperature. This is the main advantage of FSW when applied to joining aluminum-lithium alloys. Since FSW is a solid state process, the problems associated with the phase change and resolidification are eliminated. The mechanical properties of friction stir welded joints have proven to be at least as good as, and in most instances better than, fusion welded joints. The fracture strength, elongation at fracture and therefore total energy absorbed, of FSW joints are improved as compared with fusion welded joints.

The main disadvantage of friction stir welding is the reaction loads which must be accommodated in the tooling and fixturing. Conventional fusion welds require fixturing of the weldment for alignment only. There are no loads produced between the welding tool and the weldment. However, with FSW, substantial loads are produced between the pin tool and the weldment. These loads must be reacted by both the fixturing which holds the weldment and the tooling used to locate the pin tool.

## PROCESS MODEL

The goal of the process model is to develop the relationships between the dependent and independent parameters involved in FSW. The independent parameters are the pin tool rotational and travel speeds, the pin tool probe and shoulder penetration depths, and the lead angle. The dependent parameters are the axial and transverse loads on the pin tool and the temperature of the weld material. The model developed here consists of three basic aspects, a plasticity model of the parent material, energy balance within the weld region and mechanical equilibrium of the material within the weld region. A one dimensional model is developed with variations in the radial dimension only considered. It is assumed that the mechanical properties and temperature profile are independent of the coordinate along the material thickness. A schematic representation of the basic model is presented in Figure ??.



In modeling the process, it is assumed that the flow shear  $\tau_f$  dependency on temperature can be defined as

$$\tau_f = a(T - T_m)^2 \quad (1)$$

where  $T$  is the local temperature of the material and  $T_m$  is the melting temperature of the material.

An energy balance is applied to account for mechanical and thermal energy. Figure ?? represents the mechanical and thermal energy flow for a differential element within the weldment plate. Mechanical energy is introduced into the weld process through the rotating pin tool. This mechanical energy is expended in plasticizing the material and heat generation. The energy balance applied to the differential element shown, leads to the equation

$$\frac{dT}{dr} = r\omega \left( \frac{\tau_f}{k} \right) - \left( \frac{1}{r} \right) \left( \frac{A}{k} \right) \quad (2)$$

where  $r$  is the radial coordinate,  $\omega$  is the local rotational speed,  $k$  is the thermal conductivity, and  $A$  is a constant.

The torque produced by the shear forces induced on the radial faces of the differential element must balance in order for mechanical equilibrium to be maintained, Figure ?. This balance leads to a definition for the distribution of  $\tau_f$  over the plastic region

$$\tau_f = \tau_R \left( \frac{R}{r} \right)^2 \quad (3)$$

where  $R$  is the radius of the pin tool probe, and  $\tau_R$  represents the flow shear at this boundary.

Equating the definitions for the flow shear  $\tau_f$  given in Equations 1 and 3 results in an equation for the temperature distribution within the plastic region.

$$T = T_m - \sqrt{\frac{\tau_R}{a}} \left( \frac{R}{r} \right) \quad (4)$$

The temperature gradient along the radial coordinate is given by the derivative with respect to  $r$  of Equation 4

$$\frac{dT}{dr} = (T_m - T_r) \frac{R}{r^2} \quad (5)$$

where the definition  $\tau_R = a(T_m - T_R)^2$  is used.

Equating the right hand sides of Equations 2 and 5, and using the boundary condition that  $\omega = \Omega$  at  $r = R$ , we can define the constant  $A$  and derive the equation

$$\omega = \Omega - \frac{k(T_m - T_R)}{\tau_R R^2} \left[ 1 - \frac{R}{r} \right] \quad (6)$$

At the outer boundary of the plasticized region,  $r = R_p$  we can apply the boundary condition  $\omega = 0$  to obtain the relationship

$$\frac{R_p}{R} = \frac{k}{k - R^2 \Omega a (T_m - T_R)} \quad (7)$$

Applying the boundary conditions for the transfer of thermal energy results in a conflict which must be resolved. At the pin tool boundary  $r = R$ , the heat transfer from the plastic region into the pin can be defined with the use of Equation 5 as

$$Q_R = -2\pi kh(T_m - T_R) \quad (8)$$

At the boundary of the plastic zone, the heat transfer from the plastic zone is defined as

$$Q_{p1} = -2\pi kh(T_m - T_r) \frac{R}{R_p} \quad (9)$$

However, this results in heat flow from the environment into the plastic region, which seems contrary to the physical situation.

For a given radius  $R_o$  into the environment surrounding the plastic region, sufficiently distant from the plastic region, we have

$$r \left( \frac{\partial T}{\partial r} \right) = C \quad (10)$$

$$T - T_o = -C \ln \left( \frac{R_o}{R} \right) \quad (11)$$

The heat transfer into the environment at the boundary  $r = R_p$  can therefore be expressed as

$$Q_{p2} = \frac{2\pi hk(T_p - T_o)}{\ln \left( \frac{R_o}{R_p} \right)} \quad (12)$$

This represents heat transfer away from the boundary at  $r = R_p$  into the environment. Equations 9 and 12 each represent heat flow away from the boundary at  $r = R_p$ . There is no heat source at this boundary. Therefore, conduction of heat away from this boundary in both radial directions produces the conflict mentioned above. One possible explanation, is that this phenomenon involves a time dependent oscillation at the plastic region boundary which must be incorporated into the model.

If we assume no heat loss through the pin tool and allow a constant temperature distribution across the plastic region,  $T_m \approx T_R \approx T_p$ , we can balance the mechanical energy input at the pin tool with the thermal energy conducted into the environment.

$$\tau_R(2\pi Rh)R\Omega = 2\pi hk \left( \frac{T_r - T_o}{\ln \frac{R_o}{R_p}} \right) \quad (13)$$

$$\tau_R = \frac{k(T_m - T_o)}{R^2\Omega \ln \frac{R_o}{R_p}} \quad (14)$$

With the derivation of these relationships and the assumptions stated above, the following equations can be derived to relate the input requirements to the independent parameters.

The mechanical moment  $M$  and energy input  $M\Omega$  required to rotate the pin tool are given as

$$M = \frac{2\pi h k (T_m - T_o)}{\Omega \ln \frac{R_o}{R_p}} \quad (15)$$

$$M\Omega = \frac{2\pi h k (T_m - T_o)}{\ln \frac{R_o}{R_p}} \quad (16)$$

The force  $F$  and energy  $FV$  required to traverse the weld at speed  $V$  are given as

$$F = \frac{4h k (T_m - T_o)}{R\Omega \ln \frac{R_o}{R_p}} \quad (17)$$

$$FV = \frac{4h k (T_m - T_o)}{R\Omega \ln \frac{R_o}{R_p}} V \quad (18)$$

The ratio of transverse energy required to rotational energy required is given as

$$\frac{FV}{M\Omega} = \frac{2V}{\pi R\Omega} \quad (19)$$

## CONCLUSIONS

The work presented here is the first attempt at modeling a complex phenomenon. The mechanical aspects of conducting the weld process are easily defined and the process itself is controlled by relatively few input parameters. However, in the region of the weld, plasticizing and forging of the parent material occurs. These are difficult processes to model. The model presented here addresses only variations in the radial dimension outward from the pin tool axis. Examinations of the grain structure of the weld reveal that a considerable amount of material deformation also occurs in the direction parallel to the pin tool axis of rotation, through the material thickness. In addition, measurements of the axial load on the pin tool demonstrate that the forging affect of the pin tool shoulder is an important process phenomenon. Therefore, the model needs to be expanded to account for the deformations through the material thickness and the forging affect of the shoulder. The energy balance at the boundary of the plastic region with the environment requiried that energy flow away from the boundary in both radial directions. One resolution to this problem may be to introduce a time dependancy into the process model, allowing the energy flow to oscillate across this boundary. Finally, experimental measurements are needed to verify the concepts used here and to aid in improving the model.

## REFERENCES

Dawes, C.J., "An Introduction to friction stir welding and its development", *Welding and Sheet Metal Fabrication*, Volume 63, Number 1, pp. 13–16, January 1995.

Dawes, C.J. and Thomas, W.M., "Friction Stir Process Welds Aluminum Alloys", *Welding Journal*, Volume 75, Number 3, pp. 41–45, March 1996.

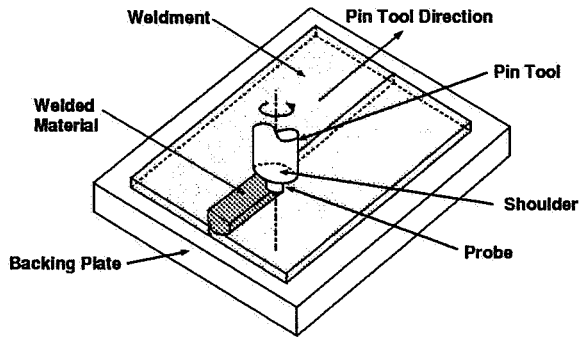


Figure 1. FSW schematic.

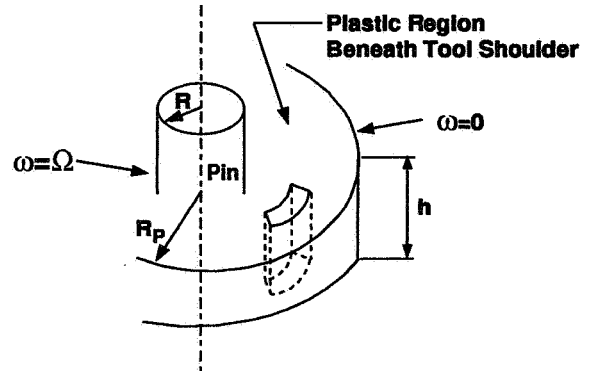


Figure 2. Basic model of FSW

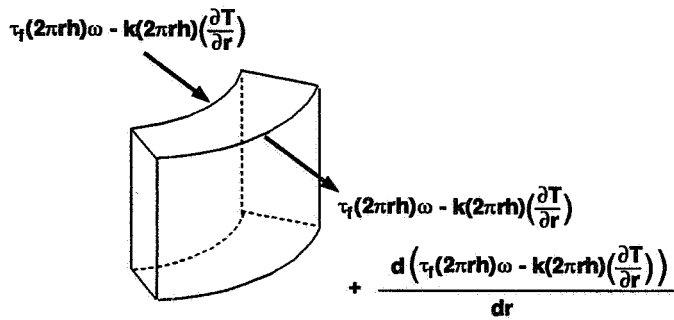


Figure 3. Energy balance.

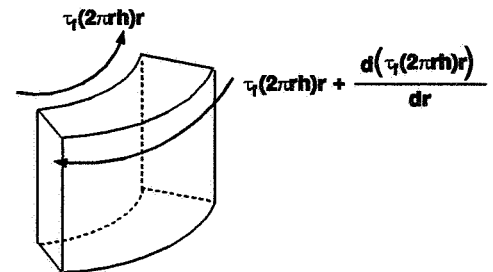


Figure 4. Mechanical equilibrium.

1996

NASA/ASEE SUMMER FACULTY FELLOWSHIP PROGRAM

MARSHALL SPACE FLIGHT CENTER  
THE UNIVERSITY OF ALABAMA

HARDWARE/SOFTWARE ISSUES FOR VIDEO GUIDANCE SYSTEMS:  
THE CORECO FRAME GRABBER

Prepared by:	John W. Bales, Ph.D.
Academic Rank:	Associate Professor
Institution and Department:	Tuskegee University Department of Mathematics
NASA/MSFC:	
Laboratory:	Astrionics
Division:	Avionics Simulation
Team:	Orbital Systems and Robotics
MSFC Colleague:	Fred Roe, Jr.

## THE CORECO OCULUS F64 FRAME GRABBER

The F64 frame grabber is a high performance video image acquisition and processing board utilizing the TMS320C40 and TMS34020 processors. The hardware is designed for the ISA 16 bit bus and supports multiple digital or analog cameras. It has an acquisition rate of 40 million pixels per second, with a variable sampling frequency of 510 kHz to 60 MHz. The board has a 4MB frame buffer memory expandable to 32 MB, and has a simultaneous acquisition and processing capability. It supports both VGA and RGB displays, and accepts all analog and digital video input standards.

## CAMERA CHARACTERISTICS

The PULNiX TM9701 is a progressive scanning full frame shutter camera. It is capable of both digital (EIA-422) and analog output. Shutter speed can be set manually or by an external double-pulse signal. Output can be in either interlace or non-interlaced mode. Whereas other CCD cameras scan only 350 lines per screen, the PULNiX scans 484. In addition, the PULNiX is available in a flight qualifiable package.

## SOFTWARE INTERFACES

All commands to the F64 frame grabber are mediated by the software driver. The driver resides in the host 486 machine as a terminate and stay resident (TSR) program which is loaded on system power-up. Coreco provides several methods of accessing the driver.

For the Windows operating environment, there is the F64Pro program. This is not for developing user applications, but solely for the purpose of demonstrating the features of the frame grabber. There is also a program, WConfig, which allows user configuration of the frame grabber from within the Windows environment.

For the DOS operating environment, Coreco provides several software alternatives. First, is the Oculus Driver Command Interface (ODCI). In its menu driven mode, ODCI is just another platform for demonstrating the functions of the frame grabber. But ODCI also operates in "shell" mode. One enters the ODCI shell mode by pressing <ESC> when in menu mode. Coreco provides a simple programming language for its ODCI shell mode. One may use this to program simple macros utilizing most of the features of the frame grabber. In addition to ODCI, Coreco provides modules for building either assembler language or C language applications. The C language modules and resulting applications may be compiled using MicroSoft C/C++ version 7.00.

## OCULUS DRIVER

The Oculus driver (ODX) is implemented as a TSR program. User applications communicate with ODX using a message passing interface. Only one command is processed at a time. Messages sent while ODX is busy are queued and processed on a

first in first out (FIFO) basis. The state of ODX and the frame grabber are specified by the 115 Oculus Parameter Registers (OPR). User applications can communicate with ODX and the frame grabber by manipulating the contents of the OPR directly, or indirectly by using the 83 Coreco supplied functions comprising the Application Programming Interface (API). Both the OPR and the API functions may be classified into five types according to their purpose: Management, Memory, Processing, Acquisition and Display.

Programmers may learn the state of the various OPR using the 'opr\_inq' function, and may change the state of a proper subset of the OPR using the 'opr\_set' function. It is possible to directly access the contents of the frame buffer (which resides on the frame grabber card) by mapping the frame grabber memory to the host 486 bus. This is accomplished using the API functions 'memopen' and 'memclose'. To grab an image one may use the functions 'fbgrab' or 'fbgrabalu'. One may check to see whether a frame grab request has been completed by checking the status of the FGON register using 'opr\_inq'. One may extract the contour of a binary object in the grabbed image using the API functions 'cntrfirst' and 'cntr'. One may perform various arithmetic logic unit (ALU) operations "on the fly" using the API functions 'fbgrabalu' and 'fbalu'. For example, one may automatically subtract the current frame from the previous frame and display the difference. Using the API function 'event' one may use the vertical or horizontal sync signals to trigger the execution of a user function.

#### EXAMPLE USER FUNCTION

Figure 1 shows an example user function using the ODX API functions. This particular application grabs one frame for reference, then grabs a second frame and subtracts it from the first, displaying the result. The API function 'odxbind' determines the number of ODX drivers installed on the host machine, and binds to those drivers. The API function 'setdmajor' selects one of the installed drivers as the major driver. First, the application determines the index of the display frame buffer (DFB) using the 'opr\_inq' function. Next, the same index is assigned to the input frame buffer (FFB) using the 'opr\_set' function. This has the effect of displaying the currently grabbed image on the display monitor. Then, using the 'fbgrab' function, a single frame is grabbed. Using the 'opr\_inq' function, one waits until the FGON register has a value of zero, indicating that the grab has been completed. Then one uses the 'fbgrabalu' function to grab a second frame, while simultaneously subtracting it from the first frame. Figure 2 shows the result of running this sample application while waving at the camera. Because of the slight displacement of the hand between the two successive grabs, the two images were not identical. Thus subtracting the second image from the first resulted in an outline of the hand.

#### APPLICATION TO VIDEO GUIDANCE SYSTEMS

Video guidance systems employ video images of moving targets to determine the range, orientation and velocity of the targets. Such systems must use the changes in successive images to extract range, orientation and velocity information in real time. The Orbital Systems and Robotics team of the Avionics Simulation Division of the Astrionics

Laboratory of Marshall Space Flight Center has an ongoing effort to develop a suitable Video Guidance System for Automated Rendezvous and Docking of space craft. The Coreco F64 frame grabber and the Pulnix TM9701 camera are potential components of such a system.



```

#include <odx.h>
#include <opr.h>

extern int FAR odxbind(void); /* Bind to ODX drivers installed */
extern void FAR setdmajor(int); /* Set working major device */

int main( int argc, char **argv)
{
    int nodx; /* Number of installed drivers */
    int fb; /* Frame buffer index */
    int key; /* Keyboard response */

    nodx = odxbind(); /* Bind to installed drivers */
    setdmajor(0); /* Select driver # 0 */

    printf("Press any key to take snapshot.\n<RETURN> to quit.\n");

    while ( (key = getch()) != '\r') /* Do until <RETURN> pressed */
    {
        fb = opr_inq(DFB); /* Get index of display buffer */
        opr_set(FFB,fb); /* Place input into display */
        fbgrab(1); /* Grab one frame */
        while( opr_inq( FGON)); /* Wait until grab finished */
        fbgrabalu(2,fb,1); /* Subtract a second grab from first */
    }
    return( 0);
}

```

Figure 1: A demonstration user application



Figure 2: Output of demonstration user application

**1996**

**NASA/ASEE SUMMER FACULTY FELLOWSHIP PROGRAM**

**MARSHALL SPACE FLIGHT CENTER  
THE UNIVERSITY OF ALABAMA**

**FINITE ELEMENT MODELING OF THE THERMOGRAPHIC  
INSPECTION FOR COMPOSITE MATERIALS**

Prepared By: Ronald B. Bucinell, Ph.D., P.E.

Academic Rank: Assistant Professor

Institution and Department: Union College, Schenectady, NY 12308  
Department of Mechanical Engineering

NASA/MSFC:

Laboratory:	Materials and Processes	Materials and Processes
Division:	Nonmetallic Materials and Processes	Engineering Physics
Branch:	Polymers and Composites	NDE and Tribology

MSFC Colleague: Alan T. Nettles, Ph.D. Sam Russell, Ph.D., P.E.

## INTRODUCTION

The need for safe, lightweight, less expensive, and more reliable launch vehicle components is being driven by the competitiveness of the commercial launch market. The United States has lost 2/3 of the commercial launch market to Europe. As low cost Russian and Chinese vehicles become available, the US market share could be reduced even further. This international climate is driving the Single Stage To Orbit program at NASA. The goal of this program is to reduce the cost per pound of payload by a factor of 10. This will be accomplished with a totally reusable launch vehicle designed for low-cost aircraft-like operations. Achieving this goal will require more efficient use of materials. Composite materials can provide this program with the material and structural efficiencies needed to stay competitive in the international launch market place.

In satellite systems the high specific properties, design flexibility, improved corrosion and wear resistance, increased fatigue life, and low coefficient of thermal expansion that are characteristic of composite materials can all be used to improve the overall satellite performance. Some of the satellites that may be able to take advantage of these performance characteristics are the Tethered Satellite Systems (TOSCIFER, AIRSEDS, TSS2, SEDS!, and SEDS2), AXAF, GRO, and the next generation Hubble Space Telescope. These materials can also be utilized in projects at the NASA/MSFC Space Optics Technology and Systems Center of Excellence.

The successful implementation of composite materials requires accurate performance characterization. The performance of composite materials is dependent on the constituent materials selected, material structural geometry, and the fabrication process. Flaws can form in composite materials as a result of the fabrication process, handling in the manufacturing environment, and exposure in the service environment to anomalous activity. Often these flaws show no indication on the surface of the material while having the potential of substantially degrading the integrity of the composite structure. For this reason it is important to have available inspection techniques that can reliably detect sub-surface defects such as inter-ply disbonds, inter-ply cracks, porosity, and density changes caused by variations in fiber volume content.

Many non-destructive evaluation techniques (NDE) are capable of detecting sub-surface flaws in composite materials. These include shearography, video image correlation, ultrasonic, acoustic emissions, and X-ray. The difficulty with most of these techniques is that they are time consuming and often difficult to apply to full scale structures. An NDE technique that appears to have the capability to quickly and easily detect flaws in composite structure is thermography [1,2]. This technique use heat to detect flaws. Heat is applied to the surface of a structure with the use of a heat lamp or heat gun. A thermographic camera is then pointed at the surface and records the surface temperature as the composite structure cools. Flaws in the material will cause the thermal-mechanical material response to change. Thus, the surface over an area where a flaw is present will cool differently than regions where flaws do not exist. Figure 1 is an illustration of a thermographic image of composite tubes that have service damage present.

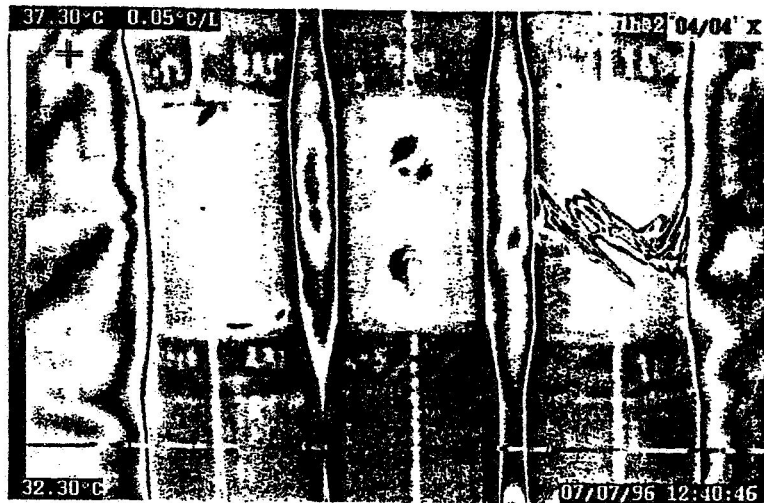


**Figure 1: Thermographic images of 2" diameter composite tubes with defects.**

In Figure 1 the thermographic image of the tube on the far left is indicating that damage is present near the top end-tab. The center tube was impacted and the dark spots indicate the impact sites. The right side tube has been cyclically loaded to a level below the life of the tube. Damage is present in the mid-section of the tube. There is no indication on the surface of these tubes that any damage exists. Although these images indicate that damage is present, they do not provide a description of the damage that would allow an engineer to determine if the damage has compromised the integrity of the structure.

To help explore the capability of the thermographic technique a finite element model was developed to study the flow of heat through composite materials so that the thermographic images can be better interpreted. Some of the issues that the model can help to resolve include the sensitivity of the technique to various types of material defects such as inter-ply disbonds, intra-ply cracking, porosity, and density changes. Modeling can help define the bounds of the technique and optimize the use of the technique.

In the remainder of this report the effort to thermo-mechanically model the thermography process will be discussed. First the material properties and physical parameters used in the model will be explained. This will be followed by a detailed discussion of finite element model used. Finally, the result of the model will be summarized along with recommendations for future work.

### **MATERIAL PROPERTIES AND PHYSICAL PARAMETERS**

The governing equation for conduction heat transfer is as follows.

$$\rho \cdot c \cdot \frac{\partial T}{\partial t} = \frac{\partial}{\partial x} \left( k_x \cdot \frac{\partial T}{\partial x} \right) + \frac{\partial}{\partial y} \left( k_y \cdot \frac{\partial T}{\partial y} \right) + \frac{\partial}{\partial z} \left( k_z \cdot \frac{\partial T}{\partial z} \right) \quad (1)$$

In Equation (1) T is temperature, t is time,  $\rho$  is material density, c is specific heat, and k is thermal conductivity in the respective directions. From this equation it is clear that the density, specific heat, and thermal conductivity need to be calculated for the composite structure under consideration in order to model the transient heat transfer problem.

Measured values of the thermal properties for the composite were not available so the material properties were predicted using micromechanics. The composite under consideration is made of HMS fiber (like IM7) and 977-2 matrix in a  $[\pm 25/90]_s$  laminate geometry. This geometry is chosen because it represents a typical rocket motor analog geometry. The lamina or ply level properties are calculated using a spherical inclusion model based on the differential scheme [3,4,5]. The laminate properties are not computed because each ply of the laminate is modeled separately in the finite element model. The thermal-mechanical lamina properties for the material under consideration are summarized in Table 1.

**Table 1: Predicted thermal-mechanical properties for the HMS/977-2, lamina**

Elastic Modulus lb/in <sup>2</sup>		Shear Modulus lb/in <sup>2</sup>		Poisson's Ratio	
E <sub>11</sub>	32.6(10 <sup>6</sup> )	G <sub>12</sub>	0.770(10 <sup>6</sup> )	$\nu_{12}$	0.414
E <sub>22</sub>	0.874(10 <sup>6</sup> )	G <sub>13</sub>	0.277(10 <sup>6</sup> )	$\nu_{13}$	0.576
E <sub>33</sub>	0.874(10 <sup>6</sup> )	G <sub>23</sub>	0.770(10 <sup>6</sup> )	$\nu_{23}$	0.414

Thermal Expansion 1/°F		Thermal Conductivity Btu/in-s-°F			
$\alpha_{11}$	-0.271(10 <sup>-6</sup> )	k <sub>11</sub>	0.0304	c	0.3032 Btu/lb-°F
$\alpha_{22}$	14.7(10 <sup>-6</sup> )	k <sub>22</sub>	0.00260		
$\alpha_{33}$	14.7(10 <sup>-6</sup> )	k <sub>33</sub>	0.00260	$\rho$	0.0621 lb/in <sup>2</sup>

When porosity is considered, voids are added to the matrix material using the spherical inclusion differential scheme. Then the lamina material properties are computed. For the case of 15% voids the fiber direction thermal conductivity is reduced by 14%, the transverse conductivity by 65%, the specific heat by 24%, and the density by 11%.

Besides the material properties the other parameter of importance to the development of this model are the heat flux input to the plate as a result of the heating of the surface and the natural convection off of the back side of the plate. In reality, the input heat flux is due to radiation. Since the emissivity of the material surface and the temperature of the heat lamps are

unknown, a heat flux input is estimated that would create a  $10^\circ$  heating of the plate surface. This is the value observed in experiments. The value of the heat flux in the model is  $0.5 \text{ Btu/in}^2\text{-}^\circ\text{F}$ . On the back surface of the plate natural convection takes the heat away. The coefficient for natural convection used is  $2(10^{-5}) \text{ Btu/s-in}$ .

### **FINITE ELEMENT MODEL**

A finite element model is used to investigate the transient heat transfer in an 8in by 8in composite plate with various types of flaws utilizing 8-node isoparametric brick elements. Each layer of the composite was one element thick. An 0.5in by 0.5in flaw was located in the center of the plate in the third ply from the top. Quarter symmetry was employed in the discretization. To avoid convergence problems the aspect ratio for each element was held to a maximum of 8 to 1. Time steps for the model are set to 0.001s up to 0.1s. The heat flux is applied to the top surface of the model for the first 0.01s and is then removed.

Figure 2 illustrate the result of the finite element analysis for the case of a 3 element by 3 element (0.24 in by 0.24 in) disbond was located between the second and third layers from the top. This figure represents the temperature distribution in the plate at 0.01s into the model. The temperature above the disbond is  $10^\circ$  warmer than the elements directly below the disbond. The temperature in the plate equilibrates at 0.05s into the model. This is not much different than what is observed in the experimental results.

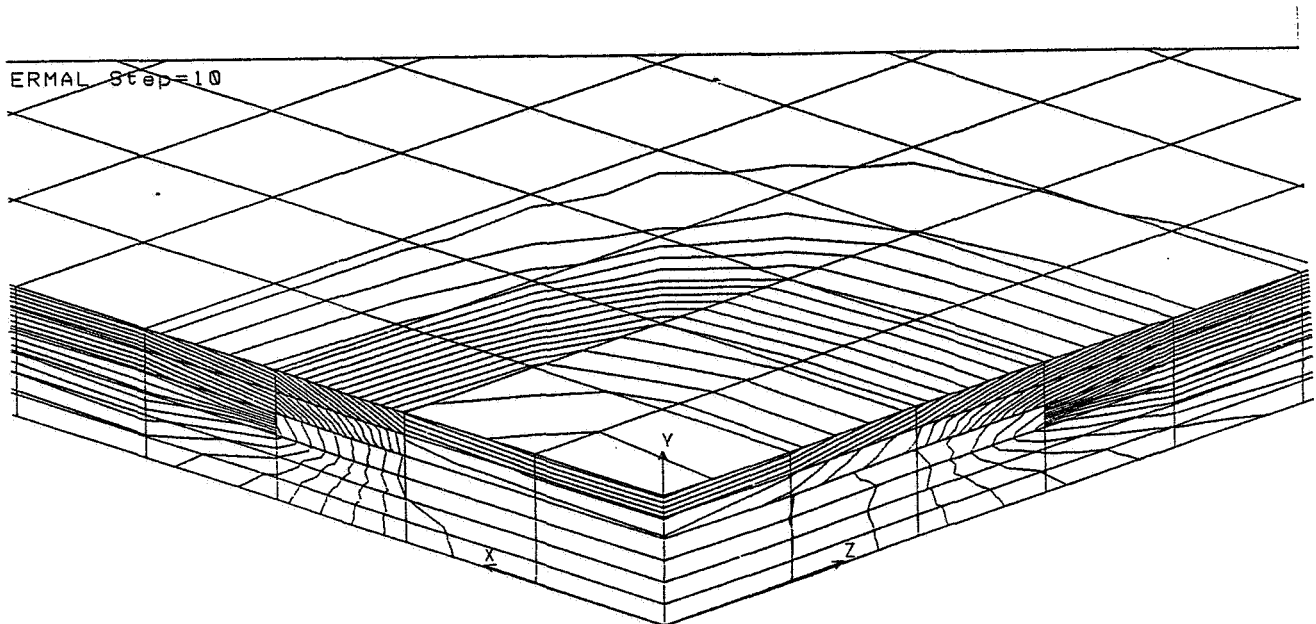


**Figure 2: Finite element result for the case of a disbond between layers 2 and 3 at 10ms into the loading**

The effect of porosity on the heat transfer is also modeled. Porosity as high as 15%, by volume, is added to the model in a 3 element by 3 element square in the third layer from the top of the plate. This model resulted in less than a 2° temperature gradient in the model.

## **RESULTS AND CONCLUSIONS**

The finite element method has been shown to be a tool that can help investigators determine the meaning of thermographic images. Finite element models can also help to determine the bounds of the thermographic technique. Areas that the finite element method can assist investigators in are:

- 1) Determine the sensitivity of the technique to transverse cracks, inclusions, and multiple flaws,
- 2) Developing a methodology for using thermography to determine the depth of flaws,
- 3) Evaluating the effects of forced convection on enhancing the thermographic results, and
- 4) Determine plate thickness bound in which the technique is valid.

If the finite element technique is going to be used to model the behavior of a specific plate, the emissivity of the composites surface, energy imparted by the heating system, and accurate material properties will have to be identified.

It is recommended that the investigation of the thermographic process using the finite element technique be continued so that a deeper understanding of the meaning of the thermographic images can be developed

## **REFERENCES**

- 
- 1 Winfree, W.P., James, P.H., "Thermographic Detection of Disbonds," *proceedings of the 35th ISA International Instrumentation Symposium*, Pg. 183-188, 1989
  - 2 Bouvier, C.G., "Investigating Variables in Thermographic Composite Inspections," *Materials Evaluation*, (May 1995), pp 544-551.
  - 3 McLaughlin, R., "A study of the Differential Scheme for Composite Materials," *International Journal of Engineering Science*, 15(1997), pp. 237-244.
  - 4 Boucher, S., "On the effective moduli of isotropic two-phase elastic composites," *Journal of Composite Materials*, 8(1974), pp. 82-89
  - 5 Christensen, R.M., *Mechanics of Composite Materials*, John Wiley & Sons, New York, 1979.



1996

**NASA/ASEE SUMMER FACULTY FELLOWSHIP PROGRAM**

**MARSHALL SPACE FLIGHT CENTER  
THE UNIVERSITY OF ALABAMA**

**NEW INTERFACES TO WEB DOCUMENTS AND SERVICES**

Prepared By:	W. H. Carlisle, Ph.D.
Academic Rank:	Associate Professor
Institution and Department	Auburn University Department of Computer Science and Engineering

**NASA/MSFC**

Office:	Program Development
Division:	Advanced Systems and Technology
Branches:	Advanced Concepts Office, Space Science and Applications

Office:	Science and Engineering Astrionics Laboratory
Division:	Avionics Simulation Division, Software Division
Branches:	Computer Systems Engineering, Requirements and Technology

MSFC Colleagues:	Dan O'Neil, MSFC Colleague Ron Newby, MSFC Colleague
------------------	---

This reports on investigations into how to extend capabilities of the Virtual Research Center (VRC)<sup>1</sup> for NASA's Advanced Concepts Office. The work was performed as part of NASA's 1996 Summer Faculty Fellowship program, and involved research into and prototype development of software components that provide documents and services for the World Wide Web (WWW)<sup>2</sup>. The WWW has become a de-facto standard for sharing resources over the Internet, primarily because web browsers are freely available for the most common hardware platforms and their operating systems. As a consequence of the popularity of the internet, tools and techniques associated with web browsers are changing rapidly. New capabilities are offered by companies that support web browsers in order to achieve or remain a dominant participant in internet services. Because a goal of the VRC is to build an environment for NASA centers, universities, and industrial partners to share information associated with Advanced Concepts Office activities, the VRC tracks new techniques and services associated with the web in order to determine the their usefulness for distributed and collaborative engineering research activities. Most recently, Java<sup>3</sup> has emerged as a new tool for providing internet services. Because the major web browser providers have decided to include Java in their software, investigations into Java were conducted this summer.

## **The World Wide Web**

The WWW functions as a client and server system. Clients request information via an address called a Uniform Resource Locator (URL). For example, the URL `http://nova.msfc.nasa.gov:80` contains the location (`msfc.nasa.gov`), the machine (`nova`) the protocol for the communication (`http` - HyperText Transfer Protocol), and a socket (`80`) to connect to for this communication. Servers are programs that listen to sockets for client requests and provide services based on the port, or on information provided by the protocol associated with the port. Although web browsers support services such as `ftp` (default port 21, protocol `ftp`), `gopher` (default port 70, protocol `gopher`), etc., the term web generally means support for the `http` protocol (default port 80, protocol `http`). Within the `http` protocol, a negotiation of service is carried out by adding a MIME (Multimedia Internet Mail Extension) header to the communication. For example, the MIME type "`text/html`" indicates that the document being communicated contains text representing the HyperText Markup Language (HTML). HTML is the most common form of communication between web browser clients and servers.

## **CGI Scripts**

In order to support dynamic creation of documents for clients or provide access to other services such as a database, servers may act as a gateway. A script or program is invoked by the server on behalf of a client request. The program or script that is executed creates or gathers information, and passes it back to the client through the web server. The Common Gateway Interface (CGI)<sup>4</sup> is the most common mechanism for communicating between a program and a Web server. CGI gateway programs can be scripts or programs written in any language. Generally the gateway programs generate HTML and provide this information to the Web server, but they can return the URL of another file indicating to the browser that it should get that file. HTML provides for forms as a means to collect information to interface with a CGI script.

If the web server and the service offered to this server are running on the same platform, then the server machine is performing most of the work associated with a client's query. Java presents an alternative capability to Web clients, and allows work to be shifted from the server to the client.

## Java

Java is a new programming language. Because of its simple design, Java has emerged as a possible contender to connect users and information in a new way within the World Wide Web. Most web browsers now come with the ability to download and execute Java code. Within an HTML page a definition such as

```
<APPLET href="MailApplet.class" WIDTH=400 HEIGHT=300> </APPLET>
```

specifies that at this point a program will be downloaded to be executed by the client. That program will appear in a frame on the page. Now the client is able to display the results of a general purpose program, can interact with CGI programs, or can communicate directly with ports on the server. Currently a client applet program is restricted to dealing only with the server, but this may change. For security, the client applet is also unable to read or write files from the client's system, but this may change since many browsers provide this capability when client permission is given. The remainder of this paper illustrates experiments performed using a Java browser to connect to services provided by the Web server for the VRC.

## A Client Server Example

The following example is a client program that displays two text widgets for input of a radius or a sphere's surface area. Additionally there is a submit button and a reset button. If the user inputs and then submits a radius, the surface area is printed in the area window. If a surface area is submitted, then the radius is printed in the window. The client does none of the calculation except the reset, and sends the numbers to a server over a socket. The server does the calculation and returns the information to the client. In this example, a server is written in C that listens to a port for a client. The client is a Java applet. Upon a connect, the server creates a child process to handle the client, and then continues to listen to the port. The child process reads from the socket

```
readin = read(new_desc, line, MAXLINE);
```

determines the two numbers, does the calculation, and returns the result to the client.

```
sscanf(line, " %f %f", &f1, &f2);
if( f1 != 0.0 )
f2 = 4*3.14159*f1*f1;
else if (f2 != 0.0)
f1=sqrt(f2/(4 * 3.14159));
```

```
sprintf(line, "%f\n%f\n", f1, f2);
```

```
write(new_desc, line, strlen(line));
```

The client is displayed from an HTML page:

```
<HTML>
<HEAD><TITLE> Surface Area of a Sphere </TITLE></HEAD>
<BODY>
<APPLET CODE="Surface3.class" HEIGHT=100 WIDTH=200></APPLET>
</BODY></HTML>
```

The code concerned with the socket is shown below.

```
public static final int PORT = 4000;

public boolean action( Event evt, Object arg) {
    if (arg.equals("Submit")) {
        // now try to get a socket
        try {
            soc = new Socket("nova.msfc.nasa.gov", PORT);
            in = new DataInputStream(soc.getInputStream());
            out = new PrintStream(soc.getOutputStream()); }
        catch(IOException e) {
            System.out.println(e.toString());
            System.exit(0); }
        out.println(r.getText());
        out.println(s.getText());
        try{
            r.setText(in.readLine());
            s.setText(in.readLine()); }
        catch(IOException e) {
            System.out.println(e.toString());
            System.exit(0); } }
```

### A Java to CGI example

The VRC has many CGI scripts that perform as gateways to other services such as database interaction. It would be nice if there was a way for an applet to use the CGI mechanism that is already present in browsers. Unfortunately the Java library does not currently provide such a communication path. A CGI script can be invoked manually, the same as a Web browser,

```
Socket s = new Socket("nova.msfc.nasa.gov", 80);
```

and deal with a cgi program through the server. But without a way to pass return information to the browser, cgi scripts that return html documents are of little use to a Java program. However Java clients will need to use CGI gateways as long as the clients are restricted to communicating with only the server machine.

An example was written to illustrate how Java applets may communicate with a VRC database via a server. The client runs as a Java applet on any system. The server runs on the VRC test web server (nova.msfc.nasa.gov), and the database is on a VRC database architecture (astrionics.msfc.nasa.gov). The Java client code is found in the appendix, but that part that

illustrates opening of the socket and manipulation of the two text windows (s is the name for the input of SQL commands, the window v is for output of the database query) is given below. Notice that the client opens a connection to the Web server, and provides a path to the CGI script that is running on the server (in this case the program /cgi-bin/sqlquery). The CGI script is a compiled C program that makes a database query and returns the text as output to the Java client.

```
public void submit(String sdata)
{
    String home = "nova.msfc.nasa.gov";
    String script = "/cgi-bin/sqlquery";
    int port = 80;
    Socket s = null;
    rdata = "";
    try
    {
        s = new Socket(home, port);
        DataOutputStream os
            = new DataOutputStream(s.getOutputStream());
        DataInputStream is
            = new DataInputStream(s.getInputStream());
        os.writeBytes("POST " + script + " HTTP/1.0\r\n"
            + "Content-type: text/plain\r\n" + "Content-length: "
            + sdata.length() + "\r\n\r\n");
        os.writeBytes(sdata);
        String line;
        while ((line = is.readLine()) != null)
            rdata += line + "\n";
        v.setText(rdata);
        os.close();
        is.close();
    }
}
```

## Other New Browser Capabilities

For security reasons, browsers have not generally provided a way for servers to access the disk of the client machine. The most recent versions of Netscape have however included this capability as an experiment. It is still open as to whether this will become a standard part of HTML. In order to experiment with this capability, Perl5 was installed on the test VRC server, and Perl libraries that interface with Oracle databases and provide CGI capabilities were installed. A script was written that provides a user the capability to name a file and upload this file to the server. The script dynamically creates the HTML page for the user, and the critical portion of this code is given below:

```
print '<b> For uploading a file, enter a fully pathed file ',
    '<p> Examples:<ul><li>/home/my/filename - in UNIX
        <li> c:\path\to\myfile - in DOS
        <li> HD 40: Desktop Folder: This File - for Macs </ul>',
    '<p>OR press Browse to browse your file system.<b>';
print $query->start_multipart_form("POST",
    "/cgi-bin/carlisle/savefile",$CGI::MULTIPART);
print $query->filefield(-name=>'uploaded_file', -default => 'ignored',
    -size=>50, -maxlength=>80);
```

```
print $query->hidden(-name=>'dirname',-default=> ["$root$file"]);
print '<br>';
print $query->submit(-name=>"Submit", -value=>'Submit this File');
print $query->endform;
```

Upon submission of this form, the cgi-script “savefile” is called. The Perl code for this script is:

```
#!/usr/bin/perl
use CGI;
$query = new CGI;
$filename = $query->param('uploaded_file');
print $query->header;
$dirname= $query->param('dirname');
# this is a hack that I am sure will fail for some systems and
#some file names
$tmp = split(/[\\\:\/]/,$filename);
$filename = pop @tmp;
$outfile = "$dirname/$filename";
#to actually write the file comment out the next line
#and uncomment the open and following while
print $dirname,'/', $filename;
#while(<$filename) { print; }
#open(fp,">$outfile") || die("You do not have write permission at $dirname");
#while($bytesread=read($filename,$buffer,1024)) {
#    print fp $buffer; }
print '<p>';
print "File saved to $outfile"
```

Notice that the actual writing of the file has been commented out. This was done because currently this script has not been installed in a secure area on the server. Thus anyone would be able to upload files to the VRC, and a malicious or careless user could fill up and crash the disk of the server machine. This illustrates why the capability to upload information of unknown size to a server is a dangerous practice.

## CONCLUSIONS AND ACKNOWLEDGEMENTS

Future work will continue to address the rapidly changing environment known as the Web, and will incorporate those features into the laboratory that create an environment for collaborative research at distributed locations.

The author would like to acknowledge those at NASA who have made this summer such an enjoyable experience.

---

<sup>1</sup> <http://nova.msfc.nasa.gov>

<sup>2</sup> <http://www.w3.org>

<sup>3</sup> <http://java.sun.com>

<sup>4</sup> <http://hoohoo.ncsa.uiuc.edu/CGI/overview.html>



**1996**

**NASA / ASEE SUMMER FACULTY FELLOWSHIP PROGRAM**

**MARSHALL SPACE FLIGHT CENTER  
THE UNIVERSITY OF ALABAMA**

**A FLEXIBLE ALIGNMENT FIXTURE FOR THE  
FABRICATION OF REPLICATION MANDRELS**

Prepared By: James F. Cuttino, Ph.D., Assistant Professor  
Michael W. Todd, Masters Student

Institution and Department: The University of Alabama  
Department of Mechanical Engineering

NASA / MSFC:

Laboratory: Astrionics Laboratory  
Division: Optical Systems Division  
Branch: Optical Systems Fabrication

MSFC Colleague: James W. Bilbro





# **FLEXIBLE FIXTURING FOR FABRICATION OF REPLICATION MIRRORS**

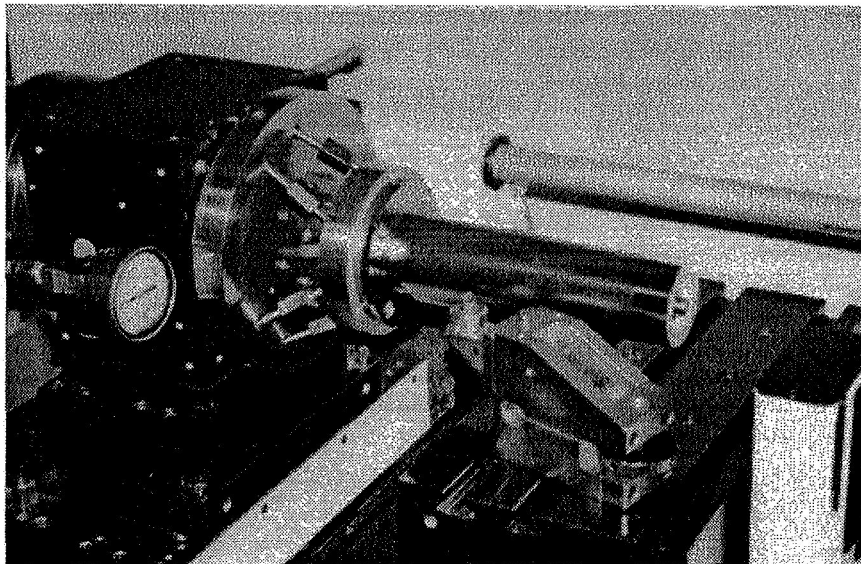
James F. Cuttino  
Assistant Professor

Michael W. Todd  
Graduate Student

Department of Mechanical Engineering  
The University of Alabama

Astrionics Laboratory  
Optics and Radio Frequency Division  
Optics Branch

James W. Bilbro, MSFC Colleague



## **INTRODUCTION**

NASA uses precision diamond turning technology to fabricate replication mandrels for its X-ray Calibration Facility (XRCF) optics. As shown in Figure 1, the XRCF optics are tubular, and the internal surface contains a parabolic profile over the first section and a hyperbolic profile over the last. The optic is fabricated by depositing layers of gold and nickel on to the replication mandrel and then separating it from the mandrel. Since the mandrel serves as a replication form, it must contain the inverse image of the surface. Figure 1 shows the components of the fabrication mandrel that are necessary to facilitate mounting, handling, and polishing during the fabrication process.

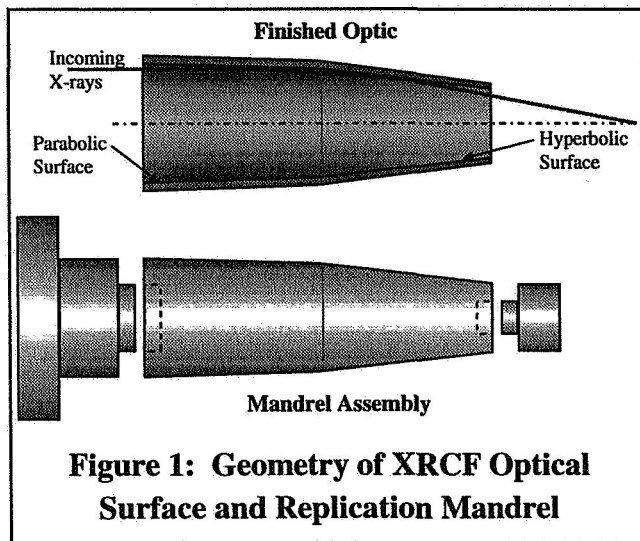


**Figure 1: Geometry of XRCF Optical Surface and Replication Mandrel**

The difficulty in aligning the mandrel comes from the fabrication steps which it undergoes. The mandrel is rough machined and heat treated prior to diamond turning. After diamond turning, silicon rubber separators which are undercut in radius by 3 mm (0.12") are inserted between the two end caps of the mandrel to allow the plating to wrap around the ends (to prevent flaking). The mandrel is then plated with a nickel-phosphor alloy using an electroless nickel process. At this point, the separators are removed and the mandrel is reassembled for the final cut on the DTM. The mandrel is

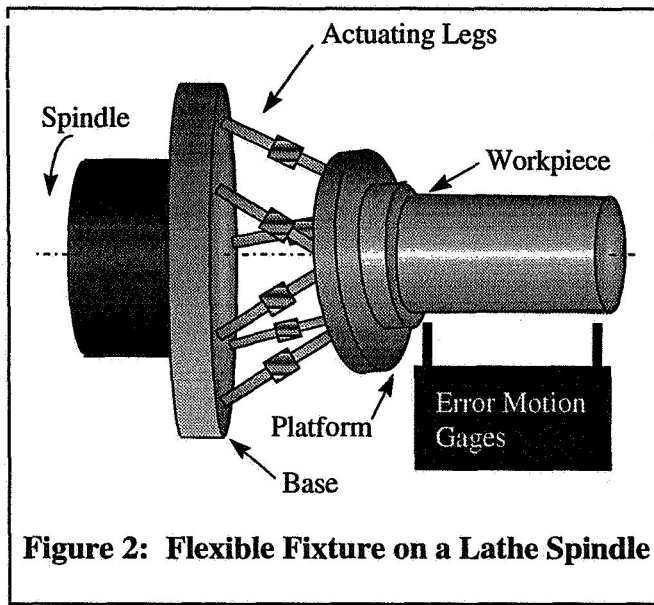
measured for profile and finish, and polished to achieve an acceptable surface finish.

Wrapping the plating around the edges helps to prevent flaking, but it also destroys the alignment surfaces between the parts of the mandrel that insure that the axes of the parts are coincident. Several mandrels have been realigned by trial-and-error methods, consuming significant amounts of setup time. When the mandrel studied in this paper was reassembled, multiple efforts resulted in a minimum radial error motion of 100  $\mu\text{m}$ . Since 50  $\mu\text{m}$  of nickel plating was to be removed, and a minimum plating thickness of 25  $\mu\text{m}$  was to remain on the part, the radial error motion had to be reduced to less than 25  $\mu\text{m}$ . The mandrel was therefore unusable in its current state.

## DESIGN OF FIXTURE

To provide the motion necessary to align the mandrels, the *Flexible Alignment Fixture*, or *FAF*, was designed to replace the vacuum chuck normally used on the DTM. The design goals were to allow for linear displacements of 250  $\mu\text{m}$  and rotations of 0.003 radians at the platform of the alignment fixture (over a 8" long mandrel, 0.002 radians results in an equivalent translation of one end of 400  $\mu\text{m}$ , or 0.016").

The design utilizes a 6 legged hexapod arrangement to provide full flexibility and high stiffness. Figure 2 is a conceptual drawing of the *FAF* mounted on a diamond turning machine. The fixture has a base that mounts directly to the spindle bearing and a platform suspended by the six legs. The workpiece is mounted directly to the platform.



Since the required motion was very small, the flexure was designed to rely on deformation of the legs rather than joints to allow relative motion of each leg. The stress was calculated for each leg based on a maximum deflection, and the legs were designed to provide a factor of safety of 8 to 10. The legs were threaded on each end and screwed directly into the base and the platform, and preloading was achieved by lowering the platform towards the base, thus introducing a bending moment in each leg.

The legs of the *FAF* utilized a differential pitch arrangement to provide high resolution motion. A 3/8-24 UNF thread was machined on the portion of the leg inserted into the base of the *FAF*, and a 7/16-20 UNF thread was machined on the end inserted into the platform. This differential pitch in the screw provides a linear displacement of 210  $\mu\text{m}$  per turn of the leg. In order to facilitate assembly of the *FAF*, the legs were fabricated in two sections joined in the middle by a hex nut. The legs were constructed from AISI 410 stainless steel and were heat treated for additional strength.

## ERROR MOTION AND KINEMATICS

Two dial indicators were used to measure the error motion of the mandrel at four equally spaced rotational positions. By placing the indicators at determined positions along the axis of the mandrel, two measurements at each of the four rotational positions provided the necessary error motion information. The required translation and rotation of the platform were determined in a MATLAB program based on these measurements. The hexapod kinematics were then developed to transform the required platform motion into leg rotations, bringing the axis of the mandrel on to the axis of rotation of the spindle.

## EXPERIMENTAL RESULTS

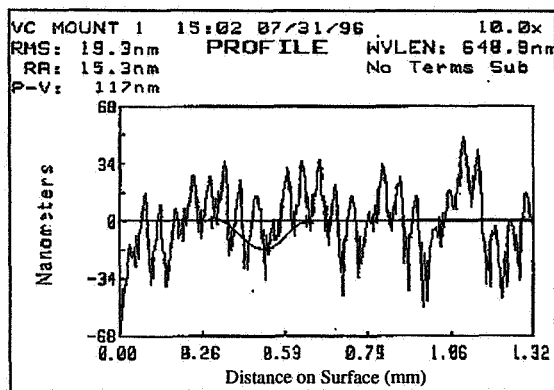
The vacuum chuck of the DTM was replaced with the *FAF* for testing. When mounted on the original equipment vacuum chuck, the test mandrel had a minimum error motion of 100  $\mu\text{m}$ , which was only achieved after significant effort to align the mandrel pieces. Mounting the mandrel on the *FAF* provided the necessary freedom to align the axis of the mandrel to that of

the DTM spindle. Once mounted, the error motion was measured by two dial indicators at four equally spaced rotations of the spindle to determine the proper adjustment. The measurement values were input to the kinematic program to determine the required leg rotations. With the *FAF*, the same mandrel was aligned to within 8  $\mu\text{m}$  error motion with minimal effort, representing a 92% reduction in the error. The 8  $\mu\text{m}$  error was significantly less than the target requirement of 25  $\mu\text{m}$ .

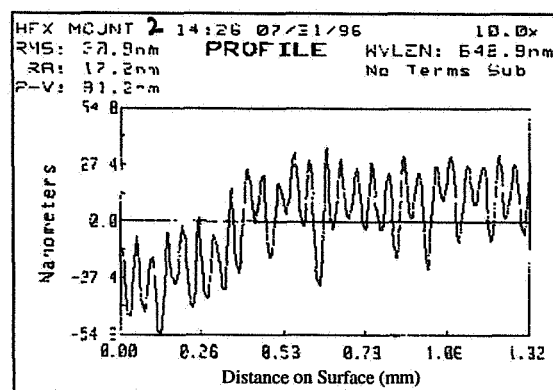
The measures for success in the project included not only the ability to diamond turn the mandrel without penetrating the nickel plating, but also to achieve surface finishes and *form* errors (low frequency errors) that were comparable to or better than those on the conventionally turned mandrels. The mandrel cut on the *FAF* was therefore compared to one that had been successfully aligned on the vacuum chuck without the *FAF*. Visual inspection of the mandrel cut on the *FAF* showed significant improvement over the mandrel cut on the vacuum chuck. This conclusion was verified using a WYKO *Topo-2D/Topo-3D* surface interferometer.

Figure 3 shows the surface profiles of the benchmark mandrel cut on the vacuum chuck and the mandrel cut on the *FAF*. The traces were limited to 1.32 mm. As shown in Figure 3a, the mandrel cut on the vacuum chuck has several components of error. The scan appears to consist of three fundamental components with wavelengths of approximately 0.25 mm, 0.05 mm, and a high frequency noise with wavelength of around 0.001 mm. The feedrate of the slide was 3 mm/min (0.05 mm/s), and the spindle speed was 1000 rpm (17 Hz). Based on the feedrate, the surface components had frequencies of 0.2 Hz, 1 Hz, and 50 Hz respectively. The fact that no component appears at 17 Hz indicates that the error motion is not one due to spindle error but rather slideway or tool post error. The rms amplitude of the error was 19.3 nm. A complex mounting configuration unfortunately prohibited more than one scan of this specimen.

Several traces were taken of the mandrel cut with the *FAF*. Figure 3b shows one trace which is representative of all of the traces taken, but a significant discrepancy was realized in the amplitude of the error, which ranged from an rms value of 17 nm to 60 nm. Since only one trace was made of the benchmark mandrel, the amplitude data is considered inconclusive. The trace shown in Figure 3b has an rms amplitude of 20.9 nm and shows an error component with a 1 Hz frequency (wavelength = 0.05 mm) superimposed on a very low frequency trend (possibly not even periodic) which is outside the scan range of the interferometer. While the discrepancies in the results require further investigation, it appears that using the *FAF* actually reduced the 0.2 Hz and 50 Hz error motions seen in the benchmark mandrel. The form error (low frequency component) is not conclusive since the trace is so small. It seems likely that this error may also show up in the benchmark case given longer surface traces. The elimination of the 50 Hz component in the mandrel cut on the *FAF* explains the visible improvement in surface finish on the part.



a) Mandrel cut on Vacuum Chuck



b) Mandrel Cut on *FAF*

**Figure 3: Surface Profiles of Mandrels**

Both parts are currently being measured off-site using a *Long Trace Profilometer* to determine the actual error in each part. The preliminary results above, however, seem to indicate that the hexapod may help to reduce the error motion while salvaging the part.

## CONCLUSION

A six-degree-of-freedom Flexible Alignment Fixture (*FAF*) has been developed to adjust the position and orientation of a workpiece on a diamond turning machine spindle. The device uses a hexapod design and kinematic analysis to reposition the workpiece. The designed range of motion allows for displacements of 250  $\mu\text{m}$  and changes in orientation of 0.003 radians.

A fabrication mandrel for NASA's XRCF project which was unusable due to alignment problems has been salvaged using the *FAF*, which was able to reduce the error motion from 100  $\mu\text{m}$  to 8  $\mu\text{m}$ . The *FAF* also greatly reduces the effort necessary in insuring the alignment of the mandrel components prior to cutting. Preliminary results indicate that improved surface finish may be an added benefit to using the *FAF*. Pending results from a long trace profilometer will yield more information on the effectiveness of the *FAF*.

## ACKNOWLEDGEMENTS

Sincere thanks go to Dr. David L. Lehner, Mr. William D. Jones, Mr. John Cernosek, and Mr. Kent Bachelor for their input and support on this project.



**1996**

**NASA/ASEE SUMMER FACULTY FELLOWSHIP PROGRAM**

**MARSHALL SPACE FLIGHT CENTER  
THE UNIVERSITY OF ALABAMA**

**INTEGRATION OF THE SHUTTLE RMS/CBM POSITIONING  
VIRTUAL ENVIRONMENT SIMULATION**

Prepared By:	Joseph D. Dumas II, Ph.D.
Academic Rank:	Assistant Professor
Institution and Department:	University of Tennessee at Chattanooga Department of Computer Science and Electrical Engineering
NASA/MSFC:	
Laboratory:	Mission Operations Laboratory
Division:	Training and Crew Systems Division
Branch:	Systems Branch
MSFC Colleagues:	Joseph Hale Richard Dabney





## INTRODUCTION

Constructing the International Space Station, or other structures, in space presents a number of problems. In particular, payload restrictions for the Space Shuttle and other launch mechanisms prohibit assembly of large space-based structures on Earth. Instead, a number of smaller modules must be boosted into orbit separately and then assembled to form the final structure. The assembly process is difficult, as docking interfaces such as Common Berthing Mechanisms (CBMs) must be precisely positioned relative to each other to be within the "capture envelope" (approximately  $\pm 1$  inch and  $\pm 0.3$  degrees from the nominal position) and attach properly. In the case of the Space Station, the docking mechanisms are to be positioned robotically by an astronaut using the 55-foot-long Remote Manipulator System (RMS) robot arm. Unfortunately, direct visual or video observation of the placement process is difficult or impossible in many scenarios. One method that has been tested for aligning the CBMs uses a boresighted camera mounted on one CBM to view a standard target on the opposing CBM. While this method might be sufficient to achieve proper positioning with considerable effort, it does not provide a high level of confidence that the mechanisms have been placed within capture range of each other [1]. It also does nothing to address the risk of inadvertent contact between the CBMs, which could result in RMS control software errors. In general, constraining the operator to a single viewpoint with few, if any, depth cues makes the task much more difficult than it would be if the target could be viewed in three-dimensional space from various viewpoints. The *actual* work area could be viewed by an astronaut during EVA; however, it would be extremely impractical to have an astronaut control the RMS while spacewalking. On the other hand, a view of the RMS and CBMs to be positioned in a *virtual* environment aboard the Space Shuttle orbiter or Space Station could provide similar benefits more safely and conveniently with little additional cost.

In order to render and view the RMS and CBMs in a virtual world, the position and orientation of the end effector in three-dimensional space must be known with a high degree of accuracy. A precision video alignment sensor [1] has been developed which can determine the position and orientation of the controlled element relative to the target CBM within approximately one-sixteenth inch and 0.07 angular degrees. Such a sensor could replace or augment the boresighted camera mentioned above. The computer system used to render the virtual world and the position tracking systems which might be used to monitor the user's movements (in order to adjust the viewpoint in virtual space) are small enough to carry to orbit. Thus, such a system would be feasible for use in constructing structures in space.

In order to investigate the properties and limitations of a system providing virtual presence in the vicinity of the end effector of the Shuttle RMS, it was proposed to create a similar virtual environment in the CAVE (Computer Applications and Virtual Environments) laboratory at MSFC. This system would be very similar to the proposed system described above, with the obvious exception that an actual Shuttle RMS could not be used. Fortunately, existing simulation facilities at MSFC include a highly detailed model of the RMS dynamics running on an Alliant FX-8 supercomputer. This model runs in real-time with an input/output loop executing every 40 milliseconds. When provided with actual or simulated six-degree-of-freedom hand controller inputs, the RMS simulation computes the position and orientation of the RMS system in space. The coordinates of the controlled CBM relative to the target, as well as other variables such as RMS arm joint angles, needed to render the visual scene displayed to the operator, are available

as simulation outputs updated every 40 milliseconds.

The integration of the "virtual RMS" simulation involved establishing data communications between a number of disparate devices. One key element of the simulation is the set of two hand controllers (identical to those used on the Space Shuttle orbiter) for the RMS. The three-degree-of-freedom controller for the user's left hand is used to input translational (X, Y, and Z axis) positioning commands for the payload on the end effector of the RMS; the right hand controller is a joystick type control used to provide angular orientation commands (roll, pitch, and yaw) for manipulating the payload. A second key element of the virtual environment simulation is the real-time RMS dynamics model described previously. The Alliant supercomputer which runs this model is located in MSFC building 4663, while the rest of the simulation system hardware resides in the CAVE laboratory in building 4610. The third key element of the simulation is a set of three-dimensional graphical models of the RMS, space station modules to be joined (with their CBMs), and surrounding objects such as the orbiter. The purpose of the simulation is for the user to be able to view the process of positioning the controlled CBM from any location in the vicinity of the mechanisms to be joined. This is accomplished by determining the position and orientation of the user's head using a six-degree-of-freedom spatial tracking system (Polhemus Fastrak) and using this information to navigate the user's viewpoint in the three-dimensional virtual environment. The scene is rendered by a high-speed Silicon Graphics Indigo<sup>2</sup> workstation and viewed by the user through a Head-Mounted Display (HMD).

All of the simulation elements just described must be integrated smoothly, and with as little temporal lag as possible, in order to give the user a sense of presence in the virtual world and allow effective control of the payload. At the commencement of the author's Summer Fellowship, procurement of necessary equipment such as the RMS hand controllers, data acquisition board, and SCRAMnet fiber optic data link boards had been accomplished, but no hardware or software integration had been done. The author was tasked with performing the necessary hardware integration; writing the software for interfacing, data communications, and navigation and object manipulation in the virtual environment; and testing and evaluating the simulator system.

## **APPROACH AND PROGRESS**

The basic requirements for integrating the simulation include acquiring user input from the hand controllers, transmitting the hand controller data to the Alliant supercomputer, communicating the RMS state information from the Alliant to the Indigo<sup>2</sup> graphics computer, and sending the user head position data from the Fastrak tracker to the Indigo<sup>2</sup> to determine the viewpoint for the rendered scene. A later enhancement to these requirements was the ability to communicate hand controller inputs to the Indigo<sup>2</sup> as an alternative means of navigating the user's viewpoint.

Several factors complicated the relatively simple scenario just described. The only available interface device capable of translating analog data from the hand controllers into the 16-bit digital values required by the RMS simulation was a National Instruments AT-MIO-16X data acquisition board designed to fit into an IBM PC/AT compatible computer with EISA bus. Communication between the CAVE laboratory and the Alliant supercomputer was to be

implemented by a SCRAMnet fiber optic link. The SCRAMnet board is a VMEbus board which is not compatible with the chassis of the PC or the Indigo<sup>2</sup>; it could only be installed in another machine, a Silicon Graphics 320 VGX. Thus, the simulation network had to include four computers rather than two: the Alliant, with network name "*cat*"; the Indigo<sup>2</sup>, referred to as "*safire*"; the SGI 320 VGX, known as "*cave1*"; and an Intel 486DX-33 based PC called "*rmspc*". All communication between machines other than *cave1* and *cat* was to be done over an Ethernet-based local area network using IP (Internet Protocol). An Internet communication link between *cave1* and *cat* also had to be established for testing and integration of the system pending the installation of the fiber optic link (which has yet to be accomplished at the time of this report).

Besides the hardware differences between the four platforms, development of software was complicated by differences between the various operating systems and language compilers. Both Silicon Graphics machines (*safire* and *cat*) are Unix-based machines; the Indigo<sup>2</sup> (*safire*) runs IRIX 5.3 and ANSI C 3.19 (which were upgraded during the summer causing some delays) while the 320 VGX (*cave1*) runs IRIX 4.0.5 and ANSI C 1.1. The Alliant (*cat*) runs a real-time Unix kernel (Concentrix 5.7.00) and Concentrix C 4.0.17. The 486 PC (*rmspc*) runs MS-DOS 6.22; PC software was developed using Borland's Turbo C++ 3.0. For the most part, C language source code is compatible between the two SGI machines. A few modifications had to be made when coding for the Alliant, but the network function calls adhered to the same RPC (Remote Procedure Call) standard used on the SGI machines. The network function calls for the PC used Novell's LAN WorkPlace for DOS Socket Library, which is quite different from RPC; this complicated programming somewhat.

One of the first tasks in the integration of the simulation was to outfit a personal computer for the task of hand controller data acquisition. The other computers were already in place and connected to the Internet via local area networks. To complete the hardware test bed, however, a suitable PC (Intel 486-based) had to be located and a network interface card and software drivers had to be installed. With the network hardware and drivers and C compiler in place, test programs were developed to acquire and display analog data using the NI-DAQ (National Instruments Data Acquisition) library functions. Subsequently, code was added to broadcast the acquired data to the other machines using UDP (User Datagram Protocol, a connectionless, unreliable messaging protocol for sending data over the Internet). Corresponding code was written for the Silicon Graphics 320 VGX to accept data from the PC and relay it to the other computers.

In testing the UDP-based communications programs, it became evident that messages were arriving out of order on a regular basis, particularly in the case of communications to the Alliant (which is not on the CAVE lab local area network (LAN)). In many cases the exit message from the PC, which is used to terminate the simulation on the other three machines, would be lost and the programs on other machine(s) had to be aborted manually. Considering these problems and the fact that other data communications to and from the Alliant are done using TCP (Transmission Control Protocol, a connection-oriented messaging protocol which is slower but more reliable than UDP), it was decided to rewrite the communications code for all four machines using TCP sockets. Once debugging was completed, the TCP-based programs offered the advantage of easy two-way communication between machines (since sockets are bidirectional) in addition to enhanced reliability due to guaranteed message delivery.

While software development was in progress, a user interface station (the "Virtual Reality Chair") was being designed and constructed by MSFC support personnel. This user station consists of a wooden chair modified with two special arm rests on which the RMS hand controllers are mounted. A wooden chair was chosen in order to minimize the amount of metal in the simulation test bed area; metal objects can interfere with the performance of the Polhemus Fastrak magnetic spatial tracking system used to track the user's head movements. The arm rests can be pivoted to allow the user to easily enter and exit the chair, and allow him/her to adjust the lateral spacing between the controllers. The arm rests can also be adjusted vertically in order to accommodate users of varying heights. Finally, the hand controller mounts are slotted to allow them to be adjusted to various positions closer or farther away from the user. This reach adjustment helps to facilitate the comfortable use of the "VR chair" by operators of varying physical sizes. MSFC and contractor support personnel also assisted with manufacture of the cables used to connect the hand controllers with the data acquisition board and the Fastrak unit with the Indigo<sup>2</sup>.

Additional software development was needed in order to extract the RMS state vector and joint angles from the real-time simulation on the Alliant. Bob Linner of MSFC was asked to assist with this part of the project since he is most familiar with the simulation. Delays in completing this part of the overall simulation loop threatened to stall progress on the project. In the interim, a program 'comm50' was written to run on *cat*. It supplies fixed joint angles so a stationary RMS arm can be rendered, and echoes the hand controller data sent to it (after converting the values to floating-point format) so the controllers can be used to "fly" the simulated arm directly. This bypasses the RMS dynamics, reducing the fidelity of the simulation, but allowed development of the communications and graphics routines to proceed.

With communications among the various machines established, additional software routines were needed to create the graphical environment and manipulate the viewpoint and payload on the image generation computer *safire*. The simulation program on *safire* was developed using Sense8's WorldToolKit (WTK), a virtual environment development package which is available for a number of computing platforms including SGI machines. Three-dimensional graphical models of the objects of interest had already been developed by Mark Slone of MSFC. These models were defined as "C" code including SGI Graphics Library (GL) calls; thus, aside from some scaling and minor modifications to suit the application, they could be used directly on the SGI Indigo<sup>2</sup>. However, since the models were developed and integrated as GL code rather than WTK objects, WTK sensor objects could not be attached directly to the payload. Instead, software was developed to convert between GL and WTK coordinate systems and manipulate the object representing the payload. Since the user viewpoint is not attached to any graphical entity in the virtual world, it can be manipulated by WTK sensor update functions. Specifically, any of three WTK sensor objects can "fly" the viewpoint: the Polhemus Fastrak, the mouse, or the hand controllers (when set to "COARSE" mode only; "VERNIER" mode manipulates the RMS and its payload). The Fastrak and mouse drivers are supplied with WorldToolKit; the hand controller driver was developed for this project. It is also possible to add other input devices such as a Spaceball to manipulate the viewpoint for the simulation if desired, though the primary method envisioned for this is the use of the hand controllers for gross movements and the head tracker for fine adjustments of position and orientation.

A simulation is initiated by running the simulation coordinator program on the Silicon

Graphics 320 VGX computer (*cave1*). This program, 'simcave1', acts as a TCP/IP server, accepting socket connections from each of the other three computers. Simcave1 first waits for a connection from the data acquisition computer (*rmspc*). This will occur when the user runs the program 'simrmspc' from the MS-DOS prompt. Once the socket to *rmspc* is connected, *cave1* waits for and accepts a similar connection from the Alliant (established by running 'comm50' on *cat*) and finally from the Indigo<sup>2</sup> (the user should run 'simsafire' on *safire*). When all three sockets are connected, *cave1* enters the main program loop, which serves to sequence the order of events and transfer the data required for each frame of the simulation. This continues until the user strikes a key on the PC keyboard, or until an unrecoverable communications error occurs (which is rare). The user keystroke causes a special flag to be set which is passed to *cave1* and thence to the other two computers, causing them to exit their programs.

## CONCLUSIONS AND RECOMMENDATIONS

The virtual environment simulation described above was integrated over a 10-week period from May 20 - July 26, 1996. While some delays were encountered in obtaining hardware components and software to interface to the RMS simulation on the Alliant supercomputer, all data communications functions necessary for integration of the simulation were accomplished during the Fellowship period. Successful operation of the virtual environment simulation (minus the RMS dynamics) has been demonstrated. A user in the "VR chair" wearing a head-mounted display experiences an immersive graphical environment which reacts to user navigational and control inputs. Users of the simulator are able to control the positioning of the space station module and its CBM in a manner similar to the boresighted camera approach if desired, by simply observing the target CBM and manipulating the hand controllers. The real advantage of the simulated environment, however, is the ability of the user to adjust the viewpoint position and orientation using head movements and hand controller or mouse commands and thus get a three-dimensional, close-up view of the capture surfaces.

Possible follow-on work would include obtaining or developing more detailed three-dimensional models of the CBM in order to add greater realism to the simulation and give the user a virtual experience even more similar to the actual task. It also would be desirable to more thoroughly evaluate the system's performance (particularly in terms of frame rate and temporal lag) with a view towards improving those parameters and enhancing the user's perception of immersion in the virtual environment. Ultimately, human factors experiments should be designed and conducted to compare the system with the boresighted camera docking approach. Many other behavioral and training experiments might be devised to take advantage of this unique simulation testbed.

## REFERENCES

- [1] Dabney, R., Hale, J., and Linner, B. (1993). "An Interactive Stereo Graphic Robotic Manipulator Control Interface." Proposal for the 1993 Marshall Space Flight Center Director's Discretionary Fund, August, 1993.



**1996  
NASA/ASEE SUMMER FACULTY FELLOWSHIP PROGRAM**

**MARSHALL SPACE FLIGHT CENTER  
THE UNIVERSITY OF ALABAMA**

**Evaluation of an Anthropometric Human Body Model  
for Simulated EVA Task Assessment**

Prepared By: Brad Etter, Ph.D., P.E.  
Academic Rank: Assistant Professor  
Institution and Department: Texas A&M University  
Bioengineering Program

NASA/MSFC:

Laboratory: Mission Operations  
Division: Training and Crew Systems  
Branch: Systems

MSFC Colleague: Charlie Dischinger





## **Evaluation of an Anthropometric Human Body Model for Simulated EVA Task Assessment**

One of the more mission-critical tasks performed in space is extravehicular activity (EVA) which requires the astronaut to be external to the station or spacecraft, and subsequently at risk from the many threats posed by space. These threats include, but are not limited to: no significant atmosphere, harmful electromagnetic radiation, micrometeoroids, and space debris. To protect the astronaut from this environment, a special EVA suit is worn which is designed to maintain a sustainable atmosphere (at 1/3 atmosphere) and provide protection against the hazards of space. While the EVA suit serves these functions well, it does impose limitations on the astronaut as a consequence of the safety it provides.

Since the astronaut is in a virtual vacuum, any atmospheric pressure inside the suit serves to pressurize the suit and restricts mobility of flexible joints (such as fabric). Although some of the EVA suit joints are fixed, rotary-style joints, most of the mobility is achieved by the simple flexibility of the fabric. There are multiple layers of fabric, each of which serves a special purpose in the safety of the astronaut. These multiple layers add to the restriction of motion the astronaut experiences in the space environment.

Ground-based testing is implemented to evaluate the capability of EVA-suited astronauts to perform the various tasks in space. In addition to the restriction of motion imposed by the EVA suit, most EVA activity is performed in a micro-gravity (weightless) environment. To simulate weightlessness EVA-suited testing is performed in a neutral buoyancy simulator (NBS). The NBS is composed of a large container of water (pool) in which a weightless environment can be simulated. A subject is normally buoyant in the pressurized suit; however he/she can be made neutrally buoyant with the addition of weights. In addition, most objects the astronaut must interface with in the NBS sink in water and flotation must be added to render them "weightless". The implementation of NBS testing has proven to be invaluable in the assessment of EVA activities performed with the Orbiter and is considered to be a key step in the construction of the International Space Station (ISS).

While the NBS testing is extremely valuable, it does require considerable overhead to maintain and operate. It has been estimated that the cost of utilizing the facility is approximately \$10,000 per day. Therefore it is important to maximize the utility of NBS testing for optimal results. One important aspect to consider in any human/ worksite interface is the considerable wealth of anthropometric and ergonomic data available. A subset of this information specific to EVA activity is available in NASA standard 3000. The difficulty in implementing this data is that most of the anthropometric information is represented in a two-dimensional format. This poses some limitations in complete evaluation of the astronaut's capabilities in a three-dimensional environment. Advances in computer hardware and software have provided for three-dimensional design and implementation of hardware with the

advance of computer aided design (CAD) software. There are a number of CAD products available and most companies and agencies have adopted CAD as a fundamental aspect of the design process. Another factor which supports the use of CAD is the implementation of computer aided manufacturing (CAM) software and hardware which provides for rapid prototyping and decreases the time to product in the design process. It is probable that most hardware to be accessed by astronauts in EVA or IVA (intravehicular activity) has been designed by a CAD system, and is therefore represented in three-dimensional space for evaluation.

Because of the implementation of CAD systems and the movement towards early prototyping, a need has arisen in industry and government for tools which facilitate the evaluation of ergonomic consideration in a three-dimensional environment where the hardware has been designed by the CAD tools. One such product is Jack which was developed by the University of Pennsylvania with funding from several government agencies, including NASA.

While the primary purpose of Jack is to model human figures in a ground-based (gravity) environment, it can be utilized to evaluate EVA-suited activities as well. The effects of simulated gravity must be turned off by turning off "behaviors". Although Jack provides human figures for manipulation, the primary instrument to be evaluated for EVA mobility is the work envelope provided by the EVA suit. An EVA Jack suit model has been developed by NASA-JSC and was utilized in this study. This suit model provided a more restrictive motion environment as expected for an EVA suited subject. As part of this study, the anthropometric dimensions for a 50th percentile male were compared with basic anthropometric data and were found to be representative for the population group expected in the NASA flight program. The joints for the suit were created in a manner which provided consistent performance with EVA reach envelopes published in NASA standard #3000.

In order to fully utilize the EVA capabilities of Jack, the EVA suited subject must be validated in some manner. The best available standard for the ISS is the NBS testing facility at Marshall Space Flight Center (MSFC). Subsequently, it was determined that the optimum test for Jack was to compare it with NBS studies.. Therefore the Jack suit model was visually compared with still photographs of an NBS testing scenario. One important aspect to consider is that the actual EVA suits do provide some adjustments for sizing to the particular dimensions of the astronaut. Therefore the photographs of actual NBS testing will document the sizes for people with varying body dimensions. A case in point is that a male astronaut whose height is 50th will probably not have a legs, arms and a torso which are all precisely 50th percentile. Subsequently, it is anticipated that there will be some variations found in comparing any "standard" computer generated model with actual subject data.

One great strength of using a computer generated subject is that the subject and environment can be manipulated with great ease. Unlike actual EVA and NBS testing, there are no time limits for breathing, etc. In addition, "camera" views can be placed

literally inside of objects to provide information that might otherwise be unavailable with physical testing. The cost per hour of computer animation is much less than current NBS testing; emphasizing the utility of this form of evaluation. The important question remains as to whether this testing is indeed indicative of the data provided by NBS testing.

The time duration of the study and length limitations of this report preclude a thorough demonstration of the visual comparison of Jack with NBS data; however the study was focused on NBS photographs which demonstrated difficult tasks performed by several different astronauts. The actual task evaluated was the deployment of an Orbiter payload which carries the Space Station Remote Manipulator System (SSRMS). This task involved removing the pallet (LDA) carrying the SSRMS from the payload bay and attaching it to a module of the ISS. After the LDA was secured, eight long bolts were removed from the SSRMS which held it to the LDA during flight. These bolts were approximately 40" in length and their removal provided a good illustration of the reach limits of the astronauts during EVA. In order to untorque and remove the bolts the astronauts feet must be secured in an Articulating Portable Foot Restraint (APFR) which could be attached to one of several different Worksite Interface sights (WIFs) located on the LDA assembly. Once an astronaut had removed the bolt, it was handed to the accompanying astronaut for stowage in a bolt stowage assembly on the LDA for the flight back to earth.

The Jack figure which illustrates the reach difficulty for this task for a 50th percentile male is illustrated in Figure 1A. The "matching" NBS photograph is illustrated in Figure 1B. It should be noted that this photograph involves a male astronaut whose basic dimensions are approximately 60th percentile. The slight difference is evident in the comparison; however the Jack model reach envelope is visually accurate to less than two inches. The Jack figure which illustrates the reach difficulty for this task for a 5th percentile female is illustrated in Figure 2A. The "matching" NBS photograph is illustrated in Figure 2B. It was fortunate for this study that a 5th percentile female astronaut was available for the NBS testing. In this case the Jack simulation was once again accurate to less than two inches.

As a final observation, the Jack model(s) evaluated in this study did function well as a simulation of the NBS testing. On the average, the Jack model reach envelopes were a conservative estimate of reach envelopes observed in NBS testing. This was viewed as a positive side effect since it would provide for a margin of safety during computer evaluation. It should also be noted that this "side effect" is expected since the computer models will provide normal, comfortable reach envelopes whereas the NBS test illustrated astronauts stretching to extend their normal reach envelopes. It is my firm conclusion that computer models such as Jack should be utilized to their fullest potential for any human-machine interaction...both EVA and IVA.

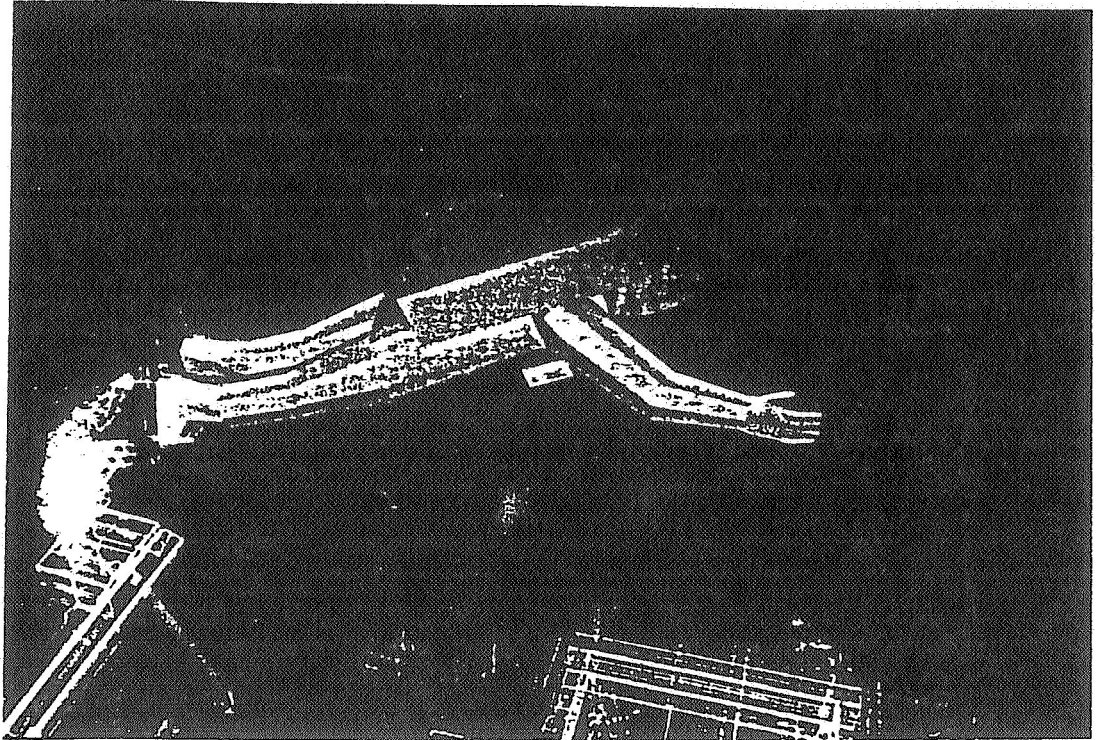
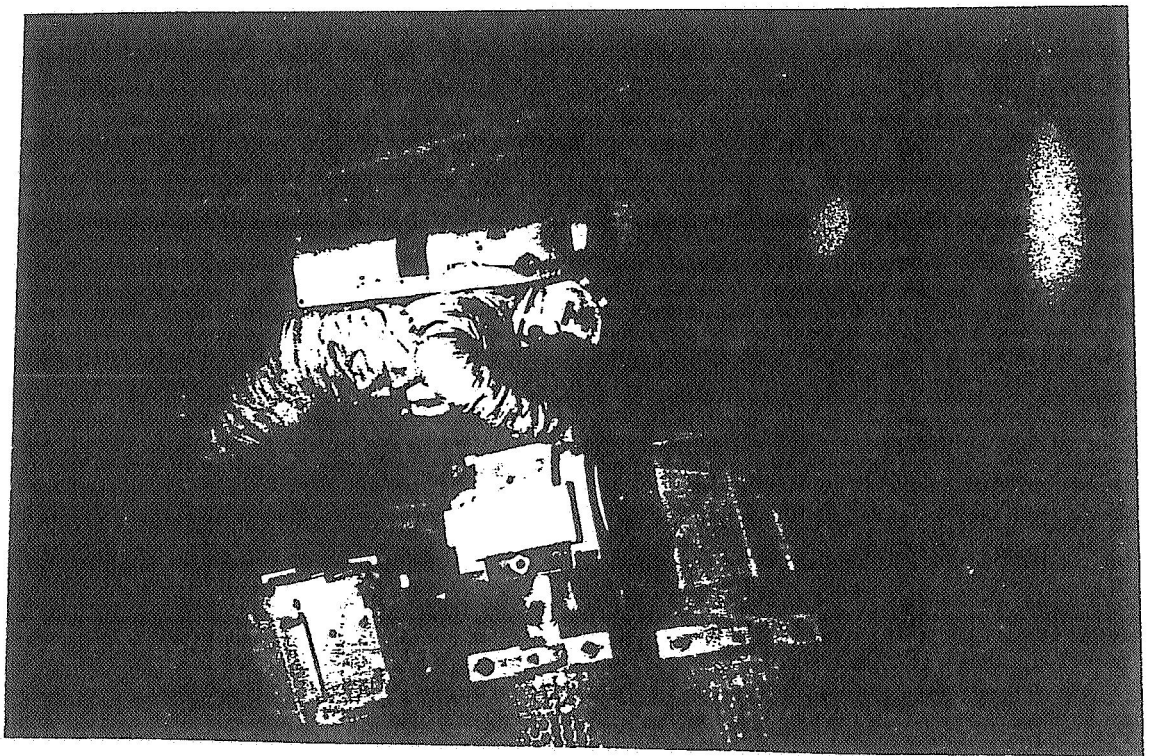


Figure 1A





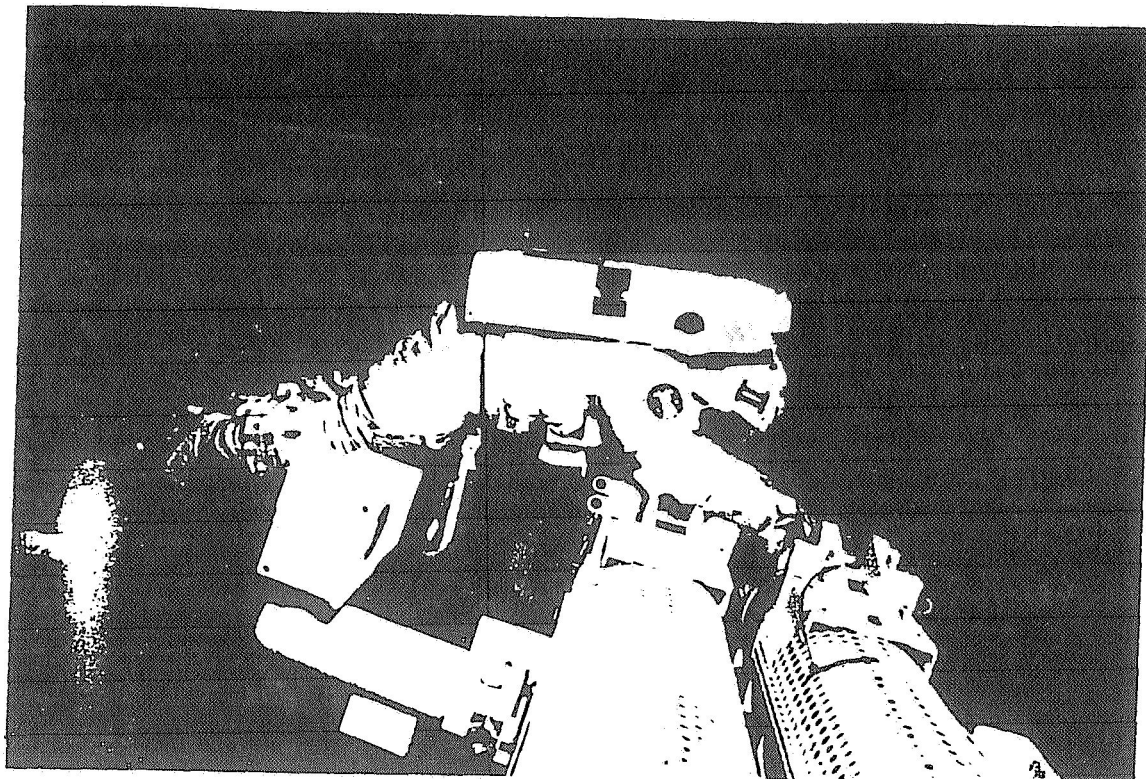


Figure 2A

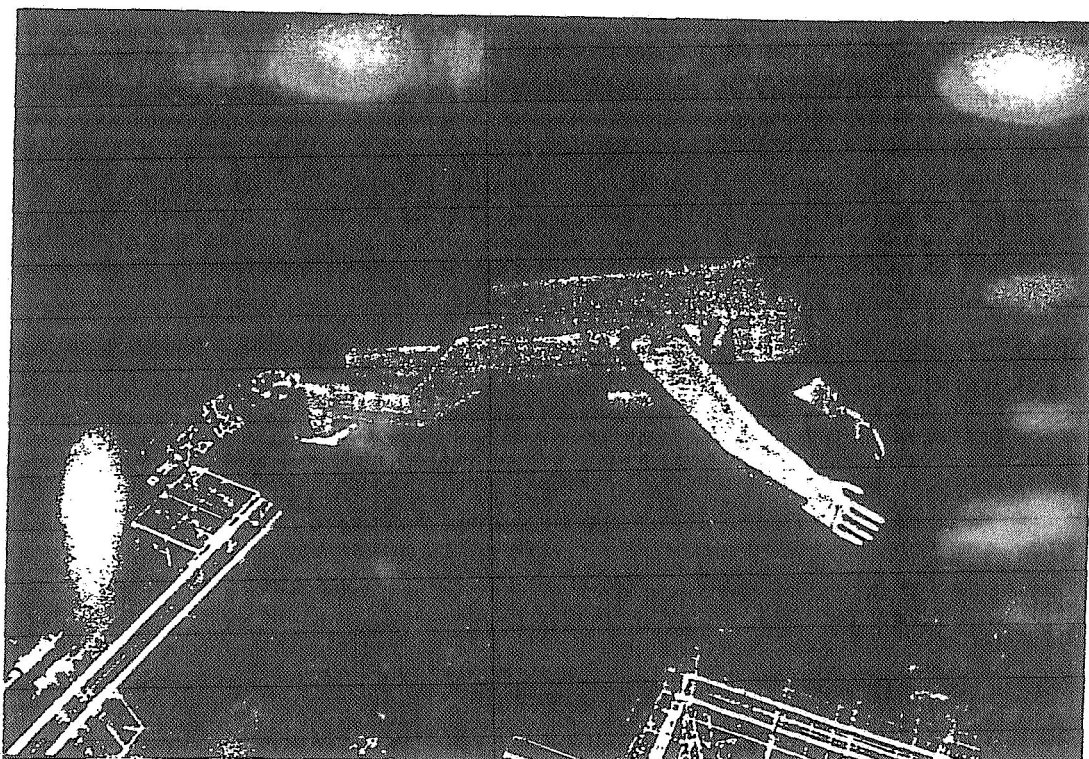


Figure 2B



**1996**

**NASA/ASEE SUMMER FACULTY FELLOWSHIP PROGRAM**

**MARSHALL SPACE FLIGHT CENTER  
THE UNIVERSITY OF ALABAMA**

**AN ASSESSMENT OF MOLTEN METAL DETACHMENT HAZARDS DURING  
ELECTRON BEAM WELDING IN THE SPACE SHUTTLE BAY AT LEO FOR  
THE INTERNATIONAL SPACE WELDING EXPERIMENT**

Prepared By:	James M. Fragomeni, Ph.D.
Academic Rank:	Assistant Professor
Institution and Department:	The University of Alabama Department of Aerospace Engineering & Mechanics
NASA/MSFC:	
Laboratory:	Materials and Processes
Division:	Metallic Materials and Processes
Branch:	Metallurgical Research & Development
MSFC Colleagues:	Arthur C. Nunes, Jr., Ph.D. Carolyn Russell





## INTRODUCTION

In 1997, the United States [NASA] and the Paton Electric Welding Institute are scheduled to cooperate in a flight demonstration on the U.S. Space Shuttle to demonstrate the feasibility of welding in space for a possible repair option for the International Space Station Alpha. This endeavor, known as the International Space Welding Experiment (ISWE), will involve astronauts performing various welding exercises such as brazing, cutting, welding, and coating using an electron beam space welding system that was developed by the E.O. Paton Electric Welding Institute (PWI), Kiev Ukraine. This electron beam welding system known as the "Universal Weld System" consists of hand tools capable of brazing, cutting, autogeneous welding, and coating using an 8 kV (8000 volts) electron beam. The electron beam hand tools have also been developed by the Paton Welding Institute with greater capabilities than the original hand tool, including filler wire feeding, to be used with the Universal Weld System on the U.S. Space Shuttle Bay as part of ISWE. The hand tool(s) known as the Ukrainian Universal Hand [Electron Beam Welding] Tool (UHT) will be utilized for the ISWE Space Shuttle flight welding exercises to perform welding on various metal alloy samples. A total of 61 metal alloy samples, which include 304 stainless steel, Ti-6Al-4V, 2219 aluminum, and 5456 aluminum alloys, have been provided by NASA for the ISWE electron beam welding exercises using the UHT. These samples were chosen to replicate both the U.S. and Russian module materials. The ISWE requires extravehicular activity (EVA) of two astronauts to perform the space shuttle electron beam welding operations of the 61 alloy samples. A third astronaut will provide processing feed back to the two EVA astronauts from the orbiter aft flight deck.

This study was undertaken to determine if a hazard could exist with ISWE during the electron beam welding exercises in the Space Shuttle Bay using the Ukrainian Universal Weld System with the UHT. The safety issue has been raised with regard to molten metal detachments as a result of several possible causes such as welder procedural error, externally applied impulsive force(s), filler wire entrainment and snap-out, cutting expulsion, and puddle expulsion. Molten metal detachments from either the weld/cut substrate or weld wire could present harm to a astronaut in the space environment if the detachment was to burn through the fabric of the astronauts Extravehicular Mobility Unit (EMU). Gravitational forces on the order of 0.001 that of the earth surface gravity in the space shuttle bay may decrease the likelihood of a molten metal detachment due to the decreased gravitational force acting on the molten metal drop. The dropout of the weld pool under the force of gravity would be more likely under terrestrial situations than in space welding. However, molten metal accumulation may be more likely at the end of the weld filler wire as a result of less gravity pulling on the drop at the wire end. Some possible ways of obtaining molten metal drop detachments would include an impulse force, or bump, to the weld sample, cut surface, or filler wire. If a large enough molten metal drop accumulated at the end of the filler wire could possible be shaken off, or the sample plate could be struck while welding or cutting so as to release a molten metal drop.

An accurate understanding between the weight, nearly zero gravity for space welding, of liquid metal drops and surface tension is necessary for developing a model which describes liquid metal drop detachments. If one considers a liquid metal drop hanging from a round cross-section, the weight of the drop can be related to the surface tension through a simple force

balance. Since the surface tension represents the force holding up or opposing the liquid metal drop from detaching and the weight of the liquid metal drop is the force that is tending to detach the molten metal drop, an expression can be determined representing the force balance. A simple approximate expression representing the force balance can be expressed as

$$2\pi r\gamma = \rho_m g V \quad [1]$$

where  $\rho_m g V$  is the weight of the liquid metal drop which is proportional to the interfacial surface tension  $\gamma$ ,  $\rho_m$  is the liquid metal density of the liquid metal drop,  $V$  is the volume of the drop, and  $g$  is the gravitational acceleration. This expression is somewhat approximate since it assumes that the entire drop detaches whereas in reality only a part of, not the whole, drop detaches. The drops that detach can be much smaller than the original hanging drops depending on the surface tension and liquid metal density. Assuming a detached spherical liquid metal drop, the volume  $V$  can be determined and thus the size or radius  $r$  of the drop given by

$$r = [3\gamma/2\rho_m g]^{0.5} = C[\gamma/\rho_m]^{0.5} \quad [2]$$

where  $C$  is a numerical constant. Thus, this expression provides an estimate for the size of a freely hanging liquid metal drop.

## Theoretical Model

A way of producing a molten metal detachment would be by an impulse or bump to weld sample. During the welding of a sample, it is possible that a quantity of molten metal could become detached by splashing the molten metal out from the weld puddle. This would in part depend on how secure the weld samples are fastened or bolted. Properly securing the weld samples will greatly minimize the effect an impact could have on lifting the molten metal above the weld puddle. If the samples are not securely bolted down and fastened then it becomes more easier for an impact force (i.e. a bump) to cause molten metal to be lifted up and possibly splashed from the weld puddle. It is possible to estimate the amount of liquid molten metal that could be displaced from a weld puddle in terms of the width and depth of the weld puddle. If the weld puddle has a depth equal to  $W/2$  and a width equal to  $W$  then the maximum volume  $V_{ps}$  of liquid metal that could be displaced from the puddle would be equal to

$$V_{ps} = \pi W^3/12 \quad [3]$$

and it may be anticipated that about 50% of this volume would exit the puddle as a molten drop.

During the welding operation, it is possible that the filler wire which is partially emerged into the molten metal weld pool might be snapped out of weld puddle so as to entrain and release a liquid metal drop with an initial velocity. As the filler wire is lifted from the weld pool it is wetted by the molten metal. As a consequence some of the molten metal comes up with it. At a certain height that the liquid metal is lifted, the normal level of the weld pool surface becomes unstable above the weld pool and breaks away. The minimum force to achieve this detachment

would be equal to the weight of the filler metal wire plus the weight of the liquid metal that is being lifted. If the filler wire, which is emersed into the molten metal weld puddle, is lifted up out of the weld puddle then a given volume of molten metal will be lifted out of the weld puddle and then become detached. The volume of molten metal  $V_{we}$  that could be lifted up and become detached would be equal to

$$V_{we} = \pi a^3 / 3 \quad [4]$$

where  $a$  is radius of the filler wire emerged into the weld puddle. The above equation would describe the maximum amount of molten metal that would be removed from the weld pool as a result of the filler wire being dipped into the weld pool and then lifted out of the weld pool.

If the filler metal wire is not in the weld puddle for a given length of time it is possible that molten metal can accumulate at the end of the filler metal wire. In order for this to occur, the filler wire must remain lifted far enough and long enough away from the molten metal weld puddle for molten metal to accumulate. If the molten metal accumulation comes in contact with the weld puddle surface, then due to surface tension the molten metal accumulation will be pulled directly into the weld puddle. However, if the filler wire is held for a long enough time away from the weld puddle, the growth rate of the metal volume on the end of the filler wire can be written in terms of the filler wire velocity, area, and time. If the volume is expressed in terms of the radius of the molten metal accumulation at the tip of the filler wire, then the rate of growth of the molten metal drop can be expressed as

$$4\pi r^3/3 = vAt \quad [5]$$

where  $v$  is the filler wire feed rate or velocity,  $A$  is the filler wire cross-sectional area,  $t$  is the time, and  $r$  is the radius of the molten metal accumulation at the end of the filler wire. A large drop could be defined as a drop with a radius approximately three times equal to or greater than the radius of the filler wire. The impact velocity to detach a large molten metal drop from the end of the filler wire would be approximately equal to

$$v = a\{2(\lambda+1)\pi\gamma/\rho_m V\}^{0.5} \quad [6]$$

where  $v$  is the impact velocity required to detach a large drop from the end of the filler wire,  $V$  is the volume of the drop,  $a$  is the filler wire radius,  $\gamma$  is the interfacial surface tension, and  $\lambda$  has a value of order 1 to 2. This expression provides a measure of the difficulty to detach or separate large drops that have grown in size at the end of the filler wire from the electric arc during electron beam welding.

During an electron-beam cutting exercise of the metallic sample, molten metal droplets can develop on the edges of the metal sample where the cutting has occurred. If a large impact or impulse force is applied to the metal sample, the molten metal droplets can pull away from the edge. If struck hard enough, the sample plate with molten metal pool or droplets on the side that is struck might release a drop of molten metal. In order for a liquid metal drop to detach, a given amount of energy must be expended to the drop to overcome the surface energy holding the drop in place. The amount of energy required to detach a molten metal drop would depend on the

interfacial surface free energy  $\gamma$  and the surface area of the drop and be approximately equal to  $\gamma \Delta a_{\text{surface}}$ . The change in the surface area  $\Delta a_{\text{surface}}$  of the drop before and after detachment is

$$\Delta a_{\text{surface}} = a_{\text{drop}} + a_{\text{residual}} - a_{\text{initial}} \quad [7]$$

where  $a_{\text{drop}}$  is the surface area of the detached drop,  $a_{\text{initial}}$  is the initial surface area of the drop prior to being detached, and  $a_{\text{residual}}$  is the residual surface area of molten metal left over on the surface after the drop has become detached. During an electron beam cutting process, the liquid metal drops that form on the edges of the cut on the sample often are diamond shaped rather than spherical. A drop can be considered as two cones joined together at a common base with a height  $h$ . The residual and initial drops are diamond shaped whereas the detached drop is spherical. Thus, for molten metal drops formed during the cutting process,  $\Delta a_{\text{surface}}$  can be expressed as

$$\Delta a_{\text{surface}} = 4\pi(d_1/2)^2 + \pi d_3 \{h^2 + (d_3/2)^2\}^{0.5} - d_2 \pi \{h^2 + (d_2/2)^2\}^{0.5} \quad [8]$$

where  $d_1$  is the detached drop diameter,  $d_2$  is the drop diameter before it was detached,  $d_3$  is the residual drop diameter left on the cut edge of the sample after the drop has been detached, and  $2h$  is the length of the initial and residual drops. As seen from the above expression, both the detached molten drop and the residual drop have the same equal length  $h$  but different size diameters whereas the detached molten metal drop is spherical. When a molten metal drop becomes detached, it acquires a velocity and thus a kinetic energy associated with the detachment. If just enough energy has been utilized to detach a drop at the interface where the drop is connected to the cut edge with no additional energy left over then the energy to detach the drop can be expressed simply in terms of the kinetic energy of the drop and thus given by

$$\gamma \Delta a_{\text{surface}} = KE_{\text{drop}} = 0.5 m_{\text{drop}} v_{\text{drop}}^2 \quad [9]$$

where  $KE_{\text{drop}}$  is the kinetic energy of the detached drop,  $m_{\text{drop}}$  is the mass of the detached drop, and  $v_{\text{drop}}$  is the velocity of the detached drop. Equation [9] provides an expression of the minimum amount of energy required to detach a free hanging liquid metal drop at the cut edge of a welding sample. However, if a large enough impact force is applied to the plate and thus the sample that energy is available to both detach the drop and to propel or accelerate the drop outward away from the cut edge, then the extra energy left over after the drop has been detached will be kinetic energy available to throw the drop outward away from the plate. Thus, the above expression can be modified to include this extra kinetic energy and therefore given by

$$\gamma \Delta a_{\text{surface}} + 0.5 m_{\text{drop}} v_{\text{ext}}^2 = KE_{\text{drop}} = 0.5 m_{\text{drop}} v_{\text{drop}}^2 \quad [10]$$

where  $v_{\text{ext}}$  is the velocity that the drop will achieve after it has been detached due to the extra energy available after the drop has been detached. Thus the drop will accelerate as a projectile a distance horizontal in the  $x$  direction and a distance downward in the  $y$  direction. If the distance the drop goes in the  $x$  direction is  $X$  and the distance the drop travels in the  $y$  direction  $S$ , then the velocity of the drop  $v_{\text{ext}}$  relative to the plate can be expressed as

$$v_{\text{ext}} = v_{\text{plate}} - X \{g/2S\}^{0.5} \quad [11]$$

where  $t$  is the time,  $X$  is the horizontal distance,  $v_{\text{plate}}$  is the velocity of the plate to which the molten metal drop is attached,  $S$  is the vertical distance, and  $g$  is the gravitational acceleration. Thus equation [10] can thus be expressed as

$$\gamma \Delta a_{\text{surface}} + V_{\text{drop}} \rho_m X^2 g / 4S + 0.5 m_{\text{drop}} v_{\text{plate}}^2 - 0.5 m_{\text{drop}} X \{g/2S\}^{0.5} v_{\text{plate}} = 0.5 V_{\text{drop}} \rho_m v_{\text{drop}}^2 \quad [12]$$

where  $V_{\text{drop}}$  is the volume of the drop,  $\rho_m$  is the molten metal drop density,  $v_{\text{drop}}$  is the drop velocity. Thus, if there is no extra energy available after the drop has been detached i.e.,  $v_{\text{ext}}=0$ , then

$$v_{\text{plate}} = X_{\text{max}} \{g/2S\}^{0.5} = (2\gamma \Delta a_{\text{surface}} / m_{\text{drop}})^{0.5} = v_{\text{drop}} \quad [13]$$

## Experimental Method

The experimental testing was performed in a 4 ft. X 4 ft. vacuum chamber at MSFC enabling protective garment to be exposed to the molten metal drop detachments to over 12 inches. The chamber was evacuated to vacuum levels of at least  $1 \times 10^{-5}$  torr (50 microTorr) during operation of the 1.0 kW Universal Hand Tool (UHT). The UHT was manually operated at the power mode appropriate for each material and thickness. The space suit protective welding garment, made of Teflon fabric (10 oz. per yard) with a plain weave, was placed on the floor of the vacuum chamber to catch the molten metal drop detachments. A pendulum release mechanism consisting of four hammers, each weighing approximately 3.65 lbs, was used to apply an impact forces to the weld sample/plate during both the electron beam welding and cutting exercises. Measurements were made of the horizontal fling distances of the detached molten metal drops.

## Results and Conclusions

The volume of a molten metal drop can also be estimated from the size of the cut. Utilizing equations [7]-[8] calculations were made to determine  $\Delta a_{\text{surface}}$  for 304 stainless steel for cutting based on measurements of metal drop sizes at the cut edges. For the cut sample of 304 stainless steel based on measurement of the drop size at the edge,  $\Delta a_{\text{surface}}$  was determined to be  $0.0054 \text{ in}^2$ . Calculations have indicated only a small amount of energy is required to detach a liquid metal drop. For example, approximately only 0.000005 ft-lb of energy is necessary to detach a liquid metal steel drop based on the above theoretical analysis. However, some of the energy will be absorbed by the plate before it reaches the metal drop. Based on the theoretical calculations, it was determined that during a weld cutting exercise, the titanium alloy would be the most difficult to detach molten metal droplets followed by stainless steel and then by aluminum. The results of the experimental effort have shown that molten metal will detach if large enough of a hammer blow is applied to the weld sample plate during the full penetration welding and cutting exercises. However, no molten metal detachments occurred as a result of the filler wire snap-out tests from the weld puddle since it was too difficult to cause the metal to flick-out from the pool. Molten metal detachments, though not large in size, did result from the direct application of the electron beam on the end of the filler weld wire.



**1996**

**NASA/ASEE SUMMER FACULTY FELLOWSHIP PROGRAM**

**MARSHALL SPACE FLIGHT CENTER  
THE UNIVERSITY OF ALABAMA**

**BPSK DEMODULATION USING DIGITAL SIGNAL PROCESSING**

Prepared By:	Thomas R. Garcia
Academic Rank:	Assistant Professor
Institution and Department:	Purdue University Department of Electrical Engineering Technology
NASA/MSFC:	
Laboratory:	Astrionics
Division:	Optics and Radio Frequency
Branch:	Radio Frequency
MSFC Colleague:	Paul Kennedy





## Introduction

A *digital communications* signal is a sinusoidal waveform that is modified by a binary (digital) information signal. The sinusoidal waveform is called the *carrier*. The carrier may be modified in amplitude, frequency, phase, or a combination of these. In this project a binary phase shift keyed (BPSK) signal is the communication signal. In a BPSK signal the phase of the carrier is set to one of two states, 180 degrees apart, by a binary (i.e., 1 or 0) information signal.

A *digital* signal is a sampled version of a “real world” time continuous signal. The digital signal is generated by sampling the continuous signal at discrete points in time. The rate at which the signal is sampled is called the *sampling rate* ( $f_s$ ). The device that performs this operation is called an analog-to-digital (A/D) converter or a digitizer. The digital signal is composed of the sequence of individual values of the sampled BPSK signal.

*Digital signal processing (DSP)* is the modification of the digital signal by mathematical operations. A device that performs this processing is called a digital signal processor. After processing, the digital signal may then be converted back to an analog signal using a digital-to-analog (D/A) converter.

The goal of this project is to develop a system that will recover the digital information from a BPSK signal using DSP techniques. The project is broken down into the following steps:

- (1) Development of the algorithms required to demodulate the BPSK signal.
- (2) Simulation of the system.
- (3) Implementation a BPSK receiver using digital signal processing hardware.

## Algorithm Development

A digital communications receiver extracts the information signal from a digital communications signal. For a BPSK signal, the receiver must be able to recreate a local oscillator (LO) signal that matches the exact frequency and phase of the transmitted signal carrier. A tracking loop for the LO will track any variation in frequency and phase that the transmitter carrier may undergo. For this project a *Costas Loop* is used [1].

The Costas loop generates a phase error term, filters it, then uses this error to adjust the LO phase. Figure 1 is a block diagram showing the algorithms used to implement the Costas loop.

The transmitted BPSK signal is sampled at the receiver by a high speed A/D. The output of the A/D is a sequence of samples called  $s(n)$ .

$$s(n) = m(n)\cos(\omega_c n + \theta_1) \quad (1)$$

where:  $m(n)$  is the information signal (+1 or -1)  
 $\omega_c n$  is the carrier frequency  
 $\theta_1$  is the carrier phase offset

$s(n)$  is downconverted by a complex LO. The downconverted signal may be expressed as:

$$b(n) = s(n)\cos(\omega_c n + \theta_2 n) - js(n)\sin(\omega_c n + \theta_2 n) \quad (2)$$

where:  $\theta_2 n$  is the LO phase offset

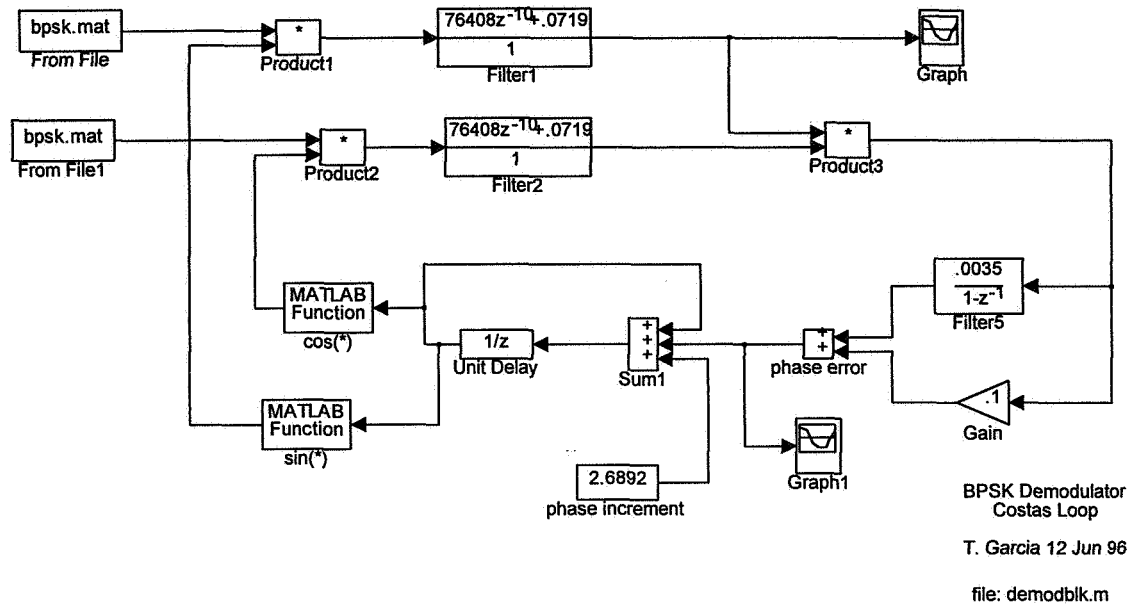


Figure 1 , SIMULINK Block Diagram of a Costas Loop

Substituting the expression for  $s(n)$  from equation (1) and filtering out the  $\omega_c$  products from this operation results in the following:

$$b(n) = \frac{m(n)}{2} [\cos(\theta_1 - \theta_2 n) - j \sin(\theta_1 - \theta_2 n)] \quad (3)$$

When the receiver is tracking the carrier, both phase offsets are equal ( $\theta_1 - \theta_2 n = 0$ ). Then:

$$b(n) = \frac{m(n)}{2} \quad (4)$$

The information signal is recovered.

In order to insure that  $\theta_2 n = \theta_1$  the Costas loop is used. First a phase error term is generated. This is accomplished by multiplying the real and imaginary parts of  $b(n)$  in equation (2) and filtering out the high frequency terms.

$$q(n) = b(n)_{real} * b(n)_{imag} = m^2(n) \cos(\theta_1 - \theta_2 n) \sin(\theta_1 - \theta_2 n) \quad (5)$$

Using a trigonometry identity this may be rewritten as:

$$q(n) = \frac{m^2(n)}{2} [\sin 2(\theta_1 - \theta_2 n)] \quad (6)$$

When the phase error,  $(\theta_1 - \theta_2 n)$ , is very small this may be approximated by:

$$q(n) \approx m^2(n)(\theta_1 - \theta_2 n) \quad (7)$$

This phase error term now passes through an infinite impulse response loop filter that determines the tracking loop dynamics. The output of the loop filter is the phase error term to be used to correct the LO phase:

$$\phi(n)_{error} = \alpha q(n) + \sigma(n) \quad (8)$$

where  $\sigma(n) = \beta q(n) + \sigma(n-1)$   
 $\alpha$  is a gain term  
 $\beta$  is the gain of the recursive part of the filter

Now that the phase error correction term has been determined, the *next* phase increment for the LO may be evaluated.

$$\phi(n+1) = \phi(n) + \omega_c T + \phi(n)_{error} \quad (9)$$

where  $\phi(n)$  is the current phase  
 $\omega_c T$  is the phase advance due to the carrier frequency

This process is repeated as each sample arrives from the A/D.

## Simulation

This system is simulated on a PC computer before hardware is assembled. Simulation on the computer allows the mathematical algorithms for digital signal processing to be developed and analyzed. The characteristics of the receiver under various conditions are analyzed.

Three different simulation methods, MATLAB [2], SIMULINK [3], and C program were used. MATLAB is a high-level numerical computation and graphics package. The Costas loop simulation is written following the above derivation. With the Signal Processing Toolbox digital filters may easily be designed and analyzed. The lowpass FIR filter was designed in this manner. SIMULINK is a graphical modeling and simulation tool for control and DSP systems analysis. It is an add on to MATLAB. The block diagram (Figure 1) for the Costas loop was drawn using SIMULINK. When the simulation is started, SIMULINK performs the mathematical processing of the connecting blocks. The C program was used since the actual DSP hardware code is developed using C. A C compiler then compiles the program into the DSP code and loads it into the hardware.

All three simulation methods yield the same results since the algorithms were identical. The simulation consists of the following components.

- (1) information signal generation
- (2) BPSK signal generation
- (3) receiver

### Information Signal Generation

A maximal-length sequence PN code was generated using MATLAB. This is realized using a linear feedback shift register [5]. A sequence of length 127 bits is used. This sequence is used as the information digital signal. In the simulation the bit rate of the PN sequence is 500 kHz.

### BPSK Signal Generation

The PN sequence has values of “1” for one state and “-1” for the other. When this sequence is multiplied by a sinusoidal waveform, BPSK modulation results. The multiplication by “1” has no effect of the sinusoid while multiplying by “-1” results in a 180° phase shift. For simulation purposes, the sinusoid signal has a frequency of 10.7 MHz

A signal of maximum frequency content  $F_{max}$  will be exactly recovered from its sample values if the signal is sampled at a rate of  $F_s > 2F_{max}$ . The rate  $F_s = 2F_{max}$  is called the Nyquist rate and represents the minimum sampling rate possible [4].

The simulation uses a 10.7 MHz carrier being modulated by a 500 Kbit/sec data sequence. Therefore a sampling rate of at least  $11.2 \text{ MHz} * 2 = 22.4 \text{ MHz}$  is needed. A sampling rate of 25 MHz was selected. The sampling rate of 25 MHz results in 50 samples of each information bit and 2.34 samples every period of the 10.7 MHz carrier.

The carrier is capable of being swept in frequency and to have a frequency step. This allows analysis of the demodulation performance when the transmitter carrier frequency is not stationary.

### Receiver

The receiver is simulated using the Costas loop algorithms. The MATLAB and C simulations use the mathematical expressions from the algorithm development in basically the same form as described above. MATLAB uses large arrays to contain the input and output data. The C program reads in the BPSK sampled data from a file and writes out the recovered data to a file to simulate actual DSP hardware operation. Plotting of results was done on MATLAB for both methods.

The SIMULINK simulation is done with pre-defined blocks of mathematical operations. These blocks are connected to form the Costas loop and the simulation is started. The BPSK sampled data is read in from a file. The output is plotted in a graph window.

The lowpass FIR filter was designed using MATLAB. MATLAB uses the Parks-McCellan algorithm using the Remez exchange algorithm and Chebyshev approximation theory to design a filter with a minimum error between the desired frequency response and the actual frequency response. The filter length is 20.

### Results

The results of a simulation of a swept frequency on the transmitter from 9.7 MHz to 11.7 MHz are shown in Figures 2 - 3. Figure 2 shows the phase error before and after filtering. As the carrier approaches the bandwidth of the system, the filtered phase error ramps up to the right showing that the LO is tracking the ramping frequency shift in the transmitter. When the carrier frequency exceeds the bandwidth on the left side, the loop loses coherency. Notice the bandwidth in which the loop may successfully track the transmitter is approximately 500 kHz. This bandwidth is set by the lowpass filter. Figure 3 shows the recovered data on the I channel.

## Hardware

Hardware implementation was not accomplished due time constrains. The DSP hardware for this project consists of the following

Sun	SARCstation 10	Microcomputer
Creative Engineering Concepts	AD700	High Speed Digitizer
Bit3	466	Bus Adapter
Pentek	4272	Multiband Digital Receiver
Pentek	4284	Digital Signal Processor

## Conclusion

Digital signal processing techniques may be developed to demodulate digital communication signals. The algorithms developed on this project successfully demodulated a BPSK signal. The carrier frequency was swept and the receiver was able to maintain lock and recover the information signal. The three simulation methods responded in the same manner. The results of the simulation show that the Costas loop designed will track the carrier signal with a  $\pm 245$  kHz frequency variation. The next step in this project is to complete the hardware realization and to develop algorithms for other digital communication signal formats.

## References

1. S.A. Tretter, *Communication System Design Using DSP Algorithms*, Plenum Press (1995).
2. The Math Works Inc., *Student Version of MATLAB, Version 4.0* (1994)
3. The Math Works Inc., *Student Version of SIMULINK* (1994)
4. J. G. Proakis, D. G. Manolakis, *Digital Signal Processing, Principles, Algorithms, and Applications*, Macmillan (1992)
5. R. E. Ziemer, R. L. Peterson, *Digital Communications and Spread Spectrum Systems*, Macmillan(1985)

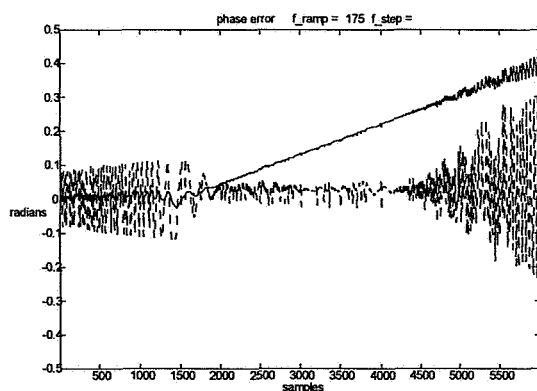


Figure 2, Phase Error filtered and Unfiltered

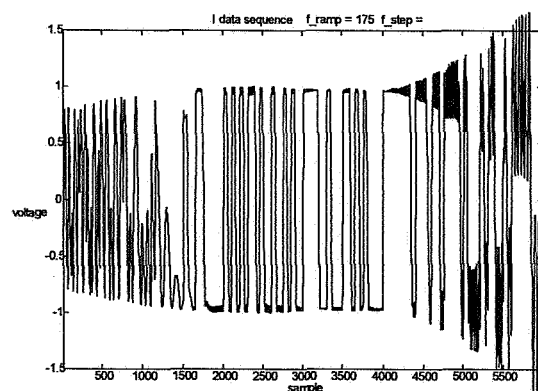


Figure 3, I Channel Recovered Data



**1996**

**NASA/ASEE SUMMER FACULTY FELLOWSHIP PROGRAM**

**MARSHALL SPACE FLIGHT CENTER  
THE UNIVERSITY OF ALABAMA**

**Development of a Technique For Separating  
Raman Scattering Signals from Background Emission  
With Single-Shot Measurement Potential**

Prepared By:	Roy Hartfield
Academic Rank:	Assistant Professor
Institution and Department:	Auburn University Aerospace Engineering
NASA/MSFC:	
Office:	Propulsion Laboratory
Division:	Motor Systems Division
Branch:	Combustion Physics Branch
MSFC Colleagues:	Richard Eskridge Chris Dobson





# **Development of a Technique For Separating Raman Scattering Signals from Background Emission With Single-Shot Measurement Potential**

## **Introduction**

Raman scattering is a powerful technique for quantitatively probing high temperature and high speed flows. However, this technique has typically been limited to clean hydrogen flames because of the broadband fluorescence interference which occurs in hydrocarbon flames. Fluorescence can also interfere with the Raman signal in clean hydrogen flames when broadband UV lasers are used as the scattering source. A solution to this problem has been demonstrated.<sup>1,2</sup> The solution to the fluorescence interference lies in the fact that the vibrational Q-branch Raman signal is highly polarized for 90° signal collection and the fluorescence background is essentially unpolarized. Two basic schemes are available for separating the Raman from the background. One scheme involves using a polarized laser and collecting a signal with both horizontal and vertical laser polarizations separately. The signal with the vertical polarization will contain both the Raman and the fluorescence while the signal with the horizontal polarization will contain only the fluorescence. This is the approach followed in Refs. 1 and 2. The second scheme involves polarization discrimination on the collection side of the optical setup. For vertical laser polarization, the scattered Q-branch Raman signal will be vertically polarized; hence the two polarizations can be collected separately and the difference between the two is the Raman signal. This approach has been used for the work found herein and has the advantage of allowing the data to be collected from the same laser shot(s). This makes it possible to collect quantitative Raman data with single shot resolution in conditions where interference cannot otherwise be eliminated.

## **Experimental Setup**

The experimental arrangement consists of a Heinken burner, a Lumonics Broadband Krypton Fluoride excimer laser (248.6 nm), a McPherson 1 m UV spectrometer, a computer controlled Princeton Instruments intensified CCD camera system, a pulse generator and a calcite crystal used for separating polarizations. The schematic found in Fig. 1 shows the experimental setup including appropriate optics for focusing the laser beam over the burner and collecting the resulting signal. The schematic includes the essential electronic connections needed for proper operation of the camera in the gated, synchronized mode. The pulse/function generator was used to fire the laser on the positive going pulse and the camera on the negative going pulse. This allowed the function generator pulse width to be used as a delay. The 15 ns. laser pulse was centered on a 100 ns. camera gate using a pulse monitor from the FG-100 pulse generator and a photomultiplier (not shown) looking at stray light from the laser beam. The key element which is unique for this setup is the polarization separator. This crystal separates a beam of unpolarized incoming light into horizontal and vertical components separated by 4 mm. The crystal was placed just inside the slit of the spectrometer. A mask approximately 3mm in diameter was placed in from of the slit resulting in a pattern on the detector composed of two strips of light, each containing one spatial dimension and one spectral dimension.

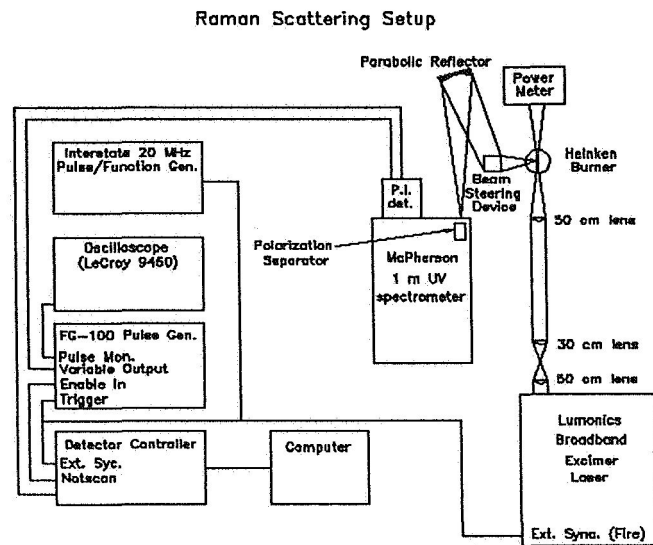


**Figure 1**

The immediate form of the data is electronic images of the horizontally and vertically polarized components of the collected scatter. The image shown in Fig. 2 represents a sample of the raw data. The vertically polarized light appears on the left band and the horizontally

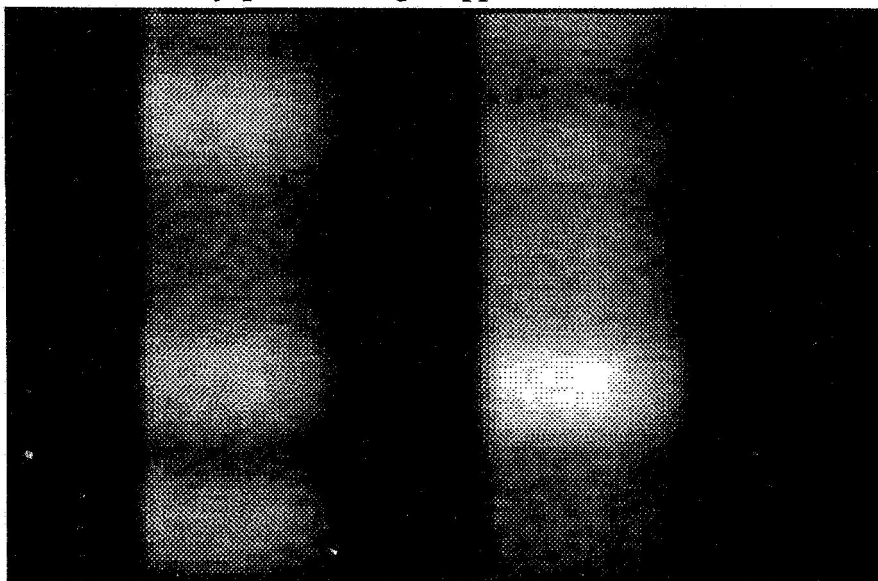


**Figure 2: Image of spectrally resolved scattering signal along a line separated based on polarization**

polarized light appears on the right band. The spectral direction is along the vertical axis with wavelength increasing from bottom to top and the horizontal direction represents distance along a linear probe volume. This particular image was collected in a lean flame ( $OF = 4$ ) with the spectrometer set at 269.8 nm. (This wavelength corresponds to the approximate center of the

image.) The horizontally polarized band is generally brighter because the spectrometer passes horizontally polarized light preferentially; however, some bands appear on the vertically polarized section which are not present on the horizontally polarized image. These areas represent Raman scatter. The two polarizations are normalized for collection efficiency and then their difference is taken to extract the Raman spectrum. This process is illustrated by the plots shown in Figs. 3 and 4.

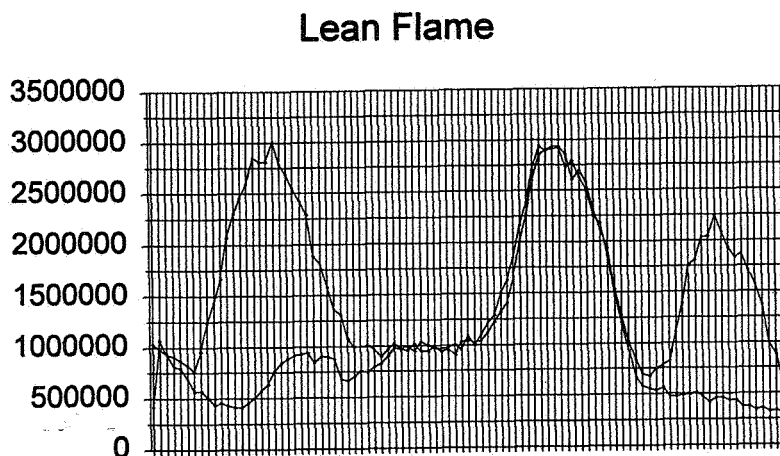


**Figure 3:** Plot comparing vertically and horizontally polarized components of induced scatter

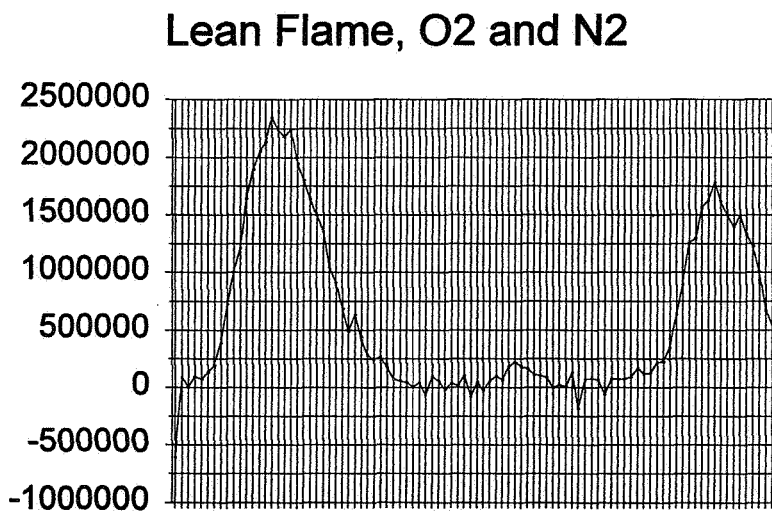


**Figure 4:** Difference between horizontal and vertically polarized components (Raman Signals for N<sub>2</sub> (left) and O<sub>2</sub> (right))

The data for figs. 3 and 4 was taken from a 500 shot average image and then binned in the spatial direction for maximum signal strength. The spatial averaging is possible because the

the spatial direction for maximum signal strength. The spatial averaging is possible because the linear probe volume segment for this image is contained entirely in the core of the flame where the conditions are uniform on a time-averaged basis.

The procedure for measuring temperature with the data available in this report is to collect data in a known flame condition to determine the correlation between the Raman signal and the number density, conduct Raman measurements in and unknown flow field at a known pressure, calculate the number density from the Raman signals and then calculate the temperature using ideal gas. It should be pointed out that, with a narrowband laser, the temperature can be determined directly from the shape of the Raman signal and then number densities (and partial pressures) can be determined from the total Raman signal strength. (This approach will be proposed for future hydrocarbon technique development.

### Summary

A novel technique for extracting Raman signals from interference has been demonstrated. This technique offers single shot measurement potential, quantitative use of Raman signals obtained using broadband UV lasers and the possibility of obtaining quantitative Raman data in hydrocarbon flames.

### References

1. Grunefeld, G., Beushausen, V., and Andreson P., "Interference-free UV-laser-induced Raman and Rayleigh measurements in hydrocarbon combustion using polarization properties," Applied Physics B 61, 473-478.
2. Hartfield, R., "Thermodynamic Measurements in a High Pressure Hydrogen-Oxygen Flame Using Raman Scattering from a Broadband Excimer Laser," Report for NASA/ASEE Summer Faculty Fellowship Program, August 1995.

**1996**

**NASA/ASEE SUMMER FACULTY FELLOWSHIP PROGRAM**

**MARSHALL SPACE FLIGHT CENTER  
THE UNIVERSITY OF ALABAMA**

**“THE INTERPRETATION AND EFFECTIVE IMPLEMENTATION OF THE  
STEVENSON-WYDLER TECHNOLOGY INNOVATION ACT OF 1996”**

Prepared By:	Pamala D. Heard
Academic Rank:	Assistant Professor
Institution:	Langston University
Department:	Department of Mathematics
NASA/MSFC:	
Office:	Education Program Office
MSFC Colleague:	Mr. Jim Pruitt



## **INTRODUCTION**

The purpose of this research is to develop a plan that gives schools the opportunity to acquire knowledge of the Stevenson-Wydler Technology Innovation Act. The law suggests that federal agencies give surplus equipment to educational entities. It would then become the school's choice to take advantage of the opportunity. The purpose of this proposal is to develop an ongoing partnership with schools around the United States. Its attempt is to inform schools about the law and organize a plan that will allow schools to take advantage of this opportunity. It would inform teachers about available resources and expose their students to educational opportunities.

## **RESEARCH APPROACH**

The initial approach to this research was to interpret Executive Order 12999, Stevenson-Wydler Technology Innovation Act. The law had to be examined carefully in order to dissect its components. The law is designed to transfer excess and surplus equipment to our nation's classrooms, and encourage federal employees to volunteer their time, to assist teachers and connect classrooms. Additional components to this law were the Omnibus Reconciliation Act of 1993, Public Law 103-66. This law refers to the Empowerment Zones and Enterprise Communities that are designed to afford communities real opportunities for growth and revitalization. The framework of the program consists of four key points -- economic opportunity, sustainable community development, community-based partnerships and strategic vision for change. In the executive order the Empowerment Zones and Enterprise Communities topped the priority list to receive surplus equipment. The priority list formed with Empowerment Zones and Enterprise Communities, Public and Private Elementary Schools, Public and Private Secondary Schools, Colleges and Universities and nonprofit organizations. The law was structured to help ease red tape for schools that need surplus equipment.

Marshall Space Flight Center currently has a pilot plan in place to address the previous act. The center recently distributed equipment to the Tri-State Education Initiative and to the State of Alabama. My research required an expansion on the site's approach for the six states the flight center services. The six states include: Alabama, Arkansas, Iowa, Louisiana, Missouri and Tennessee. The plan currently in effect would give notice to schools. The schools would then complete the necessary paperwork and return it to the Education Office. After completion of the paperwork the office would schedule a briefing for the school. Schools would be invited for the briefing and given an opportunity to view the equipment. Once school representatives select equipment for their schools' systems it would then be tagged. They would return to their schools and wait for notice to pick-up their equipment. If more than one tag was on the equipment, the education office would decide what school would get the equipment by priority list, elementary, secondary, colleges and universities. Once the schools are notified, then the schools would have fourteen days to pick-up the equipment.



An examination of the current setup indicates that change needs to be made that would better accommodate participating states. The new executive order states that newspapers, community announcements, and the Internet can be used for promotion of the act's purpose. It is my belief that NASA should use its established resources to distribute the information to each school, starting with three points of contact in each state. It should include: State Department of Education for public schools, State Department of Education for private schools and the Commission of Higher Education. I firmly believe that additional information needs to be distributed on a wider scale. I would suggest contact be made with at least two newspapers and education associations in each state. I further suggest that NASA continue to use the resources already established. These include: Teacher Resource Center Network, NASA TV, NASA Spacelink, Pamphlets, Professional Conferences, Flyers, Mobile Teacher Resource Center and Teacher Enrichment Programs.

I surveyed three hundred and sixty-two teachers, administrators around the United States. The levels included K-12, teachers and administrators- local and state levels, Colleges and University faculty member and some University administrators. The surveys consist of ten questions that was asked of the pool in effort to acquire knowledge about this law. One question was, have you heard about the Stevenson-Wydler Technology Innovation Act? Their response indicated that ninety-seven percent of them had not and three percent had. Ninety-nine percent of the people surveyed said they did not know if their organization had taken advantage of this opportunity. One hundred percent of the people did not know how long this law had been in effect. Another question asked, was what is the most effective way for an educator to gather information that will benefit his/her institution. Forty-one percent said the Internet, eighteen percent said using a mailing list, seventeen percent said newspaper, fifteen percent said journal and nine percent said using other methods. They were also asked to list three ways educational systems nationwide can effectively receive information? The top three answers were Internet thirty-four percent, direct mail twenty-two percent and Journals and Organizations twenty percent. The surveyors were asked if they knew what an Empowerment Zone and/or Enterprise Community is? Eighty-seven percent of the surveyors did not know. Ninety-five of them did not know if they lived in one of these areas. It was also asked what would be the most feasible way your institution to view excess government research equipment. Forty-seven percent said the Internet, twenty-six percent said catalog or mailouts, fifteen percent said video tapes, nine percent said site visits and three percent said other ways. The final question is what method of delivery would be most feasible for your institution to receive surplus equipment and fifty-one percent said by UPS, thirty-four percent said by freight, ten percent said mail and five percent said personal pick-up.

## **RESULTS**

Research, interviews, and site visits contributed heavily to my results. After analyzing the information and the procedures of the pilot plan, I researched and interviewed people from Marshall Space Flight Center and prospective customers. Many customers I spoke with did not know where to obtain information related to the Stevenson-Wydler Technology Innovation Act. Considering my research, NASA must distribute the information to their customers in a more

feasible manner. The biggest "hurdle" is NASA's inability to use the power of advertisement. The center should use its current resources to promote the programs that are available to the education community.

My proposal is to distribute information to our educational customers via newspapers, educational associations and NASA programs already established. After the distribution of information to prospective customers and areas, contact should be made on a state-by-state basis. This should be done across the entire spectrum of education, from top to bottom. An example would be the State Board of Education for public and private schools, and Commission of Higher Education. Once the information is distributed the opportunity will then rest on the individual school systems.

Another option for equal distribution is to let the school's view and tag surplus equipment on the Internet. If NASA would start-up a database with the schools that are participating, then they would have a file of schools who have not taken advantage of this opportunity and contact those schools directly. This related information would strengthen the lines of communication and make future contact even much easier.

Customers should also be briefed about the procedures and requirement for the program. This should be done using video tape so the customers would know what they need and what to expect when they surf the net and/or travel to the center, to tag equipment. A system should definitely be devised that would allow the customer to pickup equipment and/or have it shipped on the day it is tagged. This would be much more feasible and economical for the customers.

My personal opinion is that implementation of the Stevenson-Wydler Technology Innovation Act should begin soon. Phase I, should begin August 1, 1996, Distribute information to Newspapers, Education Associations, NASA TV, Internet, Pamphlets, Teacher Enrichment Programs and National Space Grant College and Fellowship Program State Consortium Offices should be contacted and information distributed related to the contact person and general information about the law.

Phase II, September 1, 1996, contact all school districts in the Empowerment Zones and Enterprise Communities. School representatives will complete necessary paperwork and return it to NASA's Education Office. Once the information is received the Education Program Office will mail a video tape for the district to view. After the tape is viewed it will be returned to the Education Office. The districts will later receive a letter informing the school of scheduled dates and times for the purpose of viewing and tagging equipment. The deadline for the paperwork should be returned around October 10, 1996. If the school chooses to tag equipment it should be available for delivery and/or pick-up the same day.

Phase III will begin October 1996, contact State Department of Education for public and private schools. Their deadlines for response will be November 10, 1996. Phase III will follow the same steps as Phase II. After the information is received school representatives will be given an opportunity to view the equipment.

Phase IV will begin November 1, 1996. The Commissioner of Higher Education in each state will be contacted. Phase IV will follow the same procedures as Phase II and III. Once the paperwork is received they will be able to view and tag equipment. The deadline for the paperwork will be December 10, 1996.

Phase V, the final stage of the implementation plan will allow all schools and nonprofit organizations to visit and view equipment. Once the information is stored on a database, the Education Office will have knowledge of the schools' districts that did not participate and do a follow-up. With the usage of the database other educational opportunities for the schools will be easily relayed, having direct contact in each district. After completion of all phases the school will take advantage of the information, tag and visit as often as necessary. One must also remember the second part of the law-federal employers volunteering their time to help connect our schools to technology and equipment. Since Marshall has a volunteer program already in place, Project Laser, then this could be used as an integral part of the law that is already functional. Marshall Space Flight Center must institute tagging over the Internet, the pick-up on the same day as the site visit, and allow more days to view and tag equipment on site. Besides the laws, emphasis must be placed on school districts in all six states. This implementation program should include all schools.

## **CONCLUSION**

Information that is proclaimed by law to help the needs of schools and school systems needs to find its way into these systems. With federal agencies having this information it must be distributed so all schools can take advantage of the opportunity. If we want our children to be prepared for the 21st century then all avenues must be open. These advances cannot be open for the few and privileged, but for all. If we only help the few and privileged, these United States will not be a functional, from a progressive standpoint, in the future. We have to distribute this information to everyone and let them make the decision about whether or not to take advantage. Some of this information will help schools that have no funds to obtain some of the technology available. It's in our hands how will we use it. Will we help only a few or will we help the masses. When we look at the opportunities of the Internet and the database the possibilities to open "doors" for the future seem endless.

## **ACKNOWLEDGMENT**

I would like to thank Mr. Jim Pruitt and the Education Office team for their support. I felt I was truly accepted as a team member. I appreciate the time and effort the team members contributed to my project. I appreciate the Spacelink Office for their assistance during my research efforts.

**1996**

**NASA /ASEE SUMMER FACULTY FELLOWSHIP PROGRAM**

**MARSHALL SPACE FLIGHT CENTER  
THE UNIVERSITY OF ALABAMA**

**COMPUTATIONAL MODELING  
OF  
MAGNETICALLY ACTUATED PROPELLANT ORIENTATION**

Prepared By:	John I. Hochstein, Ph.D.
Academic Rank:	Associate Professor
Institution and Department:	The University of Memphis Department of Mechanical Engineering
NASA/MSFC:	
Laboratory:	Propulsion Laboratory
Division:	Propulsion Systems
Branch:	Systems Requirements and Analysis
MSFC Colleague:	George R. Schmidt, Ph.D.



## INTRODUCTION

Unlike terrestrial applications where gravity positions liquid at the "bottom" of the tank, the location of liquid propellant in spacecraft tanks is uncertain unless specific actions are taken or special features are built into the tank. Some mission events require knowledge of liquid position prior to a particular action: liquid must be positioned over the tank outlet prior to starting the main engines and must be moved away from the tank vent before vapor can be released overboard to reduce pressure. It may also be desirable to positively position liquid to improve propulsion system performance: moving liquid away from the tank walls will dramatically decrease the rate of heat transfer to the propellant, suppressing the boil-off rate, thereby reducing overall mission propellant requirements. The process of moving propellant to a desired position is referred to as propellant orientation or reorientation.

Propulsive reorientation relies on small auxiliary thrusters to accelerate the tank. The inertia of the liquid causes it to collect in the aft-end of the tank if the acceleration is forward. Liquid Acquisition Devices (LAD's) rely on surface tension to hold the liquid within special geometries, (i.e. vanes, wire-mesh channels, start-baskets), to positively position propellants. Both of these technologies add significant weight and complexity to the spacecraft and can be limiting systems for long duration missions. The subject of the present research is an alternate technique for positively positioning liquid within spacecraft propellant tanks: magnetic fields.

LOX is paramagnetic (attracted toward a magnet) and LH<sub>2</sub> is diamagnetic (repelled from a magnet). Order-of-magnitude analyses, performed in the 1960's to determine required magnet size, concluded that the magnets would be prohibitively massive and this option has remained dormant during the intervening years. Recent advances in high-temperature superconducting materials hold the promise of electromagnets with sufficient performance to support cryogenic propellant management tasks. In late 1992, NASA MSFC began a new investigation in this technology commencing with the design of the Magnetically-Actuated Propellant Orientation (MAPO) experiment. A mixture of ferrofluid and water is used to simulate the paramagnetic properties of LOX and the experiment is being flown on the KC-135 aircraft to provide a reduced gravity environment. The influence of a 0.4 Tesla ring magnet on flow into and out of a subscale Plexiglas tank is being recorded on video tape.

The most efficient approach to evaluating the feasibility of MAPO is to compliment the experimental program with development of a computational tool to model the process of interest. The goal of the present research is to develop such a tool. Once confidence in its fidelity is established by comparison to data from the MAPO experiment, it can be used to assist in the design of future experiments and to study the parameter space of the process. Ultimately, it is hoped that the computational model can serve as a design tool for full-scale spacecraft applications.

## MATHEMATICAL MODEL

Although the practitioner of experimental or computational fluid mechanics may have familiarity with many of the features of the research problem, it is less likely that he/she will have a strong background in the magnetic and paramagnetic aspects of the problem. The author spent considerable time and effort retrieving the background information in these areas and has

collected the basic information into a single resource that it is hoped will be of value to other researchers who tackle this problem, "Magnetism and the Flow of Paramagnetic Fluids: An Introduction for the Non-Specialist." In addition to this review of the basic physics, 22 papers related to the flow of paramagnetic fluids and ferrofluids were extracted from the literature and assembled into a reference resource.

LOX and LH2 are reasonably well represented as incompressible, constant property, Newtonian fluids and therefore the flow of interest can be modeled using a modified form of the Navier-Stokes equations

$$\rho \frac{\partial \vec{V}}{\partial t} + \rho (\vec{V} \cdot \nabla) \vec{V} = -\nabla p + \mu \nabla^2 \vec{V} + \rho \vec{g} + \mu_0 \chi \nabla H \nabla H$$

where  $\rho$ ,  $\vec{V}$ ,  $p$ ,  $\mu$ , and  $\vec{g}$  have the usual definitions of density, velocity, viscosity, and gravity,  $\mu_0$  is the permeability of free space,  $\vec{H}$  is the magnetic intensity,  $\vec{M}$  is the magnetization, and  $\chi$  is the susceptibility. The last term on the right-hand side is known as the Pondermotive force and provides the coupling between the magnetic field and the fluid motion. The form shown assumes that: the direction of the magnetization vector is always in the direction of the local magnetic field, the fluid is electrically nonconducting, the displacement current is negligible, and the magnetization is linear. In addition to the usual flow boundary conditions, the normal stress boundary condition at a gas/liquid interface is given by:

$$\Delta p = \sigma \kappa + \frac{1}{2} \mu_0 \left[ (\vec{M} \cdot \hat{n})_{\text{liq}}^2 - (\vec{M} \cdot \hat{n})_{\text{gas}}^2 \right]$$

where the first term is the "pressure jump" at the interface due to surface tension and the second term is the "magnetic pressure" due to the change in magnetization across the interface.

## COMPUTATIONAL MODEL

A computational tool for the simulation of MAPO must be able to solve all of equations and boundary conditions identified above and must model the large interface deformation and mass transport associated with bulk propellant motion within the spacecraft tank. These requirements eliminate most candidate CFD codes and identify the RIPPLE code as uniquely well qualified to serve as the foundation for building the desired computational tool. RIPPLE was developed at the Los Alamos National Laboratory under an interagency agreement with NASA and source code is readily available. Except for the Pondermotive force term, the baseline code provides all of the required capabilities and the fidelity of this code in modeling propulsive propellant reorientation has been previously demonstrated.

RIPPLE models the transient laminar flow of an incompressible Newtonian fluid. The flow field is discretized into finite volumes to form a nonuniform computational mesh. A staggered-grid approximation to the continuity and momentum equations produces a nonlinear system of algebraic equations that is solved using a two-step projection method. The VOF technique is used to follow the advection of mass through an Eulerian mesh. The Continuum Surface Force (CSF) model provides a sophisticated and robust model for surface tension forces. A supporting graphics package, known as RGO, was ported to a workstation (SGI 4D/35TG) in the MSFC computational environment. The analysis code contains a sequence of subroutine

calls in which each subroutine computes the contribution of a force term to momentum equation. A new subroutine, ponder, has been written to compute the contribution of the Pondermotive force and this subroutine has been inserted into the calling sequence. Additional modifications to support the magnetic model have been accomplished including changes to the I/O subroutines, common blocks, and modification of RGO to support variables introduced by the magnetic model.

## TEST CASES

Space limitations require that only a few selected computational results be presented in this report. One set of test cases were constructed with magnetic fields corresponding to;  $dh/dx = \text{constant}$ ,  $dh/dy = \text{constant}$ , and  $dh/dx = dh/dy = \text{constant}$ . Figure 1 shows that, as required by the theory, constant pressure contours are straight lines orthogonal to the gradient of the magnetic field, (the small deflections near the walls are an anomaly of the graphics). Figure 2 shows the predictions of a test case designed to demonstrate the modified code's ability to simulate a flow, driven by the pondermotive force, with a highly deforming free surface and surface tension. An imposed magnetic field gradient in the horizontal direction produces a region of high pressure at the left edge of the cavity which drives the bubble toward the right wall. Many other test cases have been studied and excellent results were obtained for all.

The goal of this effort, modeling the MAPO experiment has proven to be the most difficult test of the code. A dipole positioned along the tank centerline just below the bottom of the tank is used to represent the magnet. During simulation, a strong vortex quickly formed around the centerline at the bottom of the tank producing a geyser along the tank centerline that is not credible. A major effort ensued to determine the cause of the vortex. The pressure contours appeared credible. A variety of variations in modeling assumptions were studied to no avail. The expressions for magnetic field intensity and its gradient were re-derived and their numerical implementation checked for correctness using three different formulations. No errors were found. Analytical evaluation of the expression for the body force induced by the dipole field verified that the force field is irrotational. After considerable detective work, it was concluded that the source of vorticity might be the finite-difference approximations used to represent the body force in the code. A numerical experiment was performed to compare the curl of the body force computed small perturbations about the location where the force is computed to the curl computed "as the computational model would see it." The results were conclusive and supported the hypothesis: the curl was being artificially generated in the code because the strong and highly nonlinear magnetic field in the neighborhood the dipole was not being adequately represented. The final analysis of the summer simulated the MAPO experiment using a mesh that is "packed" toward the region of high field strength near the dipole. The case starts with a flat free surface located at the mid-height of the tank and the gravitational field is linearly reduced from 1 g to 0.01 g during the first seven seconds to simulate the KC 135 environment. Figure 3 presents a sequence of flow fields predicted for elapsed times from problem start of 2.0, 4.0, 6.0, 10.0, and 20.0 seconds. Although this result is now credible, further testing must be performed before confidence in the quality of the flow field predictions can be established.



## FUTURE DIRECTIONS

The preceding text describes twenty weeks, (two summers), of effort. A fairly difficult problem has been approached and preliminary tests indicate a good chance of success for the methods and tools developed. The next step should be an effort to improve the accuracy of the pondermotive force model. Although mesh refinement definitely helped reduce the problem of numerical vorticity, the study shows that elimination of this artifact may impose an unacceptable computational burden on other cases. Once this is accomplished, the code should be exercised on additional test cases that have been identified during the literature search for which experimental data or analytical solutions are available. The fidelity of the code should then be evaluated by comparing computational predictions to measurements from the MAPO experiment. Successful completion of this research program will produce a valuable tool that can be used for the design of additional experiments, to study the parameter space of the MAPO process, and ultimately as a design tool for full-scale spacecraft applications.

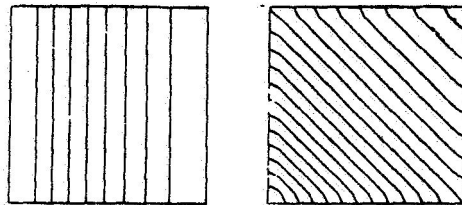


Figure 1

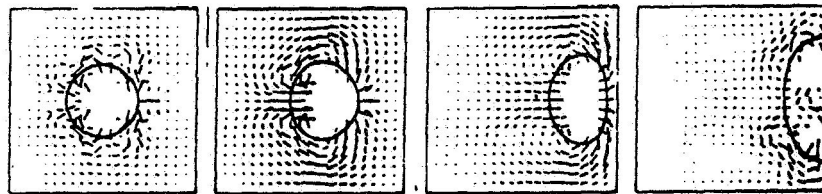


Figure 2

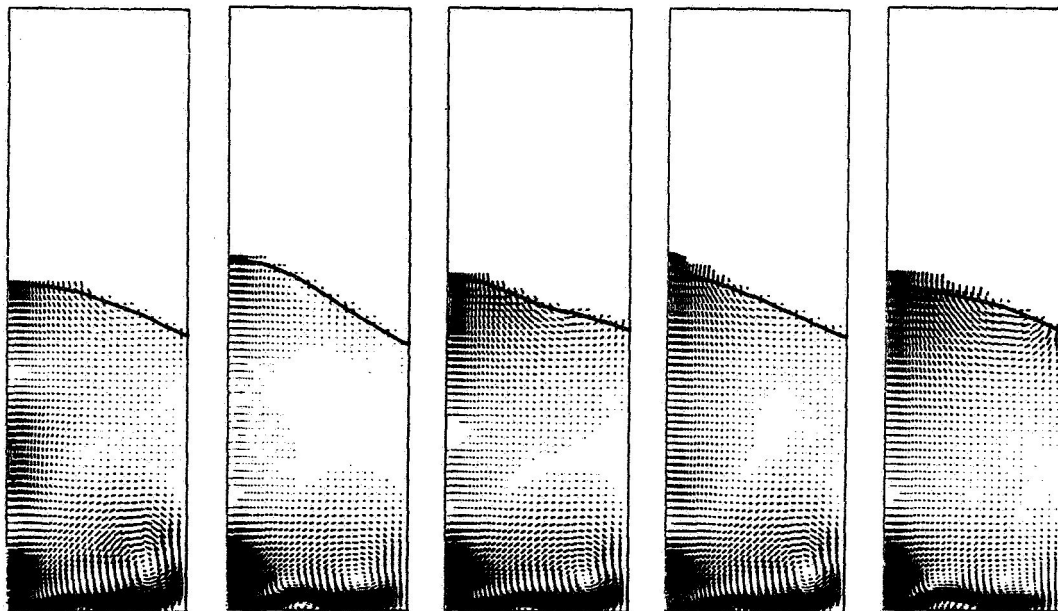


Figure 3

1996

NASA/ASEE SUMMER FACULTY FELLOWSHIP PROGRAM

MARSHALL SPACE FLIGHT CENTER  
THE UNIVERSITY OF ALABAMA

PRELIMINARY WORK IN OBTAINING SITE-DIRECTED MUTANTS  
OF HEN EGG WHITE LYSOZYME

Prepared By: Leonard D. Holmes, Ph.D.

Academic Rank: Assistant Professor

Institution and Department: Department of Physical Science  
The University of North Carolina at Pembroke

NASA/MSFC SPACE SCIENCES LABORATORY

MSFC Colleague: Marc L. Pusey, Ph.D.



## INTRODUCTION

Protein crystal growth studies are recognized as a critical endeavor in the field of molecular biotechnology. The scientific applications of this field include the understanding of how enzymes function and the accumulation of accurate information of atomic structures, a key factor in the process of rational drug design. NASA has committed substantial investment and resources to the field of protein crystal growth and has conducted many microgravity protein crystal growth experiments aboard shuttle flights. Crystals grown in space tend to be larger, denser and have a more perfect habit and geometry. These improved properties gained in the microgravity environment of space result largely from the reduction of solutal convection, and the elimination of sedimentation at the growing crystal surface. Shuttle experiments have yielded many large, high quality crystals that are suitable for high resolution X-ray diffraction analysis. Examples of biologically important macromolecules which have been successfully crystallized during shuttle missions include: lysozyme, isocitrate lyase, gamma-interferon, insulin, human serum albumin and canavalin. Numerous other examples are also available.

In addition to obtaining high quality crystals, investigators are also interested in learning the mechanisms by which the growth events take place. Crystallization experiments indicate that for the enzyme HEWL, measured growth rates do not follow mathematical models for 2D nucleation and dislocation-led growth of tetragonal protein crystals. As has been suggested by the laboratory of Marc L. Pusey, a possible explanation for the disagreement between observation and data is that HEWL tetragonal crystals form by aggregated units of lysozyme in supersaturated solutions. Surface measurement data was shown to fit very well with a model using an octamer unit cell as the growth unit. According to this model, the aggregation pathway and subsequent crystal growth is described by:

monomer <-----> dimer <-----> tetramer <-----> octamer <-----> higher order

It is believed that multimer aggregation of lysozyme occurs by interaction at specific binding sites on the surface of the protein crystals. If the presence of discrete binding sites and the aggregation hypothesis is true, then it follows that the alteration of the binding site(s) should have significant effect on the measurements obtained during growth experiments.

Site-directed mutagenesis allows the specific alteration of proteins by replacement, deletion or addition of specific amino acid residues. This report outlines the approach for this strategy and the progress made thus far toward that end.

## EXPERIMENTAL

I. Isolation of plasmid DNA. The HEWL gene was provided by the Kirsch lab (UC-B)

on a pAB24 circular double-stranded plasmid. This plasmid carries the gene for leucine synthesis, allowing for isolation and selection on leucine minus media. Figure 1. shows a map of this pDNA and the location of the genes and restriction sites.

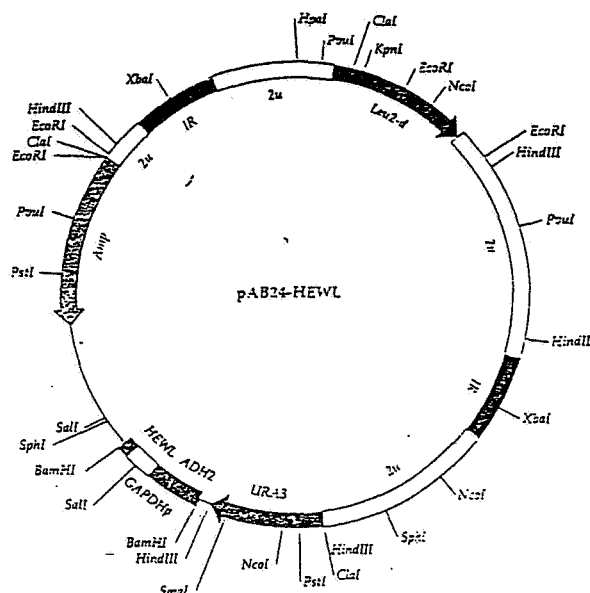


Figure 1.

The plasmid is contained in *E.coli* strain DH52. The plasmid was isolated and purified following three protocols:

a. Promega Wizard Mini-Prep Purification Systems. This approach was utilized to carry out small-scale purifications of pDNA (minipreps). An overnight 5 mL culture of *E.coli* in LB broth containing ampicillin was treated according to Promega protocol. Briefly, a cell pellet is lysed, neutralized and applied to a proprietary silica-based column resin. The plasmid DNA is then eluted with Wizard Column Wash Solution.

b. Plasmid DNA Purification by PEG Precipitation. Polyethylene glycol (PEG) precipitation is a rapid, reliable and convenient method for the purification of milligram quantities of highly purified pDNA. A culture of 500 mL in LB media containing ampicillin antibiotic is inoculated and grown overnight. the cells are harvested by centrifugation. The protocol calls for the initial preparation of a crude lysate pellet by alkaline lysis. Since plasmids are much smaller than chromosomal DNA, subsequent centrifugation permits separation of the plasmids from the chromosomal DNA and cellular debris. Although the resulting supernatant solution is enriched in plasmid, significant amounts of genomic DNA and RNA must be removed if the plasmids are to be used for mutagenesis. Finally, plasmid DNA is extracted from the supernatant with phenol/chloroform/isoamyl alcohol, followed by precipitation with PEG. This produces a DNA preparation free of any contaminants.

c. Promega Wizard Plus Maxipreps DNA Purification System. This is a fairly simple and rapid protocol for large-scale plasmid purifications. A 400 mL overnight culture will typically

yield 500 micrograms of pDNA. Plasmid yield will depend on several factors including volume of bacterial culture, plasmid copy number, culture medium and bacterial strain. An advantage of this system is that it does not require organic extractions or long overnight PEG precipitations. In brief, the protocol uses alkaline lysis to break open the cells. Genomic DNA and cell Debris is removed by precipitation and centrifugation. The Supernatant is applied to the Promega column and the pDNA is eluted by low speed centrifugation.

## II. Identity and quantity of purified pDNA.

a. Identity. The double stranded plasmid DNA may be characterized by treatment with restriction endonuclease enzymes that recognize short DNA sequences and cleave at sites within or near these regions. We attempted to cleave the pAB24 plasmids by incubation with two restriction enzymes. SalI and BamHI were added to appropriate quantities of pDNA in restriction buffers and incubated for at least one hour at 37 °C. These incubations were then loaded onto a 1% agarose submarine gel for horizontal electrophoresis at approximately 10 volts/cm of gel. The restriction treatment should have produced DNA fragments that could be visualized by treatment with ethidium bromide at 254nm. Additionally, we experimented with another commercial fluorescent visualization (SYBER Green I Nucleic Acid Gel Stain from Molecular Probes, Inc.) system. Unfortunately, the restriction experiments appeared inconclusive. The digestions were incomplete. Possible sources of this apparent low enzyme activity include: 1) contamination with phenol extraction solvent 2) impure pDNA prep 3) denaturation of restriction enzyme. It was learned also that small amounts of BSA added to the restriction digest may improve enzyme performance.

b. Quantitation. The amount of plasmid DNA and the purity was assessed by UV absorption.  $A_{260}$  is a reliable measure of nucleic acid, while  $A_{280}$  indicates total protein. Although the  $A_{260}$  measurement cannot discriminate between pDNA, genomic DNA and RNA the ratio of  $A_{260}/A_{280}$  is used as an indicator of purity. A ratio of 1.8 to 1.9 indicates highly purified DNA. Protein contaminants will lower this number. Our pDNA preps had ratios ranging from approx. 1.1 to 1.9. The best prep was obtained by using the Promega Wizard Plus Maxipreps DNA Purification System (0.750 mg/mL).

## III. Yeast Genetics.

a. Yeast cell cultures & electroporation. The aim was to transform liquid cultures of yeast cells (*S. cerevisiae*) with the plasmid DNA and induce the yeast to synthesis lysozyme enzyme. The yeast will excrete lysozyme to the liquid medium and then the protein may be purified. The purification of HEWL is routine business in the Pusey group, and should not be problematic. The concentration of lysozyme enzyme in the media will approach approx. 10milligrams/liter cell culture. Thermostatically controlled batch fermentations of yeast may be carried out. Alternatively, the Pusey lab may elect to have a single large culture prepared by contract at a facility such as the UAB Fermentation Center (Birmingham). Cultures of 500

mL of yeast cells were inoculated with 5 mL of overnight culture. The culture was grown in sterile, rich medium of yeast extract, peptone and dextrose (YPD) (30 °C, vigorous shaking). The cells were then harvested by centrifugation and made competent for uptake of plasmid DNA by electroporation. An *Invitrogen Electroporator II* instrument was used for transformation experiments. The protocol for yeast electroporation as recommended by *Invitrogen* was followed.

b. Isolation of transformed colonies. 100 microliters of the electroporated yeast cells were spread on plates containing solid selective dropout media. The media was prepared according to the recipe outlined in *Current Protocols*. Two types of media were used: a) complete b) minus leucine. The media also contained 1 molar sorbitol in some experiments. The addition of sorbitol to the solid media gave no visible improvement in colony survival and growth. The media also contained 8% glucose as according to the protocol of Shih et. al. A modification of the *Protocols* preparation included adjusting of the pH to 7.0. The specific protocol followed in this work is outlined:

1.3 g (plus or minus leu) dropout powder

1.7 g YNB (no aa, no ammonium sulfate)

5 g ammonium sulfate

300 mL water -----adjust this 300 mL solution to pH 7/filter sterilize

80 g glucose

182 g sorbitol

20 g agarose

700 mL water ----- 700 mL, autoclave

#### IV. Results of transformation experiments

Electroporation protocol is reported to result in transformation efficiencies approx. 10 to 100 times greater than chemical transformation methods. Repeated electroporation experiments did not yield any yeast transformants that survived on the (minus leucine) plates. Electroporated cells however, did grow and thrive nicely on complete media plates. These results indicate that the yeast did not take up the pAB24 plasmid via electroporation. Electroporation is expected to kill approx 70-80 percent of the treated cells. Cell counts taken before and after electroporation revealed that an expected fraction of the cells perished due to electroporation.

#### CONCLUSION AND ACKNOWLEDGMENTS

Molecular biology can be a powerful approach to studying the crystallization of biological macromolecules. Using the techniques of genetic manipulation, in principle, it is possible to alter the physico-chemical properties of enzymes and examine the effect on their crystallization behavior. Although this summer work did not achieve all goals hoped for at the outset, it did

serve as a beginning upon which continued work may build upon. The Pusey laboratory now has the a starting point to begin a more vigorous exploration into the application of molecular biology to the problem of protein crystallization.

This work was a result of teamwork with Laurel Karr (NASA) and Randy Wolfe (Visiting Summer High School Scholar). Their efforts toward making this work an educational and productive project is sincerely appreciated. Dr. Andy Britton (USRA) and Dr. Tom Prasthofer (NASA/ASEE Summer Faculty Fellow) are acknowledged for many helpful discussions, freely given instruction and personal time. A very special thanks is given to Dr. Marc Lee Pusey, my NASA host, who paid for this work and had the insight to understand its potential importance.

## REFERENCES

- Current Protocols in Molecular Biology*, Vol 1-3. John Wiley & Sons, Inc. (1995)  
*Invitrogen Electroporator Manual*, Invitrogen Co., San Diego  
*Promega Wizard Miniprep and Maxiprep Technical Bulletin*, Promega Corp, Madison, WI.  
Shih, P. et.al., *Methods in Enzymology*, 224, 576-590 (1993)





**1996  
NASA/ASEE FACULTY FELLOWSHIP PROGRAM**

**MARSHALL SPACE FLIGHT CENTER  
THE UNIVERSITY OF ALABAMA**

**SSME CONDITION MONITORING USING NEURAL NETWORKS AND PLUME  
SPECTRAL SIGNATURES**

Prepared by:	Randall Hopkins, M.S. AE Daniel Benzing, B.S. AE
Academic Rank:	Instructor Graduate Student
Institution and Department:	The University of Alabama at Tuscaloosa Department of Aerospace Engineering
NASA/MSFC:	
Laboratory:	Astrionics Lab
Division:	Propulsion Systems
Branch:	Instrumentation
MSFC Colleague:	Anita Cooper, W.T. Powers



## Introduction

For a variety of reasons, condition monitoring of the Space Shuttle Main Engine (SSME) has become an important concern for both ground tests and in-flight operation. The complexities of the SSME suggest that active, real-time condition monitoring should be performed to avoid large-scale or catastrophic failure of the engine.

In 1986, the SSME became the subject of a plume emission spectroscopy project at NASA's Marshall Space Flight Center (MSFC). Since then, plume emission spectroscopy has recorded many nominal tests and the qualitative spectral features of the SSME plume are now well established. Significant discoveries made with both wide-band and narrow-band plume emission spectroscopy systems led MSFC to develop the Optical Plume Anomaly Detection (OPAD) system.

The OPAD system is designed to provide condition monitoring of the SSME during ground-level testing. The operational health of the engine is achieved through the acquisition of spectrally resolved plume emissions and the subsequent identification of abnormal emission levels in the plume indicative of engine erosion or component failure. Eventually, OPAD, or a derivative of the technology, could find its way on to an actual space vehicle and provide in-flight engine condition monitoring. This technology step, however, will require miniaturized hardware capable of processing plume spectral data in real-time.

An objective of OPAD condition monitoring is to determine how much of an element is present in the SSME plume. The basic premise is that by knowing the element and its concentration, this could be related back to the health of components within the engine. For example, an abnormal amount of silver in the plume might signify increased wear or deterioration of a particular bearing in the engine. Once an anomaly is identified, the engine could be shut down before catastrophic failure occurs.

Currently, element concentrations in the plume are determined iteratively with the help of a non-linear computer code called SPECTRA, developed at the USAF Arnold Engineering Development Center. Ostensibly, the code produces intensity versus wavelength plots (*i.e.*, spectra) when inputs such as element concentrations, reaction temperature, and reaction pressure are provided. However, in order to provide a higher-level analysis, element concentration is not specified explicitly as an input. Instead, two quantum variables, number density and broadening parameter, are used.

Past experience with OPAD data analysis has revealed that the region of primary interest in any SSME plume spectrum lies in the wavelength band of 3300 Å to 4330 Å. Experience has also revealed that some elements, such as iron, cobalt and nickel, cause multiple peaks over the chosen wavelength range whereas other elements (magnesium, for example) have a few, relatively isolated peaks in the chosen wavelength range.

Iteration with SPECTRA as a part of OPAD data analysis is an incredibly labor intensive task and not one to be performed by hand. What is really needed is the "inverse" of the computer code but the mathematical model for the inverse mapping is tenuous at best. However, building

generalized models based upon known input/output mappings while ignoring details of the governing physical model is possible using neural networks.

Thus the objective of the research project described herein was to quickly and accurately predict combustion temperature and element concentrations (*i.e.*, number density and broadening parameter) from a given spectrum using a neural network. In other words, a neural network had to be developed that would provide a generalized “inverse” of the computer code SPECTRA.

### Radial Basis Function Networks

With most neural networks the objective is to estimate a function  $y(x)$  from a training set of representative input/output pairings:

$$\left\{(\bar{x}_i, \bar{y}_i)\right\}_{i=1}^P$$

It has been shown that traditional backpropagation (BP) neural networks can sufficiently perform this mapping with only two hidden layers provided the function is well behaved over the domain of interest. The required hidden layers are usually composed of neurons with sigmoidal activation functions which combine to form localized “bumps” or response regions within the input space. In this manner, the network paves the input space with response bumps that are only non-zero in a small region. Instead of using two hidden layers of sigmoidal units, this local behavior could also be obtained with a single hidden layer of radial basis functions. By definition, a radial basis function is one which decreases monotonically away from a central point thereby giving it an inherent bump form. Classic functions that exhibit this propensity are the Gaussian, Cauchy, and the Inverse Multiquadric. For RBF networks, the choice of function does not make much difference as long as it possesses the local response region. The Gaussian function is written as:

$$g_j(\bar{x}) = -\exp\left[\frac{-(\bar{x} - \mu_j)^2}{2\sigma_j^2}\right]$$

Thus, a given hidden RBF neuron will be centered at  $\mu_j$  within the input space and have a “receptive field” which is proportional to  $\sigma_j$ . Moreover, it will give a maximum response for input vectors ( $\bar{x}$ ) which are near the center ( $\mu_j$ ).

The goal of the RBF algorithm is to arrange an assortment of these receptive fields so that response areas are created which sufficiently cover the input space. This is done in a two part learning scheme known as hybrid learning. The initial layer of the network contains the RBF centers which are obtained through unsupervised assimilation. This is called unsupervised because there is not a well defined learning goal; instead categories must be developed from correlation’s within the input training data. The layer essentially clusters the inputs and specifies where to position the RBF centers so that the desired response coverage is obtained. Having a layer with unsupervised learning offers a significant savings in training time over the traditional BP scheme. However, the hybrid scheme is not optimal in the sense that the BP algorithm is. The reason for this has to do with the non-linear nature of the BP front-end layer. The weight parameters which contribute to the hidden layer responses are adjusted with respect to the performance of the outputs. In contrast, the RBF centers are chosen *a priori* and remain fixed throughout the output layer training. As a result, RBF networks normally require more neurons

to attain the same error goal. This disadvantage, however, is usually outweighed by the savings in training time.

The output layer of the RBF network is trained in a supervised fashion. Supervised means that the learning is based on comparison of the network output with the known “correct” answers. Thus, given that the basis function centers are fixed (making this a *linear* network), the optimal weight array for the output layer which gives the proper functional mapping can be found using multiple linear regression. Details of this procedure can be found in any decent regression book; the results are simply stated here. For a set of training input vectors,  $x$ , with corresponding RBF centers  $\mu$ , there will be an array of Gaussian neuron responses,  $G$ . Given this, the optimal weight array can be stated as:

$$w = [G^T G]^{-1} G^T y$$

where,  $y$  is the corresponding target values. The mathematical form of the weight array is also known as the normal equation in classical regression theory.

### Network Performance

Separate RBF network’s for the monitoring of each metal were created using training data generated from the aforementioned SPECTRA code. To test the validity of the network configuration a set of spectral data obtained during a January 1996 SSME Failure event at Stennis Space Flight Center were used. The spectral scans were taken every half second until the engine failure. Post test analysis revealed that the major spectral anomalies occurred at the times shown in Table 1 given below.

Table 1.  
Major Anomalous Event Times (Seconds)

130-131
276
283
404-405.5
531-Engine Failure

The neural networks were used to evaluate plume temperature, elemental number densities, and broadening parameters for every half second of data. The results are shown in Figure 1 on the next page. Temperature predictions were near perfect; a quick study of the number density predictions shows that all the major anomalies were indicated by number density spikes at the appropriate times specified in Table 1. Figure 1 represents two years of concerted effort and can speak justly of this entire paper. The neural networks passed the anomaly detection objective. Future work will involve the extension of the technology to real time flight systems.

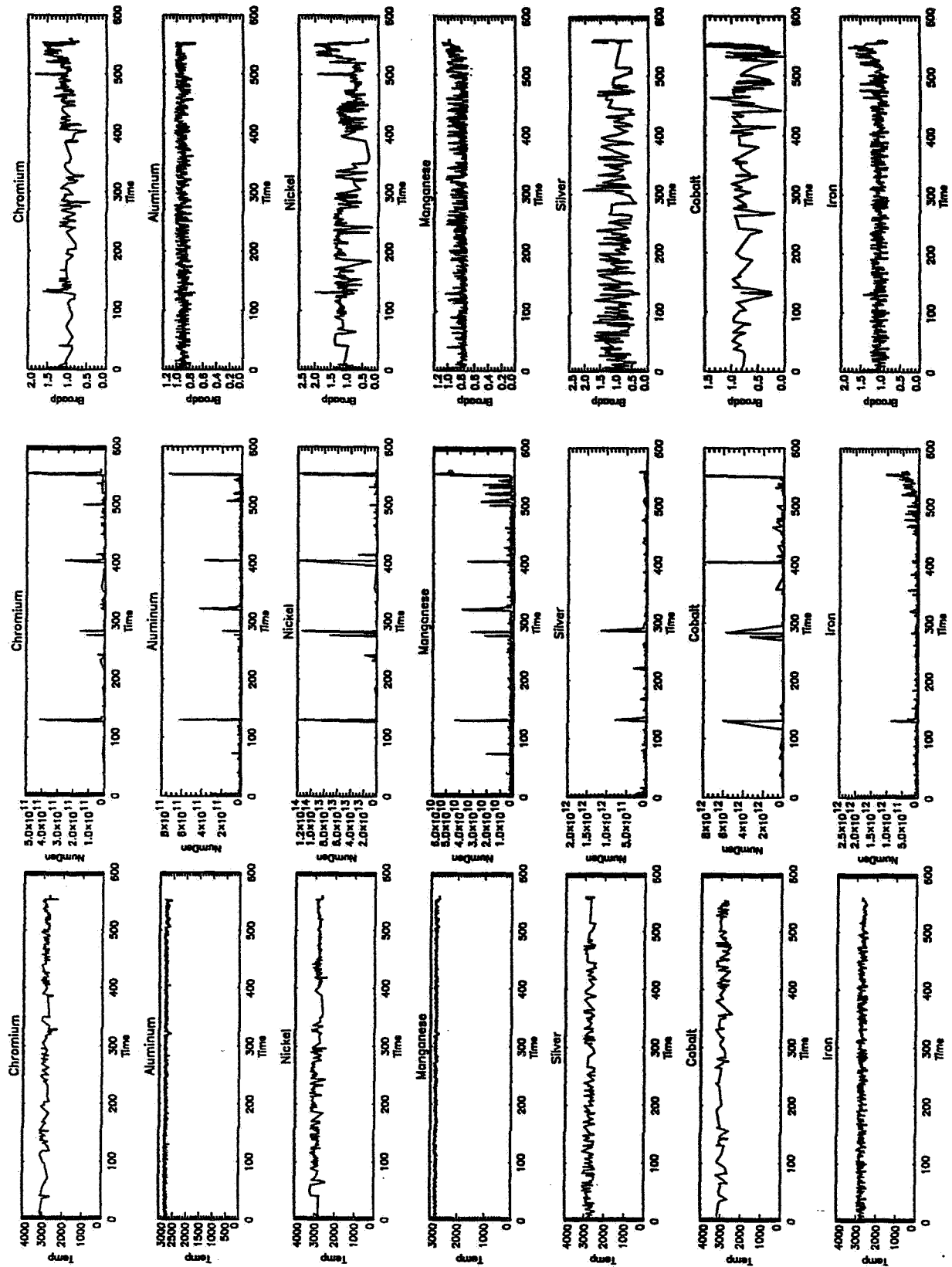


Figure 1.  
Neural Predictions for the Stennis Failure Event

**1996**

**NASA/ASEE SUMMER FACULTY FELLOWSHIP PROGRAM**

**MARSHALL SPACE FLIGHT CENTER  
THE UNIVERSITY OF ALABAMA**

**POINTING AND SCANNING CONTROL OF INSTRUMENTS  
USING ROTATING UNBALANCED MASSES**

Prepared By:	John Y. Hung, Ph.D.
Academic Rank:	Associate Professor
Accompanying Student:	David A. McGee
Institution and Department:	Auburn University Department of Electrical Engineering
NASA/MSFC:	
Laboratory:	Astrionics Laboratory
Division:	Instrumentation and Control
MSFC Colleague:	Michael E. Polites, Ph.D.





## INTRODUCTION

Motions of telescopes, satellites, and other flight bodies have been controlled by various means in the past. For example, gimbal mounted devices can use electric motors to produce pointing and scanning motions. Reaction wheels, control moment gyros, and propellant-charged reaction jets are other technologies that have also been used. Each of these methods has its advantages, but all actuator systems used in a flight environment face the challenges of minimizing weight, reducing energy consumption, and maximizing reliability. Recently, Polites invented [1] and patented [2] the Rotating Unbalanced Mass (RUM) device as a means for generation scanning motion on flight experiments. RUM devices have been successfully used to generate various scanning motions [3]. The basic principle: a RUM rotating at constant angular velocity exerts a cyclic centrifugal force on the instrument or main body, thus producing a periodic scanning motion. A system of RUM devices exerts no reaction forces on the main body, requires very little energy, and is very simple to construct and control. These are significant advantages over electric motors, reaction wheels, and control moment gyroscopes.

Although the RUM device very easily produces scanning motion, an auxiliary control system may be required to maintain the proper orientation, or pointing of the main body. It has been suggested that RUM devices can be used to control pointing dynamics, as well as generate the desired periodic scanning motion. The idea is that the RUM velocity will not be constant, but will vary over the period of one RUM rotation. The thought is that the changing angular velocity produces a centrifugal force having time-varying magnitude and direction. The scope of the present research project is to further study the pointing control concept, and to implement a microcontroller program to control an experimental hardware system.

This report is subdivided into three themes. The basic dynamic modeling and control principles are described first. Then, the controller implementation and preliminary test results are discussed. Finally, suggestions for future work are presented.

## DESCRIPTION OF THE DYNAMIC MODEL AND CONTROL

A sketch of a RUM system is shown in Figure 1. Two RUM devices are mounted on the main body so as to produce a circular scan with respect to the line-of-sight (LOS) vector. The RUMs rotate in the same direction, but are synchronized and positioned  $180^\circ$  apart to eliminate reaction forces at the center of mass. (In a zero-gravity environment, a single RUM is adequate.)

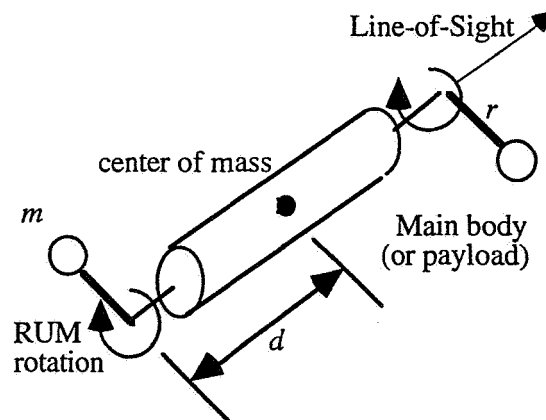


Figure 1. Sketch of a body using 2 RUMs to generate scanning.

A basic model describing the main body and RUM device dynamics is summarized below.

## Nomenclature

$m$	RUM mass
$r$	RUM radius of rotation
$d$	distance between RUM and payload center of mass, measured along the LOS.
$I$	main body inertia
$\theta_E$	main body elevation angle
$\theta_X$	main body cross-elevation angle
$\theta_R$	RUM angular position

The local coordinate system is shown in Figure 2. The axis  $\vec{P}_1$  is aligned with the main body line-of-sight (LOS). Axis  $\vec{P}_2$  is associated with the main body elevation angle  $\theta_E$ , while the main body cross-elevation angle  $\theta_X$  is associated with axis  $\vec{P}_3$ . All three axes pass through the main body center of mass. The RUM device rotates at constant speed.

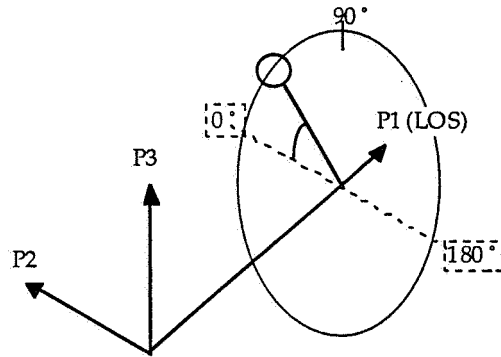


Figure 2. Coordinate system

## Plant Dynamics

Position of the RUM device relative to the  $\vec{P}_1$  axis is described by the vector:

$$\vec{\rho}(t) = r \cos[\theta_R(t)] \vec{P}_2 + r \sin[\theta_R(t)] \vec{P}_3 \quad (1)$$

Differentiating (1) twice yields the RUM mass acceleration vector. Centrifugal force is in the direction opposite the acceleration vector, and its magnitude is proportional to the RUM mass. Centrifugal force exerts a torque about the main body center of mass by acting through a moment arm of length  $d$ . In the system of Figure 1, the two RUM devices are controlled to rotate in synchronized fashion, but always pointing  $180^\circ$  opposite each other. Therefore, the total torque exerted about the main body center of mass is doubled. Angular acceleration of the main body is proportional to the torque, and can be expressed in elevation and cross-elevation components [1]:

$$\begin{aligned} \ddot{\theta}_E &= -\frac{2dmr}{I_E} \sin(\theta_R) \omega_R^2 \\ \ddot{\theta}_X &= \frac{2dmr}{I_X} \cos(\theta_R) \omega_R^2 \end{aligned} \quad (2)$$

Examination of the state-variable model yields a few interesting observations.

1. The elevation and cross-elevation angle dynamics are functions of the RUM position  $x_3$ , and RUM angular velocity  $\omega_R$ .
2. For each main body axis, the sine and cosine of RUM position can be considered as periodic weights on the “control input,” namely the RUM angular velocity squared. The influence of the “input” on a particular axis dynamics varies with respect to RUM position.

#### Pointing Control Using RUM Rate Variation

Note that the RUM angular velocity enters the main body axes dynamics in a squared function, so negative RUM angular velocities have identical effect as positive ones. Therefore, the acceleration and deceleration of the payload axes is only possible as the sine and cosine of RUM position lend changes in algebraic sign. Fortunately, such conditions occur periodically, since the RUM is turning at a nominal “constant” speed. Hence, as the RUM turns, alternating opportunities exist for each payload axis to be “steered.” Polites originally proposed to use a control signal that introduces periodic variations in the RUM rate  $\omega_R$ . The logic of such an approach can also be analytically confirmed by applying the nonlinear control design technique known as input-output linearization. The interested reader is directed to the references [4] - [6]. However, a simpler heuristic explanation is offered here. The control input is defined as:

$$\omega_R = \omega_{ro} + \Delta\omega_X \cos \theta_R - \Delta\omega_E \sin \theta_R \quad (3)$$

where

$\omega_{ro}$  : a constant (nominal RUM rate of rotation)

$\Delta\omega_X$  : a rate variation to compensate for cross - elevation gimbal error

$\Delta\omega_E$  : a rate variation to compensate for elevation gimbal error

The RUM rate variations  $\Delta\omega_X$  and  $\Delta\omega_E$  are small relative to the nominal RUM rate  $\omega_{ro}$ . Notice that the rate variations are periodic and “synchronized” to the RUM position through the  $\sin(x_3)$  and  $\cos(x_3)$  factors. Consider the model (2), and substitute the control (3) in the elevation axis dynamics. Then, the elevation axis acceleration is given by:

$$\ddot{\theta}_E = -\frac{2dmr}{I_E} \sin \theta_R (\omega_{ro} + \Delta\omega_X \cos \theta_R - \Delta\omega_E \sin \theta_R)^2 \quad (4)$$

Expand the right-hand side, but retain only the low-order terms:

$$\ddot{\theta}_E \approx -\frac{2dmr}{I_E} (\omega_{ro}^2 \sin \theta_R + \omega_{ro} \Delta\omega_X \cos \theta_R \sin \theta_R - \omega_{ro} \Delta\omega_E \sin^2 \theta_R) \quad (5)$$

Eq. (5) states that the elevation axis acceleration is influenced by three terms. Since the RUM rate variations are small, the expression can be further simplified. The second term can be omitted, since it is a higher-order “cross” term. A trigonometric identity can be applied to the third term to expose a low-order component. As a result, the elevation axis acceleration is approximately:

$$\ddot{\theta}_E \approx -\frac{2dmr}{I_E} \left( \omega_{ro}^2 \sin \theta_R - \frac{\omega_{ro}}{2} \Delta\omega_E \right) \quad (6)$$

Approximation (6) states that elevation axis acceleration has a sinusoidal component, as well as a term linear with respect to  $\Delta\omega_E$ . The sinusoidal component causes the periodic “scanning” motion of the main body, while the linear term affects the “pointing,” or line-of-sight motion. The beauty of this approach is that the scanning dynamics are governed by the first term in (6), while the pointing is affected by the second term. Polites proposed that the variation  $\Delta\omega_E$  be determined by a proportional + rate feedback controller based on an average elevation axis error. The line of reasoning for expressions (4)-(6) can be applied to the cross-elevation axis dynamics. In summary, the control of payload pointing can be achieved by introducing periodic RUM rate variations  $\Delta\omega_X$  and  $\Delta\omega_E$  for the cross-elevation and elevation axis errors, respectively.

## CONTROLLER IMPLEMENTATION

Experimental tests of the pointing control scheme have been developed in this research project. The NASA-developed experiment consists of a gimbal mounted payload with several RUM devices. The control electronics remain unchanged, but the Motorola 80196 controller code is modified to achieve pointing using only RUM devices, without intervention from auxiliary motors acting on the main body. The control input described in (3) is implemented as a new floating-point subroutine (named MOD\_RUM\_COM). RUM rate variations  $\Delta\omega_X$  and  $\Delta\omega_E$  are generated by modified gimbal control subroutines. To improve the overall system performance, several measures have been designed and implemented to increase the sampling frequency. These include:

- a) Implementing the gimbal control subroutine using integer arithmetic. In addition, the sampling frequency and controller gains are chosen to be powers of two, so that multiplication and division involving these numbers can be achieved very quickly using binary data shifts.
- b) Sine and cosine functions are implemented using a table look-up scheme with linear interpolation. This method is approximately 10X faster than using the polynomial approximation implemented with floating-point. Yet the results are correct to 5-6 decimal places, compared to 4 decimal places using the polynomial approximation.

The new controller code computation time is around 2.5 msec, which is easily fast enough to achieve a sampling frequency of 256 Hz.

Preliminary tests of the system show that pointing control using RUMs is possible, but that further work is needed. If no RUM speed variations are used, the line-of-sight axis will drift away with the slightest disturbance. In contrast, small disturbances can be accommodated when the RUM speed variations are enabled, though the steady-state error is somewhat excessive. A record of experimental results needs to be collected in the near future for more detailed analysis.

## SUGGESTIONS FOR FUTURE WORK

Improvements in pointing control performance may be possible through several approaches. Two suggestions are described here:

- 1) Improved modeling and analysis - Observation of the experiment motion verifies that the centrifugal forces generated by RUMs are the dominant effects when RUM angular velocity is constant. But if the RUM angular velocity is not constant, then it appears that the main body

also reacts to the RUM motor torques as the RUM accelerates and decelerates during each rotation. More detailed analysis of the RUM system suggests that a more complete model of the main body angular accelerations is of the form:

$$\ddot{\theta}_E = \frac{2dmr}{I_E} \left( -\sin(\theta_R) \omega_R^2 + \cos(\theta_R) \ddot{\theta}_R \right)$$

$$\ddot{\theta}_X = \frac{2dmr}{I_X} \left( \cos(\theta_R) \omega_R^2 + \sin(\theta_R) \ddot{\theta}_R \right)$$
(7)

In other words, the accelerations of the main body about the center of mass are functions of RUM angular velocity (squared) AND the RUM acceleration. Compare the acceleration models (2) and (7). Another observation is that these models are derived under the conditions that the elevation and cross-elevation angles are small. Experiments suggest consideration for large variations in these main body axes. It is recommended that a more complete model be examined or derived, perhaps using techniques from robot dynamic modeling [7].

2) Improved control design - Experimental results show that the stability margin of the RUM system is not very large. The gimbal controller subroutine that generates the RUM rate variations  $\Delta\omega_X$  and  $\Delta\omega_E$  implements a PD-type controller. Steady-state performance should be improved with the addition of integral compensation, but simulation results have not been encouraging (small stability margin). Controller improvements based on nonlinear control theory might be examined. In addition, the synchronization of the control to the RUM motion should be studied for possible improvements.

## REFERENCES

- [1] M.E. Polites, "New method for scanning spacecraft and balloon-borne/space-based experiment," *AIAA Journal of Guidance, Control and Dynamics*, vol. 14, no. 3, May-June 1991, p. 548-553.
- [2] M.E. Polite, "Rotating-unbalanced-mass devices and methods of scanning balloon-borne experiments, free-flying spacecraft, and space shuttle/space station attached experiments," U.S. Patent #5,129,600, National Aeronautics and Space Administration, Washington, D.c. July 14, 1992.
- [3] D.C. Alhorn and M.E. Polites, "Rotating unbalanced-mass devices for scanning: results from the proof-of-concept test," *Guidance and Control 1994*, Vol.86, *Advanced in the Astronautical Sciences*, Edited by R.D. Culp and R.D. Rausch, American Astronautical Society, 1994.
- [4] B. Friedland, Advanced Control Techniques, McGraw-Hill, 1995.
- [5] A. Isidori, Nonlinear Control Theory, Springer-Verlag, 1984.
- [6] J-J. E. Slotine and W. Li, Applied Nonlinear Control, Prentice-Hall, 1989.
- [7] M.W. Spong and M. Yidyasagar, Robot Dynamics and Control, John Wiley & Sons, 1989.



**1996**  
**NASA/ASEE SUMMER FACULTY FELLOWSHIP PROGRAM**

**MARSHALL SPACE FLIGHT CENTER**  
**THE UNIVERSITY OF ALABAMA**

**SPRAY DIAGNOSTICS IN ROCKET ENGINES**  
**USING PHASE DOPPLER ANALYZER**

Prepared by: Kakkattukuzhy M. Isaac, Ph. D.  
Academic Rank: Associate Professor  
Institution and Department: The University of Missouri-Rolla  
Department of Mechanical & Aerospace Engineering  
and Engineering Mechanics

NASA/MSFC:

Laboratory: Propulsion Laboratory  
Division: Engine Systems  
Branch: Combustion Physics Laboratory

MSFC Colleagues: John Hutt, Richard Eskridge





## INTRODUCTION

Characteristics such as drop velocity, drop size, number density, volume flow rate, volume flux, and evaporation rate of the fuel spray in a rocket engine are directly related to engine performance. Several studies of shear coaxial atomization have been done in the past[1, 2]. However, additional work related to sprays at supercritical and transcritical conditions would be useful. The author undertook a study of the feasibility of using a phase Doppler particle analyzer (PDPA) for spray measurements in rocket engines as a part of the Summer Faculty Fellowship Program at the NASA Marshall Space Flight Center.

The PDPA is a single particle counter (SPC) system based on light scattering from spherical particles. The PDPA instrument is based on refractive and reflective scattering as opposed to other instruments based on diffractive scattering. The main advantage of the PDPA instrument is its ability to provide point-wise information.

The following sections describe the principle of operation of the PDPA system and the data obtained using a PDPA instrument in a spray formed by a commercially available fuel injection nozzle.

## PHASE DOPPLER SYSTEM

A light ray incident on a transparent sphere will emerge at an angle dependent on the path of the ray and the size of the sphere. Snell's Law of refraction, which states:  $\cos \tau = m \cos \tau'$ , in which  $m$  is the refractive index of the drop medium, and  $\tau$  and  $\tau'$  are the angles made with respect to the interface tangent by the incident and the refracted rays, respectively, may be used to determine the path traced by a ray as it traverses a transparent sphere. For a ray emerging from the drop without any reflection, van de Hulst[3] has shown that the scattering angle  $\theta$  is given by the expression:  $\theta = 2(\tau' - \tau)$ . When there are two beams incident on the sphere, they will interfere after they emerge from the sphere. Defining a new parameter  $\eta$  as

$$\eta = 2\alpha(\sin \tau - m \sin \tau') \quad (1)$$

in which the parameter  $\alpha$  is defined as:  $\alpha = \pi d / \lambda$ .

The amplitude functions associated with beams 1 and 2 for linearly polarized light, for  $\sigma = \eta$ , are given by

$$S_{11}(m, \theta, d) = \sqrt{i_1} \exp(j\sigma_1) \quad (2)$$

$$S_{12}(m, \theta, d) = \sqrt{i_2} \exp(j\sigma_2) \quad (3)$$

The first subscript in the above equations is used to denote Polarization 1, perpendicular the scattering plane. When a spherical particle travels through the intersection of two laser beams, it will scatter light from each beam. The scattered light due to the two beams may be described using the following expressions.

$$E_1(m, \theta, d) = S_{11}(m, \theta, d) \exp(-jkr + j\omega_1 t) / jkr \quad (4)$$

$$E_2(m, \theta, d) = S_{12}(m, \theta, d) \exp(-jkr + j\omega_2 t) / jkr \quad (5)$$

where  $k = 2\pi/\lambda$ , is the wave number, and  $\omega$  is the angular frequency. The total scatter is obtained by summing the complex amplitude from each beam. The resultant intensity is given by

$$I(m, \theta, d) = ((\text{mod } E_1)^2 + (\text{mod } E_2)^2 + 2 \text{mod } (E_1) \text{mod } (E_2) \cos \sigma) \quad (6)$$

where  $\sigma$  is the phase difference between the scattered signals. Notice that the first two terms are independent of  $\sigma$ , and therefore, represent the pedestal component of the signal, and the last term involving  $\sigma$  gives rise to a sinusoidal intensity variation. Since the beam intersection angle,  $\gamma$ , is small (less than 10 deg.), the scattering angles,  $\theta_1$  and  $\theta_2$ , of the pairs of rays that reach a common point and interfere are nearly equal. Therefore, the amplitude functions,  $S_1$  and  $S_2$ , of the two beams are also nearly equal. Figure 1 (reproduced from Ref. [4]) is a photograph of the scattered light intensity pattern. When the drops travel through the probe volume, the fringe pattern appears to move at the Doppler difference frequency, which is a function of drop velocity, beam intersection angle and the light wavelength. The spatial frequency of the fringe pattern is a function of the drop diameter, angle of observation, light wave length, and drop refractive index. The fringe pattern can be detected by using a photomultiplier tube (PMT) whose output can be displayed on an oscilloscope as a Doppler burst signal.

A schematic diagram of the instrument is shown in Figure 2. The fringe spacing,  $\delta$ , is given in terms of the wave length,  $\lambda$  and the beam intersection angle,  $\gamma$ , by the following expression

$$\delta = \lambda/2 \sin(\gamma/2) \quad (7)$$

The drop velocity,  $v$ , is directly related to the Doppler difference frequency,  $f_d$ , and is given by

$$v = f_d \delta \quad (8)$$

The particle magnifies the fringe pattern onto a receiver to different degrees relative to its size. The fringes move past the detectors at the Doppler difference frequency producing identical signals, but with a phase shift proportional to the fringe spacing. The spatial wave length,  $\Delta$ , is given by the following expression

$$\Delta = 2\pi S_{1-2}/\phi_{1-2} \quad (9)$$

in which  $S$  is the spacing and  $\phi$  is the phase angle between Detectors 1 and 2.

## RESULTS AND DISCUSSION

The spray investigated in this study was that of the Delavan 27700-1 fuel injector[5] used in jet engines. The injector is a pressure atomizer having a flow rate of 0.5-1.0 kg/hr. Distilled water was used as the injection fluid, and the injection pressure was 90 psig. A flow visualization study was conducted first to establish the overall features of the spray. The spray was illuminated using a laser light sheet, and still pictures of the spray was taken at different camera shutter speeds, the maximum of which was 1/8000 s. These flow visualization pictures provided the time-averaged and instantaneous overall features of the spray. The PDPA system was then used to make quantitative measurements. Radial profiles of mean velocity and mean drop size were obtained at different axial locations. Volume flux, volume flow rate and number density information was also provided by the PDPA software.

Figure 3 is a representative result from the PDPA measurements. The figure shows a radial profile of the Sauter mean diameter (SMD) at an axial distance of 38.1 mm measured from the injector exit. Characteristic of this class of injectors, the drop size is smallest at the axis and increases to a maximum towards the edge of the spray. A few very large drops were seen at the outer edge.

## FUTURE WORK

The present work has demonstrated that the PDPA is a useful instrument for investigating rocket engine performance. The instrument, with careful implementation, can provide critical information regarding the complex mechanisms involved in the high pressure combustion environment. However, any such study should be carefully designed and implemented in order for it to provide further understanding of rocket engine behavior. It is recommended that the PDPA instrument be used to participate in the NASA/LeRC study of single particle counter (SPC) instruments[6].

## References

- [1] Isaac, K. M., Missoum, A., Drallmeier, J. A., and Johnston, A. P., "Atomization Experiments in a Coaxial Coflowing Mach 1.5 Flow," AIAA Journal, Vol. 32, No. 8, pp. 1640-1646, Aug. 1994.
- [2] Pal, S., Moser, M. D., Ryan, H. M., Foust, M. J., and Santoro, R. J., "Flowfield Characteristics in a Liquid Propellant Rocket," AIAA Paper 93-1882, Jun. 1993.
- [3] van de Hulst, Light Scattering by Small Particles, Wiley, New York, 1957.
- [4] Bachalo, W. D. and Hauser, M. J., "Phase/Doppler Spray Analyzer for Simultaneous Measurements of Drop Size and Velocity Distributions," Optical Engineering, Vol. 23, No. 5, pp. 583-590, 1984.
- [5] Mao, C. P., "Drop Size and Velocity Data for Delavan 27700-1 Fuel Injector," Private communication, July 1996.
- [6] Zaller, M., "Single Particle Counter Interlaboratory Study," Memorandum dated, May 1996.

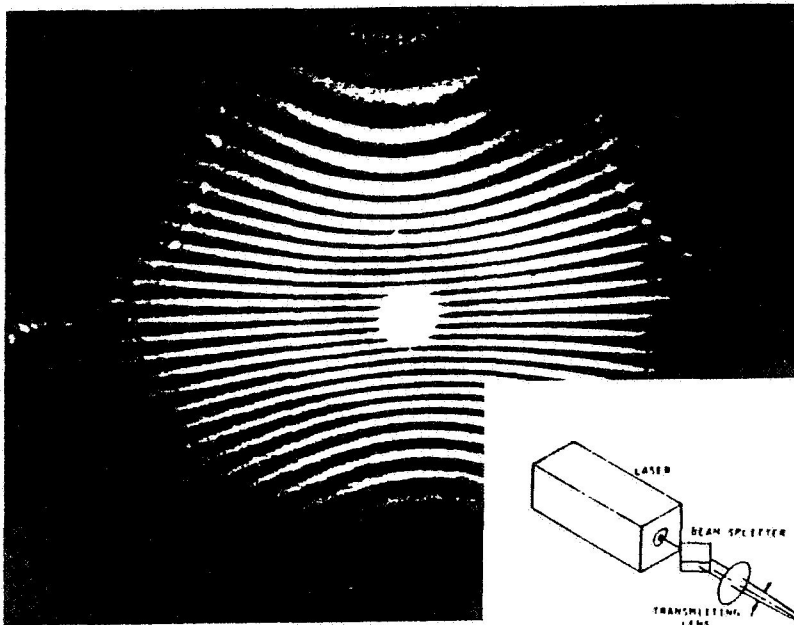


Figure 1

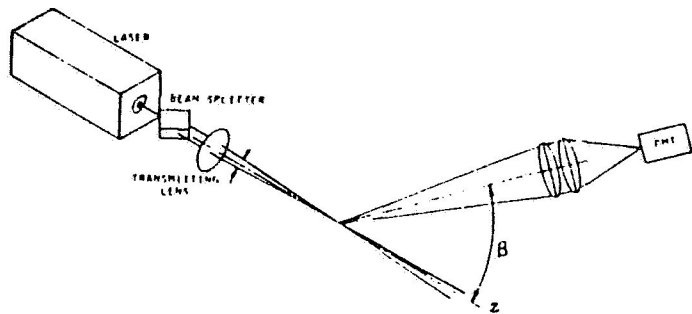


Figure 2

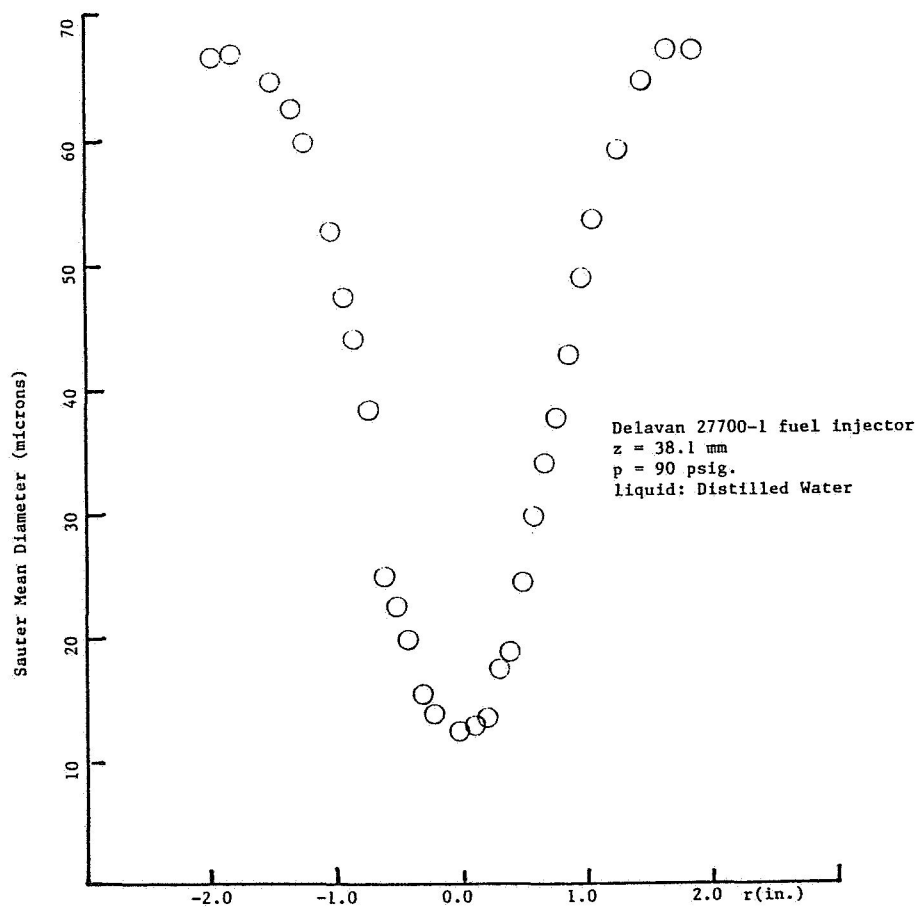


Figure 3



1996

**NASA/ASEE SUMMER FACULTY FELLOWSHIP PROGRAM**

**MARSHALL SPACE FLIGHT CENTER  
THE UNIVERSITY OF ALABAMA**

**ADAPTATION OF A MOTILITY ANALYSIS APPARATUS FOR SPACE  
SCIENCE & MICROGRAVITY GROUND-BASED EXPERIMENTS**

Prepared By: Jacqueline U. Johnson, V.M.D.

Academic Rank: Assistant Professor

Institution and Department: Alabama A & M University  
Department of Food Science  
& Animal Industries

NASA/MSFC:

Laboratory: Space Science  
Division: Microgravity Sciences  
& Applications  
Branch: Biophysics

MSFC Colleague: David A. Noever, Ph.D.





## Introduction

Previous space flight studies have described unfavorable effects of microgravity on testicular morphology and spermatogenesis (Cosmos 1887 Biosputnik flight, 9/29/87 - 10/12/87). The flight animals demonstrated small reductions in testicular and epididymal size, the phenomenon explained as resulting water loss (1). Yet, light microscopic histological preparations revealed few spermatozoa in the rete testis of the flight males compared to control animals. The cause for this finding was subjectively assessed to be due to "the anatomical dislocation of the organs... and a disturbance in testicular blood supply"(1). Unfortunately, the reported effects of microgravity on the reproductive processes (particularly within males) are few and divergent. If habitation in space is a futuristic goal, more objective testing (of male and female gametes) in a microgravity environment will provide insight to the developmental potential of these reproductive cells.

As part of the Marshall Space Flight Centers' Summer Faculty Fellowship Program within the Biophysics Branch, a key component of the research investigation was to develop a test to evaluate individual cell motility and orientation in varying gravitational environments, using computerized assessment of sperm cell concentration, morphology and motility to provide objective, quantitative experimental control. In previous work performed jointly by the author and NASA colleague, it has been shown that macroscopic motile aggregates of spermatozoa were not altered by the absence of microgravity (2). Variations in the number of normal versus abnormal sperm due to microgravity influences have yet to be established. It is therefore of interest to monitor the cytoskeletal matrix (microtubulin) of these organisms as a possible indicator of cell viability and/or function.

Using Image and cell motion analysis we can show in a simple, rapid test that chemical toxicity and other deterrents to motility can be objectively measured and quantified (3). Positive identification of the effects chemical toxicants and other potential environmental contaminants (especially from space) can have on living organisms on earth would be potentially beneficial to space science experimentation and ground - based tests developed for future shuttle and space station missions. For spermatozoa, cell motility responses were unaltered in reduced gravitational vehicles (i.e. - KC-135, RWV Bioreactor). However, developing a simple test of viability using common amino acids found normally in semen (glutamic acid, glycine, arginine, proline) we determined that reduced motility (20-45% of active sperm cells) could be established with all of the selected amino acids except glutamic acid. Glutamic acid, in contrast to the other amino acids enhanced sperm motility and maintained a good rate (i.e. vigorous movement, with about 70-85% active sperm cells) for up to 120 minutes.

For Tetrahymena, test materials consisted of twenty water-soluble chemicals, each dissolved in type II culture grade purified water. Negative controls (no chemical) and two reference standards (acetone and methanol) were used in the testing. Test samples were placed on the stage of an inverted microscope equipped with a CCD-camera coupled to a computer automated cell analysis system which captured a digitized image of the live

sample. Each sample was analysed for 30 seconds in ten frames per second. The observed number of cells and average linear velocity was determined for each chemical application.

Below are the concentrations of amino acids used to test sperm motility:

Amino Acid	Concentration		
	Low	Medium	High
Glutamic Acid	.05	.25	1.00
Glycine	.03	.10	.50
Arginine	.03	.10	.50
Proline	.03	.10	.50

Below are the Rank Order Toxicity effects on Tetrahymena from the Computerized Motility Assay: <sup>(3)</sup>

Rank order toxicity from computerized assay. Toxicity scores shown as the tolerated dose (dilution factor) with immobilized (a)  $d_{high}$ , 90 percent of the swimming cells (high dose); (b)  $d_{low}$ , 10 percent of the swimming cells (low dose); (c) the average dose as the reciprocal sum of the high and low dose ( $1/d_{avg} = 1/d_{high} + 1/d_{low}$ ). Rank orders shown for 20 organics (alcohol, ketones, ethers, esters) and salts.

Chemical	10 Percent Motile	90 Percent Motile (HTD)	Computer (ATD)	Rank Order	Silverman
Ethylene glycol	1.000	17.500	18.500	1	11.000
Ethanol	5.310	18.800	24.100	2	13.000
Isopropanol	78.000	22.500	30.300	3	
Methanol	1.000	38.900	39.900	4	
DMSO	1.000	46.500	47.500	5	9.300
3-methyl 2-butanone	18.900	40.000	58.900	6	
Isobutyl acetone	1.000	79.400	71.400	7	19.300
Methyl isobutyl ketone	13.800	58.300	72.100	8	
2-methyl 1-propanol	1.000	78.000	79.000	9	
Methyl ethyl ketone	34.800	55.900	90.700	10	60.000
Acetyl acetone	31.200	122.000	153.000	11	
Butanol	33.000	170.000	203.000	12	
Bleach	44.600	346.000	391.000	13	
Diethylanoamine	120.000	284.000	404.000	14	
2-octanone	250.000	308.000	558.000	15	
Nonanol	178.000	801.000	979.000	16	
1-pentanol	321.000	687.000	1,008.000	17	
Heptanol	694.000	2,250.000	2,944.000	18	
2-methyl 1-butanol	963.000	2,275.000	3,238.000	19	
Hexanol	2,000.000	13,000.000	15,000.000	20	

## **Conclusions**

Simulated Microgravity vehicles such as the KC-135 provides conclusive evidence that the physiological mechanisms governing motility of spermatozoa are not gravity dependent.

Ground-based testing of organisms using cell motion and image analysis further provide support of gravity independent motility of spermatozoa.

Adaptation of the motility analysis apparatus for space science experimentations will yield objective measurements of microscopic, physiological occurrences which could otherwise be misinterpreted, if one merely uses subjective visual observations.

Quantitative analysis identifies a specific range and rate of change in motility upon chemical additions.

Subtle changes in motility characteristics for spermatozoa as well as the protozoan, tetrahymena are noted as apparent changes in linear velocity and direction.

Positive identification of the effects chemical toxicants and other potential environmental contaminants ( especially from space) can have on living organisms on earth would be potentially beneficial to space science experimentation and ground - based tests developed for future shuttle and space station missions.

## **Future Work**

Summer efforts have also been focused on proposal development addressing the priority needs for space science experiments in the Microgravity Biotechnology area. Briefly, if the proposal is funded, my NASA Colleague, other University & Industry partners and I, propose to determine if microgravity alters the growth, metabolism and morphological differentiation of reproductive cells (oviductal, endometrial, embryos) cultured in vitro; and determine further, if microgravity alters the biochemical substrate utilization or synthesis of these cells. These initiatives, both ground-based and anticipated shuttle or space station experiments will explore the microgravity environment as a unique and effective 'laboratory' to study living organisms and life on earth.

## References

1. Serova, L.V, Denisova, L.A., and Baikova, C.V. (1989). The Effect Of Microgravity On The Reproductive Function Of Male- Rats. *The Physiologist*, Vol. 32, Suppl. No. 1., pp. 29-30.
2. Johnson, J.U. Biological Patterns: Novel Indicators for Pharmacological Assays. NASA Contractor Report - 184253 (1991) NASA/ASEE Summer Faculty Fellowship Program. pp. R-R2.
3. Noever, D.A., Matsos, H.C., Cronise, R.J., Looger, L.L., Relwani, R.A. and Johnson, J.U. (1994). Computerized In Vitro Test For Chemical Toxicity Based on Tetrahymena Swimming Patterns. *Chemosphere*, Vol. 29, No. 6, pp. 1373-1384.
4. Johnson, A.D. (1992) Ground Testing of Bioconvective Variables Such As Morphological Characterizations And Mechanisms Which Regulate Macroscopic Patterns. NASA Contractor Report - 184505, NASA/ASEE Summer Faculty Fellowship Program. pp. XXIV-2.
5. NASA Fact Sheet (1995) Space Science - Exploring Beyond Earth Orbit.
6. NASA Fact Sheet (1995) Life and Microgravity Sciences & Applications - Using the Space Environment to Improve Life on Earth.

**1996**

**NASA/ASEE SUMMER FACULTY FELLOWSHIP PROGRAM**

**MARSHALL SPACE FLIGHT CENTER  
THE UNIVERSITY OF ALABAMA**

**THERMAL MODEL OF THE PROMOTED COMBUSTION TEST**

Prepared By: Peter D. Jones, Ph.D., P.E.

Academic Rank: Associate Professor

Institution and Department: Auburn University  
Mechanical Engineering Department

**NASA/MSFC:**

Laboratory: Materials and Processes  
Division: Metallic Materials and Processes  
Branch: Metallurgical Research and Development

MSFC Colleague: Biliyar N. Bhat, Ph.D.



## INTRODUCTION

Flammability of metals in high pressure, pure oxygen environments, such as rocket engine turbopumps, is commonly evaluated using the Promoted Combustion Test (PCT). The PCT emphasizes the ability of an ignited material to sustain combustion, as opposed to evaluating the sample's propensity to ignite in the first place. A common arrangement is a rod of the sample material hanging in a chamber in which a high pressure, pure oxygen environment is maintained. An igniter of some energetically combusting material is fixed to the bottom of the rod and fired. This initiates combustion, and the sample burns and melts at its bottom tip. A ball of molten material forms, and this ball detaches when it grows too large to be supported by surface tension with the rod. In materials which do not sustain combustion, the combustion then extinguishes. In materials which do sustain combustion, combustion re-initiates from molten residue left on the bottom of the rod, and the melt ball burns and grows until it detaches again.

The purpose of this work is development of a PCT thermal simulation model, detailing phase change, melt detachment, and the several heat transfer modes. Combustion is modeled by a summary rate equation, whose parameters are identified by comparison to PCT results. The sensitivity of PCT results to various physical and geometrical parameters is evaluated. The identified combustion parameters may be used in design of new PCT arrangements, as might be used for flammability assessment in flow-dominated environments.

The Haynes 214 nickel-based superalloy, whose PCT results are applied here, burns heterogeneously (fuel and oxidizer are of different phases; combustion takes place on the fuel surface). Heterogeneous combustion is not well understood. (In homogeneous combustion, the metal vaporizes, and combustion takes place in an analytically treatable cloud above the surface). Thermal modeling in heterogeneous combustion settings provides a means for linking test results more directly to detailed combustion mechanics, leading to improved data analysis, and improved understanding of heterogeneous combustion phenomena.

## ANALYSIS

The vertical rod, bottom ignited arrangement for PCT is divided into liquid and solid zones (an intermediate mushy zone, appropriate for alloys, could be considered as an extension). Heat transfer in the solid is one-dimensional along the rod axis. Heat transfer in the liquid is ideally two-dimensional (symmetric about the rod axis) and coupled to the flow field arising from introduction of new material at the phase interface (solid consumption), surface tension and gravity defining the liquid surface geometry, and combustion mass transfer on the surface. However, the liquid zone is approximated as quasi-one-dimensional, in order to pursue the simplest possible descriptive model of PCT thermal transport, viz:

$$A_l(x) = \pi(x^2 + r^2), \quad V_l(x) = \frac{\rho_s A_s V_s}{\rho_l A_l(x)}, \quad \frac{dl_x}{dt} = V_l(l_x), \quad m_l = \rho_l \frac{\pi l_x}{6} (l_x^2 + 3r^2). \quad (1)$$

The liquid surface is modeled as a sphere truncated by the rod end (Fig.1). As the molten ball grows, its shape changes from an thin spherical cap, through the shape of a hemisphere.



and continues to the shape of a sphere minus a spherical cap. The velocity field accounts for mass flux continuity with the rod consumption. Velocity is considered constant over, and normal to, spherical surfaces defined by  $x$ . When the weight of the liquid exceeds surface tension, the liquid detaches, and  $l_x$  reverts to a residue  $l_{x,o}$ . Whether combustion continues at that point depends on the temperature distribution within  $l_{x,o}$  and the magnitude of the linear consumption rate,  $V_s$ . These quantities are determined here by means of transient, multiphase, combined mode heat transfer analysis of the simplified geometry defined above.

Combustion heat generation on the liquid surface is in equilibrium with conduction to the liquid, radiation to the chamber, natural convection, and transient effects. Conduction through the liquid carries heat to the phase boundary, where it is dissipated by the heat of fusion, conduction up the rod, radiation from the rod to the chamber, and transient effects. The rod is in the natural convection flow generated by the molten ball, and so convective transfer is directed into the rod. These effects are represented by the phase-separated model:

$$\rho_s c_s A_s \left[ \frac{\partial T_s}{\partial t} + (S-1) \frac{V_s}{l_s} \frac{\partial T_s}{\partial S} \right] = \frac{k_s A_s}{l_s^2} \frac{\partial^2 T_s}{\partial S^2} - P_s h_s (T_s - T_\infty) - P_s \epsilon_s \sigma_b (T_s^4 - T_w^4) \quad (2)$$

in the solid zone and

$$\rho_l c_l A_l \left[ \frac{\partial T_l}{\partial t} + (1-X) \frac{V_l}{l_x} \frac{\partial T_l}{\partial X} \right] = \frac{k_l}{l_x^2} \left( A_l \frac{\partial^2 T_l}{\partial X^2} + \frac{\partial A_l}{\partial X} \frac{\partial T_l}{\partial X} \right) \quad (3)$$

in the liquid zone, with boundary conditions of an adiabatic tip at  $s=l_s$ ,

$$T_s|_{s=0} = T_m = T_l|_{x=0}, \quad \rho_s V_s h_{sl} = \frac{k_s}{l_s} \frac{\partial T_s}{\partial S} \Big|_{s=0} + \frac{k_l}{l_x} \frac{\partial T_l}{\partial X} \Big|_{x=0} \quad (4)$$

at the phase boundary, and

$$\Delta H_c C \left( \frac{p}{p_{ref}} \right)^a \exp \left( \frac{-E_c}{RT_l|_{x=1}} \right) = \frac{k_l}{l_x} \frac{\partial T_l}{\partial X} \Big|_{x=1} + h_l (T_l|_{x=1} - T_w) + \sigma_b (T_l|_{x=1}^4 - T_w^4) \quad (5)$$

on the liquid surface. The origin of  $s$  and  $x$  is fixed at the moving phase interface, and these coordinates are made dimensionless by  $s=Sl_s$  and  $x=Xl_x$ . The coordinates are both moving and stretching, so the von Mises time transformation is applied. The combustion model is a summary rate equation governed by oxidizer transport through an oxide layer forming on the liquid. This rate is considered time-independent, though oxide thickness increases in an amount limited by stretching of the molten ball until it detaches and the layer re-initiates. The rate is considered uniform over the surface, as no bright spots or lines are observed in PCT data for the material considered (Haynes 214). The liquid convection coefficient is approximated as natural convection from a sphere. The free stream temperature is modeled as a spreading plume from a point source of strength equal to the convection from the liquid. The solid convection coefficient is defined by flow over an axisymmetric blunt body.

The model is solved numerically. Combustion and radiation terms and temperature-

dependent coefficients are linearized. The structure is iterative-tridiagonal within a time step. Convergence takes less than ten iterations, and over/under-relaxation is not necessary. Central difference conductive terms are used, though upwinding is necessary for convective terms, giving the algorithm spatial first order accuracy. The Crank-Nicholson scheme (second order accurate) is used for marching in time. Time instabilities are encountered and traced to interaction between combustion and radiation terms. It is necessary to lag the combustion temperature by several time steps. A more stable coupling must be developed analytically to avoid recourse to this device. Although the liquid radiative flux is small, it plays a vital limiting role. Temperature diverges if liquid surface radiation is neglected.

The model is sensitive to many parameters which are only approximately known (thermophysical properties of molten metal), or completely unknown (constants in the combustion rate expression). To estimate the combustion parameters, the model is solved analytically, neglecting transience, convection, radiation, and finite rod length, resulting in:

$$\Delta H_c C \left( \frac{p}{p_{ref}} \right)^a \exp \left( \frac{-E_c}{RT_{ig}} \right) = \rho_s V_s [h_{sl} + c_s (T_m - T_w)] \exp \left\{ \frac{A_s V_s}{\pi \alpha_s r} \tan^{-1} \left( \frac{l_x}{r} \right) - \left( 1 + \frac{A_s V_s}{\pi \alpha_s x} \right) \ln \left[ 1 + \left( \frac{l_x}{r} \right)^2 \right] \right\} \quad (6)$$

where  $T_{ig}$  is an effective ignition temperature. The heat of combustion (left side of Eq.(6)) is related to the linear consumption rate,  $V_s$ . This is determined from video recordings of PCT runs, stepping through frame by frame and measuring the amount of consumption (as a ratio of the rod diameter) between detachments. (A flame corona obscures the phase interface at all other times). 33 PCT recordings for Haynes 214 at six pressures between 7 and 69 MPa were examined. The results of  $V_s$  vs.  $p$  are shown in Fig.2. A power law function of pressure is chosen to fit the observed consumption rate, with the result

$$V_s = 4.944 \frac{mm}{s} \left( \frac{p}{p_{ref}} \right)^{0.06744} \quad (7)$$

where  $p_{ref}=1$  MPa. For this slight pressure dependence, the exponential terms in the right side of Eq.(6) have little influence, and the pressure exponent  $a$  is given the experimentally determined value 0.06744. Using  $T_{ig}=3000$  K,  $E_c=3 \times 10^5$  J/gmol,  $\Delta H_c=7.64 \times 10^6$  J/kg and  $h_{sl}=1.5 \times 10^5$  J/kg, the reaction rate preconstant  $C=6.6 \times 10^5$  kg/m<sup>2</sup>s is determined. Although this value is sensitive to the  $T_{ig}$  guess, it serves as a starting point for identification using the full model. Full model identification yields  $C=5.0 \times 10^5$  kg/m<sup>2</sup>s.

## RESULTS

Figure 3 shows the surface temperature history of the liquid for a base case, with a chamber pressure of 7 MPa (1000 psi), and a high pressure case at 69 MPa (10,000 psi). Figure 4 shows the linear consumption rate history. Applying the igniter energy to melt a volume of the rod and bring it to  $T_{ig}$  defines the initial state. Choice of  $T_{ig}$  is found to have very little effect after the first detachment. Base case interdetachment time is observed to be 0.5 s, and the unknown surface tension is adjusted to normalize the simulation. Surface temperature rises after detachment; faster at first, then slower as the ball grows and more of the heat of combustion goes into heating the liquid, with a total temperature rise of 400 K

(720°F) before detachment. High pressure case behavior is similar, except that it burns 200 K (360°F) hotter and detaches 0.04 s sooner. Consumption rate levels off after the first detachment, with a slight loss at each subsequent detachment. The high pressure case has a slightly higher consumption rate than the base case, as it burns hotter, has a hotter residue, and hence is more likely to maintain combustion than the base case.

Figures 5 and 6 show the effect of altering the diameter of the PCT article from the base case (3.2 mm or  $\frac{1}{16}$  in.) to a thin case of (1.6 mm or  $\frac{1}{16}$  in.). The thin case shows a longer interdetachment time and a larger temperature increase within one drop. It has twice the linear consumption rate (mm/s, half the volumetric consumption rate,  $\text{mm}^3/\text{s}$ ) of the base case. The surface tension-based drop detachment model allows a maximum drop volume which is roughly proportional to rod diameter. Since the thin case has half the surface tension perimeter of the base case, the interdetachment time might therefore be expected to be the same. However, the molten residue length has been modeled as a constant multiple of the rod diameter. Therefore, in the thin case, the new drop starts out much smaller and cooler after detachment than in the base case. Behavior very similar to that of the thin case is also found for the base case if the residue multiplier is halved. Clearly, the modeling of detachment and residue phenomena has a significant impact on PCT simulation results.

Other PCT parameters considered are: rod length and initial temperature; chamber temperature; and igniter energy. A short case (15.2 cm or 6 in. - base case is 30.5 cm or 12 in.) has results which cannot be distinguished from the base case, indicating that the cold end boundary condition has no effect. A hot case with an initial temperature of 500 K (440°F - base case is 300 K or 80°F) is also indistinguishable from the base case indicating that the high combustion temperatures dominate any uncertainty in test article initial conditions. A hot chamber case ( $T_w=500$  K or 440°F - base case is 300 K or 80°F) shows no differences. Varying igniter energy  $\pm 10\%$  has no effect beyond first detachment. However, the speed and temperature with which this point is reached are sensitive to igniter energy.

## CONCLUSIONS

Vertical rod, bottom ignited PCT arrangements are simulated. Simulation is sensitive to: modeling of drop detachment and residue phenomena; numerical stability of combustion and radiation interaction; and thermophysical properties of liquid metals for which data is sparse. Clarification of these issues will result in a more accurate simulation, which may be applied to the available PCT data to better identify heterogeneous combustion models.

The vertical rod, bottom ignited PCT is fairly insensitive to chamber pressure. This is demonstrated by a simplified solution linking combustion oxidizer mass flow rate to solid consumption rate, and by PCT data showing consumption rate to depend weakly on pressure.

The vertical rod, bottom ignited PCT is fairly insensitive to ignition conditions. Ignition has a strong effect only on the formation of the first molten ball. Subsequent balls are most strongly affected by detachment and residue modeling. Conversely, alternate PCT arrangements not subject to detachment should be more sensitive to ignition conditions. In such cases, a controlled ignition mechanism such as a laser should be considered.

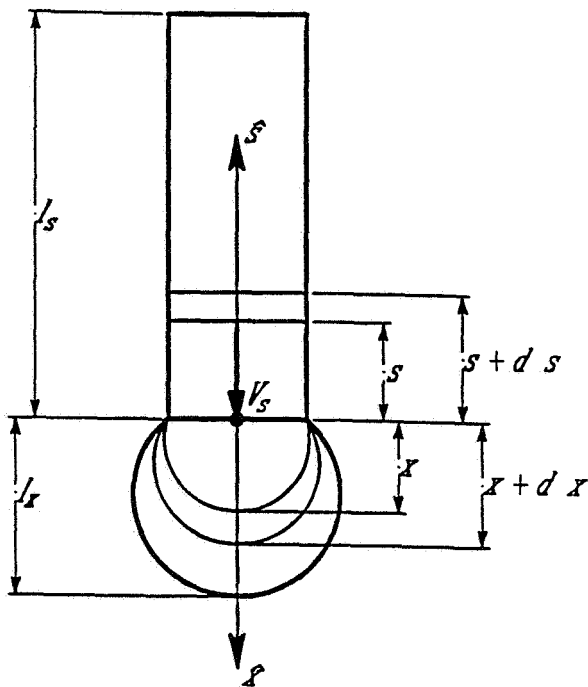


Figure 1 - Coordinate system for vertical rod, bottom ignited PCT

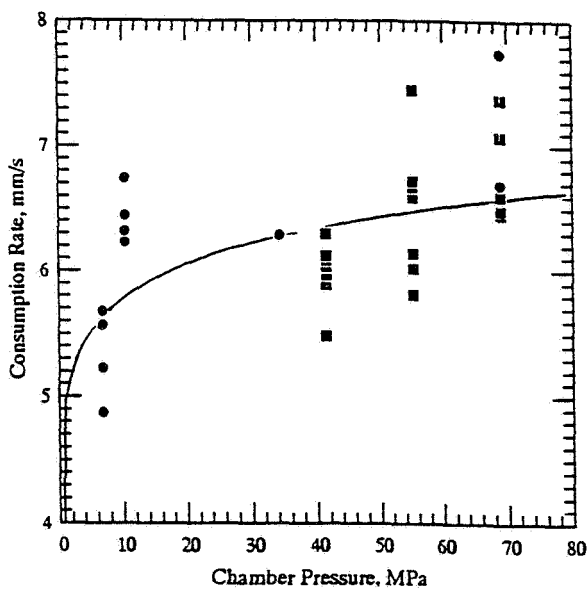


Figure 2 - Linear consumption rate of Haynes 214 - multiple tests at multiple chamber pressures with power law fit

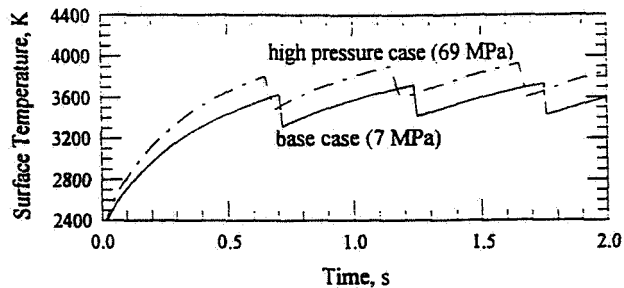


Figure 3 - Surface temperature history for base case and high pressure case

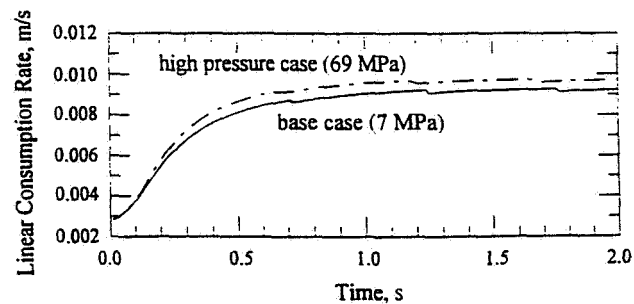


Figure 4 - Linear consumption rate history for base case and high pressure case

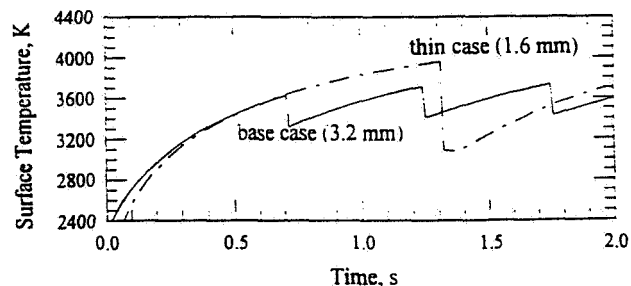


Figure 5 - Surface temperature history for base case and thin rod case

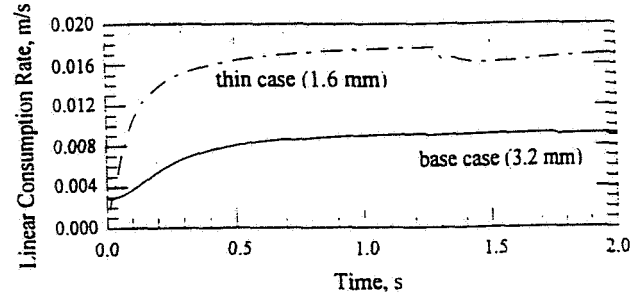


Figure 6 - Linear consumption rate history for base case and thin rod case



1996

**NASA/ASEE SUMMER FACULTY FELLOWSHIP PROGRAM**

**MARSHALL SPACE FLIGHT CENTER  
THE UNIVERSITY OF ALABAMA**

**DEVELOPMENT OF A COMPUTER ARCHITECTURE TO SUPPORT THE  
OPTICAL PLUME ANOMALY DETECTION (OPAD) SYSTEM**

Prepared by :	Constantine Katsinis, Ph.D.
Academic Rank:	Associate Professor
Institution and Department:	University of Alabama in Huntsville Department of Electrical and Computer Engineering
NASA/MSFC:	
Laboratory:	Astrionics Laboratory
Division:	Instrumentation and Control Division
Branch:	Instrumentation Branch
MSFC Colleague:	Anita Cooper



## INTRODUCTION

The NASA OPAD spectrometer system relies heavily on extensive software which repetitively extracts spectral information from the engine plume and reports the amounts of metals which are present in the plume. The development of this software is at a sufficiently advanced stage where it can be used in actual engine tests to provide valuable data on engine operation and health. This activity will continue and, in addition, the OPAD system is planned to be used in flight aboard space vehicles. The two implementations, test-stand and in-flight, may have some differing requirements. For example, the data stored during a test-stand experiment are much more extensive than in the in-flight case. In both cases though, the majority of the requirements are similar. New data from the spectrograph is generated at a rate of once every 0.5 sec or faster. All processing must be completed within this period of time to maintain real-time performance.

Every 0.5 sec, the OPAD system must report the amounts of specific metals within the engine plume, given the spectral data. At present, the software in the OPAD system performs this function by solving the inverse problem. It uses powerful physics-based computational models (the SPECTRA code), which receive amounts of metals as inputs to produce the spectral data that would have been observed, had the same metal amounts been present in the engine plume. During the experiment, for every spectrum that is observed, an initial approximation is performed using neural networks to establish an initial metal composition which approximates as accurately as possible the real one. Then, using optimization techniques, the SPECTRA code is repetitively used to produce a fit to the data, by adjusting the metal input amounts until the produced spectrum matches the observed one to within a given level of tolerance. This iterative solution to the original problem of determining the metal composition in the plume requires a relatively long period of time to execute the software in a modern single-processor workstation, and therefore real-time operation is currently not possible.

A different number of iterations may be required to perform spectral data fitting per spectral sample. Yet, the OPAD system must be designed to maintain real-time performance in all cases. Although faster single-processor workstations are available for execution of the fitting and SPECTRA software, this option is unattractive due to the excessive cost associated with very fast workstations and also due to the fact that such hardware is not easily expandable to accommodate future versions of the software which may require more processing power.

Initial research has already demonstrated that the OPAD software can take advantage of a parallel computer architecture to achieve the necessary speedup. Current work has improved the software by converting it into a form which is easily parallelizable. Timing experiments have been performed to establish the computational complexity and execution speed of major components of the software. This work provides the foundation of future work which will create a fully parallel version of the software executing in a shared-memory multiprocessor system.

## OPAD SOFTWARE PARALLELIZATION

The OPAD software consists of three major components: 1) The SPECTRA code which receives an array specifying the metal composition in the plume and uses physics-based models to produce the spectrum that would have been observed had the specified metals been in the plume,



2) the neural network code which receives an observed spectrum and produces estimates of the metal composition in the plume, and 3) the optimization, or fitting, code which uses gradient techniques to match the estimated and observed spectra. During normal operation, the OPAD system repetitively acquires the spectrum from the plume, uses the neural network code to produce an initial approximation to the metal composition, and then, under control of the optimization code, repetitively calls the SPECTRA code to produce successive approximate spectra, which are increasingly better (closer) to the observed spectrum until the difference between observed and estimated spectra becomes smaller than a specific limit.

Figure 1 shows the program flow of the SPECTRA code component. During real-time operation, metal concentrations are received from the neural network code rather than being read from a file. Although they are quite extensive and requiring some non-trivial computational resources to train and set-up, neither the spectral code nor the optimization code appear to be computationally demanding during real-time operation. The step which requires a relatively significant amount of time to execute is the one where the contribution of each individual metal to the spectrum is calculated. Table 1 shows the time required to execute that step on a workstation (of modest capabilities) for each of the nineteen metals which are currently of interest. All numbers are in milliseconds. It is apparent from the table that the execution time of that step varies significantly from negligible (less than the time resolution) for two metals to more than three seconds for two other ones. Also, the step where the convolution of the resulting spectrum with the

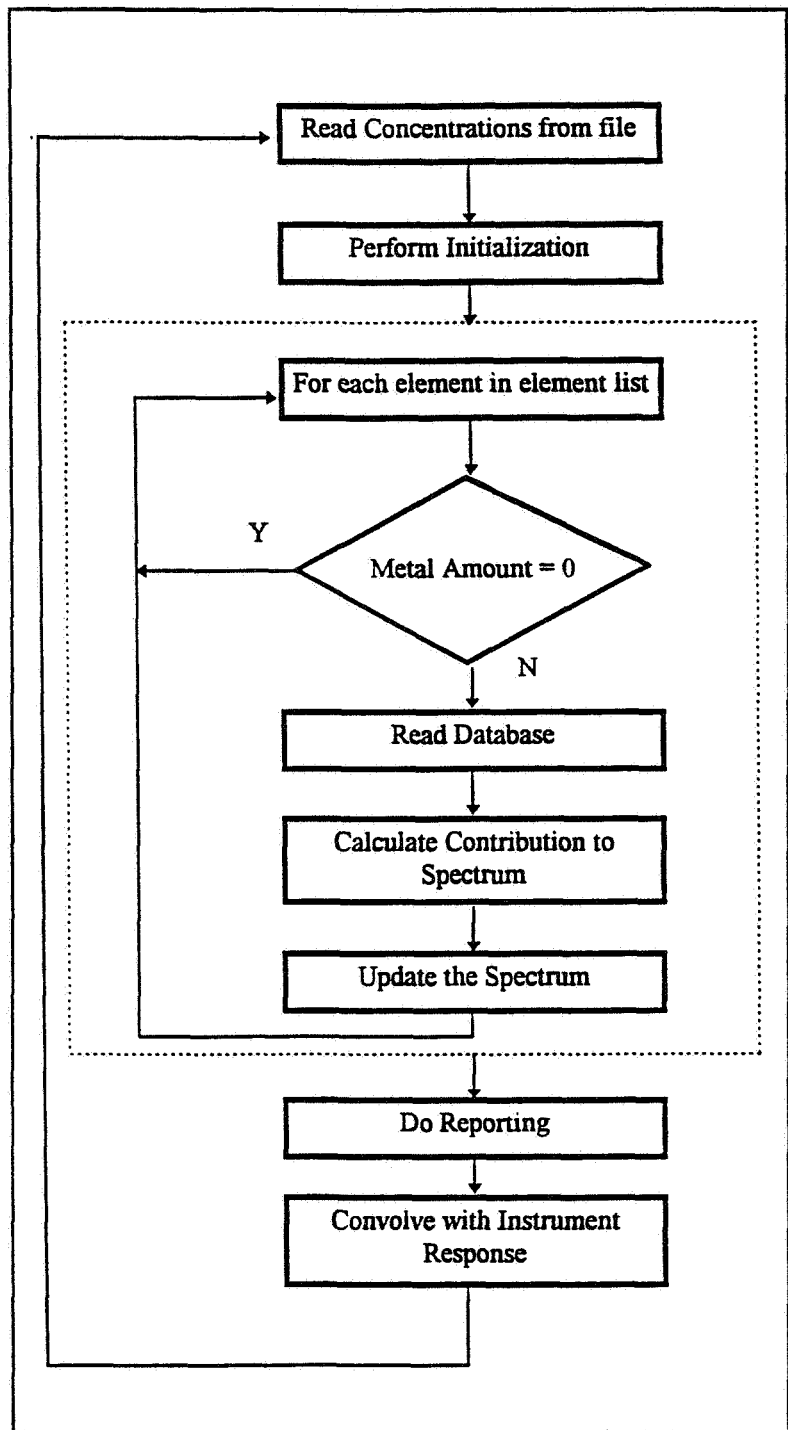


**Figure 1.** Original program flow

instrument response takes place requires some non-negligible amount of time. The total processing time, if all steps are performed serially, is approximately 14 seconds. If the processing for each metal were allocated to a different processor then all contributions to the spectrum would be calculated within approximately 3.8 seconds. Then, nineteen processors, each used for the above experiment, would be sufficient to execute the SPECTRA code once in 0.5 seconds. Of course, the above processing allocation results in many processors being idle for a significant amount of time. By optimizing the SPECTRA code so that the original 14 seconds of processing are distributed evenly over the nineteen processors, the total processing time reduces to less than 0.1 second, assuming processors 8 times faster than the workstation.

Figure 2 shows the flowchart of the SPECTRA code after its conversion to parallel form. It assumes that  $N+1$  processors are available, with one processor performing initialization and coordination and  $N$  processors performing the real work. More than one can be allocated to the same processor, the allocation being such that all  $N$  processors receive approximately the same amount of work so that idle time is minimal.

TABLE 1. Processing Times per Element (msec)			
copper	136	sodium	29
calcium	45	potassium	0
magnesium	29	lithium	15
molybdenum	3300	silver	32
aluminum	0	hafnium	1045
lead	73	scandium	45
titanium	336	vanadium	933
chromium	153	manganese	1717
iron	3787	cobalt	1239
nickel	1175		
convolution	139		

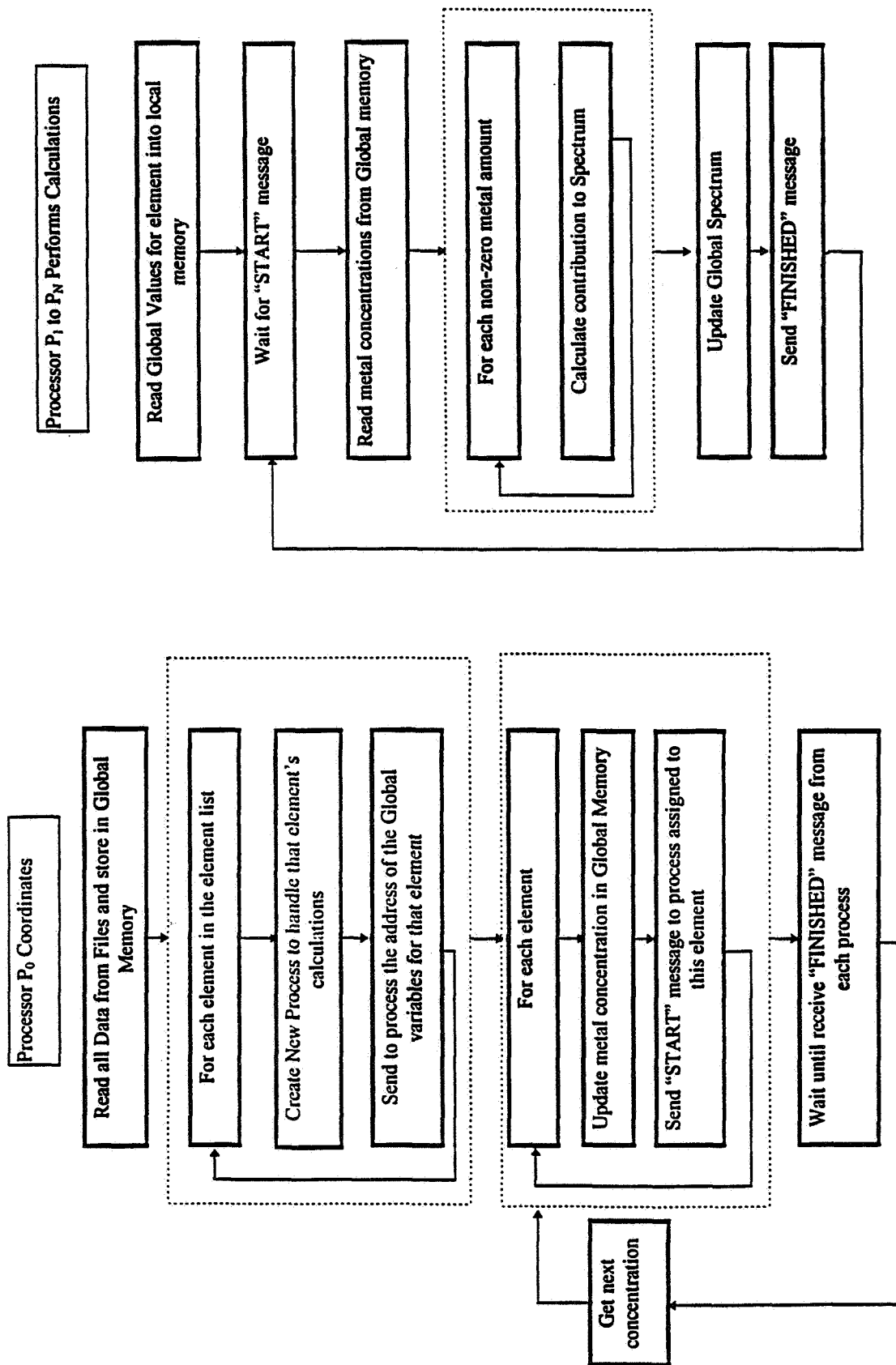


Figure 2. Parallel program flow

**1996**  
**NASA/ASEE SUMMER FACULTY FELLOWSHIP PROGRAM**

**MARSHALL SPACE FLIGHT CENTER**  
**THE UNIVERSITY OF ALABAMA**

**THE RESPONSE OF THE BATSE LADS TO RADIATION**  
**FROM THE CRAB NEBULA**  
**AND**  
**PLANS FOR RADIOACTIVITY STUDIES**  
**ON SPACE STATION**

**Prepared By:**

**C. E. Laird, Ph. D.**

**Academic Rank:**

**Foundation Professor of Physics**

**Institution and Department:**

**Eastern Kentucky University**

**Department of Physics and Astronomy**

**NASA/MSFC:**

**Laboratory:**

**Space Sciences**

**Division:**

**Physics and Astronomy**

**Branch:**

**Astrophysics**

**MSFC Colleague:**

**B. Alan Harmon, Ph. D.**



## **I. Response of BATSE Large Area Detectors**

### **Introduction**

**The Burst And Transient Source Experiment (BATSE) onboard the Compton Gamma-Ray Observatory (CGRO) was designed to measure X-rays and gamma rays with energies from about 50 keV to above 2 MeV. As with many scientific investigations, the success of the original experiment lead to additional areas of research interest. In the case of BATSE the ability to observe the radiation from sources down to about 20 keV became readily apparent. This lead to a continuing program of measuring the spectrum of radiation from stellar objects at these lower energies. One of these, the Crab Nebula, has a very steady radiation flux and, thus, has become a “standard candle” for such measurements.**

**The Large Area Detectors (LADs) on BATSE contain a 1.27-cm thick, 25.4-cm radius NaI(Tl) detector behind a 6.35-mm thick polystyrene Charged Particle Detector (CPD) (Pendleton95) used to “veto” charged particles signals. The detectors have been calibrated with a series of gamma and X-ray sources and the results carefully simulated with a Monte Carlo code. In the calibration process the computer simulation accounts for scattering from material in the counting room as well as the BATSE structure. For an orbiting detector, scattering from the entire spacecraft must be modeled as well as for all covering material over the detectors.**

**Five years after CGRO was launched on April 5, 1991, a large body of observational data has been taken of the Crab Nebula. The technique used for these observation, and for many other X-ray sources, is Earth occultation. From the perspective of the spacecraft, the Earth occults most stellar objects once an orbit, i.e., the signal is lost as the source sets and is regained as the source rises. A careful analysis of the continuing signals from all sources measured allows for an accurate measurement of the spectrum of a given source. An analysis of this data from the Crab has indicated that the LADs are very responsive at energies as low as 20 keV—at energies below the range of calibration. While the model accounts for many of the interactions of the photons with the detectors, the observation of nonstatistical deviations at low energy and at small angles has suggested a need to recalibrate at energies where the attenuation effects are increasing exponentially(Pendleton94).**

### **Spectral Shape**

**To a good approximation at low energy the count rates measured by the LADs can be approximated as**

$$C(E) = A(E) \cos(\theta) \exp(-B / \cos(\theta)) \quad (1)$$

where  $A(E)$  is the product of the flux of photons  $\Phi(E)$ , the intrinsic efficiency of the detector  $\varepsilon(E)$  and the area of the detector,  $\theta$  is the angle between the incident beam and the normal to the detector,  $B$  is the absorption factor. The absorption factor is given by

$$B = \sum_i \mu_i \rho_i t_i \quad (2)$$

where  $\mu_i$  is the mass absorption coefficient,  $t_i$  is the thickness and  $\rho_i$  is the density of the covering material.

The spectrum of radiation from the Crab Nebula as observed by BATSE has been studied using this simple model. A  $\chi^2$  minimization procedure has been used to obtain the A and B coefficients giving the best fit to this data. The quality of a typical fit is shown for LAD 3 in Figure (1) while the trend of these coefficients is give in Figures (2) and (3). This behavior of B is that expected for a rapidly decreasing mass absorption coefficient.

However, although a very good fit to the data can be obtained using Eq. (1), there is a tendency for the model to fall below the data below about  $30^\circ$ . This is most pronounced in channel 1. Since the energy window spanned by this channel is roughly 20-30 keV, the simulation of the covering material may not have been done with sufficient accuracy to properly reproduce the detector response. In particular, the hexel shape of the honeycombed aluminum covering the CPDs may be the cause, or part of the cause, for this problem.

### A Model of the Honeycombed Aluminum Sheet

The structure covering the CPDs contains two 10 mil aluminum sheets glued with epoxy to a hexel aluminum structure. This structure appears to be made by stamping three-sided "troughs" into  $\frac{1}{4}$ " wide, 2 mil aluminum strips and placing them together to form a hexel pattern. The distance between opposite sides is 0.49 cm. Incident photons entering the hexel region at  $0^\circ$  encounter the  $\frac{1}{4}$ " aluminum hexel covering 2% of the surface area. As the angle increases photons entering the hexel region in a plane of incidence normal to one wall pass through less material although the effective area increases. At  $38^\circ$  photons begin to pass though a second wall and at  $57^\circ$  a third wall.

The adjacent hexel walls are at  $30^\circ$  to the incident plane. The thickness through which the photons pass are greater than the first wall and the opposing walls are much closer. These photons are more greatly attenuated. Rotating the incident beam about the normal to the LADs produces a changing effective area and attenuation for a given angle  $\theta$ . Modeling such a structure requires a complex mathematical statement.

A simple model of the hexel structure has been chosen as a series of long parallel sheets placed perpendicular to the plane of incidence. For such a structure the effective

sheet thickness varies as  $t / \sin(\theta)$  until the angle of  $38^\circ$ . An introduction of this model into Eq. (1) gives

$$C(E) = A(E) \cos(\theta) \exp(-B / \cos(\theta) + C / \sin(\theta + D)) \quad (4)$$

where D is introduced to keep the argument of the exponential finite at  $0^\circ$ . The results of a  $\chi^2$  fit of this function to the count rates is shown in Fig. (4) for LAD 3. The  $\chi^2$  values are comparable to those for Eq. (1), but the quality of fit for small angles in channel 1 for all LADs is much better. However, the parameter C is positive, not negative as expected for an attenuation, and D is typically about  $30^\circ$ , not about  $0.5^\circ$  as might be expected from the 2 mil by  $\frac{1}{4}$ " hexel cell.

Although this seems non-physical, a physical interpretation can be made. At higher angles there are a greater number of data points than at small angles. This "forces" the B parameter to represent an effective thickness which includes several hexel walls and the increased effective thickness of the planar material. At smaller angles the C coefficient must "decrease" the attenuation factor to properly reduce the attenuation. At higher energy, higher channels, the rapidly decreasing absorption coefficients reduce the effect of the hexels. Therefore, C coefficients consistent with zero are usually found in Channel 2 and higher channels where Eq. (1) adequately fits the data.

### Energy Recalibration

The energy calibration of the BATSE detectors was performed preflight and may have changed during orbital insertion or because of thermal gradients in orbit. This will cause the preflight model of the detector responses to be incorrect. The count rates for Channel 1 in the LADs indicate sufficient differences to suggest that this has occurred. The variations in the A coefficients from Eq. (1) can be used to adjust the energy widths of the low energy channels. In addition, the values of the B coefficients give the average attenuation factor for several channels of each LAD. This is directly related to the energy range covered by a given channel. By varying the energy range to give a better fit to the data the energy calibration can be adjusted. While the small angle deviation from the model is still present, the resultant fits properly reproduce the spectra at larger angles. Corrections to other detectors can be obtained in a similar manner.

## II. Induced Radioactivity

The Long Duration Exposure Facility (LDEF) was orbited for a period of 68 months beginning in April, 1984. Nearly 400 samples taken from that mission have been studied to study the induced activity encountered while in orbit. A review of the results found in an article submitted for publication (Harmon96) shows significant scientific information on total activation and on the directionality of the proton flux encountered by LDEF. However, the delay between retrieval and sample counting resulted in only a few long-lived radioisotopes being found. This precluded attempts to determine the proton energy flux by analysis of production of radioisotopes with differing activation thresholds. For the



same reason, the possibility of measuring high energy neutron fluxes with reactions having small cross sections and short half lives was negated.

Despite this, these results indicated the potential for significant new scientific investigations. For example, similar passive experiment can be undertaken on the Space Station. A set of 1/16" samples of aluminum, vanadium, cobalt, nickel, indium, tantalum, and tungsten and another set of the same samples sandwiched between moderating material could study proton and neutron activation in orbit. Differences in the activities from the two sets would allow separation of fast and slow neutron effects.

These samples should be placed behind the racks in the first Space Station module orbited. After six months in orbit a moderated set and an unmoderated set of samples would be replaced and returned on a shuttle mission. After landing the samples would be immediately transported to a counting facility. This will allow for the determination of the abundance of the activated isotopes with half-lives of 3-4 days or less rather than the 70 day half life material typically measured on LDEF. These samples could be replaced and returned to Earth on a monthly basis, or as often as the availability of shuttle missions. This study would result in a better understanding of the flux of particles encountered by the Space Station and the onboard experiments.

An active experiment to measure the high energy neutrons could be flown on the Space Station or in an external experiment rack. A detector such as a fission fragment detector should be investigated as a possible active system. This system measures the energy of neutrons which interact with a thin sheet of uranium. Fission in the uranium produces recoiling fragments which interact with a particle detector. The signals produced by these interactions can be analyzed to determine the number and energy of the high energy neutrons.

## REFERENCES

- (Horack91) Horack, J. M., Development of the Budst and Transient Source Experiment (BATSE), NASA Reference Publication 1268, September, 1991.
- (Pendleton94) Pendleton, G., et al., Proceedings of the Second Compton Symposium, ed. by Carl Fichtel, Neils Gehrels, and Jay Norris, 1994.
- (Pendleton95) Pendleton, G., et al., Nucl. Instr. and Meth. In Phys. Res. A365 (1995) 567.
- (Harmon96) Harmon, B. A., et al., Induced Radioactivity of LDEF Materials and Structural Components, accepted for publication by Radiation Tracks.

Figure 1. Crab\_LAD3\_Chann 1

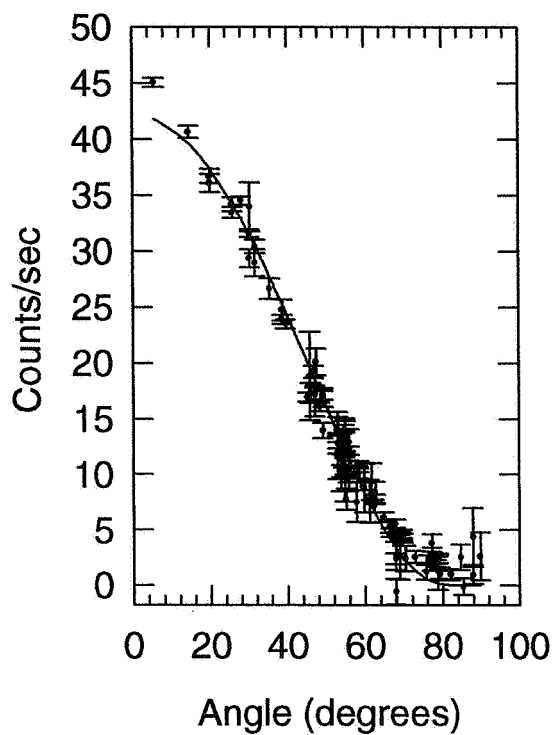


Figure 2. A Coefficients for LAD 3

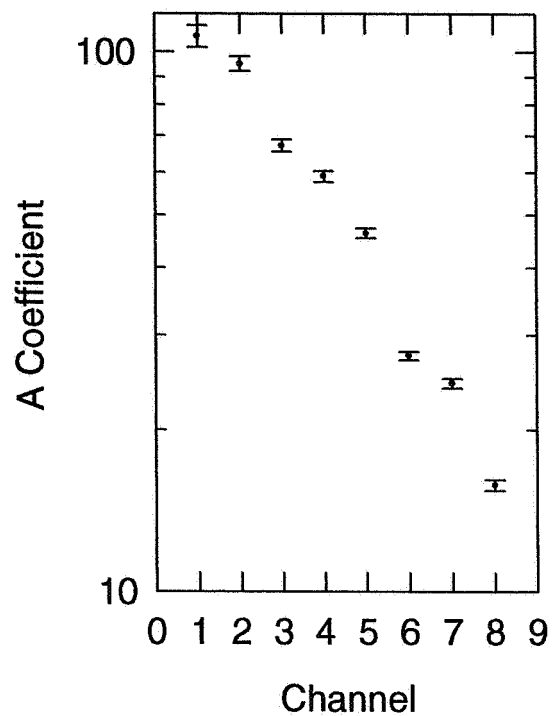


Figure 3. B Coefficients for LAD 3

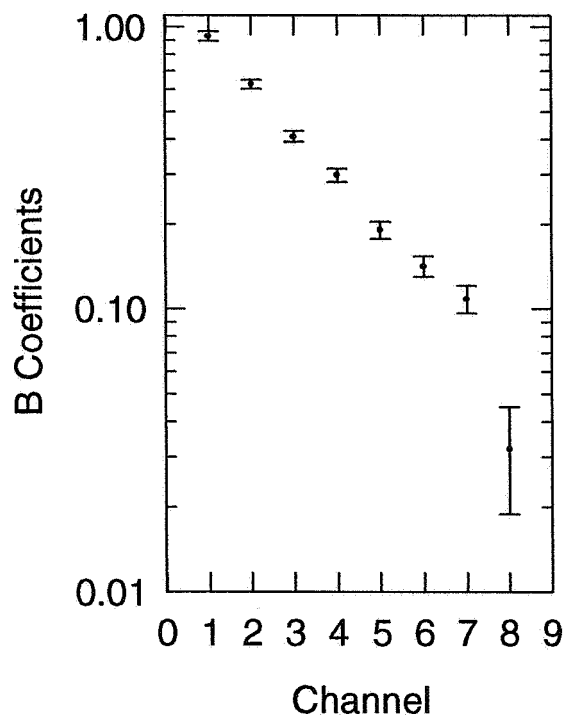
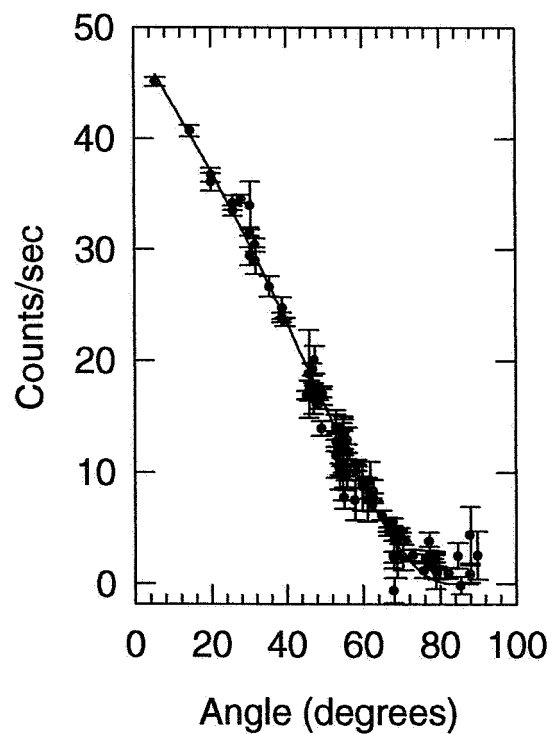


Figure 4. Crab\_LAD3\_Chann 1





**1996**

**NASA/ASEE SUMMER FACULTY FELLOWSHIP PROGRAM**

**MARSHALL SPACE FLIGHT CENTER  
THE UNIVERSITY OF ALABAMA**

**DEVELOPMENT OF AN OUTREACH PROGRAM FOR NASA:  
“NASA AMBASSADORS”**

Prepared by:	George R. Lebo, PhD
Academic Rank:	Associate Professor
Institution and Department:	University of Florida Department of Astronomy
NASA/MSFC:	
Office:	Associate Director for Science
MSFC Colleague:	Frank Six, PhD



## **DEVELOPMENT OF AN OUTREACH PROGRAM FOR NASA: "NASA AMBASSADORS"**

### **INTRODUCTION AND BACKGROUND**

It is widely known that the average American citizen has either no idea or the wrong impression of what NASA is doing. The most common impression is that NASA's sole mission is to build and launch spacecraft and that the everyday experience of the common citizen would be impacted very little if NASA failed to exist altogether. Some feel that most of NASA's efforts are much too expensive and that the money would be better used on other efforts. Others feel that most of NASA's efforts either fail altogether or fail to meet their original objectives. Yet others feel that NASA is so mired in bureaucracy that it is no longer able to function.

The goal of the NASA Ambassadors Program (NAP) is to educate the general populace as to what NASA's mission and goals actually are, to re-excite the "man on the street" with NASA's discoveries and technologies, and to convince him that NASA really does impact his everyday experience and that the economy of the U.S. is very dependent on NASA-type research.

Each of the NASA centers currently run a speakers bureau through its Public Affairs Office (PAO). The speakers, NASA employees, are scheduled on an "as available" status and their travel is paid by NASA. However, there are only a limited number of them and their message may be regarded as being somewhat biased as they are paid by NASA. On the other hand, there are many members of NASA's summer programs which come from all areas of the country. Most of them not only believe that NASA's mission is important but are willing and able to articulate it to others. Furthermore, in the eyes of the public, they are probably more effective as ambassadors for NASA than are the NASA employees, as they do not derive their primary funding from it. Therefore it was decided to organize materials for them to use in presentations to general audiences in their home areas. Each person who accepted these materials was to be called a "NASA Ambassador".

### **PROGRAM DEVELOPMENT**

An announcement was made at the first meeting of all of MSFC's summer program participants that a "NASA Ambassadors" program would be organized during the summer. It was suggested that certain NASA-related topics would make interesting presentations to general audiences. A call was made for volunteers who would be willing to collect and organize materials on these topics. At the first meeting of the

volunteers other topics were suggested. The following is a list of all of the suggested topics that came out of that first meeting.

<u>TOPICS</u>	<u>"GLITZY TITLES"</u>
Propulsion, Single Stage to Orbit, Reuseable Launch Vehicle, Future Propulsion Systems	<b>"Rocket Ships"</b>
Space Station, Shuttle/Space Lab, Human Exploration and Development of Space (a NASA enterprise)	<b>"Space Outposts"</b>
Planetary Exploration, Viking, Pioneer, Voyager, Galileo, Mars Pathfinder, Planetary Science, Ulysses, Magellan, Cassini	<b>"Destination Mars", "Space Robots"</b>
Space Technology (a NASA Enterprise), Advanced Technologies, Spinoffs	<b>"Space - For Free"</b>
Aeronautics (a NASA Enterprise), Supersonic Transport	<b>"To Fly"</b>
Mission to Planet Earth (a NASA Enterprise), Global Warming, Ozone Depletion, Atmospheric Science	<b>"The Water Planet"</b>
Orbital Science, Protein Crystals, Fluid Physics, Microgravity	<b>"Free Falling"</b>
Space Observatories: Hubble, Compton, AXAF SIRTf, Son of Hubble	<b>"Extending Our Senses Beyond Our Reach"</b>
Discovery	<b>"Ah-Ha"</b>
Economics, NASA Messages	<b>"To Lead or not to Lead"</b>
Materials Developed and/or Originated by and for the Space Program	<b>"What is it made of?"</b>

Not all of the topics were chosen for development. Each volunteer chose one or two topics. In preparing the packages the volunteers identified a NASA expert who volunteered to be available to answer technical questions posed not only by the preparer but also by those who would be delivering the presentations. Meetings were held twice weekly in which members exchanged materials and suggestions. At the time of this

writing (August 6, 1996) visual and textual packages covering the following topics were near completion and ready for distribution.

<u>TOPIC</u>	<u>PREPARER</u>
<b>Rocket Ships of the Past, Present and Future</b>	George Lebo University of Florida
<b>Spacecraft Charging</b>	Nancy Losure Mississippi State University
<b>Mars in Fact and Fiction</b>	Nancy Losure Mississippi State University
<b>NASA - The Place Where Miracles Happen</b>	Malcolm McDonald Berry College
<b>To lead or not to lead, that is the question!</b>	Malcolm McDonald Berry College
<b>Extending Our Senses Beyond Our Reach</b>	Frank Six MSFC
<b>Protein Crystal Growth</b>	Leonard Holmes UNC Pembroke
<b>The Blue Planet</b>	J. M. Wersinger Auburn University

Summer programs members are issued as many of the above pre-packaged presentations as they request. However they are required to execute the following agreement which indicates that they will deliver each presentation to a non-academic audience at least twice during the next year.



## AGREEMENT

Recognizing that: (1) NASA's missions excite people of all ages and educational backgrounds, and (2) relatively few have heard about NASA's missions, I agree to become a "NASA Ambassador." I understand that, to be named a NASA Ambassador, I must have been a participant in an MSFC summer program or I must be an employee of the MSFC. I understand that I will receive (a) package(s) of materials which I can use to give popular level talks to non-academic audiences.

The stipulations of the agreement are as follows:

NASA agrees to:

1. Provide me slides, video tapes and other appropriate audio-visual aids on selected topics.
2. Provide me written explanatory material to accompany the visual aid packages.
3. Notify me when a visual aid package on a given subject is available.
4. Keep the audio-visual and written materials up-to-date.
5. Provide me contacts within NASA who will answer questions regarding the material in the packages.
6. Recognize outstanding performance with some type of award.

I agree to:

1. Give at least two presentations per year to audiences outside my institution for each visual aid package which I receive.
2. Submit a reply card to MSFC each time I give a presentation documenting the size and nature of my audience and other pertinent statistics.
3. Distribute to the audience a one-page evaluation form. I will ask a member of the audience (probably the program chairperson) to collect this feedback and to mail it to MSFC in the envelope provided.

NASA AMBASSADOR

NASA

NAME \_\_\_\_\_

\_\_\_\_\_

DEPARTMENT \_\_\_\_\_

\_\_\_\_\_

INSTITUTION \_\_\_\_\_

\_\_\_\_\_

CITY/STATE/ZIP CODE \_\_\_\_\_

\_\_\_\_\_

SIGNATURE \_\_\_\_\_

SIGNATURE \_\_\_\_\_

DATE \_\_\_\_\_

DATE \_\_\_\_\_

PACKAGE(S) REQUESTED \_\_\_\_\_

NASA/MSFC's PAO has agreed to take responsibility for keeping the NASA Ambassadors' packages up-to-date and to maintain communication with them. The PAO will also send letters to officials at the NASA Ambassadors home institutions informing them of the program and that one of their faculty is a NASA Ambassador.

Evaluation materials were also developed. Each NASA Ambassador will be expected to fill out a reply card which will indicate the topic, audience, date and other pertinent information and return it to the PAO. He/she will also be asked to distribute evaluation forms which, after having been completed by the listeners, will be collected and sent directly to the MSFC PAO. The PAO will collate the responses and will feedback to the speaker comments, suggestions and criticisms as appropriate.

When a person becomes a NASA Ambassador he/she also receives instructions on how to go about getting invited to speak to different groups.

At the end of the 1996-1997 academic year the program will be reviewed by the PAO. It is hoped that the NAP will be come sufficiently successful that the other NASA centers will adopt it for use with their own summer participants.



1996  
NASA/ASEE SUMMER FACULTY FELLOWSHIP PROGRAM

MARSHALL SPACE FLIGHT CENTER  
THE UNIVERSITY OF ALABAMA

TESTING PROTOCOL PROPOSAL TO IDENTIFY AND EVALUATE CANDIDATE  
MATERIALS TO SUBSTITUTE FOR SILVERIZED TEFLON IN THERMAL CONTROL  
APPLICATIONS.

Prepared by:	Nancy S. Losure
Academic Rank:	Assistant Professor
Institution and Department:	Mississippi State University Department of Chemical Engineering
NASA/MSFC:	
Laboratory:	Systems Analysis and Integration Lab
Division:	Systems Definition Division
Branch:	Electromagnetic Environments Branch
MSFC Colleague:	Matthew B. McCollum



## **Introduction:**

Electrostatic discharge (ESD) has been shown to be the primary cause of several glitches in spacecraft operations [NASA RP1375]. It appears that charged particles encountered in the natural environment in certain orbits can collect on the outer surfaces of a spacecraft, building up a charge of several thousand volts. If the potential exceeds the breakdown voltage of the charged material, then an ESD will occur. ESD events involving relatively low voltages, on the order of 100 V, have been shown to damage electronic components. [Matisoff] When ESD occurs, electronic and electrical components can be damaged, computer instructions can be garbled, and ablation of material from the spacecraft may occur; degrading both the performance of the thermal control blankets, and the cleanliness of any surfaces on which the detritus becomes deposited.

There appear to be six ways to prevent or mitigate the effects of ESD. 1) Choose an orbit where charging is not a problem. 2) Carry extra electromagnetic shielding. 3) Provide redundancy in components and programming. 4) Provide for active dissipation of the charge, by generating a plasma with which to bathe susceptible surfaces. 5) Provide for passive dissipation from a plasma contactors on the susceptible surfaces. 6) Provide thermal control blankets that do not hold a charge, i.e., that are conductive enough to bleed a charge off harmlessly. These six options are discussed in detail in Losure (1996). Of these six options, number 1 is not always practical, given other requirements of the mission; 2,3,4 and 5 will require that extra mass in the form of shielding, etc., be carried by the spacecraft. The most attractive option from a mass and energy point of view seems to be that of finding a material which matches the other performance characteristics of the current thermal control blankets without their tendency to build up an electrostatic charge. The goal of this paper is to describe and justify a testing program which will lead to the approval of materials of this kind.

## **Preselection of candidate materials**

The testing program outlined below is directed toward identifying candidate materials for thermal control blankets. As such, only polymers which can be fabricated as thin, transparent film, will be considered. However, other plastic and rubber parts on spacecraft are also known culprits in ESD events, and it may become desirable to seek replacement materials for gaskets, fasteners, cable ties etc. This testing program should also serve to identify and qualify candidates for these applications, with due consideration of the desirable mechanical properties of thick section parts like gaskets.

Thermal control blankets (TCB) are assembled of multiple layers of (usually) silverized Teflon film, with some polyester netting interlayers. TCB have two main functions: to reflect as much solar energy as possible, in order to keep the spacecraft as a whole from thermal cycling, and to absorb the impact of small orbital debris. The successful candidate will possess a balance of thermal, physical and chemical properties that will allow the easy fabrication and installation of thermal control blankets, the thermal and physical protection of the spacecraft, and a long service life under the conditions of the natural space environment. The properties considered important are discussed below, and summarized in Table 1.

The mechanical properties of the TCB's should allow easy fabrication, installation and deployment; so the film should be light weight, tough, flexible, non-blocking and puncture

resistant. The tensile strength of the film is not important, above a minimum level sufficient for handling of the film. The tensile strength of Teflon is given in Table 1 as 14 MPa. Teflon is known as a low-strength plastic, and this value should be considered a minimum acceptable value for candidates. Teflon is also a polymer with a high impact strength, which is one of its main advantages. Any serious candidate should have at least 2 Nm/cm impact strength. Teflon also has a high specific gravity, at 2.1 g/cm<sup>3</sup>. This is almost double any other polymer, and should be considered a maximum acceptable value. Teflon film is quite flexible at very low temperatures, and this is a desirable for TCB applications, along with a fairly high distortion or melting temperature. Teflon is known as having a very high melting temperature among thermoplastics. Other polymers may not need to meet this high a value to be successful, and careful consideration should be given to specifying a maximum operating temperature for the TCB.

TCB's should have bright mirrored or dazzling white surfaces, so as to reflect as much sunlight as possible. That is, the solar absorptivity should be as low as possible. On the other hand, the thermal emissivity must be as high as possible, and this is generally promoted by a dark or rough surface. These seemingly mutually exclusive properties are achieved in silverized Teflon and a few other materials, as discussed in Losure (1996). These properties should not deteriorate during the expected life of the spacecraft, due to the orbital environment. Standard tests exist in the literature for these properties at the beginning of life (BOL) of a material. Properties at the end of life (EOL) require the material to subjected the space environment, either in actuality or in simulation.

The materials of TCB's should also be able to stand up to the physical and chemical effects of vacuum, atomic oxygen, and ultraviolet (and other kinds) radiation from the sun, without changing thermal properties, outgassing, or throwing off other kinds of debris. There is no standardized test for these properties, but the literature contains descriptions of testing done under simulated space conditions, which can be adopted. Of course, these earth-bound tests may need to be supplemented by flight testing.

Various kinds of TCB, mainly silverized Teflon, have satisfied the requirements listed above, with the exception of discouraging ESD. Silverized Teflon does not have satisfactory anti-static properties, as it has a surface resistivity of about 10<sup>18</sup> ohm-cm. A successful TCB candidate should have the lowest possible resistivity, with 10<sup>12</sup> ohm-cm being the practical maximum. Surface resistivity, bulk resistivity, breakdown voltage, and other electrical properties can be evaluated by means of standardized tests, as described below.

#### **Sources of material properties data.**

Materials properties data has been compiled into a number of handbooks and computerized data-bases. In general, values are available for a wide variety of materials and properties, but seldom is any particular material thoroughly treated in any of the resources discussed below. Therefore, though it seems reasonable to use published property values as a guideline to nominate candidate materials, there are enough gaps in the literature to make thorough testing of any candidate material absolutely necessary before qualifying it for flight. Indeed, some of the newer polymer formulations have not even been tested with a space environment in mind, so that no

suitable published data may exist. What follows is a discussion of the various sources of property data available to the author.

#### MATDAT.XLS

This database was compiled during the summer of 1995. It contains values gleaned from the literature for 43 properties of 118 materials. The database is only 21% complete, due to the lack of literature values for very many of the properties or materials of interest. In particular, there is no data in the open literature for silverized Teflon film, or for thermal control blankets. Such data as were gleaned for these entries came from internal NASA sources. Thus, there is a deep lack of readily available data on many materials of interest to the space program. Perhaps data that are available only in laboratory notebooks should be compiled and published to help alleviate this lack, and to avoid duplication of effort.

#### MAPTIS

MAPTIS is a database of material properties created and administered at MSFC. It concentrates on engineering properties of very specific materials, often identified by manufacturer's trade name. As such, it is useful to spacecraft designers debating the use of one alloy in favor of another. However, the database seems to be very weak in coverage of polymer materials in general, and TCB materials in particular. Indeed, the only values available in MAPTIS for MLI (Multi-layered Insulation, a relative of TCB) was the results of flammability testing. As far as could be determined, there are no values for solar absorptivity nor infra-red emissivity stored in MAPTIS. Therefore, MAPTIS is not useful for the choice of candidate materials for TCB. Indeed, the results of any testing program should be forwarded to MAPTIS, for inclusion in the database.

#### NASCAP

NASCAP is a computer program that calculates the charging potential of spacecraft surfaces, given the nature of the surface, and the nature of the space environment. It contains a small database of a dozen or so materials that are currently in use for spacecraft surfaces. The property values included in this data are all related to spacecraft charging; no tensile, thermal or environmental properties are compiled. In addition, some properties like the radiation induced conductive power, are peculiar to NASCAP, and appear nowhere else in the literature. When TCB candidates are identified, these properties peculiar to NASCAP will have to be evaluated, so that they can be incorporated in the spacecraft charging model.

#### Manufacturer's Literature

For materials that already exist in commercial grades, the manufacturer's literature on material properties can be very helpful. However, it is usually restricted to reporting those values that are of particular interest to the potential customer. Most manufacturers have neither tested nor reported material properties with an eye to the special requirements of the space program. Therefore, it is likely that the manufacturer's literature can be used as a guide for candidate screening, but not as a substitute for in-house testing.

#### In-House testing.



Equipment and procedures exist in-house at MSFC for performing tests on candidate materials. No comprehensive program to test candidate materials has been undertaken, and the results of other testing performed over the years exist as fragments in memos, short reports and laboratory notebooks. This spot-testing program no doubt was timely and useful when questions of the suitability of a particular material came up, but the fragmentary reporting is a bar to getting the full benefits or the testing that has already been done.

#### Long Duration Exposure Facility

The Long Duration Exposure Facility (L-DEF) flew with samples of various TCB materials, but no candidates for future TCB applications were flown. In fact, the only polymer films besides Teflon were some samples of Polyethylene film being evaluated for weather balloon applications. The film was destroyed by the orbital environment during the extended stay of the L-DEF on orbit. Thus, there is no data from the L-DEF that seems applicable to the search for new TCB materials, aside from estimation of orbital debris impact rate and energy.

#### **Justification for a testing program for selection of new TCB materials.**

It has been shown above, and in other reports (see Losure 1995) that the existing literature on materials properties for currently qualified TCB materials is fragmentary and scattered. Other materials which may be good candidates also suffer from a lack of reporting. Indeed, some of the materials that may be the best candidates are not fully characterized or reported in the literature because they have been commercially available only a short time. In order to solve the spacecraft charging problem by replacing silverized Teflon with a material possessing equivalent or superior physical properties, comprehensive testing must be carried out by NASA, or its contractor. The literature is not reliable except on the level of screening candidates. Material suppliers are not equipped to do the space environmental testing needed.

Therefore, a project to screen, select, and evaluate candidate materials for silver/Teflon replacement is proposed. The work is to be carried out by a Mississippi State graduate student under the supervision of the PI, who holds a faculty position at MSU. Testing will be carried out at both MSU and MSFC, to make the best use of existing facilities. As shown in Table 1, MSU is well equipped to carry on the testing of physical properties, while MSFC is equipped to do the thermal and space environmental testing.

Electrostatic discharges are a constant threat to the operation of spacecraft. Identifying and qualifying TCB materials that will eliminate ESD will greatly increase spacecraft reliability, and decrease overall mission costs due to provision of back-up systems and repair missions. This project will provide a means to approach the goal of zero ESD-related failures in future space operations.

#### **References**

- Leach, R.D.; and M.B. Alexander, Eds. Failures and Anomalies Attributed to Spacecraft Charging. NASA Reference Publication 1375. August, 1995.
- Losure, N.S.; and M.B. McCollum, The ESD Prevention Primer, in progress, August 1996.
- Matisoff, Bernard S.; Handbook of Electrostatic Discharge Controls (ESD): Facilities Design and Manufacturing Procedures. Van Nostrand Reinhold Co., New York NY. 1986.

Table 2: Materials Testing Program.

Property	Standard	Sample size & number	Time	Facility	Notes
Tensile strength and modulus	ASTM D-882	10 x 60 mm 5 ea.	24 hr cond.	MSU	This test to be performed on both as-received and SSE samples.
Puncture resistance	FTMS 101C #2031	10 x 4 in	24 hr cond.	MSU	
Flexibility: bending fatigue		film + coating, 3cm wide strips	24 hour con.	MSU	
Density	ASTM D-792	1 - 5 gram	< 1 hr	MSU	
Hardness, Shore		1 in dia.	24 hr cond.	MSU	
Absorbivity	MSFC internal	film + coating		MSFC	MSU can acquire the necessary equipment for this test.
Emissivity	MSFC internal	film + coating		MSFC	MSU can acquire the necessary equipment for this test.
Color				MSFC	
Surface and bulk resistivity	ASTM D-257 MIL-B-82646	2 x 2 in, 3 ea. 10 x 10 in, 1 ea.	24 hr cond.	MSFC	MSU can acquire the necessary equipment for this test.
ES Decay	EIA-541 Apx. F	3 x 5 in, 5 ea.	48 hr. cond.	MSFC	MSU can acquire the necessary equipment for this test.
Total Mass Loss	ASTM E-595	1 g powder or pellets, 3 ea.	24 hr cond.	MSFC	MSU can use thermogravimetric analysis for this test.
Environmental resistance	ASTM E-512	film,	52 days	MSFC	
LEO environmental resistance	No standard	film		MSFC/shuttle	



**1996**

**NASA / ASEE SUMMER FACULTY FELLOWSHIP PROGRAM**

**MARSHALL SPACE FLIGHT CENTER  
THE UNIVERSITY OF ALABAMA**

**APPLICATION OF CONSIDER COVARIANCE  
TO THE EXTENDED KALMAN FILTER**

<b>Prepared by:</b>	<b>John B. Lundberg, Ph.D.</b>
<b>Academic Rank:</b>	<b>Assistant Professor</b>
<b>Institution and Department:</b>	<b>Auburn University Department of Aerospace Engineering</b>
<b>NASA/MSFC:</b>	
<b>Laboratory:</b>	<b>Structures and Dynamics Laboratory</b>
<b>Division</b>	<b>Guidance and Control Systems Division</b>
<b>Branch:</b>	<b>Flight Mechanics, Guidance, Navigation, and Control Systems Branch</b>
<b>MSFC Colleague:</b>	<b>John M. Hanson, Ph.D.</b>



## INTRODUCTION

The extended Kalman filter (EKF) is the basis for many applications of filtering theory to real-time problems where estimates of the state of a dynamical system are to be computed based upon some set of observations. The form of the EKF may vary somewhat from one application to another, but the fundamental principles are typically unchanged among these various applications. As is the case in many filtering applications, models of the dynamical system (differential equations describing the state variables) and models of the relationship between the observations and the state variables are created. These models typically employ a set of constants whose values are established by means of theory or experimental procedure. Since the estimates of the state are formed assuming that the models are perfect, any modeling errors will affect the accuracy of the computed estimates. Note that the modeling errors may be errors of commission (errors in terms included in the model) or omission (errors in terms excluded from the model). Consequently, it becomes imperative when evaluating the performance of real-time filters to evaluate the effect of modeling errors on the estimates of the state.

## EKF WITH CONSIDER COVARIANCE

Assume that the EKF is to be applied to a system described by the (possibly) nonlinear differential equations

$$\dot{X} = F(t, X, C) \quad (1)$$

using the (possibly nonlinear) observation-state equation

$$Y = G(t, X, C) + \epsilon \quad (2)$$

where  $X$  is the state whose values are to be estimated and  $C$  is the set of consider parameters. Note that  $C$  encompasses parameters in the equations of motion and the observation equation although it will be rare that any single parameter will be in both sets of equations. Note also that the values of  $C$  are not perfectly known, i.e., the true values of  $C$  are not available; only some nominal values of  $C$  (which will be referred to as  $C_N$ ) and the uncertainties are known. The variable  $\epsilon$  represents the measurement error which is assumed to be white noise and have the following statistics

$$E[\epsilon_i] = 0 \quad ; \quad E[\epsilon_i \epsilon_i^T] = R_i \quad (3)$$

To apply the EKF, this system is converted into a linear system by expanding Eqs (1) and (2) about a reference trajectory  $X_N(t)$  that is known with the corresponding observations which are described by

$$\dot{X}_N = F(t, X_N, C_N)$$

$$Y_N = G(t, X_N, C_N)$$

The resulting system and observation equations are given by

$$\dot{x} = A(t, X_N, C_N) x + B(t, X_N, C_N) c \quad (4)$$

$$y = H_x(t, X_N, C_N) x + H_c(t, X_N, C_N) c + \varepsilon \quad (5)$$

where  $x = X - X_N$ ,  $c = C - C_N$ ,  $A = \frac{\partial F}{\partial X}$ ,  $B = \frac{\partial F}{\partial C}$ ,  $H_x = \frac{\partial G}{\partial X}$ , and  $H_c = \frac{\partial G}{\partial C}$ . Note that the solution for  $x(t)$  in Eq. (4) can be written as

$$x(t) = \Phi(t, t_k) x(t_k) + \Theta(t, t_k) c \quad (6)$$

where  $\Phi$  and  $\Theta$  satisfy

$$\dot{\Phi}(t, t_0) = A(t, X_N, C_N) \Phi(t, t_0) ; \Phi(t_0, t_0) = I$$

$$\dot{\Theta}(t, t_0) = A(t, X_N, C_N) \Theta(t, t_0) + B(t, X_N, C_N) ; \Theta(t_0, t_0) = 0$$

The filter state vector is  $x(t)$ , the estimate of  $x(t)$  is  $\hat{x}(t)$ , and the estimate of  $X(t)$  is recovered using  $\hat{X}(t) = X_N(t) + \hat{x}(t)$ .

To initialize the filter, assume that initial values for  $\hat{x}_{k-1} = \hat{x}(t_{k-1})$  and  $P_{k-1} = E[(x_{k-1} - \hat{x}_{k-1})(x_{k-1} - \hat{x}_{k-1})^T]$  as well as  $X_N(t_{k-1})$  are given. This information is to be propagated to  $t_k$  and combined with the observation  $y_k = y(t_k)$  to form the estimate  $\hat{x}(t_k)$ . Once the values for  $\Phi(t_k, t_{k-1})$  and  $\Theta(t_k, t_{k-1})$  are computed, the propagation of the filter state vector is carried out using Eq. (6) in the form

$$\bar{x}_k = \Phi(t_k, t_{k-1}) \hat{x}_{k-1} + \Theta(t_k, t_{k-1}) c \quad (7)$$

Similarly, the true state vector would be propagated using

$$x_k = \Phi(t_k, t_{k-1}) x_{k-1} \quad (8)$$

since for the true state vector there is no error nor uncertainty in the consider parameters. Using Eq.s (7) and (8), the covariance matrix corresponding to  $\bar{x}_k$  is written as

$$\begin{aligned} \bar{P}_k &= E[(x_k - \bar{x}_k)(x_k - \bar{x}_k)^T] \\ &= \Phi_{k,k-1} E[(x_{k-1} - \hat{x}_{k-1})(x_{k-1} - \hat{x}_{k-1})^T] \Phi_{k,k-1}^T + \Phi_{k,k-1} E[(x_{k-1} - \hat{x}_{k-1}) c^T] \Theta_{k,k-1}^T \\ &\quad + \Theta_{k,k-1} E[c (x_{k-1} - \hat{x}_{k-1})^T] \Phi_{k,k-1}^T + \Theta_{k,k-1} E[c c^T] \Theta_{k,k-1}^T \end{aligned}$$

For now let,  $W_{k-1} = E[(x_{k-1} - \hat{x}_{k-1}) c^T]$  which will be discussed in more detail in the following sections. The expected value expression in the last term represents the uncertainties in the consider parameters which is assumed known and can be represented as

$$E[c c^T] = \Pi$$

Thus, for now, the propagated covariance matrix becomes

$$\begin{aligned} \bar{P}_k = & \Phi_{k,k-1} P_{k-1} \Phi_{k,k-1}^T + \Phi_{k,k-1} W_{k-1} \Theta_{k,k-1}^T \\ & + \Theta_{k,k-1} W_{k-1} \Phi_{k,k-1}^T + \Theta_{k,k-1} \Pi \Theta_{k,k-1}^T \end{aligned} \quad (9)$$

Note that the first term in this equation represents the propagate covariance matrix if there were no consider parameter effects and the remaining three terms are the contributions of the consider terms.

Once the filter state vector estimate and associated covariance matrix have been propagated to  $t_k$ , it can be treated as an observation and combined with  $y_k$  to write

$$\begin{bmatrix} y_k - H_{c k} c \\ \bar{x}_k \end{bmatrix} = \begin{bmatrix} H_{x k} \\ I \end{bmatrix} x_k + \begin{bmatrix} \epsilon_k \\ \eta_k \end{bmatrix}$$

where  $E[\eta_k] = 0$ ,  $E[\eta_k \eta_k^T] = \bar{P}_k$ , and  $E[\epsilon_k \eta_k^T] = 0$ . The solution for  $\hat{x}_k$  which satisfies these equations in a least squares or minimum variance sense is

$$\hat{x}_k = (H_{x k}^T R_k^{-1} H_{x k} + \bar{P}_k^{-1})^{-1} (H_{x k}^T R_k^{-1} (y_k - H_{c k} c) + \bar{P}_k^{-1} \bar{x}_k) \quad (10)$$

For convenience, let

$$M_k = (H_{x k}^T R_k^{-1} H_{x k} + \bar{P}_k^{-1})^{-1} \quad (11)$$

which would be the state vector covariance if there were no consider parameters.

The covariance matrix associated with  $\hat{x}_k$  is formally defined by

$$P_k = E[(x_k - \hat{x}_k)(x_k - \hat{x}_k)^T]$$

From Eq.s (10) and (11),

$$x_k - \hat{x}_k = x_k - M_k H_{x k}^T R_k^{-1} (y_k - H_{c k} c) - M_k \bar{P}_k^{-1} \bar{x}_k \quad (12a)$$



Using Eq. (5) to express the observation in terms of the true state and true consider parameters ( $c=0$ ) to write

$$y_k = H_{xk} x_k + \epsilon_k$$

then Eq. (12a) can be written as

$$\begin{aligned} x_k - \hat{x}_k = & [I - M_k H_{xk}^T R_k^{-1} H_{xk}] x_k - M_k H_{xk}^T R_k^{-1} \epsilon_k \\ & - M_k H_{xk}^T R_k^{-1} H_{ck} c - M_k \bar{P}_k^{-1} \bar{x}_k \end{aligned} \quad (12b)$$

Note that from Eq. (11), it can be shown that

$$[I - M_k H_{xk}^T R_k^{-1} H_{xk}] = M_k \bar{P}_k^{-1} \quad (13)$$

Consequently, Eq. (12b) can now be written as

$$x_k - \hat{x}_k = M_k \bar{P}_k^{-1} (x_k - \bar{x}_k) - M_k H_{xk}^T R_k^{-1} \epsilon_k - M_k H_{xk}^T R_k^{-1} H_{ck} c \quad (12c)$$

The covariance matrix for  $\hat{x}_k$  can now be expressed as

$$\begin{aligned} P_k = & M_k \bar{P}_k^{-1} M_k^T - M_k \bar{P}_k^{-1} \bar{W}_k H_{ck}^T R_k^{-1} H_{xk} M_k^T \\ & - M_k H_{xk}^T R_k^{-1} H_{ck} \bar{W}_k^T \bar{P}_k^{-1} M_k^T + M_k H_{xk}^T R_k^{-1} H_{xk} M_k^T \\ & + M_k H_{xk}^T R_k^{-1} H_{ck} \Pi H_{ck}^T R_k^{-1} H_{xk} M_k^T \end{aligned} \quad (14)$$

where it has been assumed that

$$\begin{aligned} E[(x_k - \bar{x}_k) \epsilon_k^T] &= 0 & E[c c^T] &= \Pi & E[\epsilon_k \epsilon_k^T] &= R_k \\ E[c \epsilon_k^T] &= 0 & E[(x_k - \bar{x}_k) c^T] &= \bar{W}_k \end{aligned}$$

Note that the first and fourth terms of Eq. (14) can be combined to write

$$M_k (\bar{P}_k^{-1} + H_{xk}^T R_k^{-1} H_{xk}) M_k^T = M_k$$

Also note that from Eq. (10), the sensitivity matrix can be defined as

$$S_k = \frac{\partial \hat{x}_k}{\partial c} = -M_k H_{xk}^T R_k^{-1} H_{ck} \quad (15)$$

Using this notation, the covariance matrix for can be written in the form

$$P_k = M_k + M_k \bar{P}_k^{-1} \bar{W}_k S_k^T + S_k \bar{W}_k^T \bar{P}_k^{-T} M_k^T + S_k \Pi S_k^T \quad (16)$$

As was the case with the expression for  $\bar{P}_k$ , the first term in Eq. (16) represents the covariance matrix if there were no consider parameters and the remaining three terms represent the contribution of the consider parameters.

The only remaining issues to resolve are the expressions for  $W_k$  from Eq. (9) and  $\bar{W}_k$  from Eq. (16) which are defined as

$$W_k = E[(x_k - \hat{x}_k) c^T] \quad \text{and} \quad \bar{W}_k = E[(x_k - \bar{x}_k) c^T]$$

Using Eq. (12c),  $W_k$  can be written as

$$\begin{aligned} W_k &= M_k \bar{P}_k^{-1} \bar{W}_k - M_k H_{x_k}^T R_k^{-1} H_{c_k} \Pi \\ &= M_k \bar{P}_k^{-1} \bar{W}_k + S_k \Pi \end{aligned} \quad (17)$$

Using Eq.s (7) and (8),  $\bar{W}_k$  can be written as

$$\bar{W}_k = \Phi_{k,k-1} W_{k-1} + \Theta_{k,k-1} \Pi \quad (18)$$

Eq.s (17) and (18) provide the necessary equations to propagate and update  $W$  along with the covariance matrices  $M_k$  and  $P_k$ . To initialize this part of the filter, it is assumed that

$$W_o = E[(x_o - \hat{x}_o) c^T] = 0$$

i.e., the initial estimate of the state vector is not correlated to the uncertainties in the consider parameters. Note that by using Eq. (17), Eq. (16) can also be written as

$$P_k = M_k + W_k S_k^T + S_k W_k^T - S_k \Pi S_k^T \quad (19)$$

Finally, note that Eq. (7) can be used to define the propagated sensitivity matrix as

$$\bar{S}_k = \frac{\partial \bar{x}_k}{\partial c} = \Phi_{k,k-1} S_{k-1} + \Theta_{k,k-1} \quad (20)$$

## CONCLUSION

The consider covariance EKF can be used to evaluate the effect of uncertainties of dynamic and measurement modeling errors on the estimate of the state by adjustments made to the state covariance matrix. While the consider covariance EKF does not predict the actual errors since the actual model errors are assumed unknown, it does provide a means of identifying critical elements of the dynamic and observation models for real-time filtering applications.



**1996**

**NASA/ASEE Summer Faculty Fellowship Program**

**Marshall Space Flight Center**

**The University of Alabama**

**SEDSAT 1 Technologies**

Prepared By: Mark W. Maier, Ph.D.  
Academic Rank: Assistant Professor  
Institution and Department: University of Alabama in Huntsville  
Department of Electrical and Computer Engineering  
NASA/MSFC:  
Office: SEDS Project Office  
Division:  
Branch:  
MSFC Colleague: James Harrison



## **Project Goals and Summary**

The original goals of this project were to support the development of SEDSAT 1 for a tethered launch in July of 1997. This specifically required:

1. Monitoring development progress against a comprehensive delivery plan.
2. Incremental development and release of CDS and SEASIS software.
3. Supporting the integration of version 1.0 SEASIS software that will allow minimal autonomous operation without a software reload. These algorithms would include image quality evaluation, attitude determination, and autonomous earth imaging.
4. Developing software requirements and design for ground segment software, concentrating on command and data download capability; and interface to external development efforts for a more comprehensive software suite to be used after the initial mission.

Because of an unfavorable space shuttle safety review of the SEDS-3 tether deployer, and cost and schedule problems in upgrading the deployer, the mission was changed to an independent launch of SEDSAT. The original plan was to do a tether-less deployment from the space shuttle. Since this would have resulted in an unacceptable orbital lifetime, the mission was changed again to a tethered launch from a Delta II in June 1998. As a result of Marshall Space Flight Center's redirection of the SEDS-3 mission away from a tether launch, the whole question of a tether endmass had to be reconsidered.

The net result of these multiple changes was twofold. First, we completed work needed to define some aspects of ground software on SEDSAT 1 that would remain constant no matter the launch mode. Second, we developed a set of concepts for using SEDSAT-1 technology to support alternative endmass missions on SEDS-3. Both of these are included below.

## **SEDSAT Ground Software**

One area of SEDSAT design that has been worked during the summer is the ground communications architecture. Figure 1 shows the basic hardware architecture for SEDSAT-ground communications. The hardware aspects are emphasized, though the schematic breakdown of the software is also shown. Figure 2 illustrates the architecture from a software perspective.

The communications link between the SEDSAT and the ground is a digital radio link. The basic rate is 9.6 Kbits/sec, though experiments at 57.6 kbits/sec are also planned. The link carries AX.25 frames, which encapsulate application data specific packets. Software routines, provided as part of SCOS, carry out the encapsulation and pass byte blocks to the hardware. The byte blocks go out over the serial port to the transponder which transmits them. On the ground side a Yaesu radio picks up the link and passes a lowpass signal to a modem. The modem demodulates the bit stream and passes it to the TNC, which interprets the AX.25 packets internally. The data sections are re-encapsulated onto the PC serial port. The serial port is read by PC software drivers, which pass application level data to the labview front end. The labview front end interprets the packets and displays or archives the received data.

During the summer the basic ground communications system was built and tested. Configurations both with and without the transponder in place were tried. The transponder can be bypassed by connecting the serial port of the CDS board to a suitable tap point in the TNC, although not all of the TNC's will accept this.

Neither configuration has fully checked out in the lab. With the system wired directly the link is established in software and the packet stream can be observed on a monitor. However, packets containing executable program material cannot be passed so user tasks cannot be uploaded. The reason is not clear.

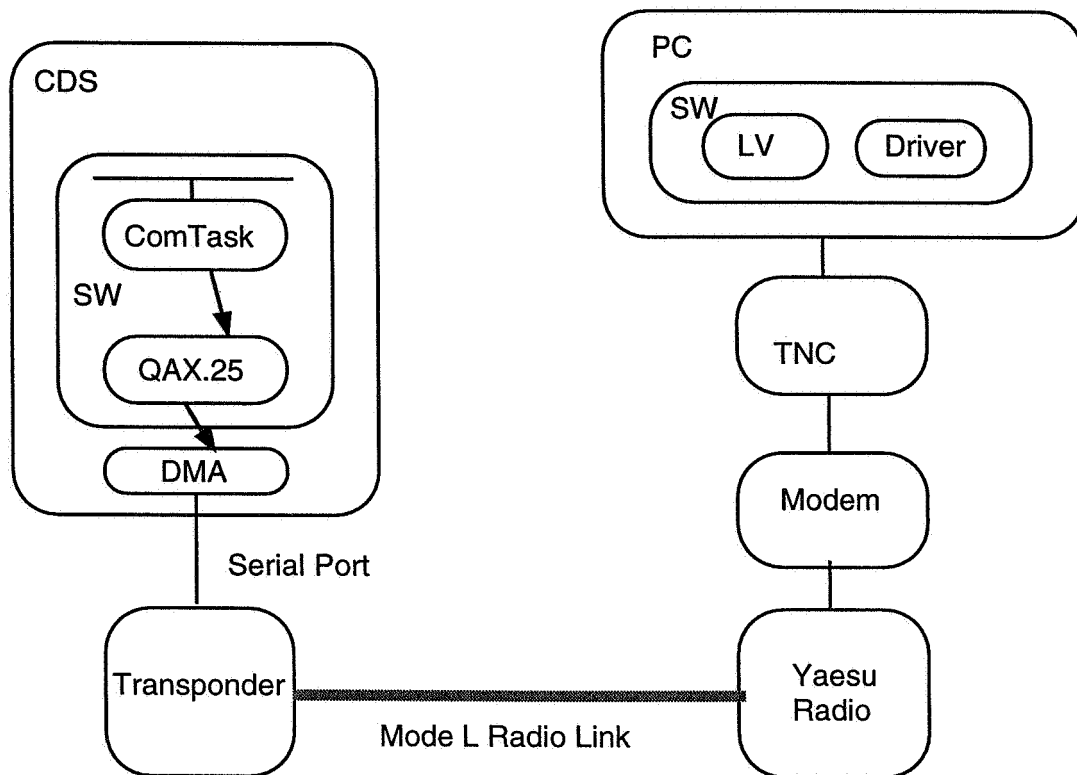


**Figure 1: Hardware architecture diagram for SEDSAT ground communications**

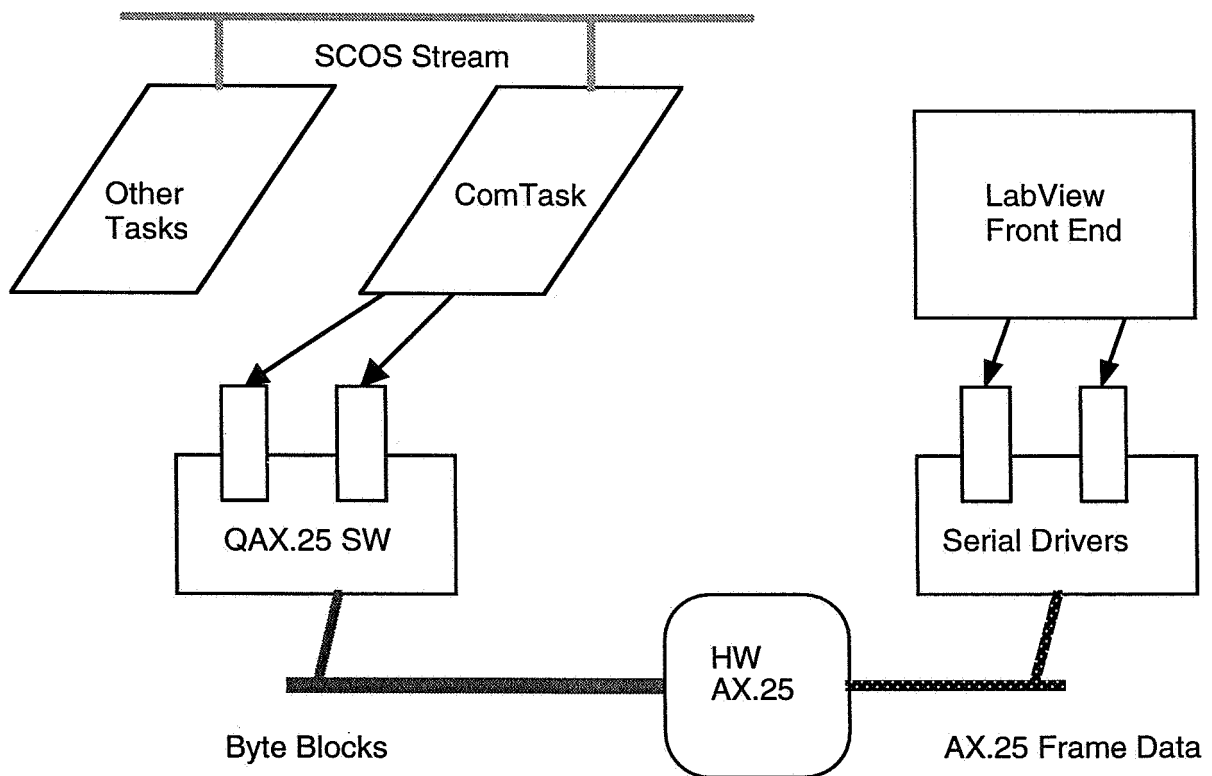


**Figure 2: Software architecture diagram for SEDSAT ground communications**

The transponder works and transmits when placed in the system chain. However, no data can be demodulated at the ground end. Based on laboratory measurements it appears that the transponder was stuck operating in 57.6 kbit/sec mode when the available ground station hardware can handle only 9.6 kbit/sec mode. This diagnosis was based on a spectrum analyzer display resembling  $\pm 17$  Khz suppressed carrier FSK coming from the transponder, which corresponded to the specified modulation pattern for 57.6 kbit/sec transmission. The transponder was returned to the vendor for calibration and its correct operation confirmed. The most likely cause of the stuck condition is incorrect wiring in the CDS motherboard backplane.

From the software perspective, the SEDSAT software tasks read a communications data stream managed through ComTask. ComTask sends and receives data through calls to QAX.25 routines. On the ground end, a front end written in LabView sends and receives application level data packets through a set of serial drivers. The AX.25 protocol encapsulation and decoding is all done in the TNC.

### **SEDS-3 Mission Concepts**

Technology developed between Marshall and UAH on SEDSAT can have wide application to potential SEDS-3 tether endmass missions. As examples the following sections examine possible missions, scenarios, and architectures for building a SEDS-3 endmass with maximum exploitation of SEDSAT 1 technologies.

#### **Objectives**

A new SEDS-3 endmass could address three principal scientific objectives:

1. Make a video record of deployment to determine the ability of astronauts to do visual discrimination of nominal and off-nominal deployment.
2. Record the three-dimensional dynamics of tether rebound during a hard snag event.
3. Record the three-dimensional dynamics of tether recoil during a simulated micrometeoroid tether cut.

A more advanced endmass concept is called a vertical, tethered camera array. This experiment would support one principal objective:

1. Demonstrate multi-camera stereo reconstructive imaging of atmospheric objects using a two dimensional image array. The horizontal dimension will be provided by satellite motion (as is conventional). The vertical dimension will be provided by the tethered endmass.

#### **Mission Scenario**

The proposed system is oriented around a mission scenario that deliberately introduces off nominal deployment to study tether dynamics. The scenario envisioned is:

1. On system power up the endmass is activated and prepares for separation. The imaging system powers up and begins transmitting real-time video before endmass deployment is commanded.
2. As the endmass separates its instruments record accelerations.
3. The video imaging system transmits real-time video of the tether deploying. Simultaneously, the stereo imaging subsystem is capturing and storing stereo stills to determine three-dimensional tether position.
4. After a desired length of tether is deployed the deployment is brought to a sharp halt to simulate a hard snag. The endmass records accelerations. The imaging system transmits and records the tether rebound. At the same time the other experiments would be



monitoring structural loads and the smart tether cutter would be firing (without actually cutting the tether).

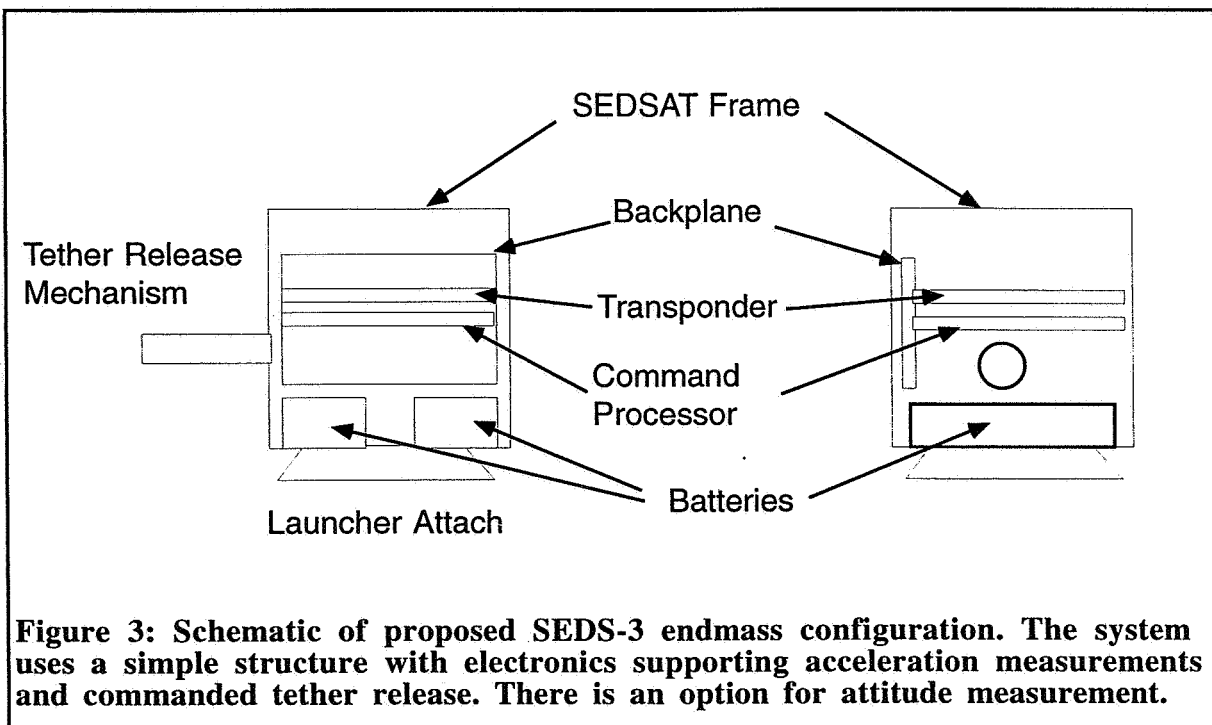
5. After the tether has begun to swing, and tension has risen to a steady high, the endmass is commanded to release the tether. The imaging system records the recoil and subsequent redeployment under gravity gradient forces.
6. After the recoiling tether stabilizes the real-time video is commanded off. The stored digital stereo stills are now transmitted using the same transmitter. If an electrodynamic tether were deployed it would now operate. Optionally, the imaging system could continue to monitor the electrodynamic tether as desired.
7. The endmass continues to operate until the end of its battery life. Depending on the orbit, it will re-enter sometime later. Since the tether is not attached to the endmass it will most likely have significant orbital lifetime.

## Requirements

Meeting these first set of objectives requires a deployment and endmass system capable of normal deployment, simulating a hard snag, and commanded release of the tether at the endmass at a suitable time. It would be desirable for the endmass to be able to record accelerations and attitude throughout deployment. A video/image recording system is required to capture video of deployment and stereo images at selected times. Of course, a data link system must be present to transfer all data to the ground as well as supporting power systems. vertical camera system requires orientable cameras in the endmass and on the deployer platform that can be coordinated.

### SEDS-3 Endmass

The proposed endmass is derived from the SEDSAT project. It uses the SEDSAT structure, battery design, tether release mechanism, and accelerometers. It uses a new electronic design based on off-the-shelf components to facilitate early software development. A schematic of the proposed endmass is shown in Figure 3.



Making use of major portions of the SEDSAT design will carry important benefits. The SEDSAT structure is well characterized, with full production drawings immediately available. It can be produced quickly at known cost and has an existing history of structural characterization and flight paperwork. The tether release mechanism has not been built, but it has full drawings and the design has already been exposed to extensive review. The accelerometer package may be available without procurement from the existing SEDSAT project. The battery system has also been designed and a NASA Marshall procurement is in progress for SEDSAT.

The electronic design of the endmass should be reconsidered in light of the needs of the SEDS-3 mission. Assuming non-amateur frequencies are used for communications, the SEDSAT electronics can be replaced with higher capability, lower power designs. An off-the-shelf board solution will be considered to facilitate immediate development of a laboratory breadboard. The features and benefits of the proposed SEDS-3 endmass are shown in Table 1.

<b>Table 1: SEDS-3 Endmass Features and Benefits</b>	
Feature	Benefit
SEDSAT derived structure	Known cost to construct, existing design reviews, designed for Delta secondary
SEDSAT proposed tether release mechanism	Existing design reviews, existing fabrication quotes
SEDSAT batteries	Existing designs, existing procurement paperwork, option for NiCAD for lower cost.
Accelerometers	Existing hardware, measures deployment accelerations
Off-the-shelf transponder	Moderate to high data rate available, known physical compatibility
COTS compatible electronics design	Rapid laboratory breadboard for software development
OPTION: PAL camera	Measures attitude during deployment
OPTION: Gyro package	Measures attitude during deployment, ring laser gyros very compact

## **Conclusions**

Unfortunately, rapid program changes are to be expected. The technologies developed under SEDSAT can be applied to other small satellite projects, and seem particularly well suited to small tether experiments. In particular, the technologies could be used on a expendable booster mission to experimentally test dangerous dynamic conditions and, hopefully, alleviate some of the concerns for manned space flight that arose during SEDS-3 planning. The tethered satellite framework is an interesting one for earth observing missions, and future experiments seem worthy.



**1996**

**NASA/ASEE SUMMER FACULTY FELLOWSHIP PROGRAM**

**MARSHALL SPACE FLIGHT CENTER  
THE UNIVERSITY OF ALABAMA**

**PLANNING AN EFFECTIVE SPEAKERS OUTREACH PROGRAM**

<b>Prepared By:</b>	Malcolm W. McDonald, Ph.D.
<b>Academic Rank:</b>	Associate Professor
<b>Institution and Department:</b>	Berry College School of Math & Nat. Sciences Physics Department
<b>NASA/MSFC:</b>	
<b>Office:</b>	Public Affairs Office
<b>Division:</b>	Public Services
<b>Branch:</b>	Community Relations
<b>MSFC Colleague:</b>	Ed Medal



## **PLANNING AN EFFECTIVE SPEAKERS OUTREACH PROGRAM**

Malcolm W. McDonald  
Associate Professor  
School of Math and Natural Sciences  
Physics Department  
Berry College

Office of Public Affairs  
Public Services Division  
Community Relations Branch

Ed Medal, Office of Public Affairs, MSFC Colleague

The National Aeronautics and Space Administration (NASA) and, in particular, the Marshall Space Flight Center (MSFC) have played pivotal roles in the advancement of space exploration and space-related science and discovery since the early 1960's. Many of the extraordinary accomplishments and advancements of NASA and MSFC have gone largely unheralded to the general public, though they often border on the miraculous. This lack of suitable and deserved announcement of these "miracles" seems to have occurred because NASA engineers and scientists are inclined to regard extraordinary accomplishment as a normal course of events.

The goal in this project has been to determine an effective structure and mechanism for communicating to the general public the extent to which our investment in our US civilian space program, NASA, is, in fact, a very wise investment. The project has involved discerning important messages of truth which beg to be conveyed to the public. It also sought to identify MSFC personnel who are particularly effective as messengers or communicators. A third aspect of the project was to identify particular target audiences who would appreciate knowing the facts about their NASA investment. The intent is to incorporate the results into the formation of an effective, proactive MSFC speakers bureau.

A corollary accomplishment for the summer was participation in the formation of an educational outreach program known as Nasa Ambassadors. Nasa Ambassadors are chosen from the participants in the various MSFC summer programs including: Summer Faculty Fellowship Program (SFFP), Science Teacher Enrichment Program (STEP), Community College Enrichment Program (CCEP), Joint Venture (JOVE) program, and the NASA Academy program. NASA Ambassadors agree to make pre-packaged NASA-related presentations to non-academic audiences in their home communities. The packaged presentations were created by a small cadre of participants from the 1996 MSFC summer programs, volunteering their time beyond their normal NASA summer research commitment. A total of eight presentations were created and made available for use by NASA Ambassadors.

A major segment of the research effort during the summer has been devoted to verifying and documenting certain "spinoff" contributions of NASA technology and in determining their relevance and impact to our society and our nation's economy. The purpose behind the verification/documentation research has been to shed light on the question of whether or not our NASA investment is a wise investment. It has revealed that NASA is a wise investment.

## INTRODUCTION

In any organization, accomplishment deserves to be recognized and saluted. This is especially true when the accomplishments are of extraordinary value, such as might have led to major improvements in our national economy or the public's standard of living. Since the creation of our U.S. civilian aerospace agency (NASA) in 1958 NASA scientists and engineers have been engaged in wide-ranging scientific research, exploration of new places and new ideas, and the discovery and development of new technologies. Many of these accomplishments and their ultimate applications have gone unheralded to the general public.

The project discussed in this report represents an attempt by the author, a college professor and a member of the larger general public, to discover or utilize mechanisms suitable for transmitting information about our civilian aerospace program to that largely ill-informed or misinformed general public.

One thesis of this report is that the public deserves to hear certain large messages about the civilian aerospace program. Those large messages include the following three: (1) **NASA**, our U.S. civilian aerospace program (hereafter simply referred to as our space program) is **OUR PROGRAM**. It is something in which each of the citizens of this country invests and in which each of us has reason to be interested in the results of that investment, (2) our space program is a **FIRST-RATE BARGAIN**, and it deserves to be recognized as such. American citizens deserve to know, in fact, how much they are investing in this program and weigh that against how much they are receiving back in return, and (3) in terms of the kind of scientific research and technological development for which our space program is noted, our space program is **GOOD FOR US**, and we **NEED MORE OF IT, NOT LESS**.

This project sought from the outset to identify messages, such as those outlined in the preceding paragraph, which need to be passed along to the public. Further, it sought to identify at the Marshall Space Flight Center those persons who could most effectively relate to the public those pertinent messages, and, finally, it proposed to identify examples of public audiences which could appreciate hearing the important messages. The final result is to lead to the creation of an effective speakers outreach program, utilizing Marshall personnel to execute the agency's charter responsibility of informing and educating the public.

While the project, as outlined above, progresses, though not yet nearly to the point of fulfillment, another parallel project, **NASA AMBASSADORS**, has been launched. NASA AMBASSADORS are volunteers selected from among the participants in the various MSFC summer programs, including: the Summer Faculty Fellowship Program (SFFP), the Community College Enrichment Program (CCEP), the Science Teachers Enrichment Program (STEP), the Joint Venture (JOVE) program, and the NASA Academy student program. NASA AMBASSADORS agree to deliver pre-packaged presentations to public audiences at locations near their home institutions. The talks, amply supported with visual slides, were created by volunteers from among the summer program participants. The NASA AMBASSADORS program will be coordinated by the MSFC Office of Public Affairs.

Much of the effort for this summer has been directed to performing interviews with NASA scientists, engineers, and contractors and to conducting research into printed materials and internet resources to ascertain links between NASA-developed technologies and products and services in use in our society. Special interest has been paid to documenting those "spin-offs" from NASA technology which are having largest measurable economic impact to American citizens.

What follows, in order, is a discussion of the large messages relevant to our space program, a discussion of the NASA AMBASSADOR program, and a discussion of the research results gathered during the documenting of the transfer of NASA technologies into the public sector.

## MESSAGES

**The first message** which needs to be emphasized to the public is the reminder that **the U.S. civilian aerospace program is our program**. It belongs to all U.S. citizens. They have a vested interest and many citizens have a desire to be included in the planning and dreaming that set the course for our space endeavors. Many U.S. citizens desire to be kept apprised of the progress and successes of our space program. They want to have a sense of ownership, inclusion, and participation. NASA personnel need to be conscious of this desire felt by many citizens and be eager to accommodate. NASA personnel need to actively combat any “us versus them” interpretation of the relationship between NASA and the general public.

**The second message** that needs to be communicated effectively to the public is that **our NASA investment is a bargain**. Much of the public is poorly informed of the cost of NASA or the relative size of the NASA budget. Many find it difficult to relate to amounts expressed in millions, billions, or trillions of dollars - they are all just huge numbers. They also have a blurry misinterpretation of the costs of our civilian space program *vis a vis* our military space ventures. The majority of the public lacks a good grasp of the relative portion of the federal budget that is the NASA budget. They deserve to be informed that the 13.8 billion dollar NASA budget is about eight-tenths of one percent of the 1.6 trillion dollar federal budget. Stated another way, each U.S. citizen is investing approximately **fourteen cents per day to operate our civilian space program**, out of the \$16.84 per day for all our government programs. More alarmingly, each U.S. citizen paid out \$3.43 per day in interest payment on the national debt in fiscal year 1995. (or the equivalent of 24 NASA budgets, as some would express it, shoveled down the proverbial rat hole!). The total interest payment was 332 billion dollars (nearly a thousand million dollars per day!). That number must be weighed against the 13.8 billion dollars spent on NASA this year.

The other side of the ledger sheet for consideration of the “cost” of NASA is the dollar value of the “spin-offs” and space technology derivative products and techniques which have brought direct benefit to our national economy and to the health and safety of our population. Examples of space program “spin-offs” will be presented later in this report.

**The third message** that begs to be related is that the **scientific research and technology** development in which NASA has been engaged and has supported for years **is good for us** and our national economy. **We need more of it, not less!** Independent econometric studies by groups such as the Midwest Research Institute and the Chase Econometric Associates reveal that, over time, **each dollar** invested in scientific research and technology, such as that conducted by NASA, **injects seven dollars** back into the national economy. The federal taxes alone on the seven dollars more than pay back the original dollar invested!

More and more modern economists are tuning in to the realization that the development of new technologies and new ideas spawned by those new technologies sets the pattern for long-range growth in a nation’s economy. For example, Paul Romer, economics professor at Berkeley, Visiting Fellow of the Hoover Institution, and the Royal Bank Fellow of the Canadian Institute for Advanced Research is regarded by many as an economist who is “turning economics upside down” and is on a certain road to a Nobel Prize in economics as a leading spokesman for the “**New Growth Theory**” of economics.

Romer’s New Growth Theory asserts that economic growth depends largely upon technology, in addition to the traditionally accepted components of capital and labor. He regards technology as being endogenous, or an internal part, in an economic system. This contrasts with traditional economists’ views that technology is external, outside of the economic system, something that happens so randomly as to be considered merely serendipitous. Romer asserts in compelling



fashion that long-term economic growth is driven by new ideas. The new ideas derive from investments in scientific research, discovery, and technology. Thus the declaration relating to the science and technology of our space program, we need more of it, not less!

## NASA AMBASSADORS

An idea, which is now being referred to as "NASA AMBASSADORS", grew out of a voluntary effort put forth by several persons who participated in the MSFC summer educational programs. NASA Ambassadors will be persons selected from the various summer educational programs who will accept responsibility for making public presentations of pre-packaged talks, fully supported by visual materials, to audiences near their home institutions. The pre-packaged talks have been prepared by the group of volunteers during the summer of 1996. It is planned that more talks will be contributed during successive summers by other volunteers. The talks range in subject matter from general discussions of NASA contributions to society to specific areas of research being conducted in the laboratories at MSFC. A total of eight presentations were developed during the summer of 1996, with the author responsible for two.

In the NASA AMBASSADOR agreement, NASA agrees to provide the presentation package, including both photographic slides and written explanatory material to accompany the slides. NASA undertakes to keep the talks updated and to notify the users of each package when new material to support the presentation is available. NASA also assures that a knowledgeable NASA scientist or engineer can be contacted if the NASA AMBASSADOR has any questions about the material in the packages. NASA will offer some type of appropriate recognition for outstanding performance by NASA AMBASSADORS.

NASA AMBASSADORS agree to give at least two presentations per year of each presentation package received. They also coordinate with the Office of Public Affairs at MSFC to report information regarding presentations, audiences, responses, *etc.*

The presentations developed during the summer of 1996 include the following topics:

1. **"Rocket Ships"** - The history of propulsion and NASA's planned new propulsion systems.
2. **"Spacecraft Charging"** - A discussion of the phenomenon of electrostatic charging of orbiting spacecraft, spurious results caused by the charging, and attempts to solve the problem.
3. **"Mars in Fact and Fiction"** - A treatment of the science fiction and the science related to our neighboring planet.
4. **"NASA - The Place Where Miracles Happen"** - A discussion of the spin-off benefits that have evolved from our space program.
5. **"To Lead, or Not to Lead, That is the Question!"** - A validation of the scientific research and technological development engaged in by NASA and its value to our nation.
6. **"Extending Our Senses Beyond Our Reach"** - A discussion of the great Orbiting Space Observatories, with emphasis on the development and utilization of the Hubble Space Telescope.
7. **"Protein Crystal Growth"** - A talk illustrating the marvelous science that is being done on the near-perfect protein crystals grown in the microgravity environment of the orbiting shuttle and its value to mankind.
8. **"The Blue Planet"** - A talk on NASA's initiative of directing its satellite and communications technology expertise toward the study the resources, environment, and weather patterns of our own planet.

## TECHNOLOGY TRANSFER RESEARCH RESULTS

Some of the most interesting time spent during the summer was devoted to verifying or corroborating information about various space program developments and spin-offs which seemed to have varying degrees of documentation supporting them. It was especially gratifying to discover links to products and services that have become integrated into our society's usage to the extent that we often are not even aware of the relationship of its development from space technology. A couple of particularly striking examples will be presented. Another exciting discovery was an example of the present-day development of a valuable technology now in the process of emerging because of a collaboration between a far-sighted MSFC scientist and a private contractor.

A link that was definitely corroborated by this research is the contribution of NASA technology to the compact disk industry. It began when NASA anticipated sending its space probes out into the solar system to photograph and send the photographic images back to earth. A NASA scientist at the Jet Propulsion Laboratory (JPL), G. Solomon, and professor I.S. Reed collaborated to develop a method for digitally encoding the image information for telemetering to earth where it was then decoded to produce the photographs. Their invention came to be known as "Reed-Solomon Coding". The code has the distinction of a clever error-correction capability. In 1982, some twenty-two years after its invention, the Reed-Solomon technique became the industry standard for the encoding of audio information on compact disks, thus launching the ubiquitous compact disk revolution throughout the world which continues today. Thus does a multi-billion dollar industry owe its flourishing existence largely to the contributions made by our space program.

One more example of an exciting development from our space program which represents a major boon to the maintenance of our nation's health is a new, advanced breast biopsy imaging system. It owes its availability to the technology created for one of NASA's more notable "failures". The reference here is to the Hubble Space Telescope (HST), initially greeted with some levels of scorn and derision after its launch, as it was learned that it suffered a little from a "vision" problem - a vision problem which was soon corrected on a subsequent mission. Admittedly, the American public invested quite a large sum of money (more than two billion dollars) into the planning and creation of this truly remarkable instrument. This is proving to be one of the wisest investments ever made into a reputed "failure". Oh, that all our failures could be of this magnitude.

A special device, known as a Charge-Coupled Device, or CCD for short, was designed to capture in a digital manner the images viewed by the HST. This was an especially high resolution imaging system that permitted the HST to send back the examples of breath-taking images of our Universe which we would never have had the opportunity to view otherwise. The CCD imaging system has "spun off" into the development, by the Lorad Corporation, of the Advanced Breast Imaging Biopsy System.

The new system permits the imaging and precise locating of very tiny tumors which can be immediately subjected to a biopsy examination by the insertion of a needle. The new technique, still in its infancy of application, allows the procedure to be conducted in a physician's office with the patient under local anesthesia. It requires little time, causes little scarring, pain, and trauma, and the healing from the biopsy is almost immediate. The procedure costs about \$850. That is to be contrasted with the traditional biopsy procedure which requires days of hospitalization, an invasive surgical removal of the biopsy sample with the concomitant pain, trauma, and healing time requirement, and a typical cost in the \$4000 range.

Different estimates found by this author of the number of breast biopsy procedures conducted in this country range from 500,000 to 800,000 per year, with some ninety percent of them candidates for the new, advanced HST-technology-derived system. A simple mathematical calculation with

the preceding data quickly reveals that the potential **savings** for our nation's **health costs** from the full implementation of this single spin-off is approximately **1.5 billion dollars per year!** That means, therefore, that the entire amount our nation has invested in the Hubble Space Telescope "failure" can be **recouped in less than two years** from this one space program spin-off. It is evidence such the two preceding examples which serve to convince that our space program investment is a wise investment and should be continued, even accelerated.

The example of the emerging technology happening currently is resulting from a "marriage" between the valuable protein crystal research being conducted by Dr. Dan Carter in his MSFC laboratory and a new x-ray focusing device created by a NASA contractor, Dr. Walter Gibson. The new x-ray focusing technology reduces the time required for establishing the molecular structure of important protein crystals, brought back to the laboratory after being grown in a microgravity environment aboard the shuttle, by approximately two orders of magnitude **from a nominal two weeks to a mere two hours!** The immediate and obvious benefit is that it speeds up Dr. Carter's research into determining the causes and possible cures of one of the world's deadliest killer diseases, schistosomiasis. The other huge benefit to society will come because the applications of the x-ray focusing technique will find immediate application in every corner of this nation's medical community where x-ray machines are operated for diagnostic and therapeutic purposes. The author predicts that this technology is destined to provide a major advancement in the usefulness and application of x-rays in the medical arts.

## ACKNOWLEDGMENTS

This has been a truly invigorating, challenging, and inspiring summer of research at the Marshall Space Flight Center. It has been made so by the hospitality and genteel graciousness of many people. I begin by thanking my NASA colleague, Mr. Ed Medal, and Director of the Public Affairs Office, Mr. John Taylor, for the privilege I have enjoyed of working with them and so many other persons in the MSFC Public Affairs Office. They have been the most gracious of hosts and supporters of the work I have attempted. My special thanks go to Ms. Jerry Ann Ise, Ms. Lynne Lowery, and Ms. Judi Hollingsworth for helping me get "set up" at the beginning of the summer and acclimated to working with the many wonderful people I have come to appreciate in the Public Affairs Office. I was given total freedom to roam, to explore, to discuss ideas, and to reap all the benefits of being present at a NASA center with its nearly unlimited possibilities for learning. I owe sincere thanks to Ms. Angela Storey who rescued me on more than one occasion by submitting rush requests on my behalf for photographic services needed to support presentations I was preparing. To Ms. Icle Blankenship, we need to get a patent on your smile and your pleasant and helpful disposition.

I thank Paul Smeyak, another Summer Faculty Fellow working in the Public Affairs area, for his thoughtful criticisms and suggestions relating to talks I was preparing, but most of all for his friendship. I had the experience of sharing desk space in a large office with the most delightful group of people I have ever worked around. My sincere thanks go to Joy Carter, Peter Cobun, Kelly McFalls, Dianna Sheram, and Tony Jacob. You made it all fun.

Finally, I thank NASA, the American Society for Engineering Education (ASEE), the Marshall Space Flight Center, and the University of Alabama for making such an outstanding summer research opportunity available. The leadership of Dr. Mike Freeman and Dr. Frank Six in coordinating the summer programs and the able work done by Ms. Debbie Ott in support of the programs is of the highest caliber and could not be improved upon. You all set a standard by which all other programs should be measured.

**1996**  
**NASA/ASE SUMMER FACULTY FELLOWSHIP PROGRAM**

**MARSHALL SPACE FLIGHT CENTER**  
**THE UNIVERSITY OF ALABAMA**

**COOLING DUCT ANALYSIS FOR TRANSPIRATION/FILM COOLED LIQUID  
PROPELLANT ROCKET ENGINES**

Prepared by:	Gerald J. Micklow, Ph.D.
Academic Rank:	Assistant Professor
Institution and Department:	The University of Alabama Department of Mechanical Engineering

NASA/MSFC:

Laboratory:	Propulsion Laboratory
Division:	Propulsion Systems
Branch:	Combustion Devices and Propulsion Design

MSFC Colleague:	Charles Cornelius, Ph.D.
-----------------	--------------------------



## Introduction

The development of a low cost space transportation system requires that the propulsion system be reusable, have long life, with good performance and use low cost propellants. Improved performance can be achieved by operating the engine at higher pressure and temperature levels than previous designs. Increasing the chamber pressure and temperature, however, will increase wall heating rates. This necessitates the need for active cooling methods such as film cooling or transpiration cooling. But active cooling can reduce the net thrust of the engine and add considerably to the design complexity. Recently, a metal drawing process has been patented where it is possible to fabricate plates with very small holes with high uniformity with a closely specified porosity. Such a metal plate could be used for an inexpensive transpiration/film cooled liner to meet the demands of advanced reusable rocket engines, if coolant mass flow rates could be controlled to satisfy wall cooling requirements and performance. The present study investigates the possibility of controlling the coolant mass flow rate through the porous material by simple non-active fluid dynamic means. The coolant will be supplied to the porous material by series of constant geometry slots machined on the exterior of the engine.

## Numerical Analysis

First, the flow through the rectangular slot on the exterior of the engine will be discussed. The flow was assumed to be one dimensional and adiabatic in a constant area duct with friction. Starting with a differential control volume with a constant area cross-section, the equation for the conservation of mass is as follows:

$$\rho V = (\rho + d\rho)(V + dV) \quad (1)$$

where  $\rho$  is the density and  $V$  is the velocity. Neglecting higher order terms gives;

$$Vd\rho = -\rho dV \quad (2)$$

From conservation of energy the following equation is obtained;

$$h + \frac{V^2}{2} = h + dh + \frac{(V + dV)^2}{2} \quad (3)$$

where  $h$  is the enthalpy. Neglecting higher order terms gives;

$$VdV = -dh \quad (4)$$

With the continuity equation given by eq (2), this expression becomes;

$$VdV = -dh = -V^2 \frac{d\rho}{\rho} \quad (5)$$

Now to investigate the linear momentum equation. From a summation of forces on the control volume the following expression results;

$$pA - \tau_w A_{wet} - (p + dp)A = \dot{m}(V + dV - V)$$

or

$$\tau_w A_{wet} - dpA = \dot{m}dV \quad (6)$$

where  $\tau_w$  is the wall shear stress, A is the duct cross-section area, p is the pressure and  $\dot{m}$  is the mass flow rate. Now the wall shear stress can be expressed as;

$$\tau_w = \frac{f\rho V^2}{8} \quad (7)$$

where f is the Darcy friction factor. Combining eqs (6) and (7) gives the following;

$$-dp = \frac{f\rho V^2 A_{wet}}{8A} + \frac{\dot{m}}{A}dV \quad (8)$$

The wetted duct area can be expressed as;

$$A_{wet} = P_w dx \quad (9)$$

where  $P_w$  is the wetted perimeter of the duct. Defining the hydraulic diameter as;

$$D_H = \frac{4A}{P_w} \quad (10)$$

and substituting this expression along with eq (9) into eq (8) gives;

$$-dp = \left( \frac{f\rho V^2}{2D_H} \right) dx + \rho V dV \quad (11)$$

For a rectangular cross-section the hydraulic diameter is given by

$$D_H = \frac{2bH}{b + H} \quad (12)$$

where b is the slot base dimension and H is the slot height. For the circular duct the hydraulic diameter is the duct diameter.

Equations (2), (5), and (11) represent a set of equations which can be used to describe the flow field. Two issues must be addressed however. First, the thermodynamic

properties of the working fluid are required. For the current problem, the coolant fluid is liquid hydrogen and a computer program was developed to produce the thermodynamic properties. Second, the problem is non-linear, therefore an iterative solution is required to obtain the flow field where the coefficients are lagged to linearize the problem. A space marching technique will be utilized for the solution.

The solution technique is as follows:

1. The inlet mass flow rate, pressure and temperature, along with the slot dimensions are specified.
2. The inlet thermodynamic properties, velocity, Reynolds number and friction factor are calculated.
3. The change in velocity at the first section is guessed.
4. From the continuity equation, eq (2), the density change is calculated based on the guessed velocity change.
5. The average density for the control volume is calculated.
6. The momentum equation, eq (11), is used to calculate the pressure.
7. The energy equation, eq (4) is used to update the enthalpy.
8. Based on the updated pressure and enthalpy, the thermodynamic property subroutine is used to update the density.
9. The relative change in the pressure is calculated and if below a specified tolerance the thermodynamic properties are updated and the calculation proceeds to the next axial location where the procedure is repeated. If the relative change in the pressure is not below the specified tolerance, steps 3-9 are repeated.

For the cooling flow through the constant diameter circular ducts into the engine gas path, a similar analysis is performed. However, the upstream and downstream boundary conditions are changed. Rather than specify the inlet mass flow rate and calculate the exit pressure, as in the rectangular exterior slot, the inlet pressure is specified from the rectangular slot flow field calculation and the inlet velocity is guessed. The calculation procedure previously discussed is implemented and the exit pressure into the engine gas path is calculated. This pressure must match the pressure at the appropriate location in the engine gas path. If it does not, the inlet velocity is changed and the calculation is repeated. This is continued until the pressure at the circular duct exit matches the pressure in the engine gas path within a specified tolerance. At this point the cooling mass flow rate through the circular duct is calculated.

## Results

First, the engine external slot to transport the liquid hydrogen to various engine gas path locations was analyzed. Figure 1 gives the resulting slot pressure distribution for various rectangular slot height/width ratios. It is clearly seen that as the slot width/height ratio or aspect ratio is increased for the same slot width that the pressure drop in the duct increases. This will have a marked effect on the coolant mass flow rate in the engine gas path through the porous wall liner. Figures 2-4 give the circular hole velocity distribution



for the porous wall liner for various hole diameters at a mid-combustion chamber location. The inlet boundary condition for the hole is the pressure set by the exterior rectangular duct location. The exit boundary condition is the pressure set by the engine gas path. It is clearly seen that for a specified hole diameter that as the rectangular slot aspect ratio increases, the velocity magnitude in the circular hole decreases. This will have a marked effect on the coolant mass flow rate into the engine gas path. Further, from figures 2-4 it is seen that as the hole diameter is increased for a set exterior slot aspect ratio that the duct velocity increases. Increased duct velocity along with increased flow cross-sectional area, caused significant increases of coolant mass flow rate into the gas path.

Figures 5- 7 give the circular hole velocity distributions as a function of exterior slot aspect ratio for various hole diameters at the nozzle throat location. As before, increasing slot aspect ratio decreased the velocity in the circular hole, while increasing hole diameter increased the hole velocity. Further, the velocity magnitude has increased in comparison to the similar geometry for the combustion chamber location. Similar trends were observed for other downstream gas path locations.

## **Conclusions and Recommendations**

For the exterior rectangular slot, the duct pressure drop increased as the slot aspect increased. As slot aspect ratio is increased, the duct surface area/cross-section area increases causing the effect of wall friction on the flow to increase. This results in a higher pressure drop due to friction. For the circular holes in the porous wall liner providing the coolant passage from the rectangular exterior slot to engine gas path, the exterior slot aspect ratio had a marked effect on the magnitude of the hole velocity distribution. As the rectangular slot aspect ratio is increased the duct pressure drops. Therefore, for a fixed engine gas path location which fixes the circular hole exit pressure, increasing slot aspect ratio will decrease the hole inlet pressure. Decreasing the inlet pressure for a fixed exit pressure will decrease the inlet velocity and therefore the coolant mass flow rate. Increasing the hole diameter increases flow cross sectional area and for a fixed exterior duct aspect ratio increased the circular hole inlet velocity. This results in a substantial increase in the coolant mass flow rate since for fixed inlet density, both the velocity and flow area increased. The reason for the increased duct velocity is due to the decreased wall surface area/flow cross-sectional area which reduces the effects of friction and a larger percentage of the hole pressure drop(which is fixed) can be associated with a velocity increase.

It is seen that the coolant passage geometry, i.e. exterior duct aspect ratio and porous wall circular hole diameter can result in a large variation of the coolant mass flow rate. Therefore, proper selection of the wall coolant circuit geometry could result in an inexpensive and effective wall cooling scheme for a re-usable launch vehicle engine. To obtain the correct coolant passage geometry, a detailed computational study is required to define the cooling requirements and assess the effect of coolant injection on overall engine performance. This will require the solution of the three-dimensional compressible turbulent Navier-Stokes equations with combustion to define the interaction between the coolant flow the the main engine gas path.

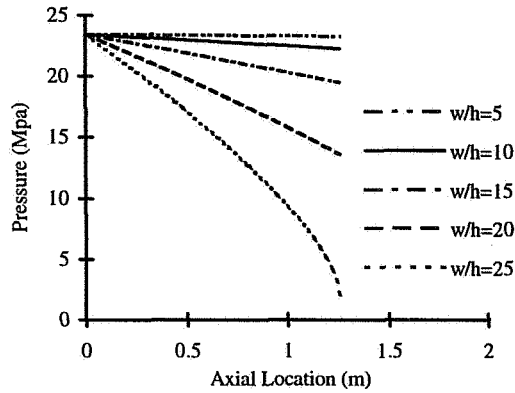


Figure 1 Rectangular Slot Pressure

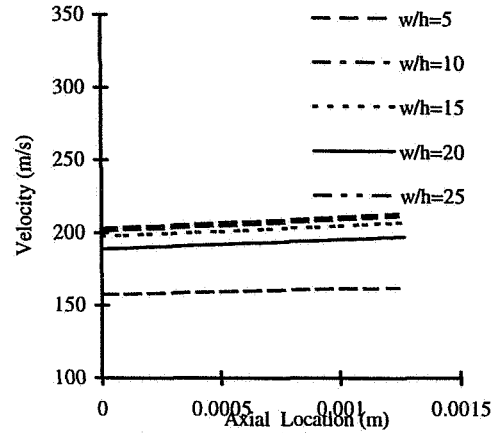


Figure 2 Velocity Distribution - 30 micron Hole

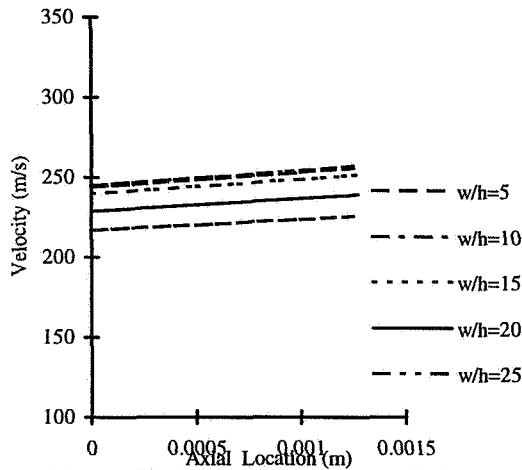


Figure 3 Velocity Distribution - 40 micron Hole

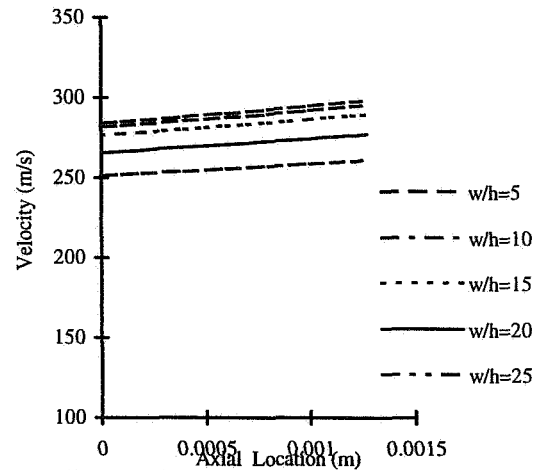


Figure 4 Velocity Distribution - 50 micron Hole

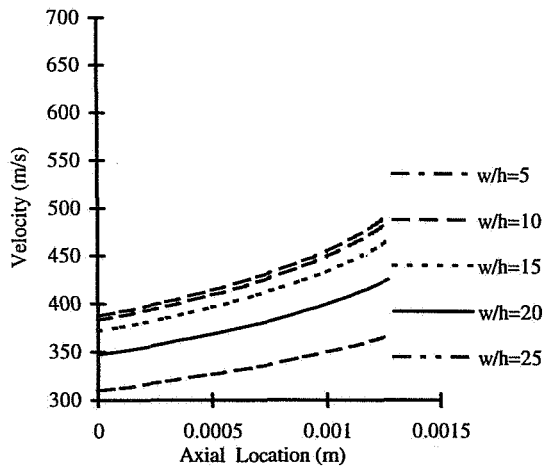


Figure 5 Velocity Distribution - 30 micron Hole

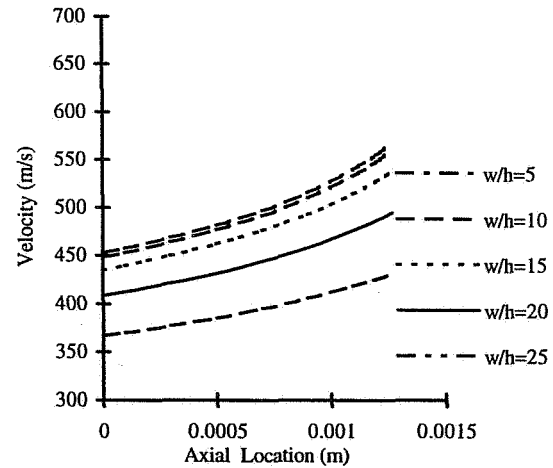


Figure 6 Velocity Distribution - 40 micron Hole

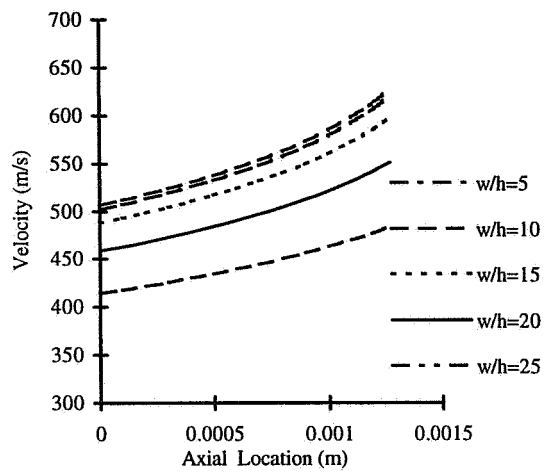


Figure 7 Velocity Distribution - 50 micron Hole

**1996**  
**NASA/ASEE SUMMER FACULTY FELLOWSHIP PROGRAM**

**MARSHALL SPACE FLIGHT CENTER**  
**THE UNIVERSITY OF ALABAMA**

**RELATIONSHIP BETWEEN EQUILIBRIUM FORMS OF LYSOZYME**  
**CRYSTALS AND PRECIPITANT ANIONS**

Prepared By: Arunan Nadarajah  
Academic Rank: Assistant Professor  
Institution and Department: University of Alabama in Huntsville  
Chemical and Materials Engineering

NASA/MSFC:

Laboratory: Space Science Laboratory



## Description

Molecular forces, such as electrostatic, hydrophobic, van der Waals and steric forces, are known to be important in determining protein interactions. These forces are affected by the solution conditions and changing the pH, temperature or the ionic strength of the solution can sharply affect protein interactions. Several investigations of protein crystallization have shown that this process is also strongly dependent on solution conditions. As the ionic strength of the solution is increased, the initially soluble protein may either crystallize or form an amorphous precipitate at high ionic strengths [1]. Studies done on the model protein hen egg white lysozyme have shown that different crystal forms can be easily and reproducibly obtained, depending primarily on the anion used to desolubilize the protein [2-4].

More recent systematic investigations of the effect of various salt ions on the solubility of lysozyme also showed that the more chaotropic anions were more effective in crystallizing lysozyme [5-7]. Thus, the more chaotropic thiocyanate ion was shown to be far more effective in crystallizing lysozyme than the less chaotropic chloride ion. There also seems to be a correlation between the crystal form obtained and the relative chaotropicity of the solution resulting from the anion used for lysozyme crystallization. The less chaotropic anions, such as chloride, bromide, sulfate, phosphate and acetate produced tetragonal crystals. The more chaotropic iodide, thiocyanate and organic anions produced monoclinic crystals [3,5]. Alcohols, which are also known to be chaotropic agents, can crystallize proteins with methyl pentane diol being a widely used crystallizing agent [8]. Propanol produces monoclinic crystals of lysozyme [9]. These results suggest that decreasing the hydrophobic force with chaotropic agents promotes protein crystallization and may also contribute to the appearance of multiple crystal forms for a protein.

Although these and other results have shown the effect of electrostatic and hydrophobic forces in protein crystallization, attempts at explaining their role in the process have been less successful. The traditional explanation used for the desolubilization of proteins is the salting-out effect [10]. In this theory the solvent ions are assumed to strip water molecules from the hydration layer surrounding the protein, with protein aggregation and desolubilization following due to hydrophobic attraction. The effectiveness of ions for this process is supposed to follow the Hofmeister series, with the less chaotropic ions being more effective in desolubilizing the protein. Colloidal aggregation has also been suggested as the mechanism for protein crystallization [11-13]. Riès-Kautt and Ducruix [6] proposed an "ion-pairing" argument, whereby counterion binding was assumed to neutralize the charged protein molecule after which aggregation leading to crystallization may take place due to the hydrophobic interactions. Thus, all proposed explanations to date have been based on hydrophobicity-driven mechanisms. However, as discussed above,

lysozyme crystallization follows the *reverse* of the Hofmeister series, with *decreases* in the hydrophobic attraction by chaotropic agents *promoting* crystallization. Consequently, it seems unlikely that crystallization proceeds by hydrophobicity-driven mechanisms.

Another difficulty is in quantifying the effect of anions on the solution. So far chaotropicity of anions has only been measured indirectly, by their effect on the desolubilization of proteins (Melander & Horvath). However, in recent years fluorescence spectroscopy has emerged as a sensitive technique for monitoring such molecular processes. Several fluorescent probes that are sensitive to the hydrophobicity/hydrophilicity of aqueous environments are now available. One such probe pyranine (8-hydroxy-1,3,6-pyrenetrisulfonate) has been successfully employed to follow the structure of water as the concentration of sucrose is increased from zero to the saturation point and beyond [14,15]. The increasing sucrose concentration was shown to progressively disrupt the bulk water networks in this manner.

In this study we employ pyranine to probe the effect of various anions on the water structure. Additionally, lysozyme crystallization was carried out at these conditions and the crystal form was determined by X-ray crystallography. The goal of the study was to understand the physico-chemical basis for the effect of changing the anion concentration on the equilibrium form of lysozyme crystals. It will also verify the hypothesis that the anions, by altering the bulk water structure in the crystallizing solutions, alter the surface energy of the between the crystal faces and the solution and, consequently, the equilibrium form of the crystals [16].

## References

- [1] W.W. Wilson, *Methods: A Companion to Methods in Enzymology*, **1**, p110 (1990).
- [2] G. Alderton and H.L. Fevold, *J. Biol. Chem.*, **164**, p1 (1946).
- [3] L.K. Steinrauf, *Acta Cryst.*, **12**, p77 (1959).
- [4] G.S.D. King, *Acta Cryst.*, **12**, p216 (1959).
- [5] M.M. Ries-Kautt and A.F. Ducruix, *J. Biol. Chem.*, **264**, p745 (1989).
- [6] M.M. Ries-Kautt and A.F. Ducruix, *J. Crystal Growth*, **110**, p20 (1991).
- [7] M.L. Pusey and S. Munson, *J. Cryst. Growth*, **113**, p385 (1991).
- [8] A. McPherson, *The Preparation and Analysis of Protein Crystals*, Wiley, New York (1982).
- [9] K. Harata, *Acta Cryst.*, **D50**, p250 (1994).
- [10] W. Melander and C. Horvath, *Arch. Biochem. Biophys.*, **183**, p200 (1977).
- [11] C.C. Young, R.C. DeMattei, R.S. Feigelson and W.A. Tiller, *J. Cryst. Growth*, **90**, p79 (1988).

- [12] Y. Georgalis, A. Zouni, W. Eberstein and W. Saenger, *J. Crystal Growth*, **126**, p245 (1993).
- [13] M.L. Grant and D.A. Saville, *J. Phys. Chem.*, **98**, p10358 (1994).
- [14] R. Chakraborty and K.A. Berglund, *AIChE Symposium Series*, **248**, 113 (1991).
- [15] R. Chakraborty and K.A. Berglund, *J. Crystal Growth*, **125**, p81 (1992).
- [16] M. Kern, in *Morphology of Crystals* (Ed. I. Sunagawa), Terra, Tokyo (1987).



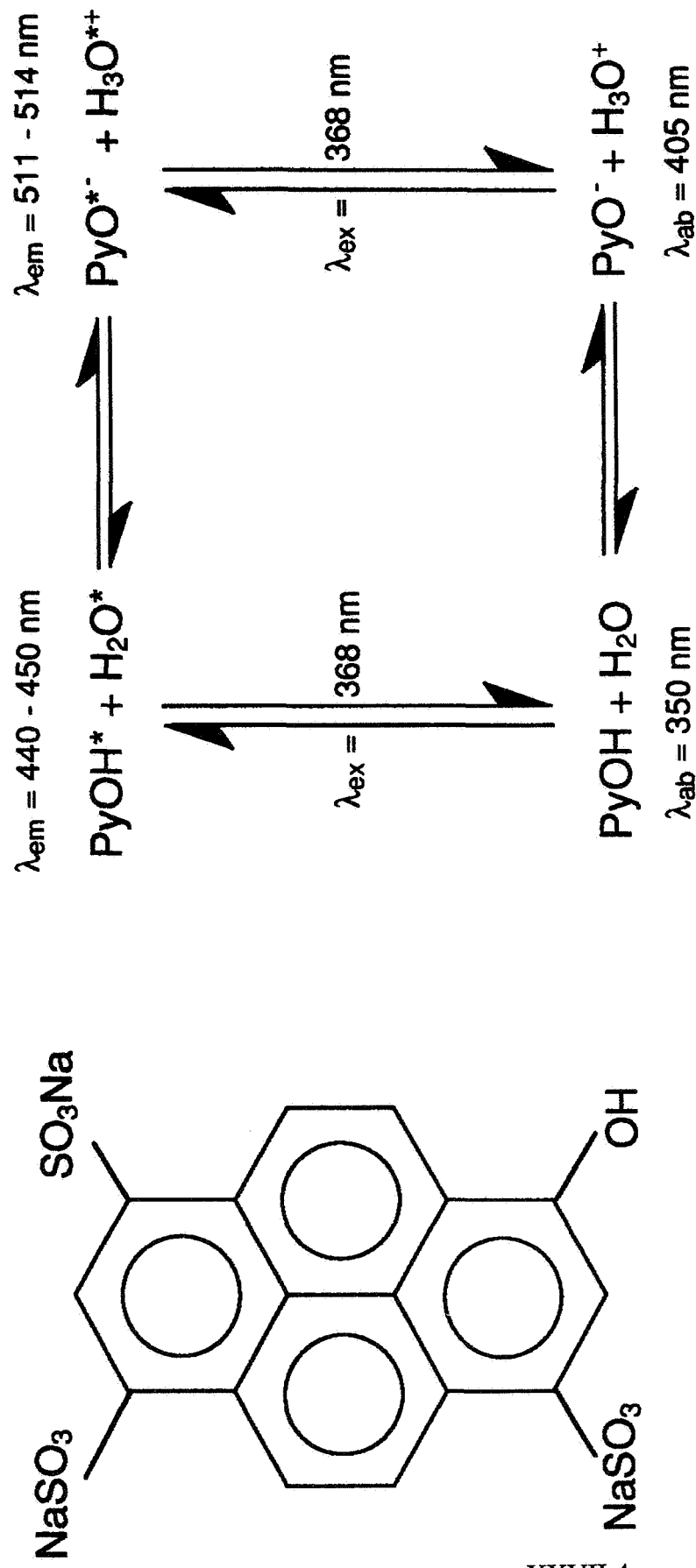


Fig. 1: The structure of Pyranine (8-hydroxy-1,3,6-pyrenetrisulfonate). The hydroxyl group is sensitive to the environment and ionizes only in the presence of bulk water networks that can exchange protons with it. The ionization of this group changes the emission wavelength of the pyrene molecule from 440 nm to 511 nm, and this is a sensitive indicator of the aqueous environment. Excessive amounts of additives to the water causes the prevalence on non-networked water and the pyranine to emit at 440 nm. In networked bulk water the emission is at 511 nm.

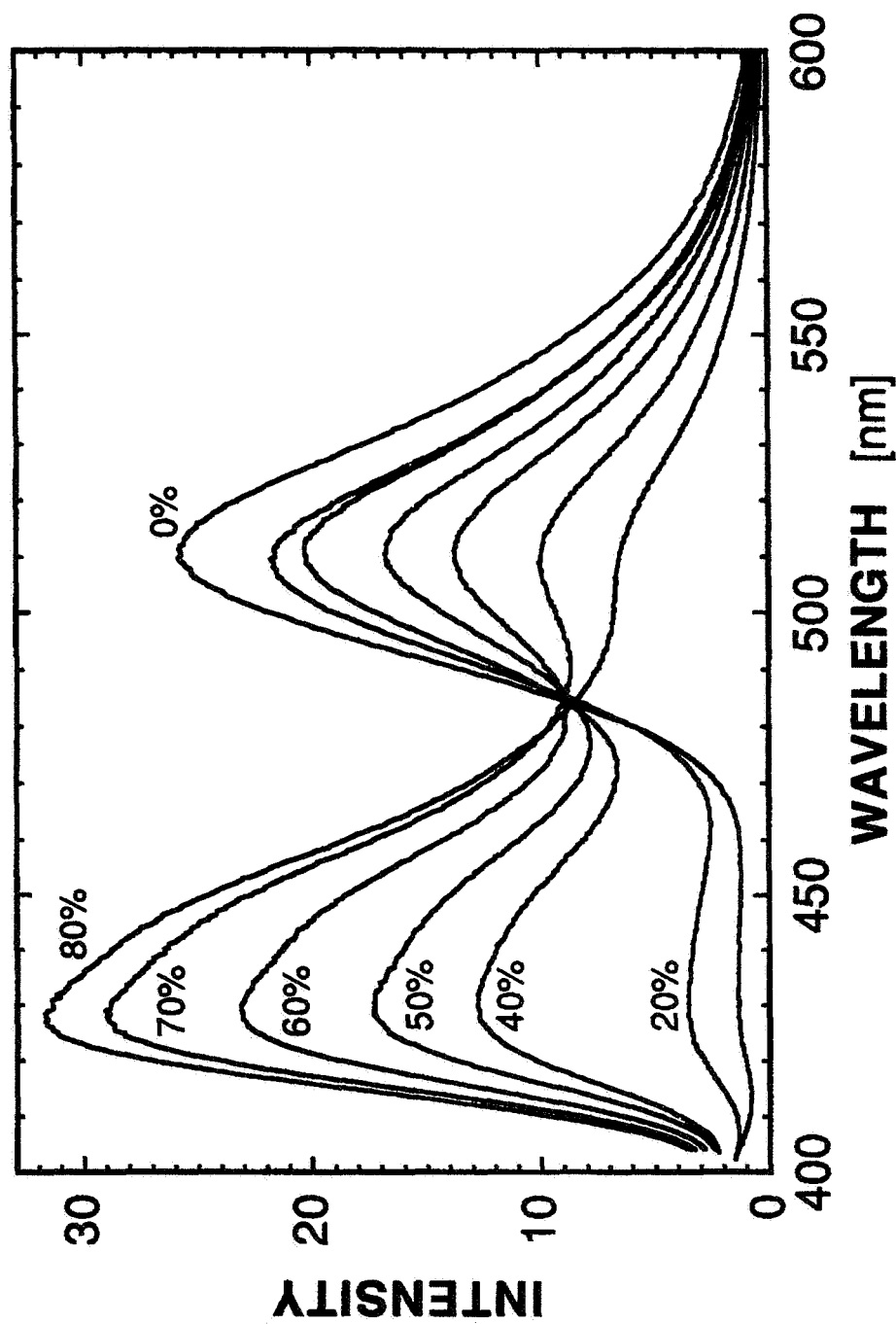


Fig. 2: Fluorescence intensities at various weight percentages of iso-propanol in water. In pure water the pyranine emits almost exclusively at 511 nm. With increasing propanol concentrations the amount of non-networked water and alcohol increases. The amount of pyranine in this phase also increases, resulting in more emission at 440 nm.

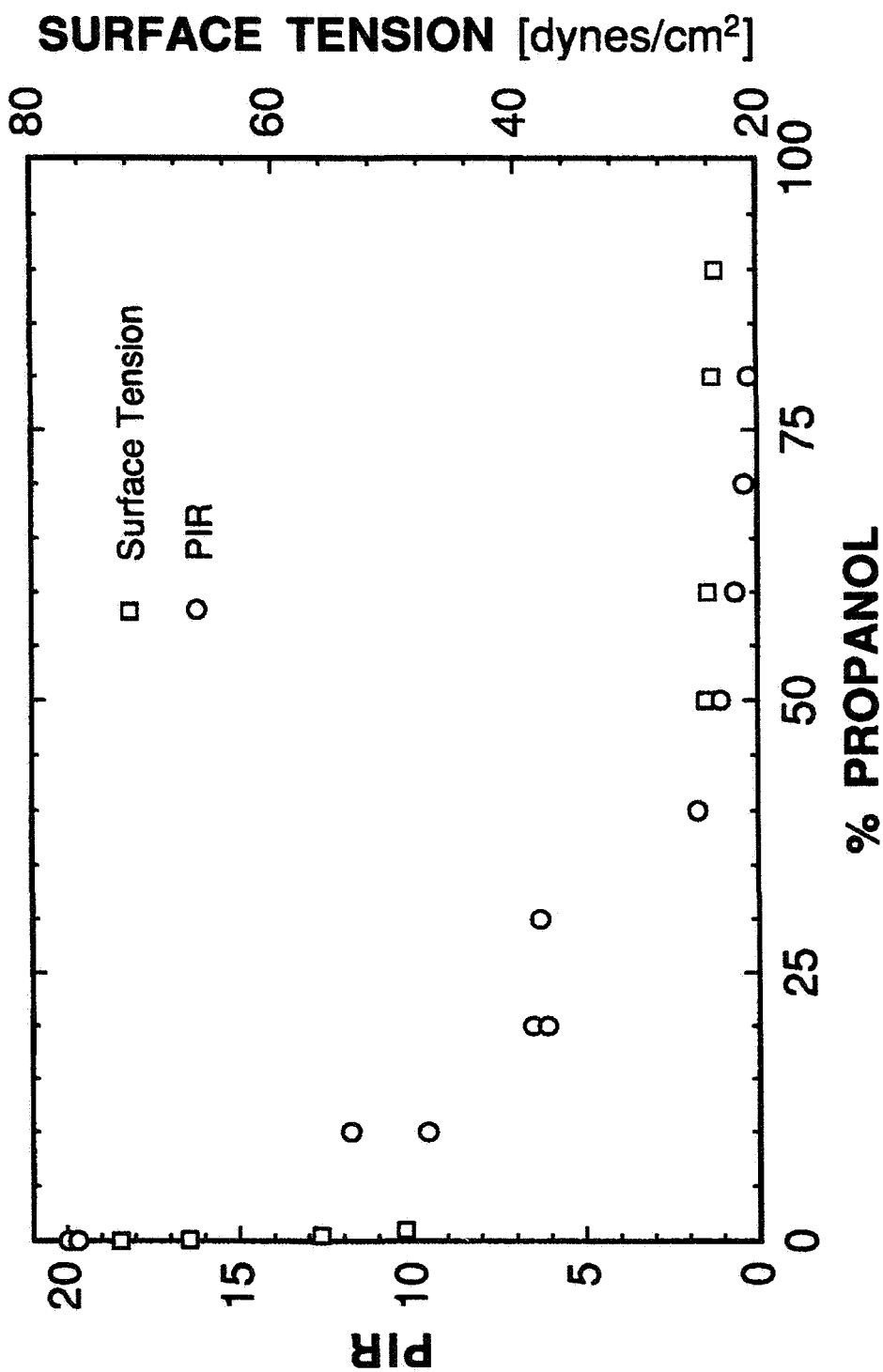


Fig. 3: The peak intensity ratio PIR (ratio of intensity at 511 to that at 440 nm) of pyranine in propanol-water solutions, and the surface tension of the solutions, plotted as a function of propanol concentration. The breakdown of the bulk water networks with increasing propanol concentration is displayed by decreases in the PIR and also results in decreases in the surface tension of the solution.

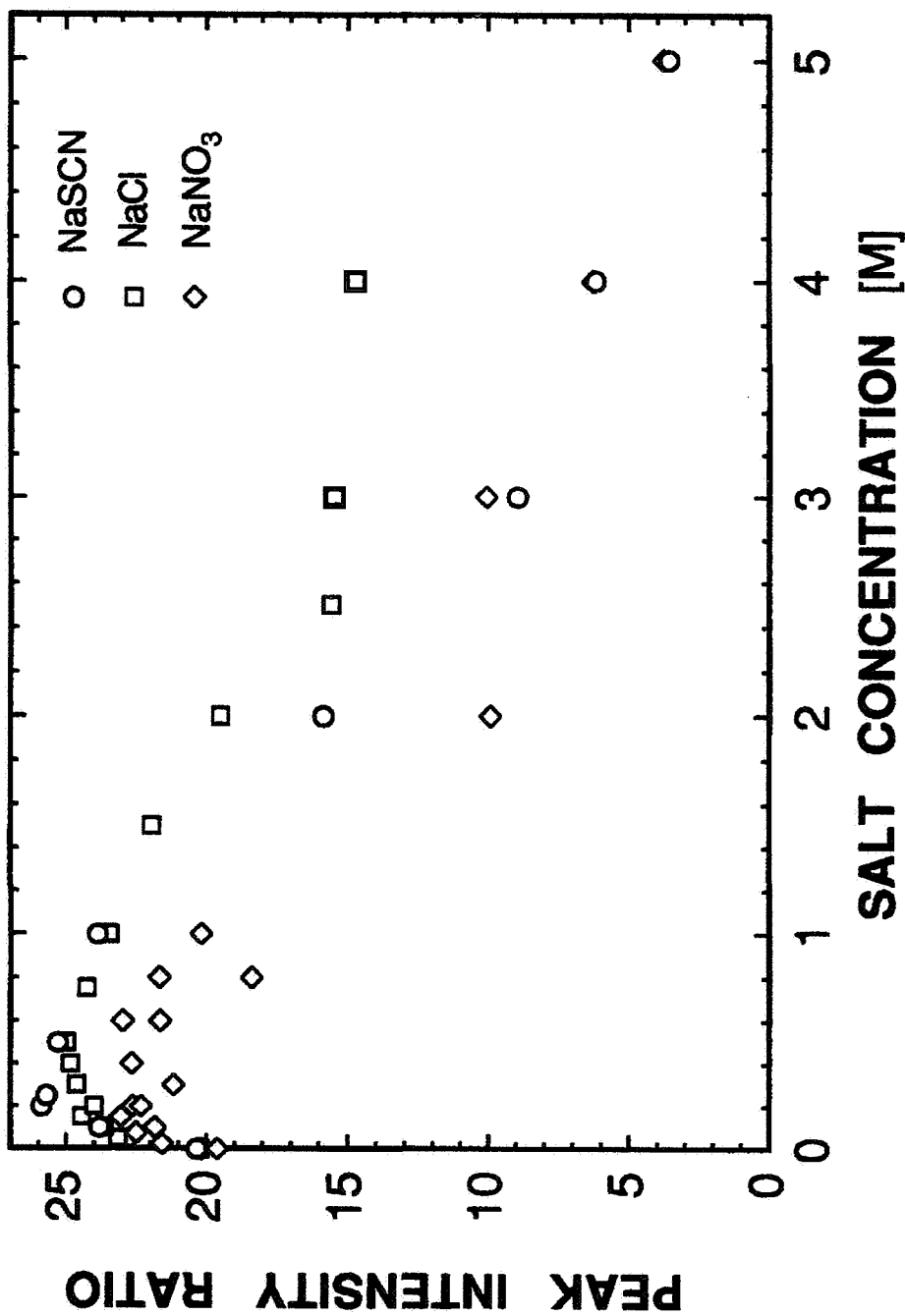


Fig. 4: The PIR values as a function of salt concentration for NaCl, NaNO<sub>3</sub> and NaSCN. Addition of both NaSCN and NaNO<sub>3</sub> results in sharp decreases in the PIR, but addition of NaCl produces comparatively moderate decreases. This is the first direct evidence of the greater chaotropicity of nitrate and thiocyanate ions.

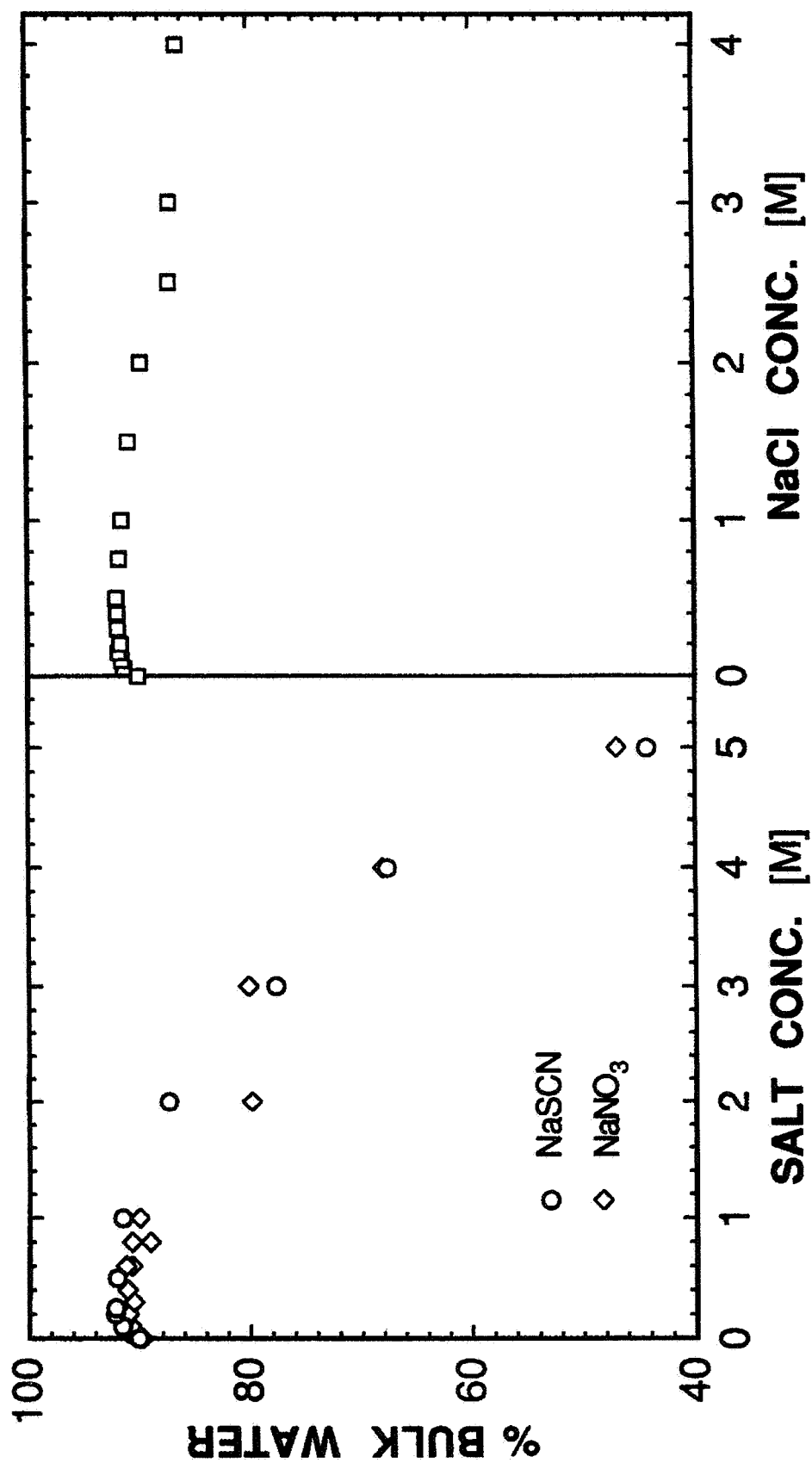


Fig. 5: The fraction of networked bulk water in salt solutions determined from the PIR values of fig. 5 and by assuming a 2:1 distribution of pyranine in networked and non-networked water. The fraction of networked bulk water falls sharply with increasing NaNO<sub>3</sub> and NaSCN concentrations, but is little affected by addition of NaCl.

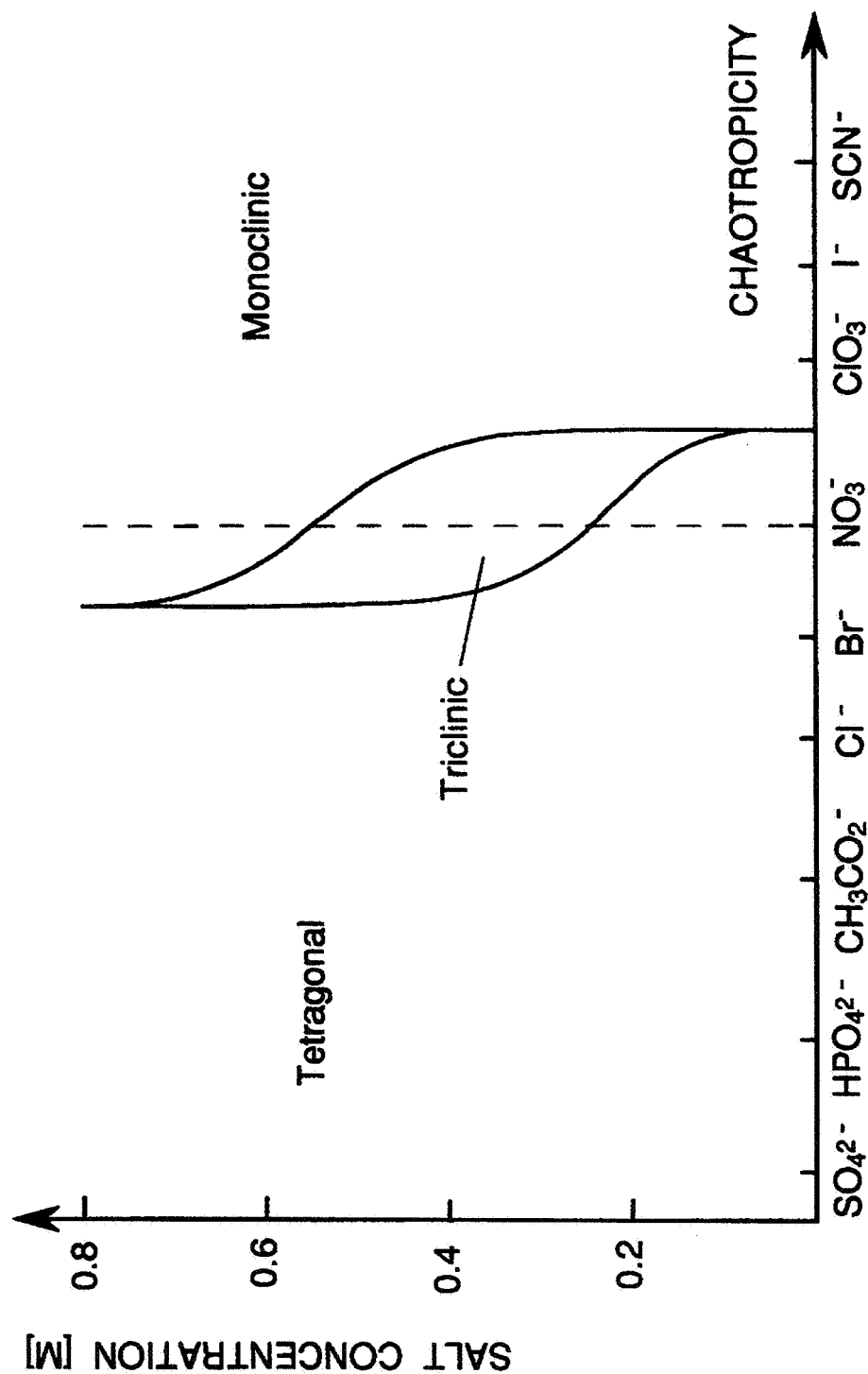


Fig. 6: Suggested phase diagram for the equilibrium forms of lysozyme crystals. (The diagram is incomplete as temperature effects resulting in the formation of orthorhombic crystals have not been included.) It is clear that less disruption of bulk water networks by added salts produces tetragonal crystals and greater disruption monoclinic ones. The triclinic form occupies a small intermediate region and has been seen only with nitrate ions, which also produces the other two forms.



**1996**

**NASA/ASEE SUMMER FACULTY FELLOWSHIP PROGRAM**

**MARSHALL SPACE FLIGHT CENTER  
THE UNIVERSITY OF ALABAMA**

**COMPUTATIONAL MODELING OF MULTI-PHASE/MULTI-SPECIES FLOWS  
WITH APPLICATIONS TO LIQUID ROCKET ENGINES**

Prepared by:	Homayun K. Navaz
Academic Rank:	Assistant Professor
Institution and Department:	GMI Engineering and Management Institute Department of Mechanical Engineering

NASA/MSFC:

Laboratory:	Propulsion Laboratory
Division:	Engine Systems
Branch:	Combustion Physics

MSFC Colleague:	Klaus W. Gross
-----------------	----------------





# COMPUTATIONAL MODELING OF MULTI-PHASE/MULTI-SPECIES FLOWS WITH APPLICATIONS TO LIQUID ROCKET ENGINES

Homayun K. Navaz  
Assistant Professor  
Department of Mechanical Engineering  
GMI Engineering and Management Institute

Propulsion Laboratory  
Engine Systems Division  
Combustion Physics Branch

Klaus W. Gross, MSFC Colleague

Accurate prediction of all physical phenomena in a combustion chamber is essential for better understanding of the system performance. Atomization, evaporation, combustion, chemical kinetics, and turbulence are those processes of great importance that need to be well understood. Processes involving the liquid phase in a combustion chamber will be further complicated under supercritical conditions. More advanced and accurate numerical techniques are required to extend our understanding of the above phenomena. A computer program for multi-species/multi-phase flow was developed for NASA/MSFC in 1992. This code, called Liquid Thrust Chamber Performance (LTCP) program takes an Eulerian-Eulerian approach and is based on the Total Variation Diminishing (TVD) technique with Lax-Friedrichs upwind method. Under the NASA/ASEE SFFP the LTCP code was used to predict the performance characteristics of several engines that were of particular interest to NASA. This code was also successful in a combustion detonation study. Converting the program to the PC platform was accomplished which extends usability and makes it available to a wider range of users. The Eulerian formulation of the liquid phase provides a suitable model that can be extended to include combustion modeling under supercritical conditions. The results have been compared against the ones of other codes and available measured data. The algorithm proved to be robust and efficient for problems with stiff source terms.

## 1.0 INTRODUCTION

Since the inception of Computational Fluid Dynamics (CFD), enormous effort has been directed toward developing an efficient and robust algorithm for stiff systems. In spite of impressive progress in these developments for pure substances, solving the coupled equations for multi-phase systems with stiff interphase interaction and chemical reactions still remains a challenge.

Most CFD solutions for such systems are obtained by ad hoc methods that deviate from the actual problem in hand, either by introducing unfounded assumptions or oversimplifying the governing equations. Some CFD codes separate the species continuity equations from the rest of the conservation equations, which yield an overdamped or

unstable system. To overcome the stability problem, an excessive damping is frequently introduced in the equations which can potentially generate a non-physical solution. Some CFD codes that are designed for two phase flows “minimize” the number of source terms that represent the inter-phase interaction. These terms will cause momentum and energy “spikes” which can trigger instability. Most of the Navier-Stokes (NS) solvers do not have a comprehensive chemical reaction mechanism to allow for the evaporation of fuel and/or oxidizer droplets, which permits them to proceed with the chemical kinetics to generate combustion products. In other words, they assume that the droplets in the gaseous phase immediately react and reach an equilibrium state.

The LTCP code was developed under a NASA/MSFC contract based on the philosophy of “minimizing” the formulation “compromises”. As a consequence all the inter-phase interaction terms are included. The evaporation models and fully-coupled finite rate chemistry permit the proper combustion modeling. The Eulerian approach was selected for the liquid phase to make the code suitable for dense spray combustion simulation.

## 2.0 MATHEMATICAL FORMULATION

The governing equations for the gas and liquid phases are given in Reference (1). Due to their extent and complexity, they will not be repeated here. The species production/destruction terms resulting from chemical reaction and evaporation are all included in the source term. It should be mentioned that in an Eulerian framework a “continuity” equation for the droplet radius change must also be contemplated. Some researchers<sup>2</sup> have chosen to solve the equation for the droplet radius change in a Lagrangian framework to avoid singularities which will be caused by very small droplets.

## 3.0 NUMERICAL MODEL

The conservation equations are linearized with respect to the following vector:

$$\mathbf{Q} = [u, v, T, P_1, P_2, \dots, P_N, k, \epsilon]^T \quad (1)$$

where  $P_N = C_N P$ , with  $P$  being the static pressure, and  $C$ 's are species mass fraction.  $P_N$  is referred to as “pseudo partial pressure”. The significance of using the above vector is in achieving robustness for flows at “all speeds”. That means the solver must be equally efficient for low speed as well as supersonic speed. For the droplet phase this vector has the following form:

$$\mathbf{Q} = [u, v, \rho, R, T]^T \quad (2)$$

The Total Variation Diminishing (TVD)<sup>3,4</sup> method is used to evaluate the fluxes for the left and right states. The Lax-Friedrichs<sup>3,4</sup> (LF) upwind technique is used in combination with TVD. The Steger-Warming<sup>1,4</sup> flux splitting is employed for the droplet phase

equations. The details of the chemistry and evaporation model can be found in Reference (1).

#### 4.0 TEST CASES AND DISCUSSION

Numerous test cases of interest to NASA were considered. From the many studies conducted in our research effort, some selected results for three testcases are presented, and the remaining ones are tabulated in Table 1. More pertaining information can be obtained from Mr. Klaus W. Gross at NASA/MSFC.

Table 1 Test Case Matrix

Test Case	Conditions*
1. Space Shuttle Main Engine (SSME) - Flowfield Variation Analysis - Finite Rate Chemistry with O <sub>2</sub> /H <sub>2</sub> - Striation with O <sub>2</sub> /H <sub>2</sub>	Pc=3000 and 6000 psia, Ideal Gas Pc=3000 psia, Tc=6215 °R, O/F = 6.0 Pc=3000 psia, (O/F) <sub>wall</sub> =4 (1%), (O/F) <sub>core</sub> =6
2. RD0120 Engine, O <sub>2</sub> /H <sub>2</sub>	Pc=3171 psia, Tc=6514 °R, O/F=6
3. 60k Motor, RP-1/O <sub>2</sub> , 8 Species Reaction	Pc=651 psia, Tc=6391 °R, O/F = 2.34
4. Solar Engine, H <sub>2</sub>	Pc=20 psia, Tc=4900 °R
5. Non-Premixed Gas Flow Single Injector with Wall Cooling H <sub>2</sub> /O <sub>2</sub> Combustion 6 Species Reaction	H <sub>2</sub> Stream Conditions: T = 180 °R U = 656 ft/sec At the Wall: T = 540 °R U = 492 ft/sec
6. Premixed Two-Phase Flow Single Injector RP-1/O <sub>2</sub> Combustion 22 Species Reaction	RP-1: T = 300 °R LOX: 180 °R N = 2.5x10 <sup>4</sup> /cc 5x10 <sup>4</sup> /cc U = 50 ft/sec 50 ft/sec D = 100 μm 100 μm
7. Pulsed Detonation Problem O <sub>2</sub> /H <sub>2</sub>	Initially: P=14.7 psia, T=540 °R, O/F=8 Pulse: T=5400 °R

\*Pc and Tc are respectively chamber pressure and temperature, O/F or MR (mixture ratio) the oxidizer/fuel mass flow rate ratios. N is the number density per cubic centimeter, D is the initial droplet diameter

Figures 1 through 4 show the results consisting of temperature and species contours for the testcase 5. It can be seen that hydrogen and oxygen start to react after a short distance downstream of the injector. The flame is concentrated at the hydrogen and oxygen interface. This testcase was selected from Reference 5, where flow measurements and visual data information are available.

Figures 5 through 8 demonstrate the Mach number, Temperature, and some selected species contours for the premixed RP1/LOX testcase No. 6. Both liquids enter the combustion chamber in form of droplets. A total of 22 species were considered for the finite rate chemistry. It appears that after a short distance from the injector face an spontaneous combustion occurs which is attributed to the chemical reactions. Therefore, the temperature rises and due to these rapid changes a pressure wave is generated. One of

the disadvantages of hydrocarbon based fuels are the amount of carbon monoxide that is generated by the combustion process. At fairly "high" mixture ratios ( $>2.0$ ) the possibility of soot production is reduced considerably, therefore, our model did not account for a soot formation mechanism. However, the model is quite capable of such modeling.

Figure 9 shows six time snapshots of the pressure field as a detonation pulse wave propagates in a duct. For this test case a total of six species and eight step chemical reactions were considered. Figure 10 demonstrates the pressure variation as a function of distance along the length of the channel. A peak pressure of about 290 psia was observed. Figure 11 shows the pressure and temperature history on the center of the left wall. Initially, the temperature is suddenly raised to 5400 °R while the pressure is at 14.7 psia. However, after a very short time the pressure starts to rise and at the same time the temperature will increase in an attempt to reach to the adiabatic flame temperature.

## 5.0 CONCLUSION

The results of this research effort demonstrated that the TVD-LF algorithm is robust and efficient in treating problems with stiff source terms. The Eulerian formulation for the droplet phase was suitable for dense spray combustion and the numerical difficulties were overcome by a fully coupled approach and an implicit Steger-Warming algorithm. Further work is necessary to enhance the capabilities of the LTCP code. The "pseudo time accurate" option of the LTCP code for detonation or ignition studies should be upgraded to a "true time accurate" solution. The higher-order terms for computation of the aeroacoustics must be included in the code for better capturing of the primary pressure wave and some of the harmonics. A fourth-order accurate method in space and time, is recommended to perform such studies.

## 6.0 REFERENCES

1. Navaz, H. K. and A. L. Dang, Liquid Thrust Chamber Performance Computer Program, Final Report prepared for NASA/MSFC, 1992.
2. Chiu, H.H. and X.Q. Zhou, GEMCHIP-CODE: Spray Combustion Process in Airbreathing Propulsion Applications, University of Chicago, Ph.D. Thesis, 1983.
3. Yee, H.C., "A Class of High Resolution Explicit and Implicit Shock-Capturing Methods", NASA Technical Memorandum 101088, February, 1989.
4. Dang, A.L., Navaz, H.K., and R.H. Rangel, "Numerical Analysis of Bipropellant Combustion in Liquid Thrust Chambers by an Eulerian-Eulerian Approach", AIAA Paper No. 92-3735, 1992.
5. Mayer, W., Schik, A., Schweitzer, C., and M. Schaffler, "Injection and Mixing Processes in High Pressure LOX/GH<sub>2</sub> Rocket Combustor", AIAA Paper No. 96-2620, 1996.



Temperature °R



Figure 1 Non-Premixed  $\text{GO}_2/\text{GH}_2$  Temperature Contour for Single Element Combustion

$\text{H}_2\text{O}$  Mass Fraction



Figure 3  $\text{H}_2\text{O}$  Mass Fraction Contours for Non-Premixed  $\text{GO}_2/\text{GH}_2$  Single Element Combustion

$\text{H}_2$  Mass Fraction



Figure 2  $\text{H}_2$  Mass Fraction Contours for Non-Premixed  $\text{GO}_2/\text{GH}_2$  for Single Element Combustion

$\text{O}_2$  Mass Fraction



Figure 4  $\text{O}_2$  Mass Fraction Contours for Non-Premixed  $\text{GO}_2/\text{GH}_2$  Single Element Combustion



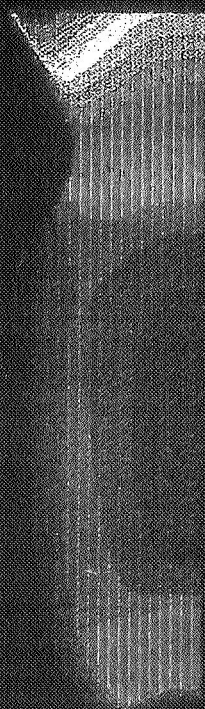


Figure 5. Mach Number Contours for Premixed RP1/LOX with 22 Species

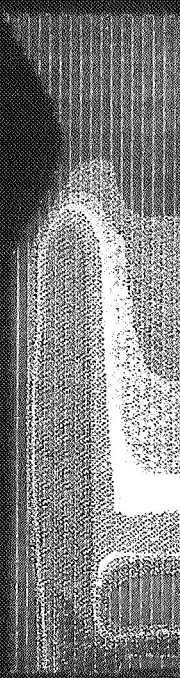


Figure 6. Temperature Contours for Premixed RP1/LOX

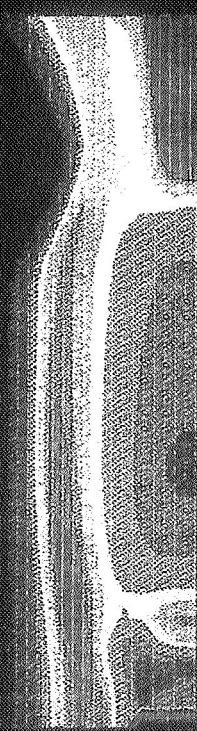


Figure 7. H<sub>2</sub>O Mass Fraction Contours for RP1/LOX

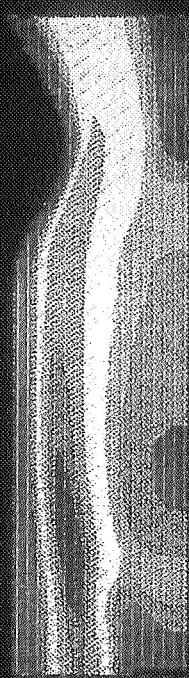


Figure 8. Carbon Monoxide Mass Fraction Contours for RP1/LOX



# Detonation Pulse Progress, Pressure, psia

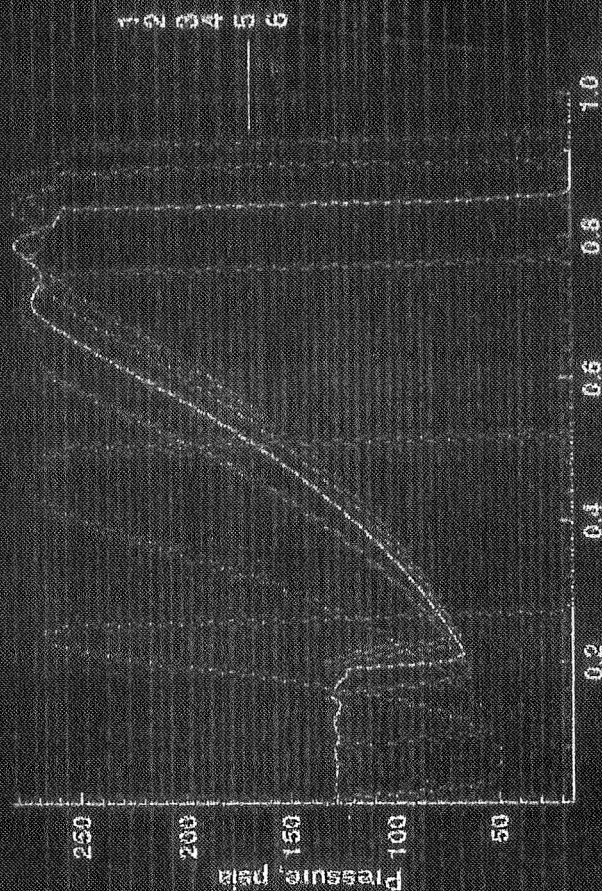


Figure 10. Longitudinal Variation of the Static Pressure for the Six Snapshots

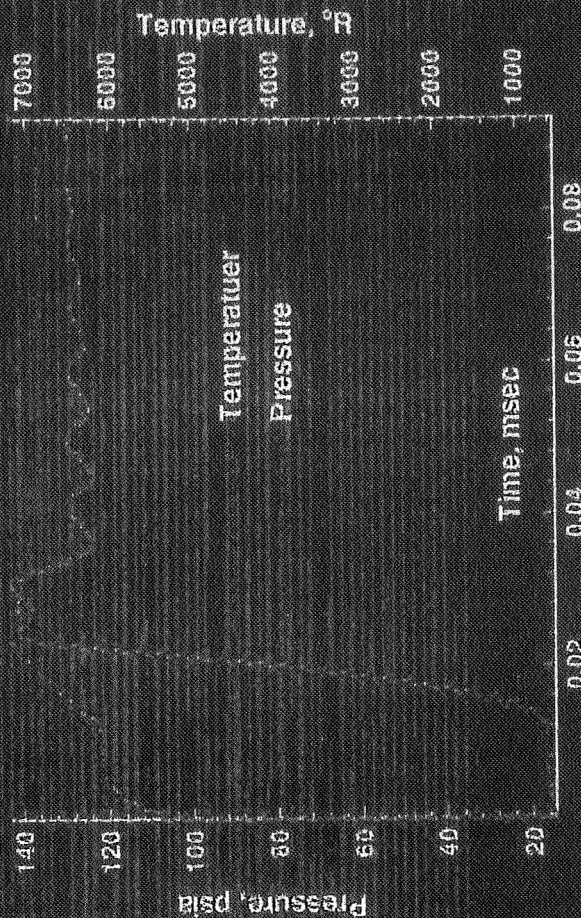


Figure 11. Pressure and Temperature History on the Left Wall

Figure 9. Detonation Pulse Progress in Time  
Initial Pressure = 14.7 psia,  
Initial Temperature = 540 °R  
Temperature Raised to 5400 °R





**1996**

**NASA/ASEE SUMMER FACULTY FELLOWSHIP PROGRAM**

**MARSHALL SPACE FLIGHT CENTER  
THE UNIVERSITY OF ALABAMA**

**DIFFRACTIVE OPTICAL ELEMENTS FOR LIDAR BEAM SCANNING**

Prepared By:	Gregory P. Nordin, Ph.D.
Academic Rank:	Associate Professor
Institution and Department:	The University of Alabama in Huntsville Department of Electrical and Computer Engineering
NASA/MSFC:	
Laboratory:	Astrionics Laboratory
Division:	Optics & Radio Frequency
Branch	Electro-Optics Branch (EB53)
MSFC Colleague:	Michael J. Kavaya, Ph.D.



## 1. Introduction

Wind measurement from space can provide critical data for understanding weather patterns and large-scale storm phenomena. An instrument of providing such measurements is currently under development at NASA's Marshall Space Flight Center.<sup>1</sup> The instrument utilizes a pulsed coherent lidar system operating at a wavelength of  $2.06\text{ }\mu\text{m}$  in order to achieve decreased weight, size, and cost compared to systems operating at longer wavelengths, and it is being developed to be compatible with the capabilities of small satellites.

A key aspect of such an orbital lidar system is that the beam must be conically scanned after it exits the final beam expansion telescope. Previous work indicates that the aperture of the beam expansion telescope should be 50 cm with a scanner half-angle of  $30^\circ$  and a rotation rate of 10 RPM.<sup>1,2</sup> Such a scanner is illustrated in Fig. 1, in which a beam deflection element is rotated to achieve the conical scan. The critical requirements for the beam scanning element include a 50 cm aperture, an induced wavefront error of less than  $\lambda/10$ , and high efficiency deflection (i.e., 95+ % of the incident light is deflected).

This report is intended to provide a brief overview and discussion of potential technologies for space-borne laser radar (lidar) beam scanning.

## 2. Scanner Approaches

### 2.1 Prism Beam Scanner

The most straightforward method of achieving the beam deflection function is to simply use a prism as illustrated in Fig. 2. The prism material should have a high refractive index to minimize the wedge angle of the prism and hence the prism's volume and weight. This necessitates a material such as germanium (wedge angle  $\sim 9^\circ$  to achieve a  $30^\circ$  beam deflection). However, it is difficult to grow germanium crystals of the requisite size to provide a 50 cm prism aperture. In addition, the mass of such an element is substantial. For example, using a 6:1 diameter to thickness rule, the mass would be 275 lb. Using a more aggressive 15:1 rule the mass is reduced to a

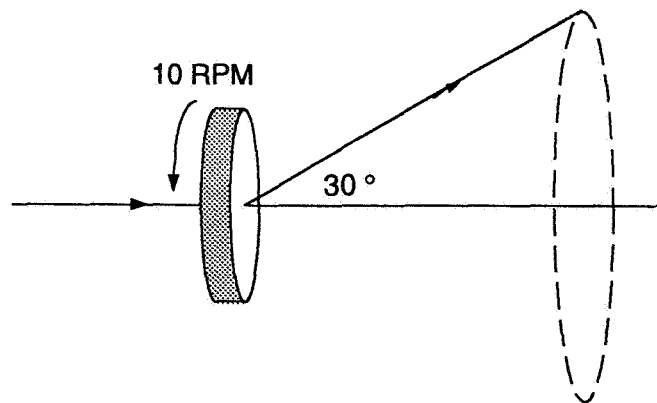


Figure 1. Schematic representation of rotating conical beam scanner.

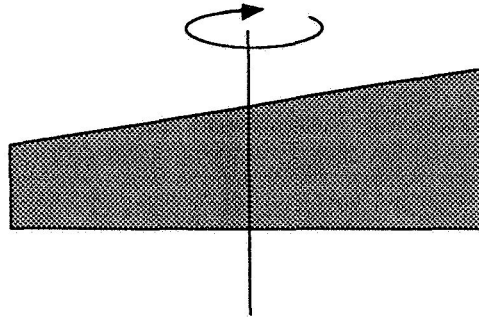


Figure 2. Simple prism beam scanner.

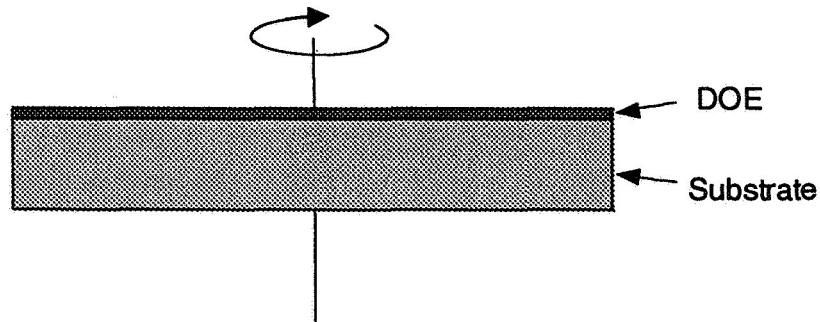


Figure 3. Schematic representation of a DOE beam scanner.

still hefty 160 lb. A further drawback of the prism approach is its asymmetric mass distribution, which complicates balancing the spacecraft dynamics.

## 2.2 DOE Approaches

A potentially attractive alternative to the prism approach is to use a very thin diffractive optical element (DOE) on top of a lightweight transparent substrate as illustrated in Fig. 3. The DOE would perform the 30° beam deflection function, while the substrate could be made from a low index material such as fused silica. Using the 6:1 rule for the substrate, the mass of the element would be 95 lb (a factor of three less than the corresponding Germanium prism case), while a 15:1 rule yields a mass of 38 lb (a factor of four improvement). A further advantage is that the element's mass is symmetrically distributed about its rotational axis.

## 2.3 Volume Diffraction Grating

As illustrated in Fig. 4, a volume diffraction grating is an attractive DOE technology because of the potentially high diffraction efficiency that can be achieved. Candidate volume holographic materials include dichromated gelatin, silver halide photographic emulsions, and DuPont's holographic photopolymer. The DuPont photopolymer is particularly attractive because of its dry development process and its availability in thicknesses suitable to achieve high diffraction efficiency. Based on preliminary experiments at a wavelength of 2.06  $\mu\text{m}$  with 10  $\mu\text{m}$  thick

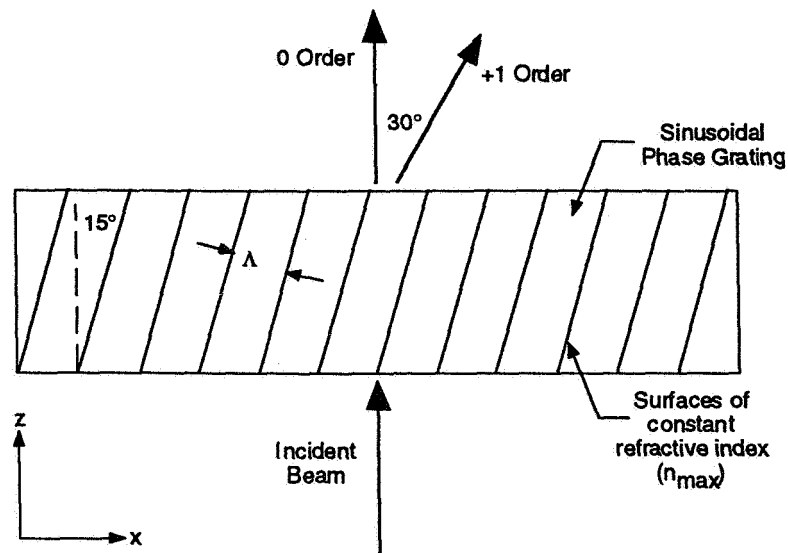


Figure 4. Volume diffraction grating beam scanner.

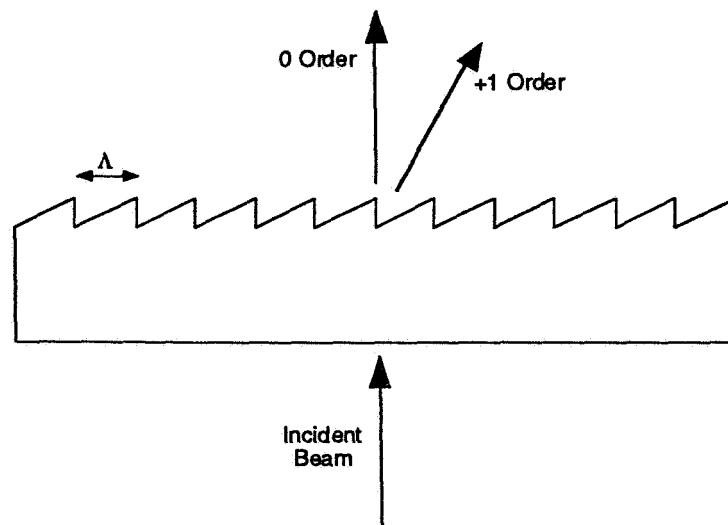


Figure 5. Schematic diagram of a blazed grating.

photopolymer samples, nearly 100% diffraction efficiency should be achievable with 70  $\mu\text{m}$  thick films. Further issues that need addressed include film shrinkage, availability of large exposure optics, polarization sensitivity, and uniformity.

## 2.4 Blazed Grating

Another attractive high efficiency DOE technology is that of blazed gratings. As illustrated in Fig. 5, a blazed grating is a surface relief profile that is etched into the substrate. By an appropriate choice of blaze angle for a given grating period,  $\Lambda$ , the diffraction efficiency into the +1

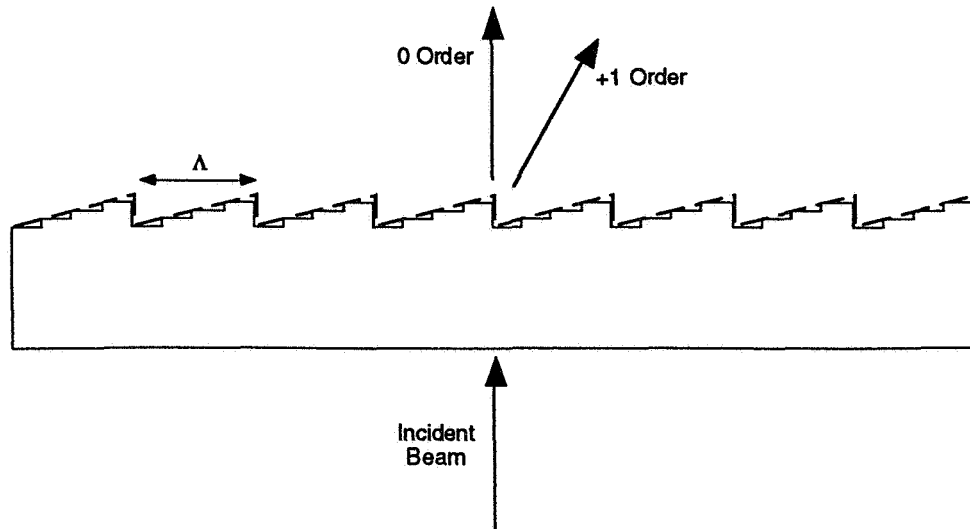


Figure 6. Multilevel diffractive optical element.

Table 1. Multilevel DOE DE and minimum feature size for a given number of phase levels

N	DE (%)	Feature Size ( $\mu\text{m}$ )
2	41	2.06
4	81	1.03
8	95	0.52
16	99	0.26

order can be nearly 100%. However, we have yet to locate a vendor who is able to fabricate such a structure over a 50 cm aperture with the required feature size and uniformity.

## 2.5 Multilevel DOE

As illustrated in Fig. 6, one can approximate the surface relief profile of a blazed grating through the use of a multilevel diffractive optical element. Such profiles are fabricated using a repeated photolithographic patterning and etch process. To achieve large diffraction efficiencies (the column labeled DE in Table 1), the number of phase levels in the surface relief profile needs to be relatively large. For example, 16 phase levels are required to achieve 99% diffraction efficiency. However, the minimum feature size in this case is 0.26  $\mu\text{m}$ , which is too small to fabricate and align over the large area required for this project. Multilevel DOE's are therefore not an option.

### **3. Summary**

There are compelling reasons to look at DOE beam deflection technologies to replace a heavy prism element for conical beam scanning in space-borne 2.06  $\mu\text{m}$  lidar wind measurement systems. Due to its simplicity, the most attractive DOE technology is that of blazed gratings. Since the fabrication of such an element is uncertain at this point, other alternatives are being explored, including volume diffraction gratings and other novel structures that are not discussed in this brief report.

### **References**

1. M. J. Kavaya, G. D. Spiers, E. S. Lobl, J. Rothermel, and V. W. Keller, "Direct global measurements of tropospheric winds employing a simplified coherent laser radar using fully scalable technology," Proc. of SPIE International Symposium on Optical Engineering in Aerospace Sensing, Technical Conference on Space Instrumentation and Dual-Use Technologies, 2214-31, April 6, 1994.
2. R. G. Frehlich and M. J. Yadlowsky, "Performance of mean-frequency estimators for Doppler radar/lidar," J. Atmospheric and Oceanic Technology 11, October 1994.





**1996**

**NASA/ASEE SUMMER FACULTY FELLOWSHIP PROGRAM**

**MARSHALL SPACE FLIGHT CENTER  
THE UNIVERSITY OF ALABAMA**

**STREHL RATIO METER FOR FOCUSING SEGMENTED MIRRORS I**

Prepared By:	Philip D. Olivier, Ph.D.
Academic Rank:	Associate Professor
Institution and Department:	Mercer University Department of Electrical and Computer Engineering
NASA/MSFC:	
Laboratory:	Astrionics Laboratory
Division:	Optics and Radio Frequency
Branch:	Fabrication
MSFC Colleague:	Martin Smithers, Ph.D.

**XXX**



## Introduction

Initial focusing segmented mirrors that must be deployed in space, such as the Next Generation Space Telescope (NGST), provide challenges not faced before in the area of adaptive optics. The devices used to focus the mirror must minimize the power used and unnecessary mechanical movement. The device described in this report requires no movable parts except for the essential actuators required to move the mirror segments. Detail description of the components can be found in Coker, 1996.

The primary mirror of the NGST will consist of 9 segments, a central annular segment, surrounded by 8 segments. The entire mirror assembly will be an 8 meter nearly filled circle (with the corners of the segments clipped to allow for storage in an Atlas IIe shroud). As the segments of the primary mirror are deployed to their operational positions, they must be positioned to within small fractions of a wavelength of near infrared light. When focused, the NGST will put most of its collected light into the small region near the center of its focal plane. The ratio of the total light in the diffraction limited spot about the center of the focal plane to the total light in the focal plane. The purpose of this research effort is to design and build a device that will measure Strehl ratio and to use demonstrate that the Strehl ratio can be used to focus a segmented mirror.

### Initial Strehl ratio meter

The Strehl ratio meter consists of a computer controllable Liquid Crystal display (LCD) and a lateral effect diode (LED). The 128 by 128 pixels of the LCD can be independently set of various shades of gray from nearly clear to nearly opaque. The LED is a silicon based device that is square, it produces 4 currents, each current is proportional position of the centroid of the beam that strikes the LED. These 4 currents can be used to compute the coordinates of the centroid of the beam that strikes the LED as well as the total intensity of the light striking the LED. To determine the Strehl ratio: first, measure the intensity of light on the LED while the LCD is clear; second, measure the intensity of the light on the LED while the LCD is nearly opaque except at the center, where it is nearly clear. The ratio of these two is the Strehl ratio:

$$SR = \frac{I_{dls}}{I_T}$$

### Control System

The Strehl ratio meter described in the previous paragraph can be used to help focus a segmented mirror in the following way. While the LCD is clear, the centroid of the beam is a measure of the x-tip and y-tip of the composite mirror. Sequentially adjusting the x-tip and y-tip of the various segments, the centroid can be centered. Further, intensity of the light striking the LED with the LCD opaque except near the center is a measure of how well the composite mirror is focused. Further adjusting the x-tip, y-tip, and piston of the segments can improve the focus. Improving the focus probably will move the centroid off center requiring further adjustment of x-

tips and y-tips. Cycling through this process will produce a focused mirror.

### **Simplified Strehl ratio meter**

The Strehl ratio meter described in the previous paragraph can be simplified by replacing the programmable LCD by a single passive mask that is clear at its center and partially transmissive elsewhere. This still provides a measure of the centroid of the beam (though not so simply related to the x-tip and y-tip of the composite mirror) and does not require the computation of the ratio. The x-tips, y-tips and pistons of the segments can be adjusted to center the centroid and to maximize the amount of light in the central clear area of the mask. Once maximized, the mirror is focused to extent allowed by the measurement and the optics. The passive mask could be a pellicle with small hole burned in it at its center.

Summer 1996 project. To Design, build and test the Strehl ratio meter first described. To use the Strehl ratio meter to focus a two mirror composite mirror in y-tip only. To design, build, and test the simplified Strehl ratio meter using an LCD with gray level capability.

The pixel size of the LVGA Smartslide, liquid crystal display must be matched to the diffraction limited spot size of the NGST beam. The LVGA Smartslide has a pixel that is 24 microns on a side. The radius of the cross section of the ideal Airy pattern for the proposed NGST is

$$r_0 = 1.22 \frac{\lambda z}{l} = 1.22 \frac{2 * 10^{-6} * 80}{8} = 24.4 \text{ microns}$$

where  $\lambda$  is the wavelength,  $z$  is the focal length, and  $l$  is the aperture diameter. The commercially available liquid crystal display has a pixel size that is closely matched to the radius of the most ideal Airy pattern for a mirror with the geometry of the NGST instrument.

### **Experimental Results**

The moveable mirror caused a beam to traverse the mask-sensor system while the stationary mirror was aimed at the transparent portion of the mask. The output of the sensor was signal conditioned and the data recorded by a data acquisition system that was triggered by the intensity going high.

- ▶ **Black Mask** This produced a significant hump while both beams illuminated the transparent portion of the mask. The position was approximately linear.
- ▶ **Clear Mask** The was a completely clear mask. The intensity was approximately constant, while the position was approximately linear as would be expected.
- ▶ **Other Masks** As the transmissivity went down the hump associated with the transparent portion of the mask became more pronounced. The position was nearly linear in all cases

## *Top View*

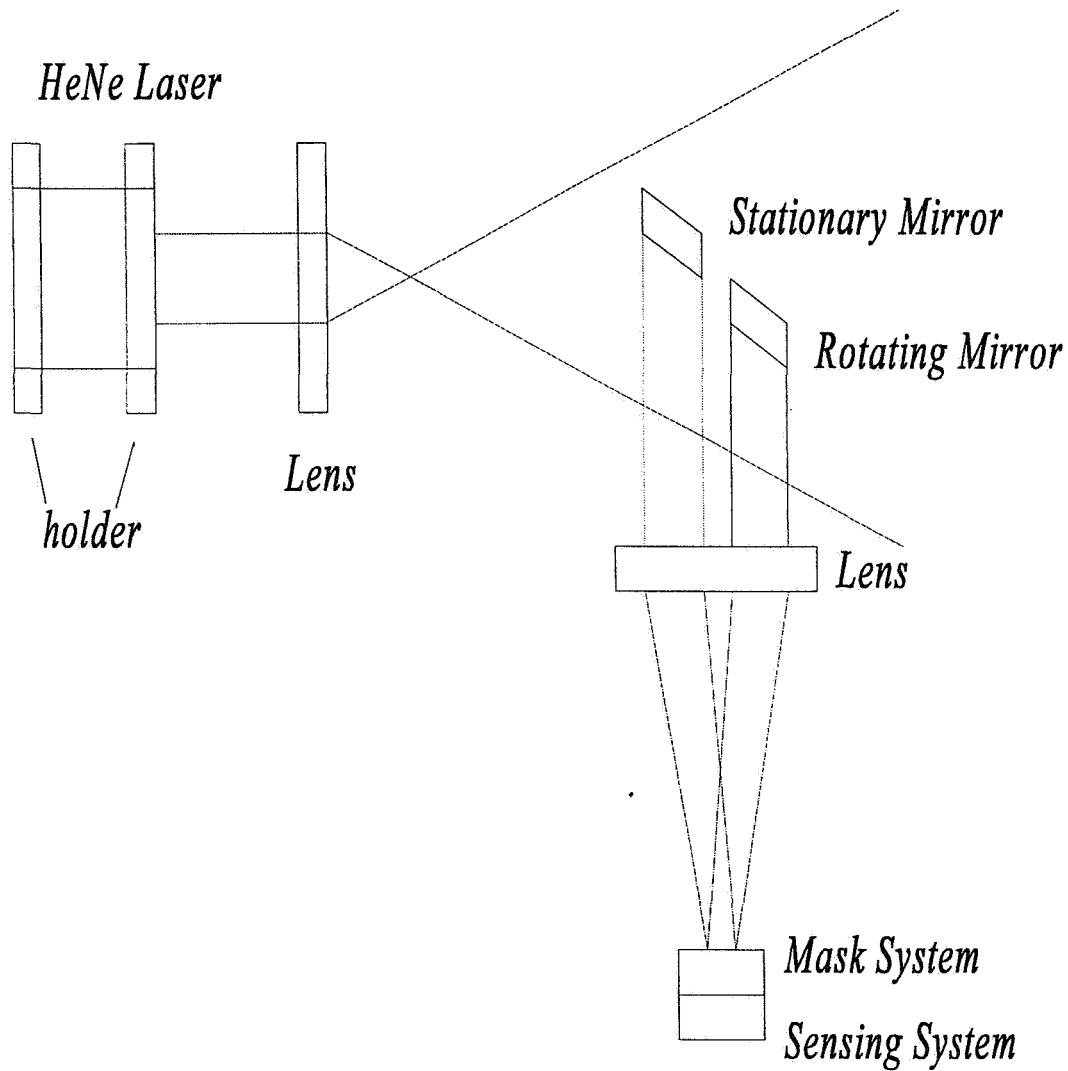


*Figure 1. Basic setup for the strehl meter*

and almost indistinguishable one from the other.

**Other optical measurements**

Conceptually, several other optical measurements can be performed by the combination of the programmable LCD display and the LED. These include:

- **x-tip, y-tip** as discussed before. See pg 126 of Tyson.
- **Foucoult knife edge test for focus:** see pg. 134 of Tyson. The LCD can be programmed to opaque in its lower (or left) region. The edge can travel up the LCD and the effect on the LED observed. This will determine if the optical system is focusing in front of, or behind, the mask.
- **Direct determination of tips and pistons for NGST** Assuming rigid segments, the NGST consists of 9 segments, each is described by three parameters (x-tip, y-tip, and piston). There are, therefore, 27 parameters that describe the mirror. To determine these 27 parameters, requires at least 27 measurements. Once these 27 parameters are known, the corrective action can be taken to adjust them to produce optimal optical performance. The LCD mask can be programmed to obtain 27 measurements in many ways, statically, or sequentially. By statically, I mean that the 27 measurements could be obtained without moving the optics. By sequentially, I mean that the 27 measurements could be taken before and after moving the segments to partially compensate for the unfocused, uncentered image.
  - ▶ Statically: By measuring the intensity and centroid on the LED when the sensor masks various areas, and comparing these to the theoretically predicted intensities and centroids. Each measurement would produce three measured quantities and therefore it would require 9 measurements.
  - ▶ Sequentially: By working backward from the effect of various changes in the parameters, it should be possible to determine the parameter values that were in effect at the beginning of the process. Redoing the changes from these initial values will determine the current values of the parameters. Knowways to build on the this work. It includes:
    - To investigate, theoretically and experimentally, the usefulness of the Strehl ratio meter as a sensing element in an adaptive optics system.
    - To investigate, theoretically and experimentally, the usefulness of the other optical build on the this work. It includes:
    - To investigate, theoretically and experimentally, the usefulness of the Strehl ratio meter as a sensing element in an adaptive optics system.
    - To investigate, theoretically and experimentally, the usefulness of the other optical measurements.

## Conclusions

A sensor composed of a liquid crystal display that is computer controllable and a lateral effect diode can be used to measure the Strehl ratio of an optical device such as NGST. A simplified sensor can be constructed from a passive mask that is clear in the diffraction limited spot, and is partially transmissive elsewhere. Such a simplified device might be preferable since it could operate below 0°C.

Additional optical sensors seem to be constructable from the computer controllable liquid crystal display and the lateral effect diode.

### **Acknowledgments**

I would like to express my sincere thanks to all in the Optics and Radio Frequency division of the Astrionics Lab at Marshall Space Flight Center. In particular, Martin Smithers, Robert Rood, Ron Eng, Helen Cole, Terri Scribbs, and Jeri Briscoe deserve special thanks for various reasons.

Also, special thanks need to be extended to Kopin Corp. for fixing, free of charge, a critical component.

### **References**

R. T. Tyson, *Principles of Adaptive Optics*, Academic Press, Inc., 1991.

J. W. Goodman, *Introduction to Fourier Optics*, McGraw-Hill, 1968.

M. R. Teague, *J. Optical Soc. Am.*, **72**, 1982.

J. Harvey, J. L. Forgham, K. Von Bieren, *Proc. Soc. Photo-opt. Instrum. Eng.* **351**, 2, 1982.

J. S. Coker, NASA contract report, STREHL RATIO METER FOR FOCUSING SEGMENTED MIRRORS II, 1996.





1996

**MARSHALL SPACE FLIGHT CENTER  
THE UNIVERSITY OF ALABAMA**

**THE EFFECT OF GRAVITY AXIS ORIENTATION ON THE GROWTH OF  
PHTHALOCYANINE THIN FILMS**

Prepared By:

Earl F. Pearson, Ph.D.

Academic Rank:

Professor

Institution and Department:

Western Kentucky University  
Department of Chemistry

NASA / MSFC:

Laboratory:  
Division:  
Branch:

Space Sciences Laboratory  
Microgravity Science & Applications  
Biophysics

MSFC Colleagues:

Benjamin Penn, Ph.D.  
Don Frazier, Ph.D.



## INTRODUCTION

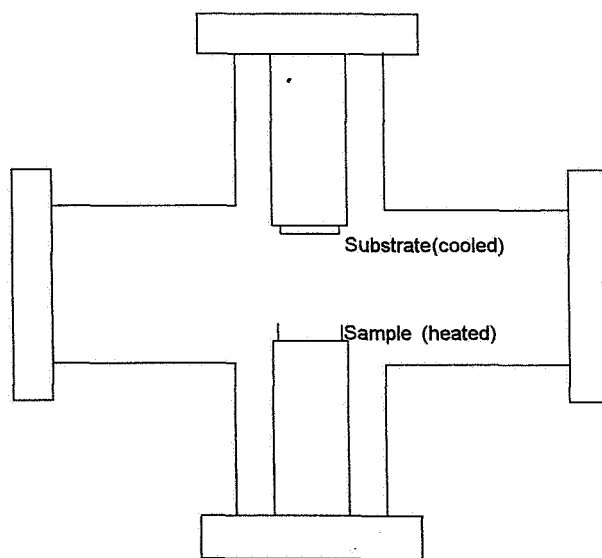
Experimentally, many of the functions of electrical circuits have been demonstrated using optical circuits and, in theory, all of these functions may be accomplished using optical devices made of nonlinear optical materials(1-5). Actual construction of nonlinear optical devices is one of the most active areas in all optical research being done at this instant(6-11).

Physical vapor transport (PVT) is a promising technique for production of thin films of a variety of organic and inorganic materials. Film optical quality, orientation of microcrystals, and thickness depends critically on type of material, pressure of buffer gas and temperature of deposition. An important but understudied influence on film characteristics is the effect of gravity-driven bouancy. Frazier, Hung, Paley, Penn and Long (12) have recently reported a mathematical modelling of the vapor deposition process and tested the predictions of the model on the thickness of films grown by PVT of 6-(2-methyl-4-nitroanilino)-2,4-hexadiyn-1-ol (DAMNA.)

In an historic experiment, Debe, et. al. (13,14) offered definitive proof that copper phthalocyanine films grown in a low gravity environment are denser and more ordered than those grown at 1 g. This work seeks to determine the influence on film quality of gravity driven bouancy in the low pressure PVT film growth of metal-free phthalocyanine.

## EXPERIMENTAL

The vapor deposition cell used in this work is illustrated in Figure 1 below.



VAPOR DEPOSITION APPARATUS

FIGURE 1

The "top" segment of the cell contains the cold finger on which the quartz substrate is mounted. The phthalocyanine is contained in a heated graphite crucible located in the "bottom" segment. The cell is mounted inside the vacuum chamber by attachment through a rotatable flange on one of the "horizontal" segments which allowed the cell to be rotated  $45^\circ$  with respect to the vertical (gravity) axis. The inside of the apparatus is evacuated through an open observation port in one of the horizontal segments. The temperature of the cold finger is maintained at  $5^\circ\text{C}$ , a temperature found to yield highly ordered films of good optical quality. The temperature of the heater was set at  $330^\circ\text{C}$  which maintained the partial pressure of phthalocyanine at approximately  $1 \times 10^{-6}$  torr. The total pressure inside the cell was maintained at  $1 \times 10^{-2}$  torr using argon as a buffer gas. The deposition time was 2 hours.

## RESULTS AND DISCUSSION

All the films appeared to be of good optical quality both visually and microscopically. The thickest film, judged by the intensity of the blue color, did appear to have scattering regions. Microscopically, these regions had the appearance of tiny "needles" composed of much smaller microcrystals covering the surface. All the films showed some imperfections consisting of crystalline "clusters", and some larger crystal segments. These imperfections will act as scattering centers and may limit the performance of such films in optical devices.

Electron microscopy was able to resolve the fine details of the film. The film grown vertically showed a more uniform appearance but appeared to be less dense. The needles on the surface were smaller and less numerous than those grown at  $45^\circ$ . The effect is probably due to the thinner vertically grown films.

The thickness of the films was measured by both ellipsometry and profilometry. The ellipsometer used a helium-neon laser source, wavelength 632.8 nm at  $70^\circ$  to the surface. The spot size was  $0.025 \times 0.086$  mm and nine readings were taken on each film. The data is summarized in Table 1. All measurements are given in Angstrom units.

film number	orientation	maximum thickness	average thickness	minimum thickness	3 standard deviations
2	vertical	802	702	657	135
5	vertical	876	872	869	7
6	vertical	868	863	856	13
7	vertical	910	904	899	11
1	$45^\circ$	915	890	875	36
3	$45^\circ$	853	837	821	33
Average (vertical)		864	838	820	42
Average ( $45^\circ$ )		884	864	848	34

TABLE 1

While there is considerable spread in the numbers, it is significant that all three values; the maximum thickness, the average thickness and the minimum thickness are thicker for the films grown at  $45^\circ$  relative to the gravity axis. The most troubling feature of the ellipsometer readings is that films #6 and #7 show thicknesses larger than or comparable to films #1, #2, and #3. The latter three films appear to be the thickest judged by the intensity of the color of the films whereas, the former two films are so faintly coated that almost no blue color is observable.

In view of the questionable readings obtained from ellipsometry, the film thickness was also measured by profilometry. The profilometer results are shown in Table 2. The thickness is measured in Angstrom units.

film #	orientation	thickness
2	vertical	350
5	vertical	185
6	vertical	70
7	vertical	75
1	$45^\circ$	280
2	$45^\circ$	410
Average (vertical)		170
Average ( $45^\circ$ )		345

**TABLE 2**

The thickness found from profilometry are in the order expected judging from a visual observation of the colored films. These readings are inconsistent with the film thickness measured by ellipsometry. At present, there appears to be no obvious reason for the discrepancy. However, the profilometer readings also show that the films grown at  $45^\circ$  relative to the gravity axis are considerably thicker than those grown with the cell axis parallel to the gravity axis.

Since there is a discrepancy between the thickness measured by ellipsometry and that measured by profilometry that is greater than the uncertainty in either of the measurements, both these readings should be repeated using different instruments. Part of the problem may result from the fact that the films are too thin. The experiment should be repeated with experimental parameters which increases the film thickness.

There are three possible ways to increase the thickness of the films: the deposition time could be increased, the evaporation temperature could be increased, or the buffer gas pressure could be lowered. A more thorough study investigating the effect of pressure should be attempted. It is surprising that a pressure as low as  $10^{-2}$  torr has such an effect on bouancy since the mean free path is long and gas density is low. An investigation to determine the minimum pressure at which gravity driven bouancy effects are measurable should be initiated.

Pressures above  $10^{-2}$  torr will be difficult because the films will be even thinner than those of this study unless other parameters are adjusted.

It will be difficult to increase the evaporation temperature. The current heater was drawing more than 7.0 amps of current at 330 °C. As viewed through the observation port, the leads connected to the heater were glowing at this current. Increasing the current may result in damage to the heater or nonuniform heating of the sample. The simplest way to increase the film thickness is to increase the deposition time. This will have the added benefit of producing a better quality thick film due to the slower deposition rate. The films will need to be about twice as thick in order to make meaningful comparisons between the thickest and the thinnest films. This will require about 4 hours of deposition time. It may be somewhat advantageous to increase the deposition time to 5 to 6 hours with a corresponding decrease in the evaporation temperature in order to protect the heater.

The films should be studied by x-ray diffraction in order to determine if gravity axis orientation has an influence on the degree of ordering of the microcrystalline film on the substrate surface. At 5°C condensation temperature, the most prominent reflection is 100 indicating significant ordering of crystal planes on the substrate surface. Nonlinear optical properties depend significantly on the extent of ordering in the films.

This study has shown that good quality films can be produced from metal-free phthalocyanine and that the film quality and thickness is affected by the orientation of the vapor deposition axis relative to the gravity axis. A rotation of 45° is observed to produce thicker films of lower quality than those grown vertically. Experimental difficulties related to the thin films obtained made it impossible to quantitate the effects. The results do indicate that a more detailed experiment is in order including comparison of films of the same thickness but grown at different orientations relative to the gravity axis. It is probable that the 45° orientation may produce better quality films of the same thickness than those grown parallel to the gravity axis.

## ACKNOWLEDGEMENTS

I would like to express appreciation to Crutis Banks for working tirelessly with me and helping with every phase of this work. He allowed me the use of his computer, his lab equipment and his considerable expertise. I would also like to thank John Reynolds for performing the ellipsometer readings and Don Gillis for the use of his optical microscope. I would also like to express appreciation to Dave Nicolas for taking the electron microscope images of the films. I am also deeply indebted to Benn Penn and Don Frazier for their leadership in directing this research and for funding this project. Lastly I would like to thank Mike Freeman, Jerry Karr and Frank Six for their organizational skills and Debbie and Ethan for making things run so smoothly.

## LITERATURE CITED

1. R. G. Hunsperger, Integrated Optics: Theory and Technology, Springer-Verlog, 1984 Chapter 12.
2. William K. Burns, "Normal Mode Analysis of Waveguide Devices. Part I: Theory", J. Lightwave Technol., 1988, 6(6), 1051-7.
3. William K. Burns, "Normal Mode Analysis of Waveguide Devices. Part II: Device Output and Crosstalk", J. Lightwave Technol., 1988, 6(6), 1058-68.
4. G. I. Stegeman, E. M. Wright, N. Finlayson, R. Zanoni, and C. T. Seaton, "Third Order Nonlinear Integrated Optics, J. Lightway Technol., 1988, 6(6), 953-69.
5. Emmanuel Van Tomme, Peter P. Van Daele, Roel G. Baets, and Paul E. Lagasse, "Integrated Optic Devices Based on Nonlinear Optical Polymers", IEEE J. Quantum. Electron., 1991, 27(3), 778-87.
6. L. R. Dalton, A. W. Harper, R. Ghosn, W. H. Steier, M. Ziari, H. Fetterman, Y. Shi, R. V. Mustacich, A. K.-Y. Jen, and K. J. Shea, "Synthesis and Processing of Improved Organic Second-Order Nonlinear Optical Materials for Applications in Photonics", Chem. Mater 1995, 7, 1060-81.
7. J. R. Sounik, R. A. Norwood, J. Popolo, D. R. Holcomb and S. S. Ghatani, "Silicon Phthalocyanine/Methyl Metracrylate Copolymer Slab Directional Couplers for All-Optical Switching", J. Appl. Polymer Sci., 1994, 53, 677-85.
8. Braja K. Mandal, Bipin Bihari, Arun K. Sinha, Manjunath Kamath, and Lin Chen, "Third-order Nonlinear Optical Response in a Multilayered Phthalocyanine Composite", Appl. Phys. Lett., 1995, 66(8), 932-34.
9. K. S. Buritskii, E. M. Dianov, V. A. Maslov, V. A. Chernykh and E. A. Shcherbakov, "Nonlinear Directional Coupler Based on Rb:KTP-Waveguides", Appl. Phys., B54, 1992, 167-69.
10. Y. Suda, K. Shigehara, A. Yamaka, H. Matsuda, S. Okada, A. Masaki and H. Nakanishi, "Reversible Phase Transition and Third Order Nonlinearith of Phthalocyanine Derivatives", SPIE, Nonlinear Opt. Prop. of Org. Mater. IV, 1560, 1991, 75-83.
11. Paul D. Tounsand, J. L. Jackel, Gregory L. Baker, J. A. Shelburne, III and S. Etemad, "Observation of Non- linear Transmission and Switching Phenomena in Polydiacetylene-based Directional Couplers", Appl. Phys. Lett., 1989, 55(18), 1829-31.
12. D. O. Frazier, R. J. Hung, M. S. Paley, B. G. Penn, and Y. T. Young, "Bouancy-Driven Heat Transfer uring Application of a Thermal Gradient for the Study of Vapor Deposition at Low Pressure using an Ideal Gas", Accepted for publication in J. Crystal Growth.
13. M. K. Debe, R. J. Poirier, D. D. Erickson, T. N. Tommet, D. R. Field and K. M. White, Thin Solid Films 1990, 186, 257.
14. M. K. Debe, R. J. Poirier, Thin Solid Films, 1990, 186, 327.





**1996**  
**NASA/ASEE SUMMER FACULTY FELLOWSHIP PROGRAM**

**MARSHALL SPACE FLIGHT CENTER**  
**THE UNIVERSITY OF ALABAMA**

**VIRTUAL REALITY SIMULATION OF THE INTERNATIONAL SPACE  
WELDING EXPERIMENT**

Prepared By:	James A. Phillips, Ph.D.
Academic Rank:	Senior Research Fellow
Institution and Department:	California Institute of Technology Division of Physics, Math, and Astronomy
NASA/MSFC:	
Office:	Mission Operations Laboratory
Division:	Operations Engineering
Branch:	Crew Systems Engineering
MSFC Colleague:	Joseph P. Hale, M.S., C.H.F.P.



# VIRTUAL REALITY SIMULATION OF THE INTERNATIONAL SPACE WELDING EXPERIMENT

## 1. INTRODUCTION

Virtual Reality (VR) is a set of breakthrough technologies that allow a human being to enter and fully experience a 3-dimensional, computer simulated environment. A true virtual reality experience meets three criteria:

1. It involves 3-dimensional computer graphics.
2. It includes real-time feedback and response to user actions.
3. It must provide a sense of immersion.

Good examples of a virtual reality simulator are the flight simulators used by all branches of the military to train pilots for combat in high performance jet fighters. The fidelity of such simulators is extremely high -- but so is the price tag, typically millions of dollars.

Virtual reality teaching and training methods are manifestly effective, and we have therefore implemented a VR trainer for the International Space Welding Experiment. My role in the development of the ISWE trainer consisted of the following:

1. I created texture-mapped models of the ISWE's rotating sample drum, technology block, tool stowage assembly, sliding foot restraint, and control panel.
2. I developed C code for control panel button selection and rotation of the sample drum.
3. In collaboration with Tim Clark (Antares Virtual Reality Systems) I developed a serial interface box for the PC and the SGI Indigo so that external control devices, similar to ones actually used on the ISWE, could be used to control virtual objects in the ISWE simulation.
4. In collaboration with Peter Wang (SFFP) and Mark Blasingame (Boeing) I established the interference characteristics of the VIM 1000 head-mounted-display and tested software filters to correct the problem.
5. In collaboration with Peter Wang and Mark Blasingame I established software and procedures for interfacing the VPL DataGlove and the Polhemus 6DOF position sensors to the SGI Indigo serial ports.

The majority of my ISWE modeling effort was conducted on a PC-based VR Workstation, described below.

## 2. THE PC VIRTUAL REALITY STATION

The first point in the 3-point definition of Virtual Reality, above, involves 3D computer graphics. The rule of thumb in digital video is that an animation must run at least 15 frames/sec to appear smooth to the human eye, so I adopted 15 frames/sec as a benchmark for evaluating PC performance. I benchmarked four different PC systems

using the Sense8 WorldToolKit software to render a virtual reality scene consisting of approximately 750 polygons. The results for shaded and shaded+textured polygons are tabulated below. Only the Pentium systems gave frame rates for complicated simulations that were above 15 frames/s. A comparison of the two 486-based systems shows similar frame rates despite the factor of two difference in system RAM. In fact, the 80 MHz system with only 8MB of RAM outperformed the 66 MHz system with 16 MB RAM by a factor of 1.21, almost exactly the ratio of the clock speeds. The relative frame rates of the two Pentium systems also scaled with clock speed, the 120 MHz system being about 25% faster than the 90 MHz system. (Note, however, that the 120 MHz Pentium had a 4 MB graphics board while the 90 MHz system had a 2 MB board.)

TABLE 1: PC Performance comparisons

Processor	Clock	RAM	Graphics Accelerator	Shaded frames/s	Textured frames/s
486DX	66 MHz	16 MB	Cirrus Logic w/1 MB ram	7.5	4.0
486DX	80 MHz	8 MB	Trident 9440CX w/1 MB ram	9.1	3.6
Pentium	90 MHz	32 MB	ATI Mach 64 w/2 MB ram	16.7	7.5
Pentium	120 MHz	32 MB	ATI Mach 64 w/4 MB ram	21.0	9.0

From Table 1 we see that a 90 MHz Pentium system, or better, will give adequate 3D graphics rendering performance.

The second point in the 3-point definition of Virtual Reality was real-time interaction to user input. The participant in a VR simulation must be able to navigate through the virtual world, select objects, and move them. I tested three devices for user interaction with WorldToolKit applications: a mouse, a Logitech Cyberman (6 degree-of-freedom mouse with limited tactile feedback), and a ThrustMaster joystick. I also tested the VPL DataGlove and a Spatial Systems Spaceball (6 degree-of-freedom controller) using VPL VR simulation software. For picking and moving objects, the DataGlove was by far the best. For navigation the ThrustMaster joystick was best. The mouse was unintuitive and difficult to learn as a navigation device, as was the Spaceball. The LogiTech Cyberman was awful. I tested two Cybermen and both were poorly constructed, overly sensitive, and nearly impossible to control. The simple tactile feedback feature (a pulse modulation of the controller stem triggered by hitting virtual walls or other objects) was satisfying but did not compensate for the other shortcomings of the device. In Table 2 I rate the peripherals on a scale of 1 to 10 (10 is best, 1 is worst) in two categories: "Picking" refers to the ease with which objects could be selected or grabbed with the device, and "Flying" refers to navigation through the virtual environment. The ratings are subjective, and are based on my own experience with the devices, and the experience of students aged 5 to 12 years who have tested the PC with a VR Human Cadaver application developed at the MSFC virtual reality lab.

TABLE 2: EVALUATION OF VR PERIPHERALS

Device:	Picking	Flying
Microsoft Mouse	8	3
Logitech Cyberman	5	1
VPL DataGlove	9	7
SpaceBall	6	6
ThrustMaster Joystick	N/A	9

Finally, the third point in my definition of Virtual Reality is that the experience must be immersive. Immersion means that you forget about all outside stimuli and become a thinking, feeling part of the computer's virtual world. In theory, total immersion would include touch, smell, temperature, visual input, and sounds. In practice, it is difficult, expensive, and, fortunately, unnecessary to attack all 5 senses to produce a sense of immersion. I find that the visual cues provided by a wide-field-of-view head-mounted display in combination with 3-dimensional sound effects are sufficient to create a powerful immersive effect. The mind fills in the gaps not covered by the HMD and the 3D sound hardware.

## 2.1 3D SOUND

3D sound technology operates on the principle that all the spatial information about a sound source is contained in its spectrum. At its source the complex Fourier spectrum of a sound is  $S(f)$ , where  $f$  is the frequency. The acoustic wave propagates to both ears and is filtered by reflections off the human body, primarily the head and shoulders, and the inner ear. When the sound reaches the inner ear, its complex spectrum is  $T_L(\mathbf{n},f)S(f)$  in the left ear and  $T_R(\mathbf{n},f)S(f)$  in the right ear;  $\mathbf{n}$  is the unit direction vector toward the sound source and  $T$  is the "transfer function." The product  $T(\mathbf{n},f)S(f)$  in the frequency domain can be expressed as a convolution in the time domain  $T(\mathbf{n},t)*S(t)$ , and this is the basis of practical 3D sound devices.

The Alphasatron is an expansion card for the PC, sold by Crystal River Engineering, that performs the 3D sound convolution. The head-related transfer function,  $T(\mathbf{n},f)$ , is loaded into a digital signal processor on a Tahiti MultiSound card, and up to 16 user-defined sounds,  $S(t)$ , can be spatialized in real time. The cost of the system is \$750 retail, and I have successfully incorporated 3D sound effects in WorldToolKit applications using the Alphasatron.

## 2.2 HEAD-MOUNTED DISPLAYS

In 1994 Virtual I/O released the *iglasses!*, the first high-quality HMD for under \$1000. The *iglasses!* feature a 25 deg (H) x 9 deg (V) field of view, with 640 x 480 active matrix pixels. It weighs only 8 oz. and features a superb ergonomic design. The restricted field of view is the main limitation of this device, but for the price (\$850 retail)

it can't be beat for low-cost educational applications. A far better HMD is the VR4 by Virtual Research, Inc. It features a 48 deg (H) x 30 deg (V) field of view with resolution comparable to that of the *iglasses!*. The wide field-of-view is critical for total immersion simulations, and the VR4 would be the helmet of choice except for its price tag, \$7000, which makes it impractical for most classroom situations.

Finally, I note that WorldToolKit is the software of choice for PC-based VR applications because of its support for nearly all the VR peripherals on the market today. Sense8 rapidly introduced a driver for the *iglasses!* very soon after the product was released, and third party software vendors, like Crystal River Engineering, are working to make their library calls compatible with WorldToolKit conventions.

### 3. SUMMARY

During the 1996 Summer Faculty Fellowship Program I collaborated with other members of the CAVE lab to implement a VR simulation of the International Space Welding Experiment (ISWE) on a PC-based VR Workstation and on a Silicon Graphics Indigo. I created texture-mapped models of the ISWE's rotating sample drum, technology block, tool stowage assembly, sliding foot restraint, and control panel. I developed C code for control panel button selection and rotation of the sample drum. I also developed a serial interface box for the PC so that external control devices, similar to ones actually used on the ISWE, could be used to control virtual objects in the ISWE simulation.

**1996**

**NASA/ASEE SUMMER FACULTY FELLOWSHIP PROGRAM**

**MARSHALL SPACE FLIGHT CENTER  
THE UNIVERSITY OF ALABAMA**

**SYNTHESIS AND CHARACTERIZATION OF A CHITOSAN DERIVATIVE FOR  
ELECTRO-OPTICAL APPLICATIONS**

Prepared By:	Thomas Prastofer, Ph.D.
Academic Rank:	Assistant Professor
Institution and Department:	Albany College of Pharmacy Department of Physical Sciences and Mathematics
NASA/MSFC:	
Laboratory:	Space Sciences Laboratory
Division:	Microgravity Division
MSFC Colleague:	Donald Frazier, Ph.D.





Chitin is a naturally occurring polymer of  $\alpha(1-4)$  poly N-acetylglucosamine found primarily in the shells of crustaceans and insects. This polymer is chemically and thermally stable and physically durable as a consequence of hydrogen bonding which causes the alignment and ordering of the polymer chains into microcrystals which aggregate into sheets with chiral nematic order. Industry has attempted to take advantage of chitin's properties and low cost (chitin is a waste product of the shellfish industry) to produce durable fibers and other products. This has been largely unsuccessful because of chitin's non reactivity and insolubility.

Chitosan is the deacetylation product of chitin and retains many of the structural properties of chitin (3). Unlike chitin, chitosan is soluble in aqueous solution at reduced pH making it easier to be processed into fibers and films than chitin (4). Chitosan and its derivatives are now used in such commercial applications as wound dressings, waste water treatment, and in pharmaceuticals (5-8).

In this study, we have synthesized a chitosan derivative, N-para-nitrophenyl chitosan (NPNPC), as a model material with potential applications in electro optics.

NPNPC was synthesized by the nucleophilic substitution of the fluorine atom in para-fluoronitro aniline by the amino groups of chitosan in the following manner. 5 grams of chitosan were placed into 100 ml of DMSO. 4 grams of triethylamine, 20 grams of potassium carbonate, and 3 grams of para-fluoronitro aniline were added with stirring. The mixture was refluxed at 50°C with stirring for 4 days. The chitosan never dissolved in this mixture but swelled and eventually changed from a white to a yellow color. The polymer was recovered by filtration, washed with ethanol, dried in a vacuum dessicator and weighed. The reaction was estimated to be 80 - 90% complete based on the increase in the mass of the polymer. The solubility of the polymer is reduced when compared to chitosan as would be expected since the secondary amine generated is more difficult to protonate than the original primary amine. The polymer is not soluble (2% by weight) in 2% acetic or 2% formic acid but is soluble in 5% formic acid (1% by weight). The solution is very viscous but sonifying the sample for 30-60 seconds reversibly reduces the viscosity. NMR spectroscopy of NPNPC revealed the expected peaks for the desired product although the high viscosity of the material broadened the peaks.

Samples used for film preparation were washed repeatedly with acetone and baked dry. 1.5 ml samples of 1% NPNPC in 5% formic acid were sonified for 30 to 60 seconds and centrifuged at room temperature (10,000RPM in a microfuge) for 10 minutes to remove any debris or undissolved polymer. Films were produced by on slides coated with oriented teflon by spin coating or allowing the sample to dry without spinning. Films on quartz discs were formed by drying 50 microliters of sample with and without shearing.

The films were examined by light microscopy through crossed polars to detect areas in which ordering had occurred. Films formed on teflon coated glass slides with and without spinning showed regions where the polymers aligned as well as large amorphous regions. Small regions displaying chiral nematic ordering were also observed. Films formed on quartz discs without shearing displayed no ordering while films formed with shearing contained a number of different ordered domains including amorphous polarizing domains, chiral nematic domains, and linearly aligned domains.

Plans for continuing this work include optimizing the formation of ordered films, comparing the NLO properties of both ordered and amorphous films, and the synthesis of other substituted chitosans.

### Acknowledgments:

I gratefully acknowledge the assistance of Donald O. Frazier, Mark S. Paley, and David N. Donovan in this work.

### References:

1. *Nonlinear optical properties of organic molecules and crystals*; Chemla, D.S. and Zyss, J.; Eds.; Academic Press: Orlando FL, 1987; Vol.2.
2. *Introduction to nonlinear optical effects in molecules and polymers*; Prasad, P.N. and Williams, D.J., Eds.; John Wiley and Sons, Inc.: New York, 1991.
3. Samuels, R.J. *J. Am. Chem. Soc.* **1981**, 19, 1081-1105.
4. East, G.C. and Qin, Y. *J. Appl. Polym. Sci.* **1993**, 50, 1773-1779.
5. *Chitin*, Muzzarelli, R.A.A.; Pergamon, New York, 1977.
6. Caihua, N. and Yuwu, X. *J. Appl. Polym. Sci.* **1996**, 59, 499-504.
7. *J. Pharm. Res.* **1996**, 59, 588-593.
8. *Eur. J. Pharm. Sci.* **1996**, 4, 23-31.

1996

NASA/ASEE SUMMER FACULTY FELLOWSHIP PROGRAM

MARSHALL SPACE FLIGHT CENTER  
THE UNIVERSITY OF ALABAMA

AN INDEPENDENT EVALUATION OF THE FMEA/CIL HAZARD ANALYSIS  
ALTERNATIVE STUDY

Prepared By:	Paul S. Ray, Ph.D
Academic Rank:	Associate Professor
Institution and Department:	The University of Alabama Industrial Engineering Department Tuscaloosa
NASA/MSFC:	
Office:	System Safety and Reliability Office
Division:	Safety and Mission Assurance
MSFC Colleague	Edward H. Kiessling William C. Smith Gordon B. Hoskins-SAIC



## INTRODUCTION

The present instruments of safety and reliability risk control for a majority of the National Aeronautics and Space Administration (NASA) programs/projects consist of Failure Mode and Effects Analysis (FMEA), Hazard Analysis (HA), Critical Items List (CIL), and Hazard Report (HR). This extensive analytical approach was introduced in the early 1970's and was implemented for the Space Shuttle Program by NHB 5300.4 (1D-2). Since the Challenger accident in 1986, the process has been expanded considerably and resulted in introduction of similar and/or duplicated activities in the safety/reliability risk analysis. A study initiated in 1995, to search for an alternative to the current FMEA/CIL Hazard Analysis methodology generated a proposed method on April 30, 1996. The objective of this Summer Faculty Study was to participate in and conduct an independent evaluation of the proposed alternative to simplify the present safety and reliability risk control procedure.

## SAFETY/RELIABILITY RISK CONTROL METHODS

**Present Method:** The present method uses analysis and reporting in two phases. The analysis for hardware failures are documented in FMEA and critical items based on FMEA is reported in CIL. The analysis for hazards are documented in HA. The Hazard Report is prepared on the basis of HA and CIL report.

**Proposed Method:** The proposed method integrates all analysis in a single phase documenting in Risk Analysis and a single report for all potential critical failures and other hazards in Risk Management Report (RMR). The method fosters a comprehensive analysis rather than the present compartmentalized one.

## APPROACH OF THE STUDY

The evaluation approach has been to review the four basic risk control documents - FMEA, CIL, HA and HR for their functions, data elements contained in them, analytical process required to develop these, document user friendliness, and the effects of project characteristics.

## ANALYTICAL PROCEDURE

**Functions of the basic document:** FMEA and HA are both analytical documents. The FMEA contains information on failure modes/causes excluding some environmental and human factor causes while HA deals with all hazards including critical failures, environmental and human factor causes. Both these two have a number of common data and are suitable for integration to eliminate duplication and/or compartmentalization of thought process. Similarly CIL and HR are both reports based on analysis done in developing FMEA and HA. These are suitable for integration to eliminate duplication of common data elements, and cross referencing between CIL and HR.

Data Elements of the basic document: The documents FMEA/HA, CIL/HR vary significantly depending on the project size, complexity and nature. The contents of the documents are of the following types:

- Introductory/identification
- Analytical
- Analysis support
- Review and approval

Integration of the analysis and reports is expected to reduce number common/similar data in integrated documents by about 20 to 30 percent as shown in table 1 and 2.

Table 1

<u>Number of Data Elements in Analysis Document(s)</u>				
	<u>Present Method</u>		<u>Total</u>	<u>Proposed Method</u>
	<u>FMEA</u>	<u>HA</u>		<u>RA Total</u>
Introductory	4	4	8	4
Analytical	9	8	17	13
Support Data	5	4	9	7
Review/Approval	1	1	<u>2</u>	<u>1</u>
Total			36	25
Data elements reduced from 36 to 25 (30.6%)				

Table 2

<u>Number of Data Elements in Report(s)</u>				
	<u>Present Method</u>		<u>Total</u>	<u>Proposed Method</u>
	<u>CIL</u>	<u>HR</u>		<u>RMR Total</u>
Introductory	4	4	8	6
Analytical	8	8	16	13
Support Data	4	1	5	4
Review/Approval	2	2	<u>4</u>	<u>2</u>
Total			33	25
Data elements reduced from 33 to 25 (24.4%)				

Analytical Process: The present method of separating failure mode effect analysis (FMEA) and hazard analysis (HA) introduces duplication and compartmentalization in the thought process. There is a possibility of incomplete analysis due to responsibility of partial analysis assigned to different groups. To complete the hazard analysis, the safety group has to obtain hardware failure mode/cause data from the FMEA group requiring coordination and/or occasional duplication of analysis due to scheduled milestones. In addition, the proposed method

of documentation has scope of simplification resulting in faster comprehension at less effort. For example, key information can be summarized in a tabular format for a hypothetical case of "Premature Release Bolt Failure" that is currently contained in three separate CILs and a Hazard Report which contains four additional hazards. The key information would include the critical failures/hazards, critical items identification, number of items required, critical/hazard effect, failure/hazard causes, single and redundant failure identification, criticality categories, severity levels, likelihood of occurrence, and hazard classification. This would provide the user key information about a critical event without having to search four different reports. User activities like planning test/inspection points, verifying redundancy, certification of flight readiness, life extension of hardware etc. at various phases of a project life. The improved presentation, reduction of cross-referencing, reduction of number of documents to deal with will result in less user effort for higher productivity for the project as a whole.

User friendliness/cross referencing: The purposed integration of analysis and reports will reduce the need of cross referencing to a significant extent. Two cases of Space Shuttle Program studied, indicated that the FMEA and/or CIL are referenced on an average of twenty-two times for each CIL or five times for each failure cause. The need of so much cross referencing between the CIL and HR, imposing a significant amount of time and effort on analyst, will be eliminated in the integrated system.

Document Retention, Storage, and Retrieval: The proposed integrated system will reduce the number of documents to retain, store, and retrieve and as such reduce the time required for assessment of safety and reliability risks in a program/project.

Effect of Project characteristics: The nature of size of a project will effect the risk management process significantly . A large and complex project will require extensive analysis while a small and simpler project may require only environmental/human error type hazards and no critical failure type hazards. This difference will result in substantially more savings for a larger project. However the integrated approach will result in some savings in all cases.

## MERITS OF THE PROPOSED METHOD

The proposed method appears to have several advantages over the current procedure as listed below:

- Focus on a single and integrated analysis process instead of the present compartmentalized system is likely to produce more comprehensive safety/reliability risk analysis. The integration will eliminate the possibility of critical situations being left out of analysis due to partial work done by each group.
- Integrated risk analysis and reporting process will greatly reduce the coordination required now between two groups FMEA/CIL and HA/HR.



- Duplication of common data elements will be eliminated in the analysis as well as in the reporting documents. This will reduce the volume of reports and result in a reduction in the effort required to review and comprehend the safety/reliability risk status.
- The possibility of occasional duplication of analysis due to different time constraints for different groups will also be eliminated.
- All safety/reliability risk data will be submitted simultaneously for review and approval to appropriate authorities. This will eliminate duplication of review/approval process.
- A more effective documentation method (e.g. tabular format, etc.), will improve comprehension of the status at a glance and reduce the frequent referencing to pages of multiple documents.
- Recording, storing, and maintaining a significantly lower volume of documents during the life time of a program will result in a considerably large savings in manpower and cost.

## RECOMMENDATIONS

In view of the substantial merits of the proposed integrated system over the present FMEA/HA and CIL/HR, the following recommendations are made:

- Develop the final formats for:
  - Risk Analysis Worksheet, and
  - Risk Management Report
- Continue to develop requirements and guidelines detailing method to follow with clear definitions of limits for analysis and reporting.
- Continue the independent and concurrent evaluation, as continuation of the Summer Research Program (1996) of The University of Alabama during the development of the proposed risk management system.
- Conduct a test run and/or parallel run of the proposed method, preferably for an in-house project.
- Debug the weak points from the system, on the basis of the test/parallel run.
- Arrange for orientation of the analysts in the proposed integrated process.
- Implement the proved-in integrated system of safety/reliability risk analysis for the future programs/projects.

## COMMENTS

The present evaluation study covered only the basic thought process and the development of documentation required to support the system. The proposed system does not exclude any analytical technique e.g. checklists, fault trees, but propose to use these as required in a cost effective way. The indication of savings at this stage (20 to 40 %) is approximate but savings will result from integrated thought process, improvement in documentation format, reduction of volume and number of documentation, and reduced effort for users at various phases of a project life.

## ACKNOWLEDGMENT

It is to acknowledge the extensive help I received from Mr. Gordon B. Hoskins of Science Applications International Corporation (SAIC) in studying the Safety/Risk Analysis process at MSFC/NASA. It would have been impossible to complete this study without his help within a few weeks of the Summer Fellowship Program (1996).

## REFERENCES

1. Department of Defense. Military Standard-System Safety Program Requirements. MIL-STD-882C. Department of Defense, January 19, 1993.
2. JSC-NASA. Methodology for Conduct of Space Shuttle Program Hazard Analysis. NSTS-22254, Revision B, Change 4. JSC-NASA, December 30, 1993.
3. JSC-NASA. Requirements for Preparation and Approval of Failure Modes and Effects Analysis (FMEA) and Critical Items List (CIL). NSTS-22206, Revision D, Change 24. JSC-NASA, July 13, 1995.
4. Reliability and Quality Assurance Publication-NASA. Safety, Reliability, Maintainability and Quality Provisions for the Space Shuttle Program. NHB 5300.4 (1D-2). Reliability and Quality Assurance Publication-NASA, October, 1979.
5. Space Station Freedom Program Office-NASA. Safety Analysis and Risk Assessment Requirements. SSP 30309, Revision D. Space Station Freedom Program Office-NASA, June 1993.
6. Science Applications International Corporation. Failure Mode and Effects Analysis (FMEA), Critical Items List (CIL) and Hazard Analysis Alternative Study Including A Proposed Risk Assessment Method. Interim Report, SAIC, February 26, 1996
7. Science Applications International Corporation. Failure Mode and Effects Analysis (FMEA), Critical Items List (CIL) and Hazard Analysis Alternative Study Including A Proposed Risk Assessment Method. Final Report, SAIC, April 30, 1996
8. Science Applications International Corporation. Risk Assessment Requirements Document. (Draft) Interim Report, SAIC, June 3, 1996
9. United Technologies USBI. Critical Items List for Space Shuttle Solid Rocket Booster And Range Safety Command Destruct System. USBI-RA-21, Item Code 60-03-12. United Technologies USBI, March 1, 1994.
10. United Technologies USBI. SRB Flight Systems Hazard Analysis Report, Boost Phase, B-60-05 Thermal Curtain Failure. USBI-49220-RA-22-B-60-05, Item Code 60-03-12. United Technologies USBI, March 1, 1994.



**1996**

**NASA/ASEE SUMMER FACULTY FELLOWSHIP PROGRAM**

**MARSHALL SPACE FLIGHT CENTER  
THE UNIVERSITY OF ALABAMA**

**INVESTIGATION OF MACHINE DESIGN FOR FRICTION STIR WELDING**

Prepared By: Peter L. Romine, Ph.D.

Academic Rank: Assistant Professor

Institution and Department: Alabama A&M University  
Department of Engineering Technology

NASA/MSFC:

Laboratory: Materials and Processes  
Division: Metallic Materials and Processes  
Branch: Metallurgical Research and Development Branch

MSFC Colleagues: Jeff Ding  
Chip Jones



## Introduction

The process of joining two pieces of metal together has not significantly changed over the last few decades. The basic idea used is to bring the pieces together and apply enough heat to melt the metal at the interface. The molten metal mixes and after cooling forms a strong joint. This process is called the fusion process. The most significant difference between the many fusion processes is how the heat is generated and applied. The Welding Institute (TWI), in Great Britain, has recently patented an innovative application of mechanical friction. TWI designed a tool and process called Friction Stir Welding (FSW) that uses friction to heat the metal to within a few hundred degrees Fahrenheit of melting, just to the point of being plastic-like. The tool then stirs the plasticized metal together forming a joint that has been shown to be as good or better than an equivalent fusion joint. The FSW process is well suited for the joining of the aluminum alloys used in the aerospace industry. The relatively low melting point of aluminum eliminates the requirements for exotic materials for pin tool design. The FSW process has been successfully used to join alloys such as 7075 which were before considered "unweldable", and aluminum-lithium 2195 which exhibits many problems when fusion welded.

The objective this summer was to investigate the design of a FSW system that could take this process from the laboratory to the manufacturing floor. In particular, it was the goal of my NASA colleague to develop a concept for applying the FSW process to the manufacturing of aluminum cryogenic oxygen and hydrogen tanks, of the sort used to make the Shuttle External Tank. Much more was accomplished this summer than was planned because of NASA's extreme interest in applying the friction process to the repair of small defects found in the fusion welds of the new Super Light Weight External Tank (SLWT). The SLWT is being made of 2195 which has presented many problems in weldability for initial welds and repair welds. It has been common with 2195 for small defects to turn into big defects after several attempts at traditional fusion repair methods. The fusion process combined with the 2195 alloy has led to problems with penetration, porosity, and residual stress. Preliminary tests have indicated that using the FSW process to repair through fusion welds leads to improved mechanical properties. For this purpose we traveled to the Michoud Assembly Facility near New Orleans Louisiana where the external tanks are manufactured by the Lockheed-Martin Aerospace Corporation. Our purpose there was to examine the actual welding tooling used on the tank to investigate the feasibility of using the FSW process. Our conclusion was that replacing fusion welding with FSW on existing welding fixtures was not going to be easy because of several issues: 1) the fixturing was designed to hold the parts together with zero forces exerted by the welding process, not the thousands of pounds of force due to the FSW process; 2) in most cases, sufficient room was not available on the backside of the welding area for the FSW backup tooling; and 3) in most cases, the modifications could not be made without impacting the regular operation of the tools. My goal after this point was to more accurately determine the FSW loads and if variation in the parameters could be used to reduce this load.

### The Friction Stir Welding Facility at MSFC

To experiment with the FSW process you need a FSW pin tool, a CNC milling machine, or similar, capable of rotating the pin tool to at least 500 RPM and pushing in the axial direction with at least 8000 pounds of force, and a positioning device or holder robust enough to take the axial loads without significant flexing.

The Metals Process Development Branch in building 4711 has such a facility. Their system consists of a very robust Kearney&Trecker five-axis CNC milling machine and an automated data acquisition computer (ADAC), Figure 1.

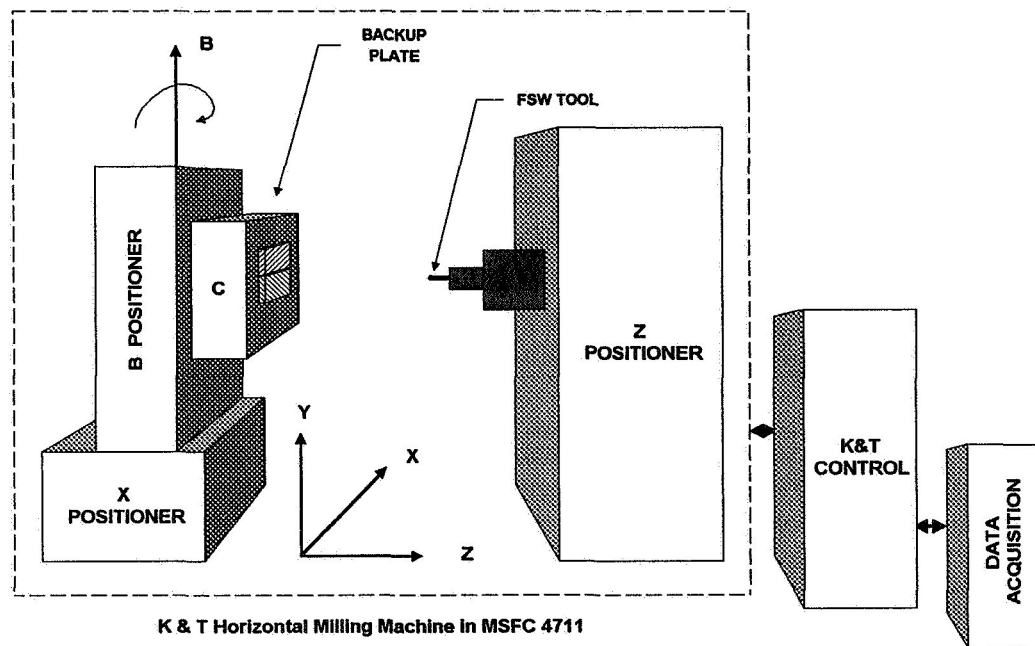


Figure 1. Friction Stir Welding System at MSFC.

### The Initial Concept for a FSW System

I worked as part of a team consisting of my NASA colleagues Jeff Ding, Chip Jones, and Dr. Arthur Nunes; Peter Oelegetz with the Rocketdyne Corporation, and Dr. Glenn Adams from the University of Arkansas, a SFFP fellow. The approach taken this summer was to develop an initial skeleton of a concept for the FSW system and then fill in the details as we discovered and quantified the parameters associated with the FSW process. I started the SFFP program two weeks early, so I developed the first concept, Figure 2. It was the vision of my NASA colleague that Dr. Adams would then carry on the mechanical design of the FSW system and I would fill in the electrical portions (instrumentation and controls).

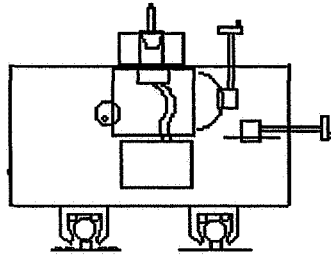


Figure 2. Initial Concept for a FSW Manufacturing System.

### Modeling the Friction Stir Process

Because of the newness of the FSW process and the proprietary (profit) attitude of the companies developing it, very little is publicly known about the science of this process. For this purpose it became obvious that it would be appropriate for NASA to lead the effort to model this process. In order to do this it was first necessary to clarify the parameters of the FSW process, that is, what are the independent and dependent variables. The independent parameters include rotational speed (RPM), shoulder depth, pin-to-backup distance, lead angle, and travel speed. The dependent parameters include the axial load, transverse load, and temperature. Drs. Nunes and Adams developed an initial analytical model for the process. I designed and implemented a small DOE to try to obtain a large-scale view of how the FSW parameters interact.

In the experiment, I chose to collect data for RPM, axial load (Z), transverse load (X), fixture load (B), and the temperature of the weld. I chose to use four thermocouples spaced evenly along the 10-inch square butt joint. A typical plot of load and RPM is shown in Figure 3, and a typical thermocouple plot is shown in Figure 4.

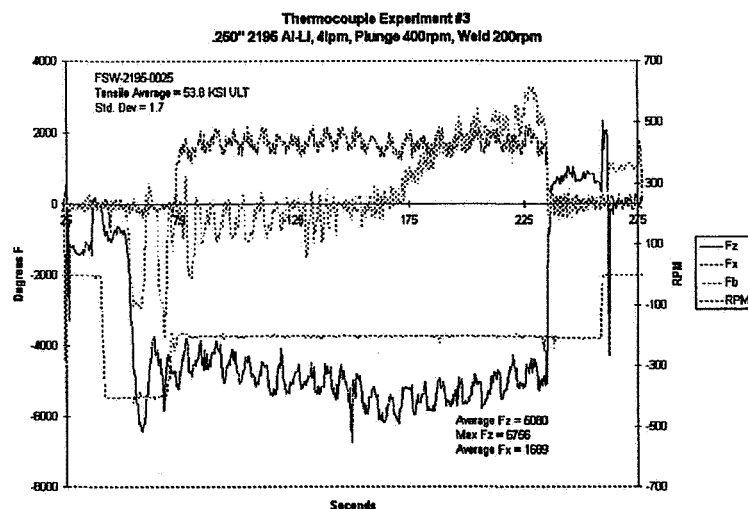


Figure 3. A typical plot of load and rotational speed.



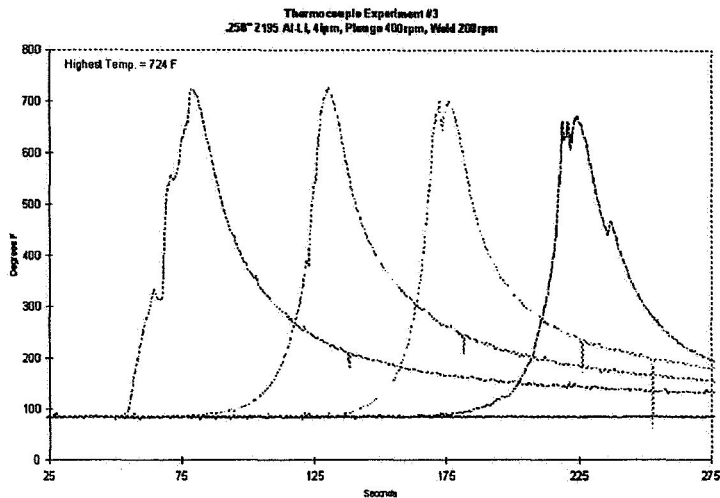


Figure 4. A typical plot of welding temperature.

### Discovery of the Backside Relief

A significant discovery was made during the thermocouple experiment. Pete Olegetz had the idea to machine four notches in the back of one plate to pass the thermocouples through so that they could be consumed in the weld but not destroyed by the shoulder. Observations made by Dr. Adams, Pete Olegetz, and myself of how the plasticized aluminum flowed nicely into the notches led to the V-groove backside relief experiment in which we intentionally produced a void on the backside of the butt joint. As in the thermocouple experiments, the plasticized aluminum flowed nicely into the V-groove filling it. The resulting weld did not exhibit the lack of penetration which commonly occurs in the FSW process when the pin is not sufficiently close to the backup, this can be seen in the microstructure of Figure 5. The resulting tensile fracture, elongation and variability of this data was significantly better than any other data collected at MSFC.

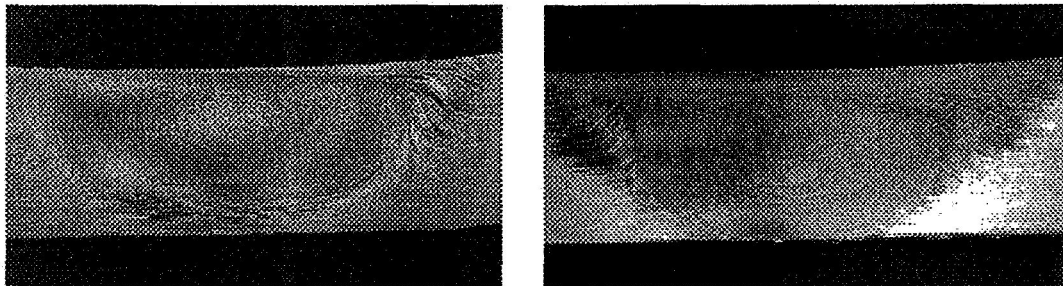


Figure 5. Microstructure without (left) and with (right) the V-groove backside relief.

**Summary and Conclusion**

The Friction Stir Welding process is sure to become a standard joining process for aluminum alloys, especially in the aerospace industry. The results of this summer have led to a better understanding of how variation of the parameters effects the loads, temperature, and resulting mechanical properties. It is strongly believed that using the FSW process for linear repairs is the superior technique for repairing defects in fusion welded aluminum-lithium. The backside relief is an obvious part of the final FSW technique and there is a clear need for a DOE to characterize the optimum relief that should be used.

**Acknowledgment**

The accomplishments of this summer would not have been possible without the technical input and direction from my NASA colleague, Jeff Ding of the Metals Processes Branch (EH23). I would also like to thank and commend all of the SFFP administrators and staff for a professionally and smoothly operated program.



1996  
NASA/ASE SUMMER FACULTY FELLOWSHIP PROGRAM

MARSHALL SPACE FLIGHT CENTER  
THE UNIVERSITY OF ALABAMA

WHAT DRIVES SPACECRAFT COST: A LOOK INTO HOW  
MATERIAL CHARACTERISTICS RELATE TO THE  
MATERIAL COMPLEXITY MULTIPLIERS

Prepared By:	Russell L. Rosmait
Academic Rank:	Associate Professor
Institution and Department:	Pittsburg State University Department of Engineering Technology
NASA/MSFC:	
Laboratory:	Engineering Cost Office
Division:	Program Planning Office
Branch:	Program Development
MSFC Colleague:	Joseph W. Hamaker



## INTRODUCTION

Today a variety of engineered materials are used to build the space vehicles and satellites that NASA, DOD and the aerospace community will use in future projects. These materials can be a significant part of the cost when designing and building these systems. Current cost models such as NASCOM, SEER-H and PRICE allow the cost analysis to select materials requirements during the development of the cost model. It should be noted however that some of these models do not always give the most detailed information with respect to material specifications for the given cost model. Instead the materials are defined within broad classification, giving questionable data with regard to specific material cost. It is the objective of this paper to present a summary of basic information on materials to assist the cost analyst in the development of their models. Specifically this paper will compare materials and their complexity multipliers to some specific material properties.

## COMPLEXITY MULTIPLIERS & PROPERTIES

For many years there has always been an attempt to correlate the cost of materials with some factor or factors. These factors can range from the material properties to material chemistry and composition and on to the actual manufacturing process itself.

Much work has been done to assist the cost estimator in the development of an accurate cost model. One item that is used are material complexity multipliers. These multipliers give the cost estimator a picture of how materials compare with each other with regard to their relative cost. One interesting question is "What Drives the Large Cost Difference?" Using material complexity multipliers generated for ramjet structures (NASA Report #CR-194428 p.54) this paper compares 1. density and the multipliers. 2. tensile strength and the multipliers and 3. Brinell hardness and the multipliers.

Figure 1 shows the comparison between density and the multipliers. Density was selected because weight is an important factor in aerospace design. Data from this comparison shows no relationship to the cost multiplier. One example is seen prominently. Three types of steel are shown, all have the same density yet the multiplier range from 1.6 to 3.4.

Figure 2 shows the comparison between tensile strength and the multipliers. It can be seen in this chart that there is some relationship between the tensile strength of the material and material complexity multiplier. Once again if we look at steel as tensile strength increases the multiplier increases. This is also seen when it comes to Nickel based alloys. There are three Nickel based materials shown in this chart. 1. Nickel 2. Inconel and 3. Haynes. These three do have some strength difference and as their strength goes up so does the multipliers.

Finally Figure 3 compares material hardness and the multipliers. The number of materials compared was reduced because of the lack of data points available. The information

seen on this chart is similar to that of the tensile strength chart. As hardness goes up so does the cost multiplier. If we look at the three Nickel based alloys however we have very similar hardness but the differences in the complexity multipliers is very great.

## RECOMMENDATIONS

From this data we can see that there is some correlation between strength and hardness to the material complexity multipliers. But within the Nickel based alloys group the question needs to be asked again Why the Large Cost Difference? Even for some of the other materials there are large difference in the multipliers. These difference, between similar materials and the multipliers need some further investigation to assist the cost estimator in producing accurate cost models. It is the recommendation of this study to look at other factor that may or could influence these large differences. The recommended areas for further investigation of the complexity multipliers are as following:

1. The actual material chemistry compared with the complexity multipliers.
2. The application of the materials compared with the complexity multipliers.
3. The manufacturing process used compared with the complexity multipliers
4. Material maturity compared with the complexity multipliers.

## CONCLUSIONS

These four areas should help to establish what factors influence the material complexity multipliers to most. We have seen in this paper the relationship between some material properties and the material complexity multipliers for ramjet structures. We have seen from this that the complexity multipliers are not driven by just material properties and that there must be other factors at work. finally recommendations have been given for future work to help determine these factor and assist the cost estimator in producing the most accurate cost model.

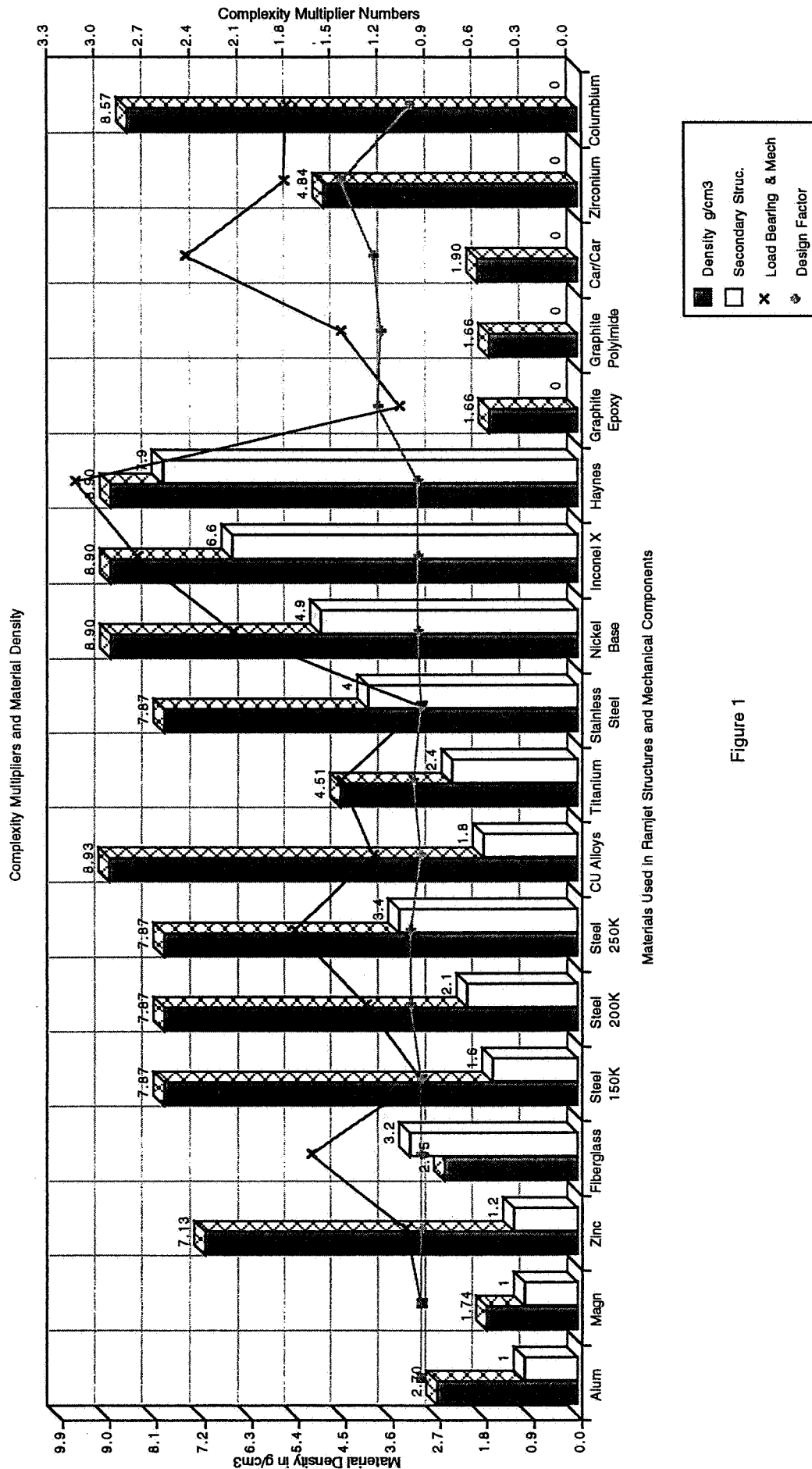
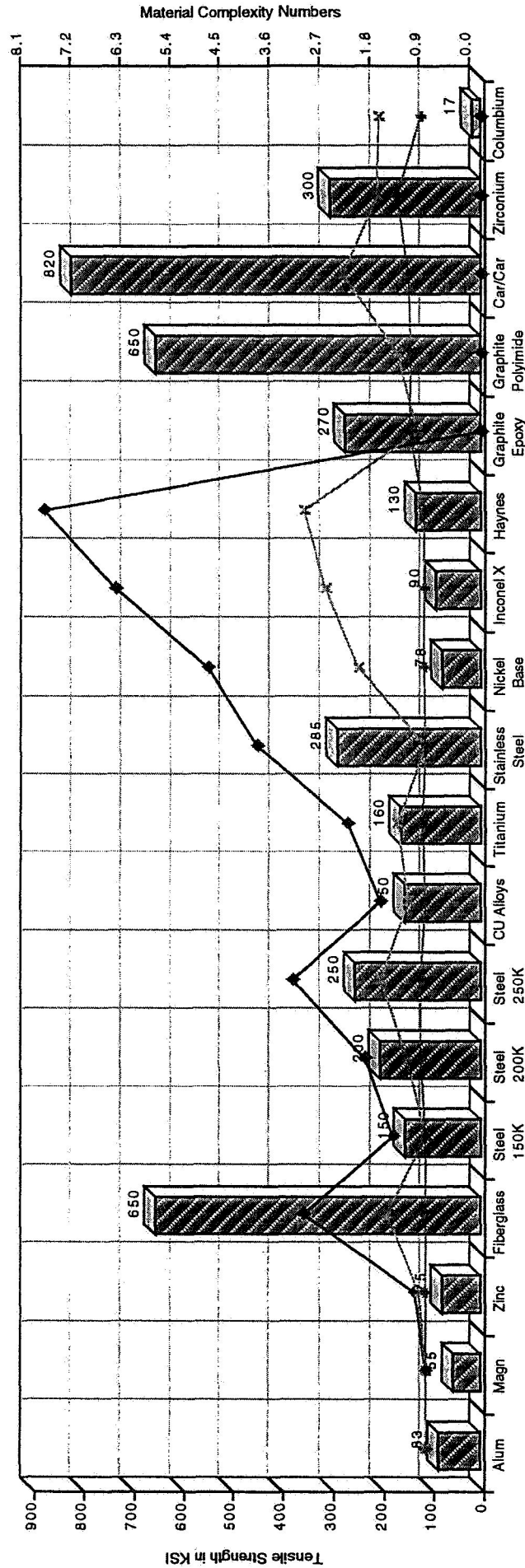


Figure 1

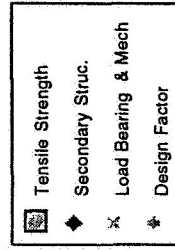


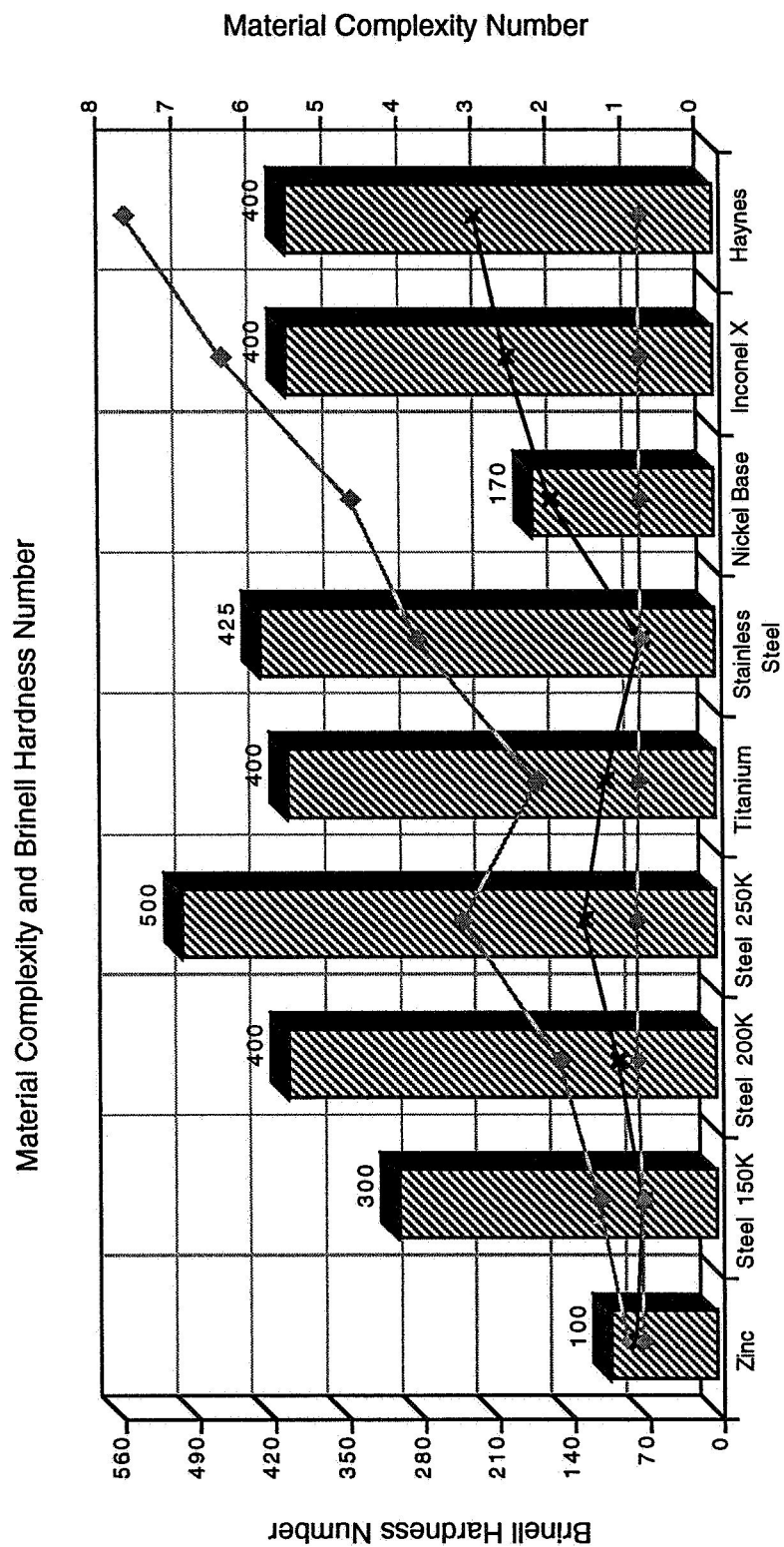
Material Complexity and Tensile Strength



Materials Used in Ramjet Structures and Mechanical Components

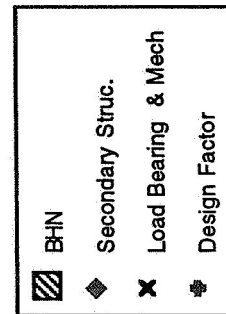
Figure 2





Materials Used in Ramjet Structures and Mechanical Components

Figure 3





1996

**NASA/ASEE SUMMER FACULTY FELLOWSHIP PROGRAM**

**MARSHALL SPACE FLIGHT CENTER  
THE UNIVERSITY OF ALABAMA**

**SCATTERING AND THE POINT SPREAD FUNCTION OF THE NEW GENERATION  
SPACE TELESCOPE**

Prepared By: Julian J. Schreur, Ph.D.  
Academic Rank: Associate Professor  
Institution and Department: Texas A&M University-Kingsville  
Physics Department

NASA/MSFC:

Laboratory: Astrionics Laboratory  
Division: Optics and Radio Frequency Division  
Branch: Optics

MSFC Colleague: James Bilbro



## INTRODUCTION

Preliminary design work on the New Generation Space Telescope (NGST) is currently under way. This telescope is envisioned as a lightweight, deployable Cassegrain reflector with an aperture of 8 meters, and an effective focal length of 80 meters. It is to be folded into a small-diameter package for launch by an Atlas booster, and unfolded in orbit, as shown in Figure 1. The primary is to consist of an octagon with a hole at the center, and with eight segments arranged in a flower petal configuration about the octagon. The corners of the petal-shaped segments are to be trimmed so that the package will fit atop the Atlas booster. This mirror, along with its secondary will focus the light from a point source into an image which is spread from a point by diffraction effects, figure errors, and scattering of light from the surface. The distribution of light in the image of a point source is called a point spread function (PSF).

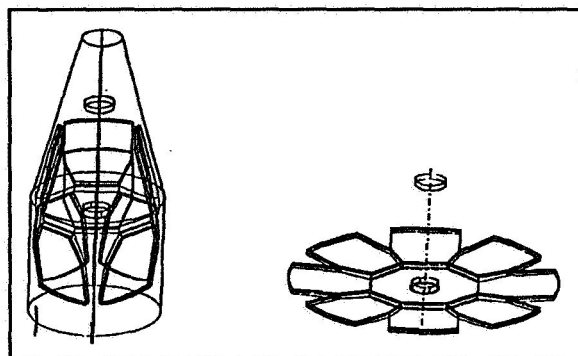


**Figure 1.** The folded and deployed configuration of the NGST.

The obstruction of the incident light by the secondary mirror and its support structure, the trimmed corners of the petals, and the grooves between the segments all cause the diffraction pattern characterizing an ideal point spread function to be changed, with the trimmed corners causing the rings of the Airy pattern to become broken up, and the linear grooves causing diffraction spikes running radially away from the central spot, or Airy disk. Any figure errors the mirror segments may have, or any errors in aligning the petals with the central octagon will also spread the light out from the ideal point spread function.

A point spread function for a mirror the size of the NGST and having an incident wavelength of 900 nm in Figure 2. Most of the light is confined in a circle with a diameter of 0.05 arc seconds. The ring pattern ranges in intensity from  $10^{-2}$  near the center to  $10^{-6}$  near the edge of the plotted field, and can be clearly discerned in a log plot of the intensity.

The total fraction of the light scattered from this point spread function is called the total integrated scattering (TIS), and the fraction remaining is called the Strehl ratio. The angular distribution of the scattered light is called the angle resolved scattering (ARS), and it shows a strong spike centered on a scattering angle of zero, and a broad, less intense distribution at larger angles.<sup>1</sup> It is this scattered light, and its

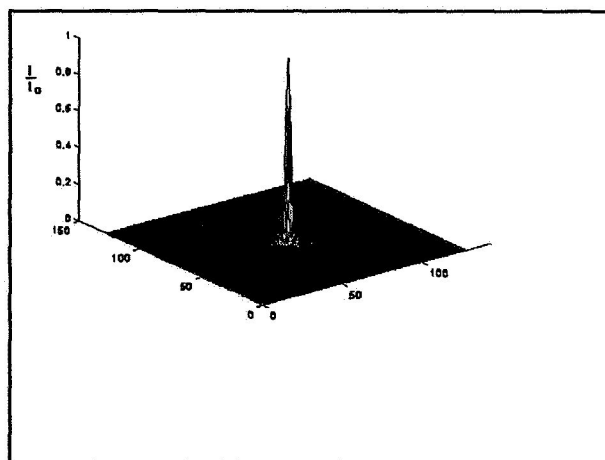


**Figure 2.** The point spread function for the NGST at 900 nm wavelength. The area covered is approximately 0.9 arc seconds on a side.

effect on the point spread function which is the focus of this study. The effects of the peculiar mirror shape, and of figure and alignment errors are left for a later date.

## CALCULATING THE PSF

A Microsoft® FORTRAN program, PFSARRAY, was written to compute the angle resolved scattering and point spread function of the NGST for a range of rms roughness values. This program was based on the program, ZERTAPER written by Mike Jones of Lockheed Martin Co. In Fort Worth, Texas. ZERTAPER computes the point spread function of a circular mirror with a central obstruction, and having known coefficients for the Zernike polynomials describing the figure errors. This program was converted from code for a Sun workstation to code for a PC. It was also modified to compute the angle resolved scattering, and total integrated scattering, and to use them to compute a final point spread function. PFSARRAY also stores the arrays representing the ARS and PSF on a floppy disk in a format which can be read by the software package MATLAB. MATLAB was used to plot this data, and to store the images in PCX files which can be imported into documents on the PC.

PSFARRAY begins by building a complex array representing a pupil function for the telescope. The primary mirror is covered by a square array 80 elements on a side. Each element falling on the mirror is given a magnitude of 1.0, and each element outside the mirror edge, or inside the central obstruction, is given a magnitude of zero. The coefficients of the Zernike polynomials are then used to find the wave front errors, and then the phase angles of the array elements, and from them the real and imaginary parts of the complex array elements.

The complex pupil function is then transformed by a fast Fourier transform subroutine into an original PSF array having a size of 256 by 256. The center 128 by 128 elements of this array are then taken as a complex image array. The square of the magnitudes of the image array produce the elements of an intensity array which is the actual original PSF for the telescope.

A profile of the surface roughness of a mirror can be used to produce an autocovariance function for the surface. A fast Fourier transform of the autocovariance yields the power-spectral-density (PSD) function of the surface microstructure. A default, normalized PSD function is stored in PSFARRAY, with an option to change it. This default function was taken from Bennett and Mattsson<sup>1</sup>, and came from a profile of a nickel mirror with an rms surface roughness of 5Å. The general form of this normalized function represents surfaces with roughly Gaussian distributions of surface height, regardless of what the rms roughness is measured to be. If the Fourier transform of the PSF is multiplied point for point by the PSD, the inverse Fourier transform of the product is the ARS for the telescope. PSF array uses its complex FFT subroutine to perform these operations.

The PSD function must be converted into an array for use by the FFT routine. The first task is to determine the size of an array element in this (spatial) frequency space. This array element size corresponds to the lowest frequency, or longest wavelength in the spatial plot of the PSF. The longest wavelength would be the array size,  $N$ , times the width of one array element,  $\Delta x$ . The inverse of this longest length is the element size in the frequency domain of the PSD function,  $\Delta \text{PSD}$ . The size of  $\Delta x$  is determined from the fact that the first dark ring in the Airy pattern occurs 4 array

elements from the center, and that distance is given by

$$r_o = \frac{\lambda D}{d} ,$$

where D is the diameter of the telescope objective, and d is the effective focal length. The result is that

$$\Delta PSD = \frac{1}{N} \left( \frac{8\pi d}{\lambda D} \right) .$$

The PSD array is filled in using the calculated element size by interpolation from the linear PSD function stored in the program.

A second fitting problem arises out of the fact that the PSD function is normalized, and produces an ARS distribution with an undetermined intensity level. The general form of the ARS is shown in Figure 3, and was taken from Maradudin and Mendez<sup>2</sup>. It looks like an inverted parabola, with a spike at the center. The light is scattered into a full hemisphere, but with decreasing intensity at increasing scattering angles,  $\theta_s$ . The same amount of scattered light, if uniformly intense would fill a solid angle of 3.7 steradians. The area under the ARS curve is simply the total integrated scattering (TIS), which is calculate from the rms surface roughness,  $\delta$ , and the incident wavelength,  $\lambda$ , by the relation given by Bennett and Mattsson<sup>1</sup>,

$$TIS = \left( \frac{4\pi\delta}{\lambda} \right)^2 .$$

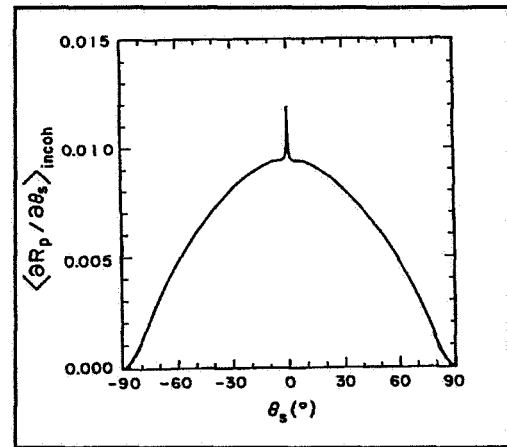


Figure 3. ARS for a silver surface with a TIS of 1.9%.

From the TIS, the intensity at the top of the inverted parabola which would be scattered into a solid angle the size of one array element in the PSF array may be calculated. Since the intensity of the ARS was still decreasing at the edge of the ARS array, it was assumed it would continue to decrease by a factor of ten before it reached the nearly horizontal portion of the general ARS function. This method of fitting the calculated ARS to the TIS is somewhat inexact, but should not cause substantial errors in the intensities of the ARS array.

$$Strehl = e^{-\left( \frac{4\pi\delta}{\lambda} \right)^2} .$$



The Strehl ratio is given by the expression<sup>3</sup>, It is the fraction of the incident light that is not scattered. If the original PSF of the telescope is diminished by the Strehl ratio, and the ARS, calculated as described above, are added together, the result is the final PSF of the telescope<sup>4</sup>.

## RESULTS

The ARS and PSF arrays for a telescope the size of the NGST were calculated for a number of rms roughness values, ranging from 5A to 500A. Figure 4 shows the intensity of the scattered light for an rms roughness of 500A. As can be seen, the intensity is  $10^{-9}$  of the intensity in the PSF. This has a negligible effect when added to the PSF. On the other hand, this large a surface roughness produces a Strehl ratio of only 0.51, meaning that the intensity of the light in the PSF has been cut nearly in half by the light which was scattered out of it. One would not like to lose this much light from the image.

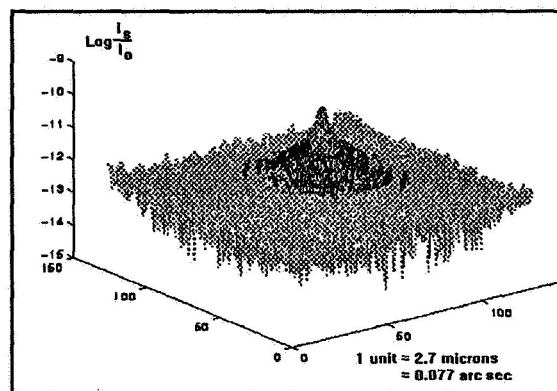


Figure 4. ARS for a surface roughness of 500A.

Figure 5 shows a cross section through the center of the PSF array for a roughness of 100A. Here the Strehl ratio is 0.98, and at an rms roughness of 50A it would be 0.995. In Figure 5 the central disk of the Airy pattern, and the surrounding bright rings can easily be seen, and there is essentially no contribution by scattered light. At longer wavelengths the scattered light would have even less effect.

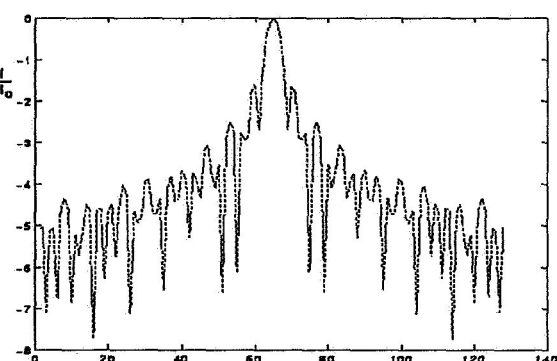


Figure 5. The PSF with 100A rms surface roughness

## CONCLUSION

Scattered light will not degrade the image quality of the NGST. A Strehl ratio, or TIS value, which will not appreciably diminish the intensity of the original PSF is sufficient to specify an acceptable finish of the mirror. A value of 50A for the rms roughness would have a negligible effect on the image.

## BIBLIOGRAPHY

1. J. M. Bennett, L. Mattsson, "Introduction to Surface Roughness and Scattering", Optical Society of America, 1989.
2. A. A. Maradudin, E. R. Mendez, Enhanced Backscattering of Light from Weakly Rough, Random Metal Surfaces, 1993, Applied Optics, 32, 3335.
3. P. N. Swanson, J. B. Breckinridge, A. Diner, R. E. Freeland, W. R. Irace, P. M. McElroy, A. B. Meinel, A. F. Tolivar, System Concept for a Moderate Cost Large Deployable Reflector (LDR), 1986, Optical Engineering, 25, 1045.
4. P. Glenn, Space Telescope Performance Prediction Using the Optical Surface Analysis Code (OSAC), 1986, Optical Engineering, 25, 1026.
5. Bidirectional Scattering Distribution Function: a Systematized Bibliography, 1991, J. Res. Natl. Inst. Stand. Technol. 96, 215.



**Dr. Eugene A. Olsen  
Associate Professor  
Department of Management & Marketing  
The University of Alabama in Huntsville**

**Technical Training Office  
Management of Technology**

**Mr. Robert McAnnally, MSFC Colleague**

**Abstract**

**Not available at time of printing**



1996

NASA/ASEE SUMMER FACULTY FELLOWSHIP PROGRAM

MARSHALL SPACE FLIGHT CENTER  
THE UNIVERSITY OF ALABAMA

ELECTRON FLOW TO A SATELLITE AT HIGH POSITIVE POTENTIAL

Prepared by:	John W. Sheldon, Ph.D.
Academic Rank:	Professor
Institution and Department:	Florida International University Physics Department

NASA/MSFC:

Laboratory:	Space Sciences Laboratory
Division:	Space Plasma Physics
Branch:	Magnetospheric Physics

MSFC Colleague:	Nobie H. Stone, Ph.D.
-----------------	-----------------------



## INTRODUCTION

The Tethered Satellite System (TSS) is designed to deploy a 1.6 m diameter spherical satellite a distance of 20 km above the space shuttle orbiter on an insulated conducting tether. Because of the passage of the conducting tether through the earth's magnetic field, an emf is generated producing a positive satellite potential of about 5000 V. Electron flow under the influence of this high positive potential is the focus of the present analysis.

The ionospheric parameters at TSS orbit altitude are; thermal velocity of electrons,  $1.9 \times 10^5$  m/s, thermal velocity of the ions,  $1.1 \times 10^3$  m/s, velocity of the satellite  $8 \times 10^3$  m/s. The electrons, with a Debye length,  $\lambda_D = 0.49$  cm, spiral about the earth's magnetic field lines (0.4 Gauss) with a radius of about 3 cm and the ions spiral with a radius of 5 m. Under these conditions, the electron thermal energy,  $kT$  is 0.17 eV. The TSS satellite radius,  $r_p$  is 163 Debye lengths.

There is an extensive literature on the interaction of satellites with the near-earth ionospheric plasma. The space charge limitation to the electron current collected by a sphere at positive electrical potential was calculated by Langmuir and Blodgett (1924). Parker and Murphy (1967) recognized the importance of the influence of the earth's magnetic field and used the guiding center approximation to calculate the electron current collected by a positive charged satellite. More recently Ma and Schunk (1989) have calculated the time dependent flow of electrons to a spherical satellite at positive potential utilizing numerical methods and Sheldon (1994) used similar methods to solve this problem for the steady state.

In order to analyze some of the phenomena that occurred in the ionosphere during the TSS flights, it would be useful to have analytic expressions for these electron flows. The governing equations are very complex and an exact analytical solution is not likely. An approximate analytical solution is feasible however, and the results of one attempt are presented herein.

## MATHEMATICAL MODEL

Electron flow to the spherical satellite is modelled here by the use of the cold plasma one-fluid momentum and continuity equations with the Poisson equation used previously [Sheldon (1994)]. In the present calculation, it is assumed that there will be a sheath region around the satellite devoid of ions due to positive satellite potential being much higher than the ram ion energy. Electrons drift toward this sheath along the earth's magnetic field lines with an average velocity  $(kT/m)^{1/2}$ , neglecting the average initial velocity due to their ambient spirals. At the outer boundary of this sheath there will be a negative space charge potential barrier approximately equal in magnitude to the electron ambient thermal energy. The governing



equations are written in non-dimensional spherical coordinates  $(r, \theta, \phi)$  with the magnetic field aligned with the polar axis. The steady-state momentum equations for  $u_r$ ,  $u_\theta$  and  $u_\phi$ , the  $r$ ,  $\theta$ , and  $\phi$  components of the average velocity of the electron flow, are then:

$$u_r \frac{\partial u_r}{\partial r} + \frac{u_\theta}{r} \frac{\partial u_r}{\partial \theta} - \frac{u_\theta^2}{r} - \frac{u_\phi^2}{r} - \frac{\partial V}{\partial r} + B u_\phi \sin \theta = 0 \quad (1)$$

$$u_r \frac{\partial u_\theta}{\partial r} + \frac{u_\theta}{r} \frac{\partial u_\theta}{\partial \theta} + \frac{u_\theta u_r}{r} - \frac{u_\phi^2}{r} \cot \theta - \frac{1}{r} \frac{\partial V}{\partial \theta} + u_\phi B \cos \theta = 0 \quad (2)$$

and

$$u_r \frac{\partial u_\phi}{\partial r} + \frac{u_\theta}{r} \frac{\partial u_\phi}{\partial \theta} + \frac{u_r u_\phi}{r} + \frac{u_\phi u_\theta}{r} \cot \theta - B u_r \sin \theta - B u_\theta \cos \theta = 0 \quad (3)$$

where  $r$  is in units of  $\lambda_D$  and the velocities are in units of  $u_A = (kT/m)^{1/2}$ , where  $m$  is the electron mass. The electric potential energy,  $V(r, \theta)$  is in units of  $kT$  and  $B = \omega_c / \omega_{ep} = 0.2$ , where  $\omega_c$  is the electron cyclotron frequency in the earth's magnetic field and  $\omega_{ep}$  is the electron plasma frequency. The continuity equation is

$$\frac{1}{r} \frac{\partial}{\partial r} (r^2 n u_r) + \frac{1}{\sin \theta} \frac{\partial}{\partial \theta} (\sin \theta n u_\theta) = 0 \quad (4)$$

where  $n(r, \theta)$  is the electron density in units of the ambient electron density,  $n_A$  and Poisson's equation is

$$\frac{\partial}{\partial r} (r^2 \frac{\partial V}{\partial r}) + \frac{1}{\sin \theta} \frac{\partial}{\partial \theta} (\sin \theta \frac{\partial V}{\partial \theta}) = n r^2 \quad (5)$$

## SOLUTION

In order to get an approximate solution to Eqs(1)-(5) the magnetic field parameter,  $B$  is considered a perturbation parameter. Using the perturbation expansion in (1)-(5), the zero order equations (no magnetic field) are,

$$u_r^0(r) \frac{\partial u_r^0(r)}{\partial r} - \frac{\partial V^0(r)}{\partial r} = 0 \quad (6)$$

$$\frac{1}{r} \frac{\partial}{\partial r} [r^2 n^0(r) u_r^0(r)] = 0 \quad (7)$$

$$\frac{\partial}{\partial r} (r^2 \frac{\partial V^0(r)}{\partial r}) = n^0(r) r^2 \quad (8)$$

The equations to first order in B are

$$\frac{\partial}{\partial r} [u_r^1(r, \theta) u_r^0(r) - V^1(r, \theta)] = 0 \quad (9)$$

$$u_r^0(r) \frac{\partial}{\partial r} [r u_\theta^1(r, \theta)] - \frac{\partial V^1(r, \theta)}{\partial \theta} = 0 \quad (10)$$

$$u_r^0(r) \left[ \frac{\partial u_\phi^1(r, \theta)}{\partial r} + \frac{u_\phi^1(r, \theta)}{r} - B \sin \theta \right] = 0 \quad (11)$$

$$\begin{aligned} \frac{1}{r} \frac{\partial}{\partial r} [r^2 (n^1(r, \theta) u_r^0(r) + n^0(r) u_r^1(r, \theta))] \\ + \frac{1}{\sin \theta} \frac{\partial}{\partial \theta} [n^0(r) u_\theta^1(r, \theta) \sin \theta] = 0 \end{aligned} \quad (12)$$

$$\frac{\partial}{\partial r} [r^2 \frac{\partial V^1(r, \theta)}{\partial r}] + \frac{1}{\sin \theta} \frac{\partial}{\partial \theta} [\frac{\partial V^1(r, \theta)}{\partial \theta} \sin \theta] = n^1(r, \theta) r^2 \quad (13)$$

The solution to the zero order Eqs.(11)-(13) can be obtained from Langmuir and Blodgett (1924). They considered a spherical electron emitter of radius  $r_m$  outside of a collector with negligible initial velocity of the electrons leaving the emitter. The boundary conditions were  $V^0(r_m) = 0$  and  $(dV^0/dr)_{r_m} = 0$ . In the present case the outer boundary condition is taken at a virtual cathode of radius  $r_0$ , where  $u_r^0(r_0) = 1$  and  $n^0(r_0) = 1$ .

With the boundary condition,  $u_\phi^1(r_0, \theta) = 0$ , Eq.(11) gives,

$$u_\phi^1(r, \theta) = B \frac{\sin \theta}{2r} (r_0^2 - r^2) \quad (14)$$

The remaining first order perturbation equations are linear and allow the separation of variables. Defining  $u_r^1 = g_r(r) g_\theta(\theta)$ ,  $u_\theta^1 = h_r(r) h_\theta(\theta)$ ,  $n^1 = k_r(r) k_\theta(\theta)$ ,  $V^1 = f_r(r) f_\theta(\theta)$ , the separated  $\theta$ -dependent Eqs. yield the following results

$$h_\theta(\theta) = -\sum_i A_i P_i'(\cos \theta) \sin \theta \quad (15)$$

$$f_\theta(\theta) = g_\theta(\theta) = \sum_i A_i P_i(\cos \theta) \quad (16)$$

$$A_\ell = \frac{2\ell+1}{2} \int_{-1}^{+1} (1-x) P_\ell(x) dx \quad (17)$$

$P_\ell(\cos\theta)$  is the Legendre polynomial of the first kind.

The r-dependent equations can be combined into a coupled set, of linear Eqs. which do not reduce to a standard form. An approximate solution is obtained by expanding the dependent variables in a Taylor's series about  $r_0$ . Only the leading terms are used here. Combining with the  $\theta$ -dependent functions, the final results largest order are

$$u_r(r, \theta) \approx u_r^0(r) = [(9/2) r_m^2 \alpha^2]^{1/3} \quad (18)$$

$$u_\theta(r, \theta) \approx \left(\frac{r_0}{r}\right) \sin\theta \quad (19)$$

$$u_\phi(r, \theta) \approx \frac{\sin\theta}{2r} (r_0^2 - r^2) \quad (20)$$

$$n(r, \theta) \approx n^0(r) = i \left(\frac{r_m}{r}\right)^2 \left[\frac{2\alpha^2}{9r_m^2}\right]^{1/3} \quad (21)$$

$$V(r, \theta) \approx V^0(r) = (2^{-1/3}) [(3/2) r_m \alpha]^{4/3} \quad (22)$$

$$\alpha(\gamma) = \gamma + 0.3\gamma^2 + 0.075\gamma^3 + 0.01432\gamma^4 + 0.00216\gamma^5 \quad (23)$$

where  $\gamma = \ln(r_m/r)$  and  $i = 4\pi r_0^2 n_A u_A$ .

The results for the azimuthal velocity, Eq.(14), are compared with the numerical results of earlier work [Sheldon(1994)] in Fig. 1. While the present method introduces considerable error in the actual values  $u_\phi$ , the radial profiles have the correct shape. Similar results were obtained for

$u_r(r,\theta)$ ,  $V(r,\theta)$  and  $n(r,\theta)$ .

## CONCLUSIONS

The perturbation method has allowed approximate determination of the electron flow in the proposed model. The previous numerical solution was more accurate, however the intention here was not accuracy, but a better understanding of the influence of the controlling parameters. This is available in Eqs(18)-(23).

## ACKNOWLEDGMENT

I am indebted to Dr. Nobie Stone for many helpful suggestions and stimulating conversations during the course of this work.

## REFERENCES

- Langmuir, I. and Blodgett, K. B., Phy. Rev. 24, 49 (1924).  
Ma, T. Z. and Schunk, R. W., Planet. Space Sci. 37, 21 (1989).  
Parker, L. W. and Murphy, B. L., J. Geophys. Res. 72, 1631 (1967).  
Sheldon, J. W., J. Geophys. Res. 99, 6227 (1994).

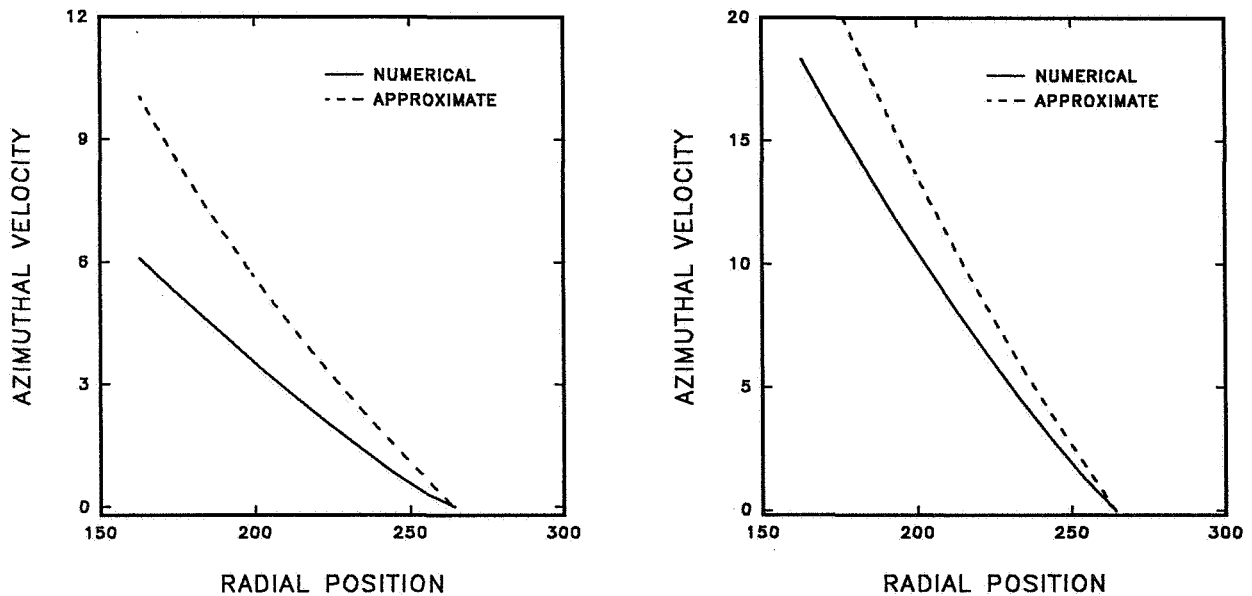


Figure 1. Radial profiles of the azimuthal electron velocity.  $V_p=1000$ . Nondimensional units  $\lambda_D$  and  $u_A$  defined in text. (a)  $\theta=22.5^\circ$ , (b)  $\theta=67.5^\circ$ .



**1996**  
**NASA/ASEE SUMMER FACULTY FELLOWSHIP PROGRAM**

**MARSHALL SPACE FLIGHT CENTER**  
**THE UNIVERSITY OF ALABAMA**

**ANALYSIS AND MODELING OF A TWO-PHASE JET PUMP OF A FLOW  
BOILING TEST FACILITY FOR AEROSPACE APPLICATIONS**

Prepared By:	S.A. Sherif, Ph.D.
Academic Rank:	Associate Professor
	Justin M. Steadham, Undergraduate Student
Institution and Department:	University of Florida Department of Mechanical Engineering
NASA/MSFC:	
Laboratory:	Structures and Dynamics Laboratory
Division:	Thermal and Life Support
Branch:	Environmental Control and Life Support
MSFC Colleague:	Jon B. Holladay



## NOMENCLATURE

### Latin Symbols

$A$	cross-sectional area
$A_b$	cross-sectional area of plenum containing secondary fluid
$C_p$	specific heat at constant pressure
$C_v$	specific heat at constant volume
$D$	diameter
$F$	friction force
$f$	friction factor
$g$	acceleration of gravity
$L$	length
$\dot{m}$	mass flow rate
$p$	static pressure
$R_g$	gas constant
$r_a$	primary nozzle exit-to-mixing throat exit area ratio, $A_{ne}/A_{mi}$
$r_b$	secondary fluid plenum exit-to-mixing throat exit area ratio, $A_b/A_{mi}$
$r_e$	entrainment ratio, $\dot{m}_s / \dot{m}_n$
$r_p$	jet pump compression ratio, $(p_{de}-p_s)/(p_{ne}-p_{de})$
$T$	absolute temperature
$V$	velocity

### Greek Symbols

$\beta$	liquid phase-to-mixture mass ratio
$\gamma_g$	gas phase ratio of specific heats
$\epsilon$	heat transfer parameter, $(T_L-T_o)/(T_g-T_o)$
$\eta$	jet pump efficiency, $r_e r_p$
$\rho$	density
$\bar{\rho}$	distributed phase density over total mixture volume
$\sigma$	slip parameter, $V_L/V_g$

### Subscripts

$d$	zone of diffuser from downstream of shock to diffuser exit
$e$	exit
$g$	gas phase
$i$	inlet
$L$	liquid phase
$m$	mixing tube, mixture
$n$	primary nozzle
$o$	stagnation conditions
$s$	secondary fluid conditions at mixing throat entrance
$sd$	conditions downstream of re-equilibrium region of shock
$su$	conditions immediately upstream of shock
$u$	zone of diffuser from its inlet to upstream of shock

## INTRODUCTION

Jet pumps are devices capable of pumping fluids to a higher pressure employing a nozzle/diffuser/mixing chamber combination. A primary fluid is usually allowed to pass through a converging-diverging nozzle where it can accelerate to supersonic speeds at the nozzle exit. The relatively high kinetic energy that the primary fluid possesses at the nozzle exit is accompanied by a low pressure region in order to satisfy Bernoulli's equation. The low pressure region downstream of the nozzle exit permits a secondary fluid to be entrained into and mixed with the primary fluid in a mixing chamber located downstream of the nozzle. Several combinations may exist in terms of the nature of the



primary and secondary fluids in so far as whether they are single or two-phase fluids. Depending on this, the jet pump may be classified as gas/gas, gas/liquid, liquid/liquid, two-phase/liquid, or similar combinations.

The mixing chamber serves to create a homogeneous single-phase or two-phase mixture which enters a diffuser where the high kinetic energy of the fluid is converted into pressure energy. If the fluid mixture entering the diffuser is in the supersonic flow regime, a normal shock wave usually develops inside the diffuser. If the fluid mixture is one that can easily change phase, a condensation shock would normally develop. Because of the overall rise in pressure in the diffuser as well as the additional rise in pressure across the shock layer, condensation becomes more likely. Associated with the pressure rise across the shock is a velocity reduction from the supersonic to the subsonic range. If the two-phase flow entering the diffuser is predominantly gaseous with liquid droplets suspended in it, it will transform into a predominantly liquid flow containing gaseous bubbles (bubbly flow) somewhere in the diffuser.

Literature dealing with jet pumps is abundant and covers a very wide array of application areas. Example application areas includes vacuum pumps which are used in the food industry, power station work, and the chemical industry; ejector systems which have applications in the aircraft industry as cabin ventilators and for purposes of jet thrust augmentation; jet pumps which are used in the oil industry for oil well pumping; and steam-jet ejector refrigeration, to name a few. Examples of work relevant to this investigation includes those of Holmes et al. (1987), Cunningham and Dopkin (1974), Cunningham (1995), Elger et al. (1991), Marini et al. (1992), Jiao et al. (1990), Neve (1991), Bredikhin et al. (1990), and Fairuzov and Bredikhin (1995).

While past researchers have been able to model the two-phase flow jet pump using the one-dimensional assumption with no shock waves and no phase change, there is no research known to the authors apart from that of Anand (1992) which accounted for condensation shocks. One of the objectives of this research effort is to develop a comprehensive model in which the effects of phase slip and inter-phase heat transfer as well as the wall friction and shock waves are accounted for. While this modeling effort is predominantly analytical in nature and is primarily intended to provide a parametric understanding of the jet pump performance under different operating scenarios, another parallel effort employing a commercial CFD code is also implemented. The latter effort is primarily intended to model an axisymmetric counterpart of the problem in question. The viability of using the CFD code to model a two-phase flow jet pump will be assessed by attempting to recreate some of the existing performance data of similar jet pumps. The code will eventually be used to generate the jet pump performance characteristics of several scenarios involving jet pump geometries as well as flow regimes in order to be able to determine an optimum design which would be suitable for a two-phase flow boiling test facility at NASA-Marshall.

Because of the extensive nature of the analytical model developed, the following section will only provide very brief highlights of it, while leaving the details to a more

complete report submitted to the NASA colleague. This report will also contain some of the simulation results obtained using the CFD code.

## **HIGHLIGHTS OF THE ANALYTICAL MODEL**

This analysis deals with a jet pump whose primary fluid is a two-phase mixture and whose secondary fluid is either a subcooled or saturated liquid having the same chemical composition as the primary fluid. The two-phase primary fluid flows through a converging-diverging nozzle (primary nozzle) and exits at a high velocity and low pressure. The low pressure at the primary nozzle exit induces the flow of the secondary fluid which mixes with the primary fluid in a mixing section. The mixing section is typically comprised of two parts; a throat and a mixing tube. The mixing throat is a short converging section where the flow accelerates slightly and the pressure drops correspondingly. The mixing tube serves to enhance the mixing that has already started in the throat. Two common types of mixing may be employed in the mixing tube; constant pressure or constant area mixing. Literature dealing with this subject reports that the compression ratios of jet pumps employing constant-pressure mixing are a bit higher than those employing constant-area mixing. However, for the sake of simplicity, this analysis will deal with a jet pump employing constant-area mixing in the mixing tube. Nevertheless, because of the slight drop in pressure in the mixing throat, the mixing process in the latter will be handled using a more general set of fluid dynamical equations applicable to variable pressure/variable area mixing.

Because the cross-sectional area of the mixing tube is assumed constant, the pressures at the inlet and exit of the tube are assumed to take distinct values. The two-phase flow leaving the mixing tube enters a diffuser where it undergoes a normal shock across which the mixture pressure rises and the flow becomes subsonic. The flow downstream of the shock in the diffuser continues to decelerate while the pressure continues to rise until the fluid exits the diffuser.

While it is customary to expect some condensation in both the mixing tube and the diffuser primarily due to the rise in pressure, this analysis deals with a simplified case involving no phase change. Partial justification for this assumption is based on the hypothesis that the condensation of the gaseous phase due to the pressure rise may be offset by a counter effect due to the associated rise in temperature. While in a typical situation the former effect is more dominant than the latter, the hypothesis in question is assumed valid for purposes of simplifying the analysis a bit. While the model as presented does not account for phase change per se, the fact that the liquid phase-to-mixture mass ratio can be assigned separate values as we proceed from one zone to another gives the model some flexibility to artificially account for the possibility of phase change.

One of the objectives of this effort is to develop a generalized formulation for the jet pump compression ratio as well as the jet pump efficiency in terms of the relevant flow and heat transfer parameters and examine the conditions under which both quantities can be maximized. In order to achieve the above objectives, the jet pump will be divided into

several sections for purposes of performing the analysis. These segments are the primary nozzle, the mixing throat, the mixing tube, the diffuser upstream of the shock, the shock layer itself and the diffuser downstream of the shock.

### **Primary Nozzle**

The velocity, temperature, and pressure fields of both the liquid and gaseous phases for this segment of the jet pump have been resolved by Sherif et al. (1994) and the reader is advised to consult this reference as well as the longer version of this report for details.

### **Mixing Throat**

The mixing throat is a short converging section connecting the secondary fluid plenum to the mixing tube. The plenum also contains the primary nozzle. The secondary fluid is allowed to enter the mixing tube as a liquid mist by action of the pressure drop generated by the flow of the primary stream. This mechanism of introducing the secondary fluid is one of two mechanisms typically used in jet pumps. The volume of literature dealing with the mechanism described here is massive and includes the works of Francis et al. (1972) and Tsung (1972), to name a few. The other mechanism allows the secondary fluid to be directly injected employing spray nozzles stationed at an angle to the axis of the mixing tube. Literature dealing with this mechanism of injection is not as extensive and includes the work of Fairuzov and Bredikin (1995). Details of the mathematical treatment of this section can be found in the more detailed report submitted to the NASA colleague.

### **Mixing Tube**

The mixing tube is a constant-area duct downstream of the converging section labeled as the mixing throat. The analysis dealing with this section includes the effects of wall friction which can be expressed by:

$$F_m = \frac{\pi f_m L_m^2}{2} [\beta_m \sigma_m + (1 - \beta_m)] \left[ \beta_m \rho_{L,m} + \frac{(1 - \beta_m) p_m}{R_g T_{g,m}} \right] V_{g,m}^2$$

To give a flavor of the nature of the analysis, the equations that follow provide a complete set for computing the mixing tube exit velocity of the gas phase as well as the mixture exit pressure:

$$V_{g,me} = \left[ V_{g,mi}^2 - 2 \left\{ \frac{\beta_m \epsilon_m C_{L,m} + (1 - \beta_m) C_{p,g,m}}{1 - \beta_m + \beta_m \sigma_m^2} \right\} (T_{g,me} - T_{g,mi}) \right]^{\frac{1}{2}}$$

$$\begin{aligned}
p_{me} = & \frac{p_{mi} \left[ \frac{E_1}{2E_3} \text{Log}_e \{ (E_3 T_{g,mi} + E_4) T_{g,mi} \} + \left\{ \frac{2E_2 E_3 - E_1 E_4}{2E_3 E_4} \right\} \text{Log}_e \left\{ \frac{E_3 T_{g,mi}}{E_3 T_{g,mi} + E_4} \right\} \right]}{\left[ \frac{E_1}{2E_3} \text{Log}_e \{ (E_3 T_{g,me} + E_4) T_{g,me} \} + \left\{ \frac{2E_2 E_3 - E_1 E_4}{2E_3 E_4} \right\} \text{Log}_e \left\{ \frac{E_3 T_{g,me}}{E_3 T_{g,me} + E_4} \right\} \right]} \\
& + \frac{B_2 B_4}{2E_3 E_4} \left[ 2(E_1 E_4 - E_2 E_3) (E_3 T_{g,me} + E_4) \text{Log}_e (E_3 T_{g,me} + E_4) - (E_3 T_{g,mi} + E_4) \text{Log}_e (E_3 T_{g,mi} + E_4) \right] \\
& + 2E_2 E_3 \left[ (E_3 T_{g,me} + E_4) \text{Log}_e T_{g,me} - (E_3 T_{g,mi} + E_4) \text{Log}_e T_{g,mi} \right] \\
& + \left[ (2E_2 E_3 - E_1 E_4) E_3 \text{Log}_e E_3 - 2E_1 E_3 E_4 \right] (T_{g,me} - T_{g,mi}) \\
& + E_4 (E_2 E_3 - E_1 E_4) \left[ \left\{ \text{Log}_e (E_3 T_{g,me} + E_4) \right\}^2 - \left\{ \text{Log}_e (E_3 T_{g,mi} + E_4) \right\}^2 \right] \\
& - 2E_2 E_3 E_4 \left[ \text{Log}_e T_{g,me} \text{Log}_e (E_3 T_{g,me} + E_4) - \text{Log}_e T_{g,mi} \text{Log}_e (E_3 T_{g,mi} + E_4) \right] \\
& + (E_1 E_4 - 2E_2 E_3) E_4 \text{Log}_e E_3 \text{Log}_e \left( \frac{E_3 T_{g,me} + E_4}{E_3 T_{g,mi} + E_4} \right) + E_2 E_3 E_4 \left[ \left\{ \text{Log}_e T_{g,me} \right\}^2 - \left\{ \text{Log}_e T_{g,mi} \right\}^2 + \text{Log}_e \left( \frac{T_{g,mi}}{T_{g,me}} \right)^2 \right] \\
& + 2E_2 E_3 E_4 \text{Log}_e E_3 \text{Log}_e \left( \frac{T_{g,me}}{T_{g,mi}} \right) + \frac{2E_2 E_4^2}{T_{g,me} T_{g,mi}} (T_{g,me} - T_{g,mi}) \left[ 1 - \frac{E_4}{4E_3} \left( \frac{T_{g,me} + T_{g,mi}}{T_{g,me} T_{g,mi}} \right) \right. \\
& \left. + \frac{E_4^2}{9E_3^2} \left\{ \frac{T_{g,me}^2 + T_{g,me} T_{g,mi} + T_{g,mi}^2}{T_{g,me}^2 T_{g,mi}^2} \right\} \right] \Bigg] / \left[ \frac{E_1}{2E_3} \text{Log}_e \{ (E_3 T_{g,me} + E_4) T_{g,me} \} + \left\{ \frac{2E_2 E_3 - E_1 E_4}{2E_3 E_4} \right\} \text{Log}_e \left\{ \frac{E_3 T_{g,me}}{E_3 T_{g,me} + E_4} \right\} \right]
\end{aligned}$$

$$\begin{aligned}
B_2 &= \frac{\beta_m \epsilon_m C_{L,m} + (1 - \beta_m) C_{p,g,m}}{\sigma_m^2 \beta_m + (1 - \beta_m)} \\
B_4 &= \frac{4f_m L_m^2}{D_m^2} \rho_{L,m} \beta_m [\beta_m \rho_m + (1 - \beta_m)] \\
E_1 &= \frac{(1 - \beta_m + \beta_m \sigma_m) \{ 4f_m L_m^2 (1 - \beta_m)^2 - D_m^2 \} \{ \beta_m \epsilon_m C_{L,m} + (1 - \beta_m) C_{p,g,m} \}}{D_m^2 (1 - \beta_m) (1 - \beta_m + \beta_m \sigma_m^2)} \\
E_2 &= \frac{-2f_m L_m^2 (1 - \beta_m) (1 - \beta_m + \beta_m \sigma_m) \left[ (1 - \beta_m + \beta_m \sigma_m^2) V_{g,mi}^2 + 2 \{ \beta_m \epsilon_m C_{L,m} + (1 - \beta_m) C_{p,g,m} \} T_{g,mi} \right]}{D_m^2 (1 - \beta_m + \beta_m \sigma_m^2)} \\
E_3 &= \frac{[R_g D_m^2 (1 - \beta_m + \beta_m \sigma_m^2) - 4f_m L_m (1 - \beta_m) (1 - \beta_m + \beta_m \sigma_m) \{ \beta_m \epsilon_m C_{L,m} + (1 - \beta_m) C_{p,g,m} \}]}{R_g D_m^2 (1 - \beta_m + \beta_m \sigma_m^2)} \\
E_4 &= \frac{2f_m L_m^2 (1 - \beta_m) (1 - \beta_m + \beta_m \sigma_m) \left[ (1 - \beta_m + \beta_m \sigma_m^2) V_{g,mi}^2 + 2 \{ \beta_m \epsilon_m C_{L,m} + (1 - \beta_m) C_{p,g,m} \} T_{g,mi} \right]}{R_g D_m^2 (1 - \beta_m + \beta_m \sigma_m^2)}
\end{aligned}$$

### Diffuser Portion Upstream of the Shock

Equations describing the velocity of the gas phase and the mixture pressure upstream of the shock are given below:

$$V_{g,su} = \left[ V_{g,me}^2 - \frac{2\{\beta_m \epsilon_m C_{L,u} + (1 - \beta_m) C_{p,g,u}\}}{(1 - \beta_m + \beta_m \sigma_m^2)} (T_{g,su} - T_{g,me}) \right]^{\frac{1}{2}}$$
$$p_{su} = p_{me} \left( \frac{T_{g,su}}{T_{g,me}} \right)^{n_u}$$

### Shock Wave Analysis

Details of this analysis can be found in Jackson et al. (1996).

### Diffuser Portion Downstream of the Shock

Equations describing the velocity of the gas phase and the mixture pressure at the diffuser exit are given below:

$$V_{g,de} = \left[ V_{g,sd}^2 - \frac{2\{\beta_d \epsilon_d C_{L,d} + (1 - \beta_d) C_{p,g,d}\}}{(1 - \beta_d + \beta_d \sigma_d^2)} (T_{g,de} - T_{g,sd}) \right]^{\frac{1}{2}}$$
$$p_{de} = p_{sd} \left( \frac{T_{g,de}}{T_{g,sd}} \right)^{n_d}$$

## RESULTS OF CFD SIMULATION

Figures 1 and 2 provide sample results of simulating the flow in a jet pump for both a two-dimensional as well as an axisymmetric version of this problem.

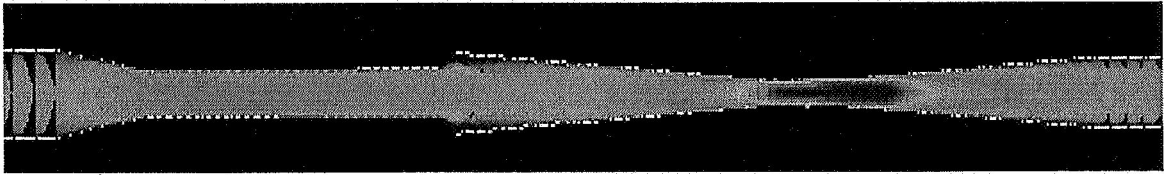


Figure 1. 2-D velocity profile.

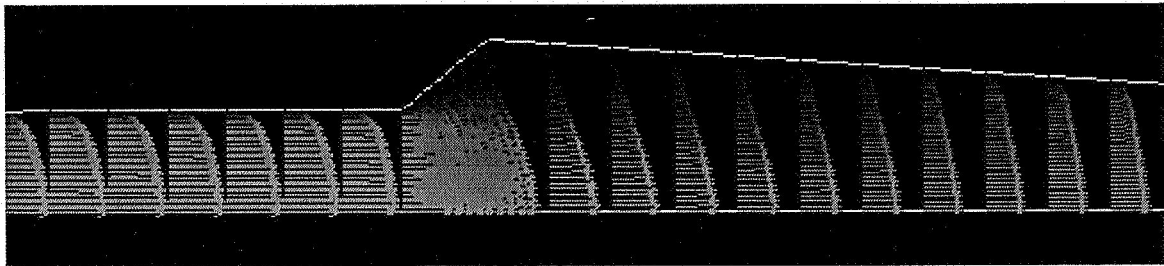


Figure 2. Axisymmetric velocity profile.

1996  
NASA/ASEE SUMMER FACULTY FELLOWSHIP PROGRAM

MARSHALL SPACE FLIGHT CENTER  
THE UNIVERSITY OF ALABAMA

COMMENTS ON SEE:  
COMPARATIVE ADVANTAGES AND EXPERIMENTAL CONSEQUENCES

Prepared By:	Larry L. Smalley, Ph.D. <sup>1</sup>
Academic Rank:	Professor
Institution and Department:	University of Alabama in Huntsville Department of Physics
NASA/MSFC:	
Laboratory:	Program Development
Division:	Payload & Orbital Systems
Branch:	Space Science & Application Group
MSFC Colleague:	Jonathon Campbell, Ph.D.

---

<sup>1</sup>Telephone: 205-890- 6276 ext 378;  
Email address: smalley@pluto.cs.uah.edu



## COMPARATIVE ADVANTAGES OF SEE

The Satellite Energy Exchange experiment measures the periodic, near-miss encounters between a *sheppard* satellite and a small test body (satellite) in approximately the same orbit about a primary. Several important experimental requirements have been chosen to enhance capabilities: (a) The satellite be flown in a sun-synchronous orbit at an altitude of about 1350 Km, (b) *Passive* temperature system stabilized by spacecraft axial rotation with sunshade baffles at the end of the spacecraft, (c) Test bodies with different material composition be available for experiments, (d) The containment spacecraft *fly* about the sheppard mass in a zero-g environment whereas the test bodies, experience average zero-g environment over an orbital period, (e) Primary attitude and station-keeping uses magnetic field alignment plus micro-Newton thrusters such as Field Emission Electric Propulsion, and (f) Very low power (nW) laser tracking systems minimize impulse delivered to test bodies.

With the above conditions, SEE has the capabilities: (1) Long duration (several years lifetime) flight experiment (2) Long-term, active (with historical time record), self-calibration of satellite mass distribution (capsule geodesy) over lifetime of the spacecraft. (3) Novel passive thermal stabilization systems designed to attain cryogenic temperatures around 78K. (4) Novel spacecraft stabilization systems. (5) Ability to measure  $G$  to 1 part in  $10^{6-7}$  depending on ultimate duration of experiment. (6) Ability to place limits on both temporal and spacial variations on  $G$ . (7) Ability to set experimental limits on the Post Newtonian parameters (PPN)  $\alpha_2$  and  $\zeta_2$ . (8) Ability to measure (or place limits on) the non Einsteinian eccentricity of the Earth-Sun system (and the parameter  $\alpha_1$ ) for long duration flight. (9) Ability to measure  $\Delta\dot{G}/G$  to 1 part in  $10^{12-13}$ .

The MiniSTEP, competes in a limited way with Project SEE. It is designed to improve the measurement of the equivalence principle by seven orders of magnitude using active, low temperature (1.8 K) cooling for SQUID based, differential superconducting circuits. The experiment consists of a small cylinder concentrically located within a larger cylinder at its null gravitational point. The satellite is operated in zero-g mode using four differential accelerometers consisting to two test bodies of different material composition. The SQUIDS are needed to measure test body motion to precisions of  $10^{-18}$  over a four orbit period. The entire satellite moves in a very precise zero-g mode since the accelerometers are rigidly attached to the satellite. This limits the experiment to an approximately six month due to limitations on helium storage used in cryogenic cooling and thrust control to maintain the zero-g operation .

## PARAMETRIC ANALYSIS OF EXPERIMENTAL DATA

The extraction of experimental limits on the PPN parameters involves the measurement of certain (postulated) effects that can occur in the satellite, test bodies, earth, moon, sun system as either measured on board the SEE satellite using laser tracking [sheppard-test body encounters] or using satellite laser-ranging experiments from Earth-based lasers to the SEE capsule [resonant earth-satellite-moon (or sun) configurations]. These experiments then give raw data that is related to various combinations of the PPN parameters. No *a priori*



values of PPN parameters (with the exception of Whitehead term) will be used that might predetermine the best statistical fit of the data. These relationships are described below.

## GRAVITATIONAL CONSTANT

For more than a decade, the poignant comments of the scientific correspondent and reviewer, John Maddox, Nature Magazine [310, 723, 30 Aug 1984] on the "Continuing doubt on gravitation" expresses even today the frustration in the usual torsional methods used to measure  $G$ . Even at the time of Maddox' editorial review, the most accurate measurement of  $G$  (and it's standard deviations) due to Luther and Towler (1982) fell entirely within the internationally accepted CODATA value of the time. There was at least some hope that more accurate experiments would steadily improve the statistical significance of future CODATA values . Recent experiments seem to have improved statistical and systematic error analysis, but these measurements differ amongst themselves by more than any of the standard deviations claimed. At least one of the mean values for  $G$ , with exceptionally good statistics due to the long, minutely detailed, and systematic ten-year experiment by the German Bureau of Standards, differs very radically from the most recent CODATA value for  $G$ . Arguably the combined value  $GM$  of about 1 part in  $10^7$  at the time of Maddox's comments has *improved* steadily by at least two orders of magnitude over the last decade [See the article by K. Nordtvedt on the continual improvment of data from lunar-laser ranging, "From Newton's moon to Einstein's moon," Physics Today, 49, 26 (1996).]. The value of  $G$  has stubbornly remained at the 1 part in  $10^4$  range. However it is the coupling constant  $G$  (and its subsequent renormalization in a unified theory) that *contains* many of the clues that will answer some of the more fundamental questions about unification of gravity with the other forces. That is, it must contain some residual *backbone* that shows up in a partial (perhaps strong-gravity) and eventually in an ultimate unification scheme.

The locally measured gravitational constant depends (in a generic theory) on the influence of external sources through its potential  $U_{ext}$  and its local motion moving with the velocity  $w_1$  with respect to a preferred frame . In the PPN framework this becomes

$$G_L = 1 - [4\beta - \gamma - 3 - \zeta_2]U_{ext} - \frac{1}{2}[\alpha_1 - \alpha_3 - \alpha_3 \left(1 - \frac{I}{m_1 r_p^2}\right)]w_1^2 + \frac{1}{2}\alpha_2 \left(1 - \frac{I}{m_1 r_p^2}\right) (w_1 \cdot e)^2$$

where the second term represents preferred location effects , and the last two are preferred frame effects.

## NORDTVEDT EFFECT

For breakdown of the weak equivalence principle (WEP) there will be a difference between inertial and passive mass given by

$$\frac{m_p}{m_I} = 1 - [4\beta - \gamma - 3 - \alpha_1 + \frac{2}{3}\alpha_2 - \frac{2}{3}\zeta_1 - \frac{1}{3}\zeta_2]\frac{\Omega}{m_I}$$

which will then lead to a polarization of the orbits of Earth satellites due to the additional perturbations caused by the WEP breakdown.

## PERIGEE SHIFTS

The perigee shift in excess of the predicted general relativistic value of a satellite orbiting the earth is

$$\dot{\omega} = \frac{6\pi m}{p} \left[ \frac{1}{3}(2\gamma + 2 - \beta) + \frac{1}{6}(2\alpha_1 - \alpha_2 + \alpha_3 + \zeta_2) \frac{\mu}{m} + J_2 \frac{R^2}{2mp} \right]$$

where  $\mu$  is the reduced mass of the earth-satellite system,  $p$  is the semi-latus rectum,  $m$  is the total mass of the earth plus satellite, and  $R$  and  $J_2$  are the radius and the quadrupole moment of the Earth respectfully. There will be additional accelerations due to preferred frame effects which will add to the above.

## NON CONSERVATIVE THEORIES

Fitting experimental data to the PPN parameters is in general complicated by including the, so-called, non conservative theories. However many of these theories can be shown to have global conservation laws. Therefore the presumption of non conservation is somewhat misleading. Nevertheless, the results from two examples are worth citing:

### MODIFIED BRANS-DICKIE THEORY

[See L.L.Smalley, Phys Rev D **12** ,376 (1975)] Global conservation laws are satisfied without any constraints on the PPN parameter. The only PPN parameter which differs from the usual Brans-Dicke values is

$$\zeta_2 = \frac{8\sigma}{(2\omega + 3)^3}$$

where  $\omega$  is the Brans-Dicke parameter and  $\sigma$  is the strength parameter of the non zero divergence. The Nordtvedt parameter now becomes (assuming the usual form for the PPN parameters for a Brans-Dicke theory except for above)

$$\eta = \frac{1}{\omega + 2} - \frac{1}{3}\zeta_2$$

which says that the Nordtvedt effect is not just a test for the Brans-Dicke parameter but a test of  $\omega$  and  $\zeta_2$  jointly.

### MODIFIED MALIN THEORY

The Malin theory assumes that the gravitational fields take the form

$$R_{\mu\nu} = 4\pi G T_{\mu\nu}$$

This theory can be modified in such a way that the theory differs from general relativity only in the parameter

$$\zeta_4 = -\frac{1}{3}(3 + 2\tau)$$



**1996**

**NASA/ASEE SUMMER FACULTY FELLOWSHIP PROGRAM**

**MARSHALL SPACE FLIGHT CENTER  
THE UNIVERSITY OF ALABAMA**

**AN ANALYSIS OF MSFC PUBLIC AFFAIRS TELEVISION AND  
TARGET AUDIENCES WITH SUGGESTIONS FOR FUTURE  
GROWTH AND DIRECTIONS**

Prepared By:	Gerald P. Smeyak, Ph.D.
Academic Rank:	Professor
Institution and Department:	The University of Florida Department of Telecommunication College of Journalism & Communications
NASA/MSFC OFFICE:	Public Affairs
MSFC Colleague	Dave Drachlis



## **INTRODUCTION**

Because of profound changes in government and the space program, this may be an ideal time to evaluate MSFC's Public Affairs television efforts. The changes are continued downsizing of government programs; reduction in research and development; changes in the space program from periodic manned launches to a full-time presence in space with Space Station; and greater emphasis on science and communicating science information.

At the same time that NASA is undergoing change, the media and society are also undergoing substantial upheaval. Twenty-five years ago, the three main over-the-air television networks (ABC, CBS and NBC) had a 93 share of the television audience. We now have four popular over-the-air networks (ABC, CBS, NBC and Fox) who maintain a 52 percent share of the television audience. Technological development, competition, and changing consumer tastes have created specialized media and audiences. This media fragmentation is part of a normal maturation cycle of use or adoption. While phases in the cycle vary in length due to many factors, the cycle has been consistent and reflects patterns of adoption. The cycle is: (1) Elite Media usage, (2) Popular or Mass Media usage, and (3) Specialized Media usage.

Another factor that affects the media development and adoption cycle is the creation of new and competing mass and personal mediums. While television remains the dominant and most popular mass medium, it is declining and we see (via cable television) specialized networks catering to small audience segments. Because of changing technology and consumer behavior, we may not see a dominant mass media like television again.

### **NASA Television & Specialized Audiences**

The fact that the mass media is becoming smaller, less dominant and more specialized, will have an affect on how institutional public relations or government public affairs accomplishes its mission.

Network news focuses on popular news themes to increase audiences and advertising revenues. Because the networks have downsized, they are unable to cover as many stories as they used to and this translates into fewer national or regional news stories being fed to network affiliates in news feeds. To fill this void, local television stations have formed co-operatives or regional news networks and specialized program production firms create and send to affiliates stories of regional or specialized interest. Local news organizations are broadening and redefining what is considered a local story and they actively seek out national news events which have local angles or ties to their communities. Network news coverage of NASA missions has declined in this transition because NASA is no longer considered a "must cover" story by national and international media. Continuing successes have made NASA launches routine events and Marcia Dunn of the AP says the general population has become less interested in space and NASA missions.

As special interest television/cable networks develop, their programming and audiences tend to divide into three broad categories. They are: (1) Tabloid Media/Audiences, (2) Popular Media/Audiences, and (3) Specialized Media/Audiences.

The important distinction for this report is between Popular and Elite media and their audiences, and news programs targeted to these audiences. Popular news organizations are best defined by the general news products of ABC, CBS, NBC, CNN1 and most local television stations. The audience is large and defined by average socio-economic demographics. Elite television news programs tend to contain longer, in-depth stories that focus on issues, or important societal themes, such as environment, government spending,

race and the economy. Elite television does not ignore event coverage but hard news does not dominate news programs.

Most Popular news programs contains many short, simplistic stories with strong visual appeals. It is not uncommon to see highly visual stories of dubious news value replace more important news events with weak or no visuals. Gatekeepers in the Popular media feel that their audiences are not interested in science news unless the story is able to highlight direct and obvious benefits. In many instances, science becomes part of a larger story that capitalizes on more popular themes. Popular news programs concentrate on event coverage (crimes, fires and accidents) and themes immediately relevant to their audiences. These themes are health, heart, pocketbook and human interest.

Elite (specialized) news programs are usually found only on Elite television/cable networks such as Public Television, CNBC, or CNN2. While not specifically news programs, the Elite television/cable networks produce and carry programs that have a news or science base. Elite television viewers can best be described as "upscale." Their demographics reflect higher incomes and educational levels, political involvement, and selectivity in media consumption. Elite media consumers tend to be political and business forces in their communities and they are politically active people who try to affect political decisions. One final, and very important point is that the demographics of Elite television users are very similar to the demographics of that small population segment termed "science literate" who seek out and understand science news. (Miller & Prewitt, 1979; Miller, 1982, 1994; Warren Burkett, 1986) Estimates regarding the size of the "science literate" audience ranges from 6-18 percent of media consumers. Broadcasters estimate that no more than 10-20 percent of their audience is interested in science news.

## **Conclusions**

Separate communication and outreach programs should be developed for gatekeepers in the Popular and Elite media which will capitalize on the demographics and interests of these diverse audiences.

The coordination and focus of MSFC television efforts would benefit from the hiring of a television content specialist to oversee the program.

NASA Public Affairs should start positioning itself to deliver consumer and high-quality, broadcast video via Internet through computers and modem connections.

### **Elite Media/Audiences**

This is a highly desirable audience to reach because members of this audience are active politically and will try to affect political decisions. The number of gatekeepers of science or space related program content in the Elite media is rather small and individuals can be identified easily. Personal relationships should be established with these gatekeepers.

Information sent to Elite gatekeepers should be personalized and targeted.

An outreach program should be established and small groups of Elite gatekeepers should be invited to MSFC for carefully organized tour and briefings. Tours should be scheduled to coincide with major rocket tests or neutral buoyancy simulations. During the tour, individuals might be allowed to experience some of the same training or educational experiences that astronauts or missions specialists experience.

### **Popular Media/Audiences**

There are many Popular media outlets and MSFC Public Affairs should continue to provide news releases and television products to these media. Additional efforts should be made to seek out and cater to specialized areas of interest in the Popular media.

MSFC should try to get television stations in the Southeast United States to redefine "local" to include MSFC. This could be done by using telephone, Fax or e-mail to notify gatekeepers that specific NASA events or themes might have interest in their markets.

Television gatekeepers should be identified and efforts should be made to create a personal relationships that might stimulate a greater interest in events at NASA. A modest outreach program similar to the one proposed for Elite gatekeepers might prove useful in creating relationships with stations in Alabama, Mississippi, Georgia and Tennessee. An opportunity to visit NASA, go on tours and briefings and report "live" via MSFC facilities could help establish interest in NASA and reinforce the idea that MSFC is a local or regional news story.

### **Recommendations - Specific**

Marshall Space Flight Center Public Affairs is responsible for five television efforts. These efforts can be categorized as Event News (Mission Coverage), and Thematic News. Mission Coverage is composed of Mission Briefings, Mission Updates and Live Mission Coverage programs. Thematic news refers to the Video File and Live Shot programs. Event, or hard news, will draw national and international media attention. Thematic, or softer news, tends to be less dramatic and less interesting to a national or international audience but it can be of interest to local or regional specialized media.

#### **Event News (Mission Coverage) Recommendations**

For the short term or until the international Space Station is operational, few substantial changes should be made in Mission Coverage. These efforts seem well conceived and targeted for their intended audiences who are the Elite and Popular science journalists who cover the space program. These gatekeepers are not as attentive to Live Mission Coverage as they used to be, but they still rely on Live Mission Coverage when something of interest occurs. While Mission Coverage activities are designed to keep media gatekeepers current on mission events, one element, the Live Shot program, is designed for Popular and Elite television viewers. The Live Shot program has great potential to communicate both mission and thematic news. The success of the Live Shot program during missions capitalizes on the desire of local stations to localize and participate in on-going national or international news which results in prestige for the station and news organization.

In the long-term, once the international Space Station is operational, NASA will not be able to maintain daily Mission Briefings and Mission Updates and indefinite, full-time Live Mission Coverage. Once initial interest in Space Station starts to wane, NASA television should go to a weekly schedule of Mission Updates and Mission Briefings. Live Mission Coverage should be available only during dockings or unusual scientific events.

The main problem observed with Mission Coverage television activities was the lack of good or illustrative video/graphics for many scientific experiments. Animation in Mission Updates, Mission Briefings and Live Mission Coverage would improve comprehension and audience attention. Studies have shown that news releases with illustrative graphics or visuals receive substantially greater usage and space in newspapers, and it can be assumed that animation would have a similar benefit with television.



## Thematic News Recommendations

The video shot for Video Files, and other television efforts, is technically good but visually dull and does not contain the "visual elements" that would immediately gain the attention of news assignment editors or producers. Too many Video Files contain video of incomprehensible lab experiments, people working on computers or interviews shot in an office far from the news event. Another problem is that an unacceptable number of Video File interviews must be reshot because the interviewee gave long and complex answers.

### *Recommendations:*

A greater use of animation would improve the visual element of Video File stories, and it is assumed, lead to increased use.

Where appropriate, human interest elements should be highlighted to provide a hook upon which MSFC science can be conveyed.

When possible, interviews should be shot "in the field" where there is a natural dynamic that enhances the interview.

The interviewer should spend more time "coaching" the interviewee about the types and length of answers that will be needed before the interview starts. If long, complex answers are given, the interviewer must press for usable, comprehensible answers that will serve the needs of the media.

Many assignment editors and news producers do not pay sufficient attention to NASA press releases, Video Advisories and Video Files. The perception is that NASA press releases and related Video File stories are national in scope and would not fit into a local newscast.

### *Recommendations:*

Try to localize and target the content or news angle of press releases, Video Advisories and Video Files in the same manner that Live Shots are targeted and marketed. Where possible and appropriate, individualized Faxes or e-mail messages outlining the local or specialized news angle should precede Video Files.

There seems to be confusion about the relationship, or lack of relationship, between news releases and Video File material. Press releases related to Video Files may not go out at the same time as the Video File.

### *Recommendations:*

Video Files and news releases should be numbered or coded so it is obvious that they are related. Video File slates should also contain directions on where and how to obtain related news releases off the Internet and its code number.

A number of television stations do not have the equipment, ability or desire to reposition satellite dishes to monitor NASA Television.

### *Recommendations:*

Start preparing to move Video File to a computer/digital base so that stations and individuals will be able to download video information via computer through cable, T1 telephone lines or inexpensive home satellite systems. NBC NewsChannel and several weather services are currently delivering video, graphics and animation to affiliates through computer and telephone or fiber links. As technology and compression modules improve, the move to computer/Internet delivery of video will accelerate.

The Live Shot program is targeted and sold to various markets based on specialized content or local angles. Unlike the Video File program, the impact of the Live Shot program is easy to evaluate because stations sign up for the service and it is easy to determine market size and station position. The Live Shot program has great potential to deliver thematic news with a local angle or specialized content. As was noted, during the Mission Coverage segment, the Live Shot program is productive and focused on mission

events. During other times, however, the program does not appear to be as well focused or productive. Much of the video b'roll and studio interviews suffer from the same problems outlined in the Video File section. Video b'roll and studio interviews are dull and do not capitalize interesting locales at MSFC which are available through a fiber optic network.

*Recommendations:*

Public Affairs contractors who maintain beats should relay information about story ideas and contacts to the Live Shot Coordinator.

An annual plan for Live Shots should be developed. The plan should be proactive rather than reactive regarding planned events, missions, MSFC conferences and ongoing scientific programs.

Several visual locations should be established for Live Shot interviews.

## **Sources/References**

- Burkett, Warren. 1986. *News Reporting: Science, Medicine, and High Technology*. Ames, Iowa: The Iowa State University Press.
- Derelian, Doris and Tucker, Kerry. "Packaging messages and media to cut through the Clutter." *Public Relations Journal*. Feb. 1991, V. 47.
- Dizard, Wilson P. *Old Media, New Media: Mass Communications in the Information Age*. White Plains, NY: Longman Publishing Co., 1994.
- Ettema, James S. and Whitney, Charles. *Audiencemaking: How the Media Create the Audiences*. Thousand Oaks, California: Sage Publications, 1994.
- Greenberg, Keith. "Video Releases With A Twist Make News." *Public Relations Journal*. August/Sept 1994, Vol. 50.
- Grunig, James. *Decline of the Global Village*. Bayside, NY: General Hall, Inc., 1976.
- Lowry, Brian. "TV Networks Pull Off Gloves." *The Huntsville Times*, July 2, 1996.
- Major, Michael J. 1995 (May), "How Tech-Friendly Companies Communicate." *Public Relations Journal*, Vol. 61.
- Markow, Eugene. "Sophisticated 'News' Videos Gain Wide Acceptance e." *Public Relations Journal*. August/Sept 1994, Vol. 50.
- Minnis, John and Pratt, Cornelius. "Let's Revisit the Newsroom: What Does a Weekly Newspaper Print." *Public Relations Quarterly*, Vol. 40.
- "Hi-Tech Editors Lead Charge into Cyrberspace." *Public Relations Journal*. May 1995. V. 61.
- "NBC Tests Option to Satellite Delivery." *Television Broadcast*, May 1966, p. 1.

## **Interviews and Additional Work**

- Interviews with Public Affairs Officers (3)
- Interviews with assignment editors/producers (19)
- Interviews with NBC NewsChannel managers (3)
- Interviews with Global Hydrology and Climate Center personnel (2)
- Viewed Mission Updates productions (5)
- Viewed Mission Briefings (4)
- Viewed Video Files (23)
- Viewed Video File productions (3)
- Developed Data Base of Broadcast/Cable Television News Program Producers



**1996**

**NASA/ASEE SUMMER FACULTY FELLOWSHIP PROGRAM**

**MARSHALL SPACE FLIGHT CENTER  
THE UNIVERSITY OF ALABAMA**

**DESIGN, FABRICATION AND TESTING OF MULTILAYER COATED X-RAY  
OPTICS FOR THE WATER WINDOW IMAGING X-RAY MICROSCOPE**

**Prepared By:** Dwight C. Spencer

**Academic Rank:** Instructor

**Institution and Department:** Mississippi Delta Community College  
Department of Science

**NASA/MSFC:**

**Office:** Space Sciences Laboratory  
**Division:** Physics and Astronomy Division  
**Branch:** Solar Physics Branch

**MSFC Colleague:** Richard B. Hoover



## INTRODUCTION

Hoover *et al*<sup>1</sup> built and tested two imaging Schwarzschild multilayer microscopes. These instruments were constructed as prototypes for the "Water Window Imaging X-Ray Microscope," which is a doubly reflecting, multilayer x-ray microscope configured to operate within the "water window." The "water window" is the narrow region of the x-ray spectrum between the K absorption edges of oxygen ( $\lambda = 23.3 \text{ \AA}$ ) and of carbon ( $\lambda = 43.62 \text{ \AA}$ ), where water is relatively highly transmissive and carbon is highly absorptive. This property of these materials, thus permits the use of high resolution multilayer x-ray microscopes for producing high contrast images of carbon-based structures within the aqueous physiological environments of living cells. We report the design, fabrication and testing of multilayer optics that operate in this regime.

## MULTILAYER DESIGN

Normal - incidence x-ray optical instruments have mirrors coated with multiple thin atomic layers ("multilayers"), also known as LSM ("Layered Synthetic Microstructures") or ("thin film multilayers"). The concept of multilayer and multilayer interference coated optics is deceptively simple; materials with contrasting optical properties are stacked with Angstrom scale precision, on a suitably figured substrate so that reflections from successive interfaces are coherently added to form a strong reflected beam<sup>7</sup>.

Normal-incidence multilayer x-ray optics are made by coating (in a vacuum) ultrasMOOTH surfaces with a series of alternating layers of two different materials, one a strong x-ray scatterer with high atomic number, and the second a weak x-ray scatterer or "spacer" with low atomic number. This synthetic structure acts as an x-ray Bragg diffractor. X-ray reflectivity is maximized when the condition for constructive interference is satisfied as indicated by the Bragg equation  $n\lambda = 2d \sin \theta$ , where  $n$  is the order of diffraction,  $\theta$  is the angle of incidence with respect to the surface,  $d$  is the layer-pair thickness, and  $\lambda$  is the wavelength of the incident radiation<sup>8</sup>. For mirrors operating at normal incidence ( $\theta = 90^\circ$ ), the equation becomes;  $\lambda = 2d$ , where  $\lambda$  is the wavelength of peak reflectivity of the first order Bragg diffracted light and  $d$  is the sum of the two layer thicknesses. Therefore, to make a multilayer x-ray optic with maximized reflectivity at a wavelength  $\lambda = 35 \text{ \AA}$  the layer pair thickness needs to be  $17.5 \text{ \AA}$ .

Although the reflectivity at each interface is small, when tens to hundreds of layer pairs are used, excellent reflectivities (more than 50% near normal incidence) can be achieved<sup>8</sup>. The properties of the reflected light such as intensity, bandpass, and image quality are, however, strongly dependent on a number of factors, including the relative thickness and absorption coefficients of the materials, the uniformity of the layers and the nature of the interfaces, the stability of the multilayer, and the smoothness of the substrate. Furthermore, the performance of a multilayer optical system is strongly dependent on the use of filters to exclude long wavelength

light which is specularly reflected by the multilayer, and high resolution detectors to record the image<sup>7</sup>.

The prototype mirror systems for the Water Window Imaging X-Ray Microscope were coated with Molybdenum/Silicon (Mo/Si) multilayers for operation near 135 Å<sup>9</sup>. Coatings using Nb/Si multilayers optimized for this wavelength have also been fabricated at MSFC and have exhibited excellent reflectivity in test carried out at NIST<sup>9</sup>.

OSMC<sup>9</sup>, successfully applied 200 layer pair Tungsten/Boron Carbide (W/B<sub>4</sub>C) multilayer coatings with a d spacing of 17.35 Å to the 30X hemlite grade sapphire optics for the Water Window Imaging X-Ray Microscope. They achieved, with the normal incidence reflectivity of the finished mirrors, about 2% at 35 Å; about 25% of theoretical. They also demonstrated 3% reflectivity at  $\lambda = 42.8$  Å using W/B<sub>4</sub>C fabricated with a d spacing of 20.6 Å.

MSFC<sup>10</sup>, in an effort to develop multilayer coatings with higher reflectivity in the water window used Nickel/Titanium (Ni/Ti) multilayers because theoretical studies revealed that very high reflectivity might be achieved in the 35 - 43 Å regime<sup>9</sup>. Coatings with 200 layer pair Ni/Ti multilayers with a d spacing of 17.6 Å have been fabricated on float glass, silicon wafers, and ultra smooth concave spherical substrates of fused silica<sup>9</sup>. They did not achieve admirable results.

Theoretical studies show that 200 layer pair Nickel/Boron Nitride (Ni/BN) multilayer coatings with a d spacing of 17.7 Å might achieve a maximum reflectivity of  $\approx 21\%$  in the 34 - 36 Å regime, (Figure 1). Due to the design of the MSFC sputtering setup it was decided, as a first attempt, to use only 75 layer pair Ni/BN.

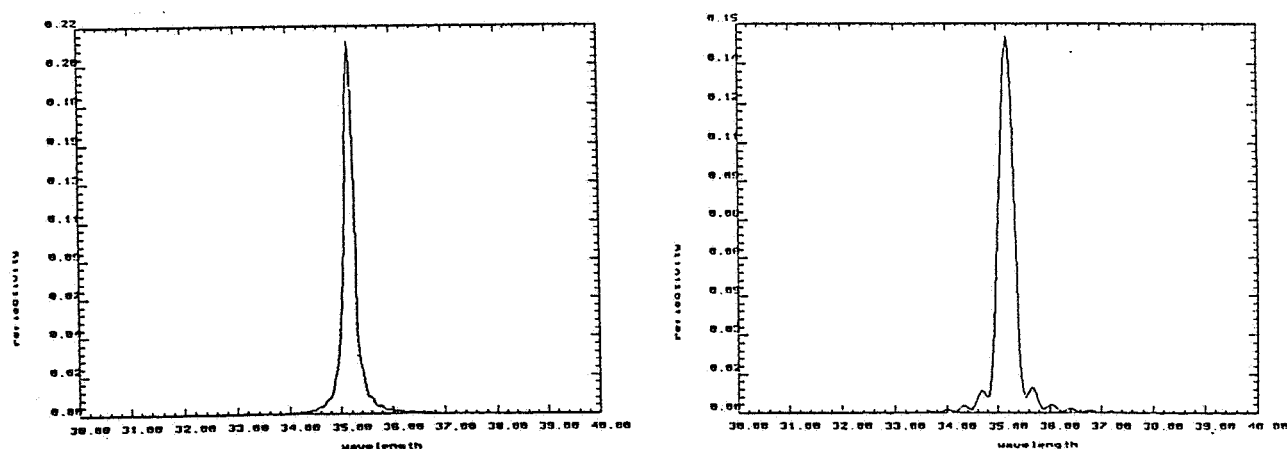


Figure 1. Theoretical x-ray reflectivity for 200-L and 75-R layer pair Nickel/Boron Nitride

## MULTILAYER FABRICATION AND TESTING

There are many different methods for depositing thin films. However, for the purpose of depositing thin, uniform layers nanometers thick "sputtering", with deposition rates from 5 - 50 nm/minute, is slow enough to be relatively well controlled. Sputtering is the process by which atoms from a target are knocked off via collision by another species<sup>3</sup>.

In the setup at MSFC's Space Sciences Laboratory<sup>4</sup>, a planar diode radio frequency - sputtering system modified to triode operation by addition of a ring filament surrounding the anode in an ordinary laboratory environment has been used to produce several two - component multilayer optics (Figure 2)<sup>3</sup>.

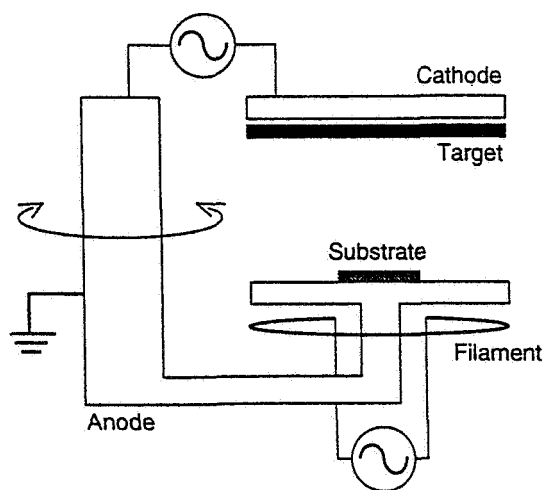


Figure 2. MSFC R.F. Diode Set-Up

High purity argon is introduced into the evacuated sputtering chamber. A forward power at 1300 KHz is applied while the filament ejects free electrons into the chamber. These electrons, having high mobility, collide with argon gas and produce + argon ions with much lower mobility. During the production of the argon plasma the water cooled anode carrying the substrate to be coated, floats to a DC potential higher than the cathode containing the target. This accelerates the ions toward the target knocking off atoms which float to the substrate<sup>3</sup>.

Deposition rates can be determined by depositing a substance onto float glass (or similar smooth surface) and using a stylus profilometer to determine the thickness of a film deposited for a known time. It has been found that only the central 5 cm of the 15.2 cm target produces fairly uniform deposition rate<sup>3,4</sup>.



We decided, as a first trial, to deposit 75 layer pairs of Ni/BN on float glass and silicon wafers. Our first task was to change to the Nickel and Boron Nitride targets in the sputtering chamber and determine the rate of deposition of each target. We placed four (4) squares of 7059 float glass on the anode, one with a razor blade mask. The chamber was then evacuated to  $10^{-6}$  torr. After introducing  $10\text{ }\mu\text{m}$  argon at  $10^{-2}$  torr., we presputtered the targets onto the shutter for 20 minutes each. We partially covering two of the squares with the shutter, then we sputtered BN on the substrates at 75 watts forward power at - 290 volts bias for 20 minutes. After moving the razor blade mask over slightly we then sputtered Ni for 20 minutes at 75 watts forward and - 744 volts bias. These samples were then removed to determine the rate of deposition of each of the materials on the substrate

It was determined from stylus profilometer traces and densitometer transmittance that the Ni film was about  $450\text{ }\text{\AA}$  thick and the total film was about  $1350\text{ }\text{\AA}$  thick, therefore BN was about  $900\text{ }\text{\AA}$  thick. This gives Nickel a deposition rate of  $.375\text{ }\text{\AA}/\text{s}$  and Boron Nitride a deposition rate of  $.75\text{ }\text{\AA}/\text{s}$ . Nickel, then, should be sputtered twice as long as Boron Nitride. Since we want reflectivity at  $\lambda = 35\text{ }\text{\AA}$ , the d spacing needs to be  $17.5\text{ }\text{\AA}$ , therefore, Boron Nitride should be sputtered 12 seconds.

We placed two (2) squares of 7059 float glass and two (2) pieces of silicon wafer on the anode, then evacuated the chamber to  $10^{-6}$  torr. After presputtering the Ni target for 15 minutes at 75 watts forward, - 750 volts bias and the BN target for 7.5 minutes at 75 watts forward, - 245 volts bias in  $10\text{ }\mu\text{m}$  argon at  $10^{-2}$  torr., onto the shutter, we deposited 75 layer pairs of Ni/BN onto 2 samples of float glass and 2 samples of silicon wafer, sputtering Ni 2 X 12 seconds at 75 watts forward, - 713 volts bias and BN 1 X 12 seconds at 75 watts forward, - 239 volts bias.

Stylus profilometer traces of the coatings indicated a total thickness of the 75 layer pairs of Ni/BN to be  $1400\text{ }\text{\AA}$ , giving a d spacing of  $18.7\text{ }\text{\AA}$ . Theoretical reflectivity for normal incidence x-rays  $\lambda = 37\text{ }\text{\AA}$  (since  $\lambda = 2d$ ) should be  $\approx 10\%$ . Reflectivity tests with the Rigaku Bede Diffractometer using a Cu  $K\alpha$  source at  $\lambda = 1.54\text{ }\text{\AA}$  should indicate a reflectance of  $\approx 33\%$  at  $2.40^\circ$  grazing angle. The actual test, however, did not indicate any significant reflectance on the float glass or the silicon wafers.

Our second trial was to produce a 30 layer pair Ni/BN multilayer optic at double the sputtering time, 24 seconds BN, 48 seconds Ni, under the same conditions as our first try using four (4) squares of 7059 float glass. Stylus profilometer traces of this coating measured a total thickness of  $\approx 1400\text{ }\text{\AA}$  /30 layer pairs, giving a d spacing of  $46.7\text{ }\text{\AA}$ ;  $\lambda = 93.4\text{ }\text{\AA}$ . Diffractometer tests, using  $1.54\text{ }\text{\AA}$  x-rays revealed good reflectivity on all four squares. The Bragg equation suggest that at a grazing incidence angle of  $2\theta = 1.90^\circ$  for first order maximum:

$$\begin{aligned}\sin \theta &= n\lambda/2d = 1 (1.54\text{ }\text{\AA})/ 2 (46.7\text{ }\text{\AA}) = .0165 \\ \theta &= .945^\circ ; 2\theta = 1.90^\circ\end{aligned}$$

The best results were from sample 7/17/96 - 2, where  $2\theta$  at approximately  $1.90^\circ$  for first order peak had over 150,000 counts ( Figure 3) giving a  $\lambda = 93.1\text{ }\text{\AA}$ .

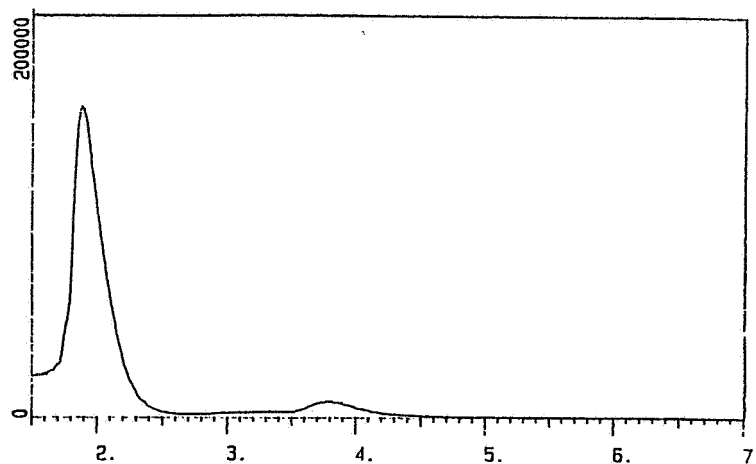


Figure 3: Reflectivity sample 7/17/96 -2 Ni/BN

Considering the success of the second trial, as a third trial we decided to fabricate 40 layer pairs of Ni/BN on two squares of 7059 float glass, reducing the time, to try to fabricate an x-ray optic that would operate in the water window. Using the same conditions as our previous two trials, but shortning the sputtering time to 14 seconds for BN and 28 seconds for Ni.

Stylus profilometer traces of this coating measured a total thickness of approximately 840 Å/40 layer pairs, giving a d spacing of 21 Å;  $\lambda = 42$  Å. Diffractometer tests exhibited reflectivity on sample 7/18/96 - 2, but at half the expected angle. The Bragg equation suggest that maximum reflectivity should occur at  $2\theta = 4.2^\circ$ , but diffractometer test show maximum reflectivity at  $2\theta = 2.2^\circ$  (Figure 4). This may be harmonic, second order diffraction or from two pairs.

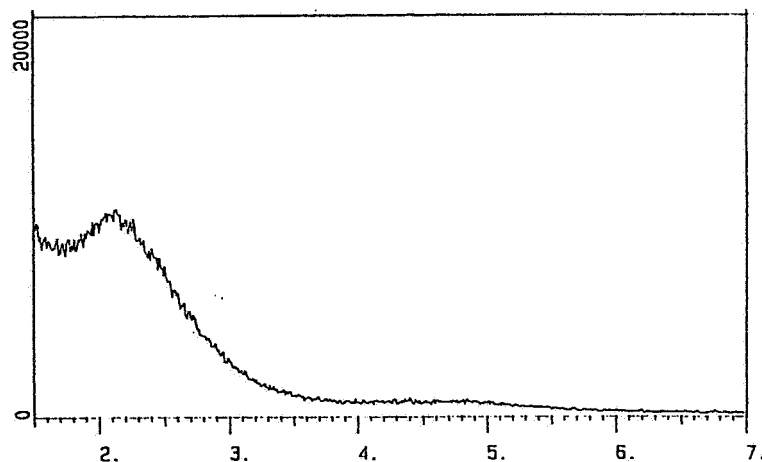


Figure 4: Reflectivity sample 7/18/96 -2 Ni/BN

## CONCLUSION

Three multilayer coated x-ray optics were designed, fabricated and tested. We have demonstrated that Ni/BN multilayer x-ray optics do produce predictable reflectivity at wavelengths in the 93 Å regime and reflectivity in the 42/84 Å regime. Theoretical evidence indicates that they should also produce reflectivity at wavelengths well within the water window, however, careful attention must be given to depositing layers an integral number of atomic layers thick to achieve a smooth layer interface.

## ACKNOWLEDGEMENTS

Dwight C. Spencer was supported by a NASA-ASEE Summer Faculty Fellowship Grant. I wish to thank Dr. Frank Six, University Affairs Officer; Dr. L. Michael Freeman, University Programs Co-Director; Mr. Richard Hoover, Mr. Marcus Vlasse and Mr. Ed J. Reichmann, Space Sciences Laboratory, MSFC; and Mr. David Gore, Department of Physics, UAB for their support. A special thanks to Mr. Palmer N. Peters my MSFC SSL laboratory colleague.

## REFERENCES

- (1). R. B. Hoover *et al.*, "Imaging Schwarzschild Multilayer X-Ray Microscope," SPIE Proc., 1742, pg. 501, 1992.
- (2). D. L. Shealy *et al.*, "Design of a Normal Incidence Multilayer Imaging X-Ray Microscope," SPIE Proc. 984 pg. 234, 1988.
- (3). D. B. Gore, "A Soft X-Ray Fabry-Perot Bandpass Transmission Filter for Imaging Systems," Unpublished Dissertation Proposal," pp 3-5, 9-11, 1996.
- (4). P. N. Peters, *et al.*, "Fabrication of Multilayer Optics by Sputtering: Application to EUV Optics with Greater Than 30% Normal Reflectance," SPIE Proc. 2515, pp.576-579, 1995.
- (5). D. L. Shealy, R. B. Hoover, D. R. Gabardi, "Multilayer X-Ray Imaging Systems," SPIE Proc. 691, pg 83, 1986.
- (6). D. B. Gore, *et al.*, "Optical Focusing and Alignment of the Multi-Spectral Solar Telescope Array II Payload," SPIE Proc., 2515, pg. 532, 1995.
- (7). A. B. C. Walker, Jr., R. B. Hoover, and T. W. Barbee, Jr., "Chromospheric and Coronal Observations with Multilayer Optics," SPIE Proc. 1742, pg. 515, 1992.
- (8). A. B. C. Walker, Jr., Troy W. Barbee, Jr., Richard B. Hoover, Joakim F. Lindblom, "Soft X-ray images of the Solar Corona with a Normal - Incidence Cassegrain Multilayer Telescope," SCIENCE, 241, pp.1781-1787, Sep. 1988.
- (9). R. B. Hoover, *et al.*, "Development of the Water Window Imaging X-Ray Microscope," SPIE Proc. 2070, pp 195-208, 1994.
- (10). P. N. Peters and R. B. Hoover, Laboratory Notes Unpublished, pp 240-241, 1995.

**1996**

**NASA/ASEE SUMMER FACULTY FELLOWSHIP PROGRAM**

**MARSHALL SPACE FLIGHT CENTER  
THE UNIVERSITY OF ALABAMA**

**HIGH TEMPERATURE ANALYSIS OF ALUMINUM-LITHIUM 2195 ALLOY  
TO AID IN THE DESIGN OF IMPROVED WELDING TECHNIQUES**

**Prepared By:** George E. Talia, Associate Professor, Ph.D.  
Christian Aragon Widener

**Institution:** Wichita State University  
Department of Mechanical Engineering

**NASA/MSFC:**

**Office:** Materials and Processes Laboratory  
**Division:** Metallic Materials and Processes  
**Branch:** Metallurgical Research

**MSFC Colleague:** Arthur C. Nunes, Jr., Ph.D.



## Introduction

Aluminum-lithium alloys have extraordinary properties. The addition of lithium to an aluminum alloy decreases its density, while making large increases in its strength and hardness. The down side is that they are unstable at higher temperatures, and are subsequently difficult to weld or even manufacture. Martin Marietta, though, developed an aluminum-lithium alloy 2195 that was reported to have exceptional properties and good weld-ability. Thus, it was chosen as the alloy for the space shuttles super light external tank.

Unfortunately, welding 2195 has turned out to be much more of a challenge than anticipated. Thus, research has been undergone in order to understand the mechanisms that are causing the welding problems. Gas reactions have been observed to be detrimental to weld strength. Water vapor has often been identified as having a significant role in these reactions [1] [2]. Nitrogen, however, has also been shown to have a direct correlation to porosity [3] [4]. These reactions were suspected as being complex and responsible for the two main problems of welding 2195. One, the initial welds of 2195 are much weaker than the parent metal. Second, each subsequent welding pass increases the size and number of cracks and porosity, yielding significant reductions in strength.

Consequently, the objective of this research was to characterize the high-temperature reactions of 2195 in order to understand the mechanisms for crack growth and the formation of porosity in welds. In order to accomplish that goal, an optical hot-stage microscope, HSM, was used to observe those reactions as they occurred. Surface reactions of 2195 were observed in a variety of environments, such as air, vacuum, nitrogen and helium. For comparison, some samples of Al - 2219 were also observed. Some of the reacted surfaces were then analyzed on a scanning electron microscope, SEM. Additionally, a gas chromatograph was used to analyze the gaseous products of the high temperature reactions.

## Procedure

The samples observed in the HSM were machined into a bullet-like shape, reference Figure 1, ( $d = 7\text{mm}$ ,  $h = 12\text{mm}$ ). The bottoms of the samples were then polished and etched. The inverted microscope had a stainless steel vacuum chamber with a quartz window in the bottom. The electric heater used two tungsten heating elements to nearly completely surround the sides of the sample. The temperature was measured using a K-type thermocouple. It was inserted into a small hole in the side of the sample. The environments used were helium, air, nitrogen, and vacuum. Pressures varied from 1 bar down to  $1.0 \times 10^{-7}$  bars. Each sample was video taped and temperature measurements were recorded at regular intervals and at the initiation of reactions.



Figure 1: HSM sample

In order to aid the optical observations on the HSM, some of the samples were analyzed on an SEM. The reacted surface of the samples were examined for porosity, cracks, and anything unusual. High definition photographs and composition analyses were taken of the most important features.

An apparatus was constructed to analyze the gaseous products of the high temperature reactions of 2195 with a gas chromatograph. A long alumina tube was connected to a flexible hose and valve via a short piece of rubber tubing. A piece of 2195 was inserted into the tube. The tube was completely evacuated and filled to 1 psia with either room air or 99.999% N<sub>2</sub>. The apparatus was then connected to the gas chromatograph. A small "clam shell" type ceramic heater (@ 620 °C) heated the bottom portion of the alumina tube for 15 minutes. At the end of this time, the sample was immediately analyzed by the gas chromatograph.

## Results and Observations

Some dramatic and surprising results were observed in the hot-stage optical microscope, especially by comparison with 2219, bubbling, inhomogeneity, effects of degassing and worms. The most startling was bubbling through a liquid surface layer. The thickness of the liquid changed with various parameter changes. Bubbling was seen to occur at temperatures as low as 350 °C in weld metal and 530 °C in the parent metal. The bubbling usually started at the grain boundaries, cracks, pores, and second phases. Then later the reaction spread until the whole surface was reacting. The reactions often produced porosity throughout the metal. The reactions were self-sustaining. Once the reaction had begun to take place, even if the power to the heater was reduced or cut off completely, the reaction would continue and the temperature remain elevated.

Inhomogeneity was also observed in the 2195 samples. Both melting temperatures and reaction temperatures were observed to differ by as much as 40 °C within the same viewing area of a single sample. Inhomogeneity was seen coupled with the supposed presence of impurities when a small section of a sample was seen to react internally, melting at 350 °C. The section then quickly re-crystallized as the heat from the reaction was dissipated into the rest of the sample. The whole region later began to melt and react at 534 °C.

Violent surface reactions were observable in any atmosphere if the sample was not degassed. If the sample was degassed, the reactions in a nitrogen environment were reduced and the liquid layer was thinner, but bubbling still occurred. If the samples were not degassed and were heated at atmospheric pressure in any gas environment, worms were seen growing out of the parent metal at 400 °C. The reacted surface of the samples were also covered with a white, water soluble substance, probably LiOH. Satisfactory degassing was accomplished by vacuum baking the samples at  $1.0 \times 10^{-7}$  bars and 300 - 400 °C for 1-2 hours in the HSM. Degassing didn't have much effect when samples were heated in air, above  $1 \times 10^{-4}$  bars.

The scanning electron microscope also gave important results. The reacted surface of several of the samples tested revealed that large amounts of Nitrogen and Oxygen, generally around 70%, were present at the surface. Unfortunately, lithium and hydrogen are not detectable by an SEM, so complete analyses were not possible. Craters and pores were observed on the surface of reacted samples, reference Figure 3. Also, one should note that the pores or craters were created in the parent metal, so these are not merely pre-existing pores from a poor weld that migrated to the surface. Polished cross sections of the reacted samples show that porosity and cracks can be formed in the parent metal by exposure to air or nitrogen at high temperatures.

The gas chromatograph provided excellent results. This experiment proved that hydrogen is indeed bubbling from the surface of 2195. When the tube was initially filled with air, the reacted sample released hydrogen, nitrogen was consumed, and the oxygen level remained basically the same. In an atmosphere of pure nitrogen, 1 mole of hydrogen was produced for every 1.1 moles of nitrogen consumed. There aren't any 1:1 molar reactions possible with these reactants, nitrogen is always consumed much slower than hydrogen is released. But, because the  $H_2$  that is produced will react with  $Li^+$  forming  $LiH$ , it is conjectured that lots of hydrogen is produced, but only one mole actually escapes for every mole of nitrogen consumed.

## Chemical Reactions

An important step to solving the welding problem is to characterize the actual chemical reactions that are taking place. Some thought and research has already been put into this, however, it is difficult because there are a number of reactions that are occurring simultaneously. The main mechanism for the creation of porosity in 2195 is the reaction of lithium with water vapor and nitrogen, but it is the release of hydrogen that actually forms the pores. The reactions begin with  $H_2O$  that is adsorbed and bonded onto the surface of the metal. It is bonded to hydroxides, oxyhydroxides, and hydrous oxides, like aluminum oxide,  $Al_2O_3 \cdot 3H_2O$  and some other compounds like  $LiNO_3 \cdot 3H_2O$ . [1] The reaction of  $Li$  with  $H_2O$  produces  $LiOH$  and evolves  $H_2$ . The fact that bubbling is seen in a Helium environment if the sample is not degassed, supports that. If both nitrogen and water vapor are available, then the following reactions are believed to be in effect:



The liquid layer observed on the surface of the metal during reaction is thought to be mainly a melted mixture of those compounds. Such a homogeneous mixture would have some median melting point, perhaps around 530 - 570 °C, which is the temperature range at which the surface is observed to be liquid and begin bubbling. Lithium will also react with aluminum oxide to form  $AlLiO_2$ , a much more porous oxide. There are also many other compounds that can be present formed from reactions of aluminum and magnesium. Clearly this is a complicated process.



## Some Implications For Welding

Many studies have been done by the Soviets to demonstrate that there is a large amount of water vapor adsorbed into to the surface of 2195 that causes porosity when welding. They showed that the removal of 0.2 - 0.3 mm of material from the surface is essential. They were able to eliminate porosity and generate welds of 82% of the base metal properties. [1] Studies in the U.S. have shown that hydrogen has the highest concentration 0.2 mm from the surface, reference Figure 2, supporting the

Russian results. [2] The Russians also demonstrated that water vapor can be re-absorbed into the surface of the metal at room temperature. Weld porosity was observed with materials chemically milled 16 days prior to welding. Which leads to an important word of caution for welding: Although the metal may be free from discoloring oxides, it can still be totally re-saturated with water vapor.

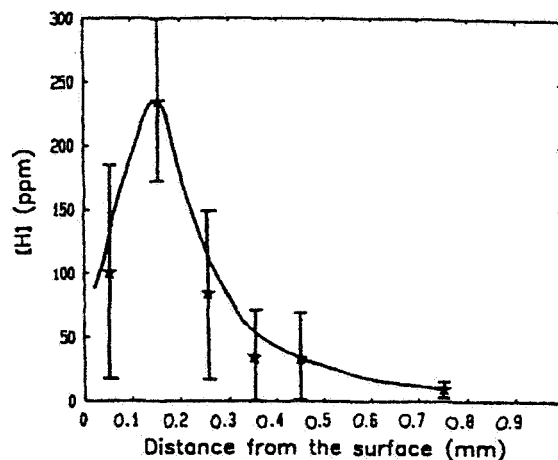


Figure 2: Hydrogen Distribution in Al-Li Alloy

Another fact that came out of this research is that previously welded 2195 is susceptible to violent surface reactions if exposed to air while at temperatures as low as 350 °C. Also, worms of material were seen growing out of the parent metal at 400 °C, yet to the naked eye the surface appeared unreacted. That underscores the importance of shielding the weld for a length of time that allows the metal to cool below those temperatures, as well as the necessity to back shield for cover passes and repair welds.

## Conclusions

In conclusion, weld zone cracks and porosity arise principally out of a reactions of lithium with nitrogen and water vapor adsorbed or bonded to the surface of the metal, which releases a large amount of hydrogen into the weld pool. Thus, this research has led to two important applications for welding:

- One, the time lapse after surface preparation of Al-Li 2195 is extremely important. Milling the surface must be performed immediately prior to welding because water can be re-adsorbed from humid air, over time.
- Two, Al-Li 2195 needs to be shielded when it is at temperatures above 350 °C. Back shielding is a necessity, even for partial penetration cover passes. Pending temperature profile studies behind the weld, a trailing shield should be considered.

Work still needs to be done to attempt to further understand the way in which porosity and crack growth are propagated in this material. Work, too, should be performed to analyze how quickly Al-Li 2195 adsorbs water. Lastly, work should be done directly in the shop environment, in order to devise ways of improving current shop practices, based on an understanding of the reactivity and sensitivity of this alloy.

### Acknowledgements

The authors are extremely grateful to Dr. Arthur C. Nunes, Jr. for helpful discussions and to James Perkins for experimental assistance.

### References

1. Canaby, J.L., F. Blazy, J.F. Fries. "Effects of high temperature surface reactions of aluminum-lithium alloy on the porosity of welded areas." Materials Science and Engineering, A136, pp. 131-139, 1991.
2. Pickens, J.R. "The weldability of lithium-containing aluminum alloys." Journal of Materials Science, v. 20, pp. 4247-4258, 1985.
3. Talia, G.E., A.C. Nunes. "Microstructural Analysis of the 2195 Aluminum-Lithium Alloy Welds." Prepared for Marshall Space Flight Center, 1993.
4. Talia, G.E., A.C. Nunes. "Microstructural Analysis of Cracks Generated During Welding of 2195 Aluminum-Lithium Alloy." Prepared for Marshall Space Flight Center, 1994.



Figure 3: Reacted surface of Parent Al-Li 2195 ( Room Air, Pressure =  $4 \times 10^{-4}$  bars)



**1996**

**NASA/ASEE SUMMER FACULTY FELLOWSHIP PROGRAM**

**MARSHALL SPACE FLIGHT CENTER  
THE UNIVERSITY OF ALABAMA**

**AUGMENTATION OF ROCKET PROPULSION: PHYSICAL LIMITS**

<b>Prepared By:</b>	<b>Charles R. Taylor, Ph.D.</b>
<b>Academic Rank:</b>	<b>Assistant Professor</b>
<b>Institution and Department:</b>	<b>Western Oregon State College Department of Physical and Earth Sciences</b>
<b>NASA/MSFC:</b>	
<b>Office:</b>	<b>Program Development</b>
<b>Division:</b>	<b>Advanced Systems and Payloads</b>
<b>Branch:</b>	<b>Space Science &amp; Applications Office</b>
<b>MSFC Colleague:</b>	<b>Jonathan W. Campbell, Ph.D.</b>



## INTRODUCTION

Consider a vehicle of initial mass  $m_0$  moving at velocity  $v_0$  through a medium which is initially at rest. One dimensional motion will be assumed. The vehicle initially has stored energy  $E_s$ . At a later time, the stored energy has all been used, and the vehicle has mass  $m_p$  and velocity  $v_p$ . The vehicle has interacted with a total mass  $m_a$  of the medium. The vehicle exhaust of mass

$$m_r = m_0 - m_p$$

has been expelled into the medium. Conservation of momentum and energy lead to the following equations.

$$m_0 v_0 = m_p v_p - (m_a + m_r)(v_r)_{av}$$

$$E_s + \frac{1}{2} m_0 v_0^2 = \frac{1}{2} m_p v_p^2 + \frac{1}{2} (m_a + m_r)(v_r)_{av}^2$$

$(v_r)_{av}$  is the average velocity of the medium with which the vehicle interacts together with the expelled exhaust products, taken to be in the opposite direction from  $v_0$  and  $v_p$ . The total mass of medium with which the vehicle interacts is  $m_a$ . The two equations can be combined to give the following equation for the variance of the air velocity distribution.

$$\sigma^2 = (v_r)_{av}^2 - (v_r)_{av}^2 = \frac{-m_p(m_0 + m_a)v_p^2 + 2m_p m_0 v_p v_0 + m_0(m_p + m_a)v_0^2 + 2E_s(m_r + m_a)}{(m_r + m_a)^2}$$

The equation above can be rearranged as an equation for the velocity increase.

$$v_p - v_0 = \frac{-m_a v_0 + \sqrt{m_0 v_0^2 + \frac{(m_0 + m_a)}{m_p} \left[ 2(m_r + m_a)E_s - m_0(m_p - m_a)v_0^2 - \sigma^2(m_r + m_a)^2 \right]}}{m_0 + m_a}$$

The vehicle velocity increase is greatest for the smallest variance in the velocity imparted to the medium. In this case, we have

$$\frac{v_p - v_0}{u} = \frac{\sqrt{(\mu + \mu_a - 1) \left( \mu + \mu_a + \mu \mu_a \frac{v_0^2}{u^2} \right) - \mu \frac{v_0}{u}}}{\mu + \mu_a}$$

where

$$\mu = \frac{m_0}{m_p} \quad \text{and} \quad \mu_a = \frac{m_a}{m_p}$$

Even if we assume  $\sigma^2=0$ , the momentum transfer is not well defined until a model is specified for the mass of the interacting medium. It is instructive to consider a limiting case before proceeding to a more realistic model. In the limit  $m_a \rightarrow \infty$  we have the following.

$$\frac{v_p - v_0}{u} = \sqrt{\mu \frac{v_0^2}{u^2} + 1} - \frac{v_0}{u}$$

This limit is appropriate if a vehicle pushes against an entire planet. It would apply to an automobile, for example (assuming the automobile carries its own oxygen and the exhaust is left at rest with respect to the road). For  $v_0=0$ , the right-hand side approaches unity, which means that all of the initial stored energy becomes payload kinetic energy.

The model above is not realistic because of the assumption  $\sigma=0$ . In order to control  $\sigma$ , one would need a means of storing some of the energy when fuel is burned in order to use it at a later time. More realistically, the energy must be used at the time the fuel is burned. Despite this, the calculation correctly shows that a performance benefit can be realized when a rocket pushes against the medium through which it travels.

### OPTIMAL PROPULSION IN A MEDIUM

I now construct a more realistic model in which the energy from the fuel is used immediately to accelerate air and propellant. This implies that

$$dE = \gamma dm$$

where  $\gamma$  is the specific energy of the fuel. Also, the interacting air mass in any time interval is proportional to the volume swept out by the vehicle in the same interval.

$$dm = \rho A v dt$$

Conservation of momentum and energy in any time interval can be written as follows.

$$mv = (m + dm)(v + dv) - (dm_a - dm)v_r$$

$$E + \frac{1}{2}mv^2 = E + dE + \frac{1}{2}(m + dm)(v + dv)^2 + \frac{1}{2}(dm_a - dm)v_r^2$$

The quantities  $dm$  and  $dE$ , the changes in mass and stored energy of the vehicle in a time interval, are both negative. The density of the medium is  $\rho$  and the cross-sectional area of the medium swept up for propulsion is  $A$ . The acceleration can be used to eliminate the time increment.

$$dt = \frac{dv}{a}$$

The reaction speed  $v_r$  can be eliminated to give the following differential equation for the velocity change as a function of the mass change.

$$dv = \frac{-2\gamma dm}{\sqrt{2\gamma m \left( m + \frac{2\rho A v^2}{a} \right) + \left( \frac{\rho A v}{2a} \right)^2 (2\gamma + v^2)^2 - \left( \frac{\rho A v}{2a} \right) (2\gamma + v^2)}}$$

The equation has been integrated numerically for constant  $A$ ,  $\rho$ , and  $a$  to give the curves of Figure 1.

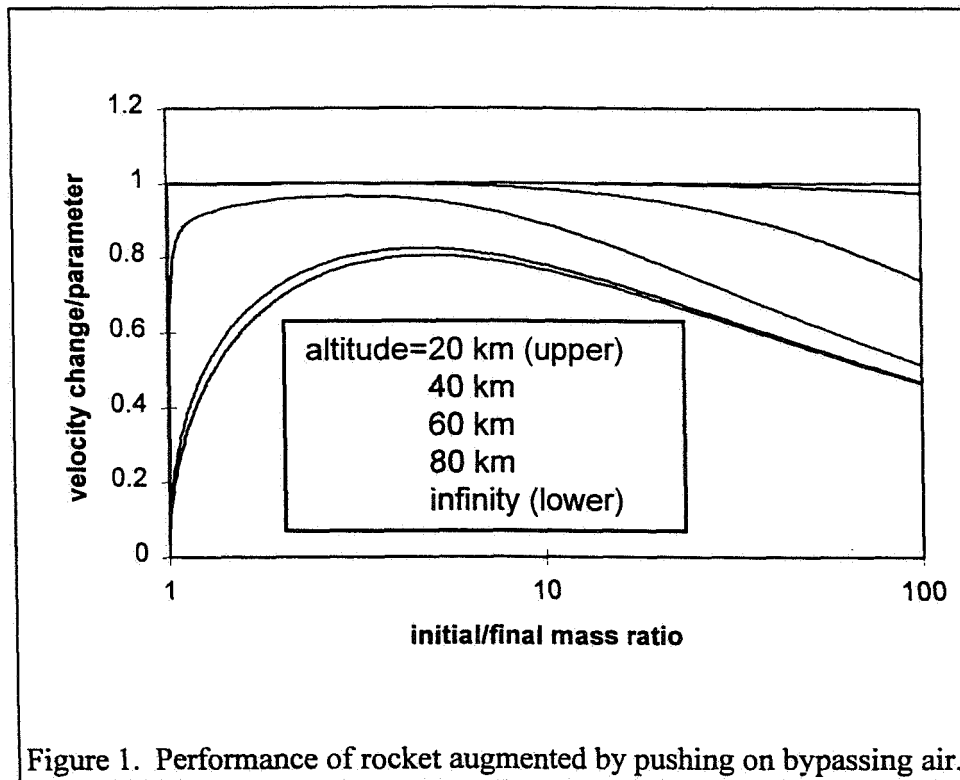


Figure 1. Performance of rocket augmented by pushing on bypassing air.

performance advantage over a conventional rocket for vehicles with a high initial to payload mass ratio. When the vehicle is used at 80 km, however, the advantage of air pushing is very little.

### OPTIMAL MEDIUM INTAKE

We have seen that the physical performance limits are higher for a vehicle which pushes on its medium than for a completely closed system, particularly at low initial to final mass ratios. The analysis so far has not included drag. It will now be shown that when drag is included, there is a well-defined intake size for optimum performance.

With drag, the momentum and energy equations are as follows.

The four curves of Figure 1 apply to atmospheric densities typical of altitudes of 20, 40, 60, and 80 km, for a cross-sectional area, payload mass, and specific energy typical of the space shuttle with the external tank attached. At the higher densities, the performance graphs are near unity. Even at an air density representative of 60 km, the optimal air pusher has a large



$$mv = (m + dm)(v + dv) - (\rho A_a v dt - dm)v_r + \rho A_d v^2 dt$$

$$E + \frac{1}{2}mv^2 = E + dE + \frac{1}{2}(m + dm)(v + dv)^2 + \frac{1}{2}(\rho A_a v^2 dt - dm)v_r^2 + \rho A_d v^3 dt$$

The drag area  $A_d$  is usually related to the frontal area  $A$  with the drag coefficient. The effective intake area is  $A_a$ . The elimination of  $v_r$  can be done as before, which leaves the following relation among  $dm$ ,  $dv$ , and  $dt$ .

$$0 = 2\gamma dm^2 - \rho A_a v dt (2\gamma + v^2) dm - m^2 dv^2 - \rho v^2 dt [2mdv(A_a + A_d) + \rho A_d v^2 dt (2A_a + A_d)].$$

Instead of eliminating  $dt$  at this point, I will consider flight at constant  $v$ . This enables the analysis of the optimum intake size at various speeds and air densities. The full treatment of accelerated motion should be in qualitative agreement, except that very large intakes will be discouraged by the mass penalty.

The rate of fuel consumption as a function of velocity for  $v < u$  is approximately

$$\frac{dm}{dt} = \frac{-\rho A_d v^3 (2A_a + A_d)}{2\gamma A_a}$$

Note that the area factors are separate from the density and velocity, so that within this model the intake size scales independently of the velocity and the density. The fuel consumption rate can be written

$$\frac{dm}{dt} = \frac{-\rho v^3 F}{2\gamma}$$

where the geometric factor  $F$  is given by

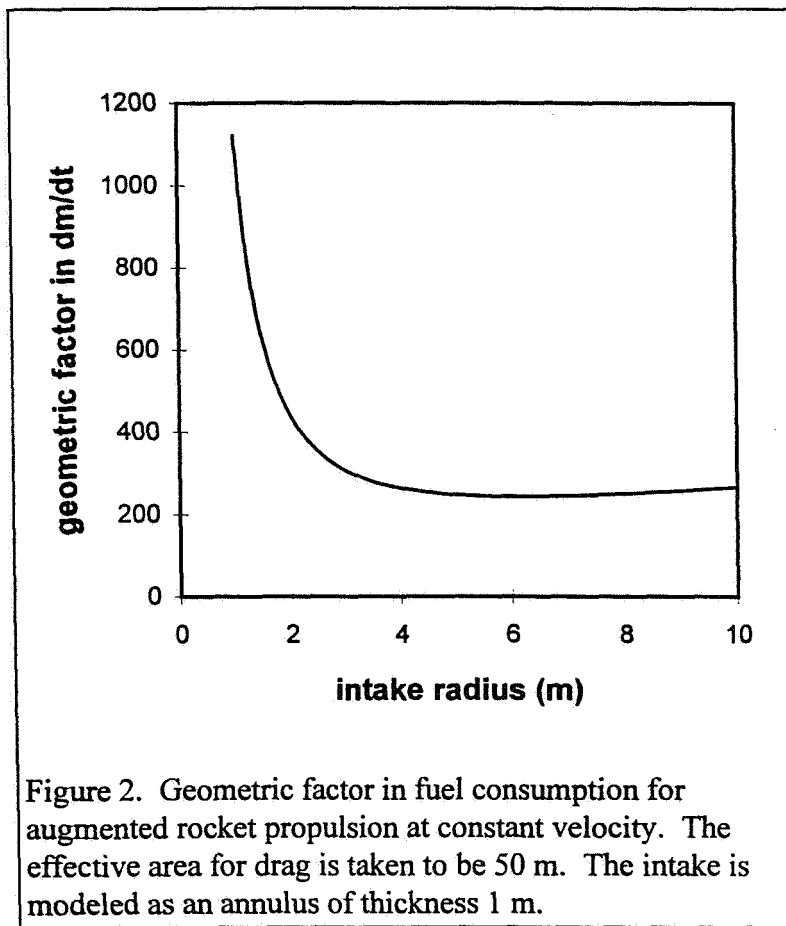
$$F = \frac{A_d (2A_a + A_d)}{A_a}$$

At first glance it would appear that  $A_a$  should be made as large as possible, but this is not correct, since  $A_a$  is not independent of  $A_d$ . A simple model for the areas includes an irreducible area  $A_p$  associated with the payload. In addition, there is an intake which can be modeled as a thin annulus of radius  $r$  and width  $w$ . Then the geometric factor in the fuel consumption is

$$F = \frac{(A_p + 2\pi r w)(2\pi r^2 + A_p + 2\pi r w)}{\pi r^2}$$

As an example, suppose  $A_p = 50 \text{ m}^2$  and  $w = 1 \text{ m}$ . Figure 2 shows the geometric factor  $F$  for this example. The optimal radius is 6.1 m. The intake area in this case is about 2.3 times the effective frontal area of the payload. When the mass is taken into account for an accelerating

vehicle, the optimal intake area will be somewhat smaller. Note that the minimum is such that the performance suffers only slightly if the radius is decreased to about 3m, but then the performance degrades severely for smaller intakes. For the smaller intake, the intake area is about 60 % of the effective area for drag.



## CONCLUSIONS

Rocket propulsion is not ideal when the propellant is not ejected at a unique velocity in an inertial frame. An ideal velocity distribution requires that the exhaust velocity vary linearly with the velocity of the vehicle in an inertial frame. It also requires that the velocity distribution variance as a thermodynamic quantity be minimized.

A rocket vehicle with an inert propellant is not optimal, because it does not take advantage of the propellant mass for energy storage. Nor is it logical to provide another energy storage device in order to realize variable exhaust velocity, because it would have to be partly unfilled at the beginning of the mission.

Performance is enhanced by pushing on the surrounding because it increases the reaction mass and decreases the reaction jet velocity. This decreases the fraction of the energy taken away by the propellant and increases the share taken by the payload. For an optimal model with the propellant used as fuel, the augmentation realized by pushing on air is greatest for vehicles with a low initial/final mass ratio. For a typical vehicle in the Earth's atmosphere, the augmentation is seen mainly at altitudes below about 80 km. When drag is taken into account, there is a well-defined optimum size for the air intake.

Pushing on air has the potential to increase the performance of rockets which pass through the atmosphere. This is apart from benefits derived from "air breathing", or using the oxygen in the atmosphere to reduce the mass of on-board oxidizer. Because of the potential of these measures, it is vital to model these effects more carefully and explore technology that may realize their advantages.



1996

NASA / ASEE SUMMER FACULTY FELLOWSHIP PROGRAM

MARSHALL SPACE FLIGHT CENTER  
THE UNIVERSITY OF ALABAMA

A REAL-TIME POSITION-LOCATING ALGORITHM FOR CCD-BASED  
SUNSPOT TRACKING

Prepared By:	Jaime R. Taylor, Ph.D.
Academic Rank:	Assistant Professor
Institution and Department:	Austin Peay State University Physics Department
NASA/MSFC:	
Laboratory:	Astrionics Laboratory
Division:	Instrumentation & Control
Branch:	Instrumentation
MSFC Colleague:	Ron McIntosh



## 1. Introduction

NASA Marshall Space Flight Center's (MSFC) EXperimental Vector Magnetograph (EXVM) polarimeter measures the sun's vector magnetic field<sup>1</sup>. These measurements are taken to improve understanding of the sun's magnetic field in the hopes to better predict solar flares. Part of the procedure for the EXVM requires image motion stabilization over a period of a few minutes. A high speed tracker can be used to reduce image motion produced by wind loading on the EXVM, fluctuations in the atmosphere and other vibrations. The tracker consist of two elements, an image motion detector and a control system. The image motion detector determines the image movement from one frame to the next and sends an error signal to the control system.

For the ground based application to reduce image motion due to atmospheric fluctuations requires an error determination at the rate of at least 100 hz. It would be desirable to have an error determination rate of 1 kHz to assure that higher rate image motion is reduced and to increase the control system stability.

Two algorithms are presented that are typically used for tracking. These algorithms are examined for their applicability for tracking sunspots, specifically their accuracy if only one column and one row of CCD pixels are used. To examine the accuracy of this method two techniques are used. One involves moving a sunspot image a known distance with computer software, then applying the particular algorithm to see how accurately it determines this movement. The second technique involves using a rate table to control the object motion, then applying the algorithms to see how accurately each determines the actual motion. Results from these two techniques are presented.

## 2. Algorithms in use for Tracking

### 2.1 Centroid Tracker

A centroid tracker works by calculating the centroid of each successive image then determining the shift in the centroid location from one image to the next. The centroid is calculated using

$$X_{cen} = \frac{\sum \sum x \cdot f(i,j)}{\sum \sum f(i,j)}, \quad Y_{cen} = \frac{\sum \sum y \cdot f(i,j)}{\sum \sum f(i,j)} \quad (2)$$

where  $f(i,j)$  is the image intensity for a given pixel<sup>2</sup>. This method involves a multiply and two adds per pixel. It also involves some post processing of data to remove linear trends in the data.

## 2.2 Marek's Method

In reference 3 a method was described which involved comparing the current image with a light distribution model. This algorithm has been modified to use a reference image instead of a light distribution model. This method works by taking an integral of errors over the pixels of interest. This integral is

$$E_x = \sum \sum \text{sign}(x_{\text{ref}} - i) (f_{\text{ref}}(i,j) - f(i,j)) , \quad (4)$$

where  $f_{\text{ref}}(i,j)$  is the reference image,  $f(i,j)$  is the current image, and  $x_{\text{ref}}$  is the x location of the peak intensity value of the reference image or the minimum if using the non inverted sunspot intensity profile. The location of the peak value of the current image is given by,

$$x_o = \alpha E_x + x_{\text{ref}} , \quad (5)$$

where  $\alpha$  is an error parameter that must be determined from the initial reference image. The parameter  $\alpha$  is determined by shifting the reference image one pixel, then applying Equation 4 with the shifted image used as  $f(i,j)$ , this is shown in Figure 1 with the "dotted" line representing the shifted image. Figure 2 shows the difference between the reference image and the shifted image. In this case  $x_o$  would be equal to  $x_{\text{ref}} + \text{pixel size}$ , and  $\alpha$  could be determined from Equation 5.

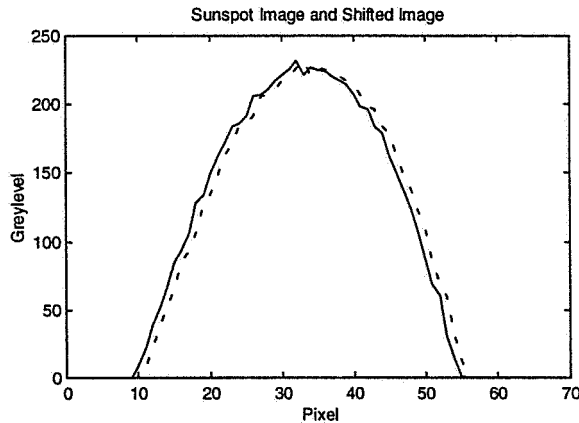


Figure 1

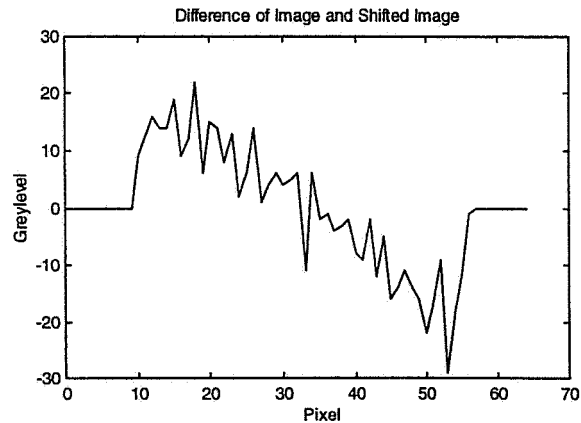


Figure 2

Marek's method requires one subtraction and one addition per pixel. This is a one addition reduction over the centroid method and it changes a multiplication to a subtraction. For high end DSP processors (for ground based applications) changing a multiplication to a subtraction does not represent a savings in time. However for a space based application a DSP might be excluded because of power, size and radiation-hardening limitations. For an 8086 Marek's method increases execution speed by nearly a factor of 20 over using the centroid algorithm<sup>3</sup>.

A savings in time of a factor of  $N/2$ , where  $N$  is the array length, can be obtained by using one column and one row of pixels (2-axis), as opposed to using an entire  $N \times N$  matrix of CCD pixels. This would save time in both the acquisition of the image data and the processing of the data. Linear CCD arrays can also be made to a higher quality. Since a sunspot has an irregular shape the question arises as to how accurate this method would be? This issue is addressed in the next two sections.

### 3. Algorithm Test Results with Computer Simulation

To test the algorithms an image was moved using computer software then an algorithm was applied and the calculated image motion was compared with the known image motion. The image was obtained by fitting a polynomial to a sunspot image. This polynomial was then sampled on the subpixel level and integrated over the pixel area. Once the pixel value was obtained gaussian noise was added to the image. A cross section of the sunspot image with gaussian noise added is shown in Figure 1. The image was moved randomly 100 time within a specified radius. Table 1 shows movements confined to a radius of 1 pixel, 3 pixels on up to 15 pixels. The image was divided into 65 pixels and 256 grey levels were used. The error is reported as

$$\text{error report} = | \text{known movement} - \text{calculated movement} | / \text{pixel size} \times 100\%. \quad (6)$$

Table 1. Results of Centroid and Marek's Method using 2-axis for Tracking

	Centroid Method with 2-axis		Marek's Method with 2-axis	
Random Motion	x error %	y error %	x error %	y error %
stationary	3.63	3.15	6.95	3.94
1 pixel	4.76	3.22	6.99	4.23
3 pixel	10.03	5.19	12.33	5.76
5 pixel	15.79	7.33	19.61	7.85
10 pixel	31.67	12.95	44.43	19.97
15 pixel	47.12	20.13	80.34	59.10

If the control system works correctly the motion should be confined to a radius of less than 1 pixel. In this region both method provide similar results and it is clear that using a 2-axis tracking system would be sufficient.



#### 4. Rate Table Experiments

A Reticon MC9128 camera and an EPIX frame grabber were used in conjunction with a rate table to uniformly rotate the Reticon camera with a simulated sunspot in the field of view (FOV). This experiment was performed twice, once for a simple compact sunspot and a second time with a more complex scene.

Figure 3 shows the results of applying Marek's method and the centroid method both using a 2-axis scheme. In Figure 3 an error pattern developed which repeated for each pixel. This pattern was produced due to a none uniform response across each individual pixel<sup>4</sup>. This nonlinear response produced more error than gaussian noise and is the primary limiting factor in obtaining subpixel accuracy. In Figure 3 one also notices that Marek's method tends to trail off. It eventually went to half a pixel error, see Figure 4, after moving further than four pixels, even though the reference image was update each time a pixel was crossed. It has not been determined why this occurred.

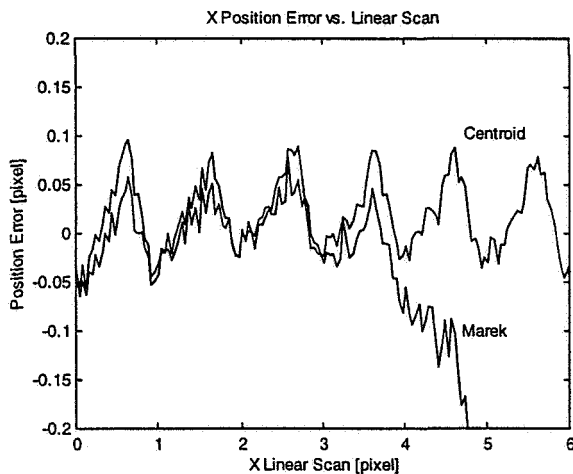


Figure 3

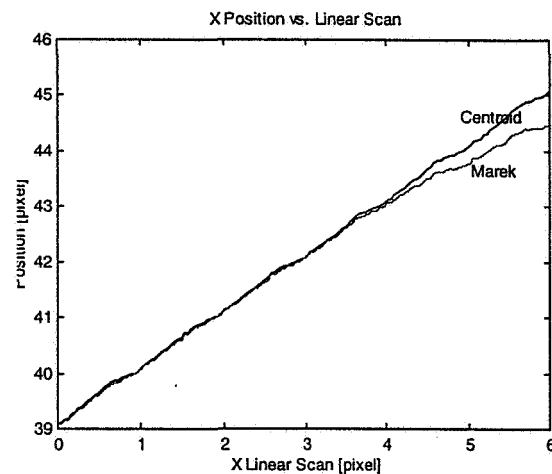


Figure 4

Next a more complex image was used to test the two algorithms. The digitized image is shown in Figure 5. The centroid algorithm was unable to track on this image. In Figure 6 the horizontal axis represents how much the image actually moved and the vertical axis is the calculated movement. Marek's method was able to track on this image, which is demonstrated in Figure 6. Figure 7 shows the error for Marek's method. Note the centroid method is not shown in Figure 7 since it would be off scale.

For a high-end DSP a subtraction, an addition, a multiply or a move between memory and register takes one clock cycle. Using the centroid method with a 64x64 array and a DSP with a clock cycle of 40ns would produce a 300 Hz rate. Using Marek's method and the 2-axis approach with two 256 linear CCD arrays would provide over a 10 kHz rate for image position error determination and increase the accuracy by nearly a factor of four over using a 64x64 array.

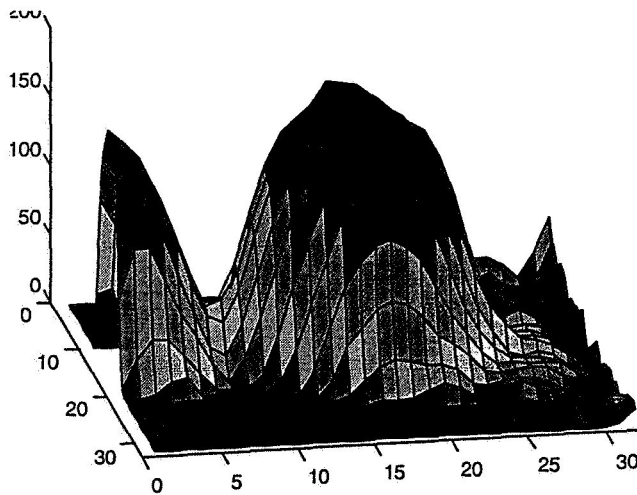


Figure 5

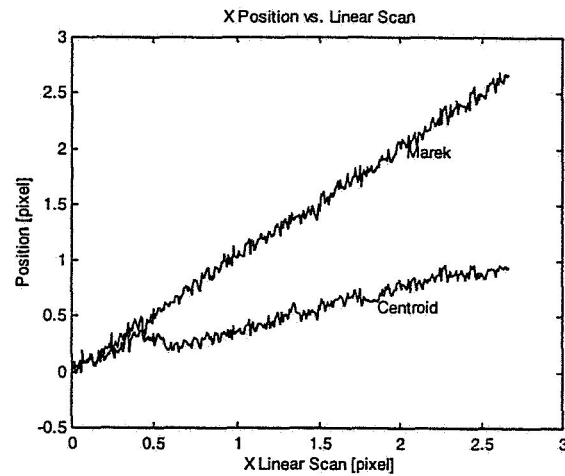


Figure 6

## 5. Conclusions

Using a 2-axis approach to sunspot tracking is feasible. The critical point is that the error determination and control system must operate at a rate greater than the highest frequency of image motion. Using a DSP and Marek's method would provide a position error determination system that could operate well above 1kHz, the rate of a high-end mirror based control system.

## Acknowledgments

The author would like to thank Ron McIntosh, Ed West, and Don Hediger for their suggestions and support of the work presented here. He would also like to thank Marek Chmielowski for the many phone conversations they had discussing this problem. This work was supported by NASA/ASEE SFFT.

## References

- 1 West, E. A., and Smith, M. H., "Polarization Characteristics of the MSFC Experimental Vector Magnetograph," SPIE, vol. 2265, pp. 272-283, July 1994.
- 2 Mansfield, P., "Machine Vision Tackles Star Tracking," Laser Focus World, pp. S21-S24, May 1996.
- 3 Chmielowski, M. and Klien, L., "A High-Precision, Real-Time Position-Locating Algorithm for CCD-based Sun and Star Trackers," PASP, vol. 105, pp. 114-116, January 1993.
- 4 Chmielowski, M., "On-Chip Image-Processing Algorithm for Real-Time CCD-Based Star Trackers and Wavefront Sensors," PASP, vol. 106, pp. 523-531, May 1994.



1996

**NASA/ASEE SUMMER FACULTY FELLOWSHIP PROGRAM**

**MARSHALL SPACE FLIGHT CENTER  
THE UNIVERSITY OF ALABAMA**

**TECHNOLOGY TRANSFER EXTERNAL METRICS, RESEARCH, SUCCESS  
STORIES, AND PARTICIPATION ON EVALUATION TEAM FOR THE  
REUSABLE LAUNCH VEHICLE (RLV)**

<b>Prepared By:</b>	<b>George W. Trivoli, Ph.D.</b>
<b>Academic Rank:</b>	<b>Professor of Finance/Eminent Scholar</b>
<b>Institution and Department:</b>	<b>Jacksonville State University Department of Finance &amp; Statistics</b>

**NASA/MSFC:**

<b>Laboratory:</b>	<b>Technology Transfer Office</b>
<b>Branch:</b>	<b>Program Control &amp; Management Support Office</b>



## INTRODUCTION

This research report is divided into four sections. The first section is related to participation on the team that evaluated the proposals for the X - 33 project and the Reusable Launch Vehicle (RLV) during mid-May; prior to beginning the 1996 Summer Faculty Fellowship. The second section discusses the various meetings attended related to the technology evaluation process. The third section is related to various research and evaluation activities engaged in by this researcher. The final section discusses several success stories this researcher aided in preparing.

Despite the fact that this researcher is not an engineer or science faculty, invaluable knowledge and experience have been gained at MSFC. Although related to the previous summer's research, the research has been new, varied, and challenging. This researcher was fortunate to have had maximum interaction with NASA colleague, David Cockrell. It would be a privilege and honor to continue a relationship with the Technology Transfer Office. In addition, we will attempt to aid in the establishment of a continuous formalized relationship between MSFC and Jacksonville State University. Dr. David Watts, Vice President for Academic Affairs, J.S.U., is interested in having the Technology Division cooperating with MSFC in sharing information and working tech transfer inquiries.

The principal benefits gained by this researcher include the opportunity to conduct research in a non-academic, real world environment. In addition, the opportunity to be involved in aiding with the decision process for the choice of the next generation of space transportation system was a once in a lifetime experience. This researcher has gained enhanced respect and understanding of MSFC/NASA staff and facilities.

## EVALUATION OF RLV

Prior to the beginning of the 1996 NASA/ASEE Summer Faculty Fellowship this researcher participated on the team evaluating the three proposals for the X-33 project and the Reusable Launch Vehicle (RLV) during mid-May. This researcher was primarily responsible for aiding in the evaluation of the industry business plans submitted by Lockheed Martin, Rockwell, and McDonnell-Douglas.

## TECHNOLOGY TRANSFER MEETINGS

This researcher participated in an all-day meeting with representatives from the National Association of Public Administrators (NAPA) on June 19, 1996 related to how tech transfer is conducted at MSFC. The following day a follow-up meeting was held to review, with David Cockrell, William Fieselman and the Auburn University team, the results of the NAPA meeting. Further research and activities were discussed during this meeting; including the analysis of SBIR data and the relationship of the economy's production frontier to job opportunities.

Working with Jeff Cornelius, Fred Schramm and David Cockrell, this researcher helped with proposing a plant visitation with a major appliance manufacturer in Tennessee. Although the technology assistance provided by MSFC was of a sensitive

nature, there remains an opportunity to forge a continuing relationship with the research and development department of this appliance manufacturer.

## TECHNOLOGY TRANSFER RESEARCH

This researcher prepared a brief analysis and review of an article entitled, “Will Metrics Really Measure Up,” by Randy Barrett. The article refers to the problem of gaining a consensus on whether jobs creation is a good measure of technology transfer’s success. The author specifically questions the MSFC technology transfer study for extrapolating the gains reported by survey respondents to the total of the participating industrial partners. However, with response rates of between 30 and 50 percent there can be no question that these responses are representative of the entire group of industrial partners. Moreover, non-participants were contacted by phone whenever possible to gain insight into the non-response bias. For instance, gaining further information from those businesses that did not respond answers critics claim that the sample of respondents is not representative.

In addition, a brief analysis was performed comparing the RIMS II approach and Computable General Equilibrium (CGE) model. The working paper entitled, “The Use of Multipliers: An Assessment of RIMS II,” by Henry Thompson and Clint LeNoir was reviewed. This paper was written in response to a Working Paper, entitled “Measuring the Economic Benefits of Technology Transfer From A National Laboratory: A Primer”, by R. B. Archibald, et.al. of the College of William & Mary. The authors of the William & Mary paper advocate the use of the CGE model instead of the RIMS II approach to measuring the impact of technology transfer. Listed briefly below are three major reasons related to the advantages of RIMS II over the CGE model.

(1) National versus Regional Approach - The RIMS II approach, with its emphasis upon the regional impact of effects from technology improvements, is more applicable to essentially smaller enterprises that receive SBIR grants and technology assistance.

(2) CGE Model’s Assumptions and Simplifications Reduce Reliability - As with the RIMS II approach, the CGE model is based upon assumptions and simplifications. But, since the CGE model attempts to derive estimates of the impact of economic changes upon the entire economy, it is necessary to make many more assumptions and simplifications leading to gross aggregations of data. The RIMS II approach, on the other hand, being a direct input type approach that considers primarily regional effects, does not need the added complexities of a greatly aggregated model in treating economic improvements.

(3) Adapting CGE Model Expensive/Difficult - It may be possible to adapt the CGE model for the specific purpose of measuring the impact of technology improvements. However, in order to keep the costs of applying the CGE model down, numerous assumptions and simplifications would be necessary. Indeed, the

model would probably have to utilize the estimates of the production function of the RIMS II approach.

Another research project involved describing a simple economic model of the impact on the economy of technological advances by shifting outward the economy's production frontier (see Figure 1). Figure 1 shows a flow chart of a simple model of the economy's production frontier (Y<sub>0</sub>) in Panel A. The production frontier shows the ability of an economy to produce goods (G<sub>0</sub>) and services (S<sub>0</sub>) with existing capital (K<sub>0</sub>), labor (L<sub>0</sub>), and technology (T<sub>0</sub>). The classical economic model assumes both capital and labor are fixed at any given time; and that technology is imbedded in the existing stock of capital and labor. Under these constraints, if the economy wants more goods it must give up some services (see graphic, Panel A). The only way to shift the production frontier outward is to increase capital and labor.

However, we now recognize that technological improvements and innovation need not be imbedded in capital (see Panel B, Figure 1). For instance, the development of a computer program to, say, increase the production flow in a plant, or the order flow, or improve shipping or billing. All of these improvements increase the productivity of existing capital and labor. Therefore, technological improvements are capable of shifting the production frontier outward with existing capital and labor, as well as allowing the production of improved capital.

Panel C, Figure 1 shows the economy with an outward shift in the production frontier as a result of, say, technological innovation. Now, with the higher level of the production frontier (Y<sub>1</sub>), the economy is able to produce more goods (G<sub>1</sub>) and services (S<sub>1</sub>). The outward shift in the production frontier increases job opportunities.

MSFC Technology Transfers are contributing to the outward shift of the economy's production frontier. A great preponderance of evidence gathered both by surveying participants in MSFC technology transfer assistance and the SBIR program supports the contention that technology transfer helps industry to improve innovation. This, in turn, enables industry to increase productivity, which allows an increase in the nation's production frontier. Outward shifts in the production frontier increase job opportunities for the Southeast region and the entire economy.

This researcher was also involved in attempting to determine the source of the often quoted ratio of \$7 for every \$1 spent on R & D. Upon reviewing all available studies, it was determined that there are several studies that are the likely source of the above ratio. The most likely source are two studies by the Midwest Research Institute (MRI) that analyzed the macroeconomics effects of the U.S. space program on technological progress. The study concluded that each dollar spent on NASA R&D resulted in returns of an average of seven dollars in GNP over an eighteen year period following the expenditure (MRI, 1971, 1988).



Upon reviewing the above studies, H.R. Hertzfeld, in his book Measuring Returns to Space Research & Development (1992), questions two major assumptions made in these studies. The first assumption was that NASA R&D was not separated from other R&D in the economy. MRI calculated returns for total R&D (Federal and private), and assumed that space R&D was the same as all other R&D. One could argue the space R&D carries much larger benefits to the economy due to the often "break-through" nature of the research. A second assumption of the MRI study was that R&D has an 18-year lifetime from outlay to terminal value. After 18 years had elapsed in the study, no further returns were measured. Many NASA technologies take a longer period before they reach full commercial potential and impact on the economy. The above assumptions appear to be too conservative, which implies that the ratio for NASA technology transfer may be higher. But, lacking further hard evidence, specific numbers should be avoided.

This researcher recommends that no aggregate figures be quoted, but instead focus on specific examples of successful transfers of NASA technology to the private sector. All that can be said of all the studies reviewed is that the economic benefits far exceed the costs of transferring the technology to the private sector.

A final research activity involved preparation of a description of the statistical techniques used by the U.S. Bureau of Labor Statistics (BLS), Division of Labor Force Statistics in measuring employment in the economy. Based on a brief summary it is determined that the BLS relies on two major surveys to determine the level of employment in the economy. These surveys are the (1) Current Population Survey (Households), and (2) Current Employment Survey (Establishments). These surveys differ in emphasis, i.e. household employment versus establishment employment, measurement techniques, and inclusiveness. Each one provides a monthly estimate of total employment in the economy. By tracking employment over time, these surveys provide a good measure of the general employment trends, especially on a revised quarterly basis.

#### TECH TRANSFER SUCCESS STORIES

This researcher worked closely with TecMasters, Inc. (William Fieselman) and Louis Galipeau to scan responses received from companies that received MSFC technical assistance for potential success stories. Several firms were contacted to determine the extent of help provided by MSFC, and their willingness to allow us to develop success stories.

Currently, this researcher is working with Bob Lessels to investigate several potential success stories. Listed below are some of these success stories.

(1) Specialty Plastics, Inc., Baton Rouge, LA - MSFC assisting them in developing innovative joining and fitting technologies for advanced composite piping systems for the U.S. offshore oil and gas drilling industry. This story is currently in coordination with the company.

(2) A steel fabricating manufacturer in Alabama - MSFC assisting in solving serious welding problems in the manufacture of stainless steel sheets and trim for major appliances. This story is waiting for further development and verification of the new technology.

The above are on going activities, with results still pending. However, they appear well enough along to indicate successful outcomes. The managers were contacted by this researcher and they appear willing to cooperate with MSFC/Tech Transfer Office in telling their stories.

In addition, this researcher developed a positive success story related to the Tethered Satellite System flight. The story emphasizes the many significant discoveries accomplished by the exploratory experiment. Several suggestions are offered for handling so-called failures as an introduction to the story.

Finally, this researcher developed a success story about the new Pratt & Whitney engine for the Boeing 777. MSFC, in partnership with Pratt & Whitney, helped them to develop a clocking system for the turbine airfoils on the new engine. This improvement in design allows an increase in engine efficiency of a full half-percent. This, in turn, saves fuel making the U.S. less dependent upon imported oil

#### CONCLUSIONS AND RECOMMENDATIONS:

On the whole all of the activities of the Technology Transfer Office that this researcher has been involved with are carefully planned and efficiently implemented. This Office is serving as a leader in targeted marketing of MSFC capabilities. In addition, this Office is literally breaking new ground in surveying technical assistance partners; and evaluating and analyzing data gathered from the returned questionnaires. Moreover, this Office is taking the lead in surveying and analyzing responses from SBIR's. As with any pioneering effort there are critics and set-backs, but the results will surely satisfy the impartial reviewer. Summarized below are several observations and suggestions for the continued effort.

(1) Continue developing the data base for the SBIR surveys. The Auburn "team," working in conjunction with this Office and TecMasters, Inc. is a good approach.

(2) Continue collecting and refining data collected from the tech-assistance surveys. The data collection process is sound; the use of the RIMS II regional multipliers is appropriate for the task; and the reporting process is conservative but realistic.

(3) Continue to develop success stories in cooperation with business partners who have been helped by MSFC/NASA technology transfer. Based on this researcher's experience and discussions with Cathy Funston, David Cockrell and William Feiselman, a suggested outline of an approach for identifying and developing success stories is offered (see Table 1).

(4) This researcher will continue to write about tech transfer success stories as they relate to investment opportunities in the weekly column, "Your Investing". Currently, a story on the Lockheed Martin X-33 and RLV is being developed.

**Figure 1. FLOW CHART - TECHNOLOGY & PRODUCTION FUNCTION**

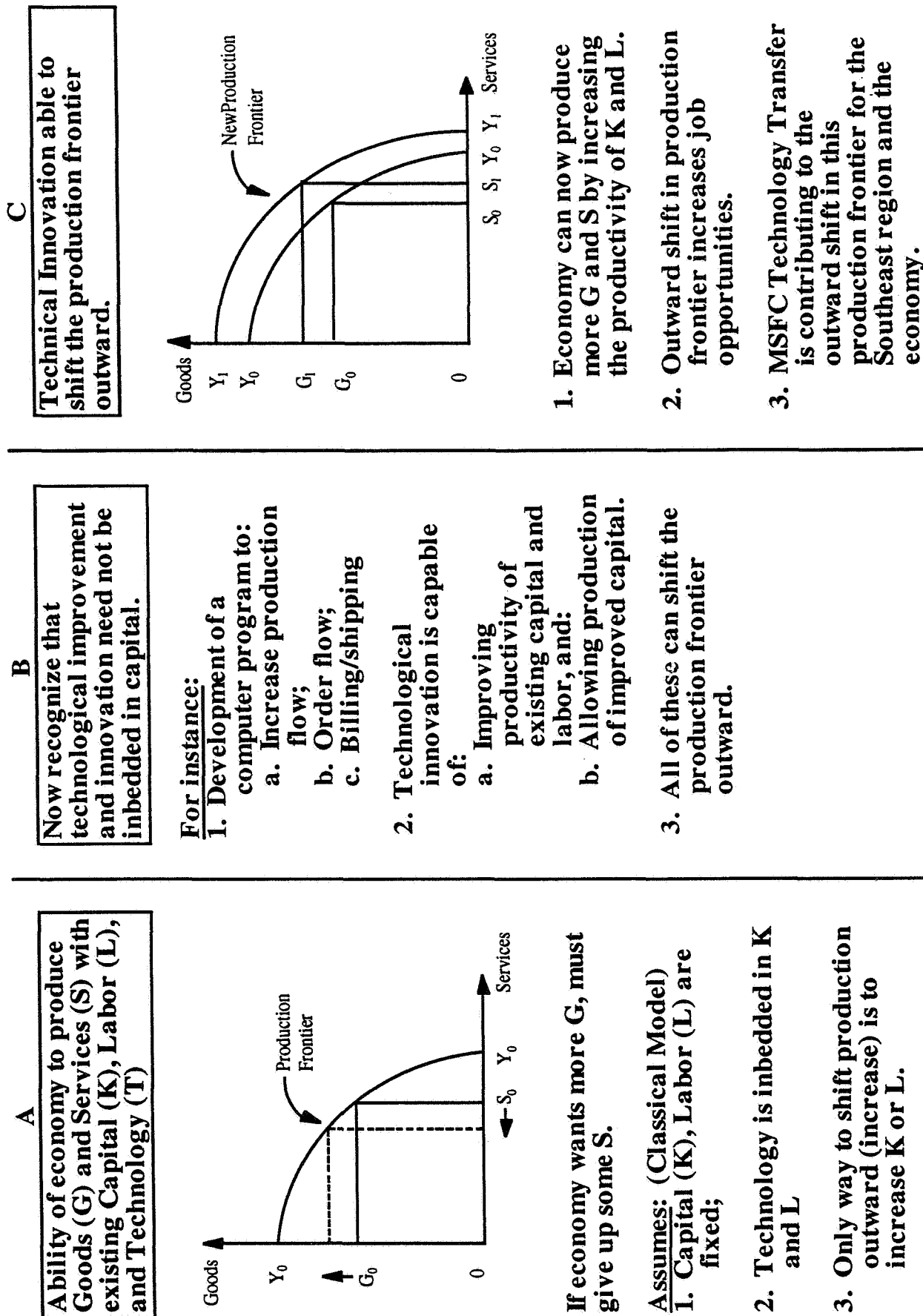


Table 1. Suggested Outline of Approach for Identifying and Developing Success Stories

Listed below is a suggested outline for an approach for identifying and developing new technology transfer success stories.

A. Periodic review by TecMasters, Inc. of all returned questionnaires from enterprises receiving technical assistance from MSFC/NASA in the Southeast region to:

1. Identify potential success stories.
2. Identify respondents with unusually large employment or revenues numbers.

B. There is a need to create a position of Success Story Coordinator, who would be responsible for the following.

1. Screening all possible success stories from all sources by verifying:
  - a. The nature of the problem worked ,
  - b. The extent of MSFC/NASA help in solving the problem,
2. Maintain a time-sensitive matrix of all potential success stories to determine progress, need for further technical assistance, or possible release of the story.
3. Schedule a Quarterly Review Luncheon to be held with Lab POC's to discuss actual or potential success stories.
4. Check to see if there are human interest stories, such as medical developments or environmental benefits.

C. Upon closure of Space Act Agreements and Cooperative Agreements, a summary of potential success stories should be provided by the responsible parties to the Success Story Coordinator.

1. The State Representatives should alert the TAB Board of any potential success stories.
2. The TAB Board should verify and pass along possible success stories to the Success Story Coordinator.
3. Success Story Coordinator should participate in TAB Board meetings.

D. The person devoted to writing success stories should be responsible for:

1. Verifying all information on success stories with success story Success Story Coordinator, the LA Office, the Lab chief, and the customer with appropriate signatures.
2. Writing and publishing the final success stories
3. Publishing success stories in Tech-Tracs.
4. The assistant should be responsible for maintaining a spread sheet record of all success stories submitted for publication by State, SIC code, and topic for easy reference.



**1996**

**NASA/ASEE SUMMER FACULTY FELLOWSHIP PROGRAM**

**MARSHALL SPACE FLIGHT CENTER  
THE UNIVERSITY OF ALABAMA**

**THE INFRASTRUCTURE OF AN INTEGRATED VIRTUAL REALITY  
ENVIRONMENT FOR INTERNATIONAL SPACE WELDING EXPERIMENT  
(ISWE)**

Prepared By:	Peter Hor-Ching Wang, Ph.D.
Academic Rank:	Assistant Professor
Institution and Department:	Alabama A&M University Department of Computer Information Science
NASA/MSFC:	
Laboratory:	Mission Operation Laboratory
Division:	Operations Engineering Division
Branch:	Crew Systems Engineering Branch
MSFC Colleague:	Joe Hale



# **The infrastructure of an integrated Virtual Reality environment for International Space Welding Experiment**

## **1. INTRODUCTION**

This study is a continuation of the summer research of 1995 NASA/ASEE Summer Faculty Fellowship Program. This effort is to provide the infrastructure of an integrated Virtual Reality (VR) environment for the International Space Welding Experiment (ISWE) Analytical Tool and Trainer and the Microgravity Science Glovebox (MSG) Analytical Tool study. Due to the inavailability of the MSG CAD files and the 3D-CAD converter, little was done to the MSG study. However, the infrastructure of the integrated VR environment for ISWE is capable of performing the MSG study when the CAD files become available. Two primary goals are established for this research. First, the essential peripheral devices for an integrated VR environment will be studied and developed for the ISWE and MSG studies. Secondly, the training of the flight crew (astronaut) in general orientation, procedures, and location, orientation, and sequencing of the welding samples and tools are built into the VR system for studying the welding process and training the astronaut.

## **2. EXPERIMENTAL APPROACH**

The objective of the infrastructure of the VR environment is to integrate the essential peripheral devices into the VR system and provide the procedures and orientations, and locations of the welding samples and tools. There are five peripheral devices studied in this research: the Polhemus Fastrak sensors, the 6-DOF Spaceball, the MSFC/CAVE RMS hand controller HC-Hand, the VPL Dataglove model II hand, and the mouse. The device drivers of the 6-DOF Spaceball, the Polhemus Fastrak sensors, and the mouse are provided by the Sense8 WorldToolKit. The device driver of MSFC/CAVE HC-Hand and the VPL Dataglove model II hand are studied and developed as part of this research effort. One of the Polhemus Fastrak sensor is attached to the Kaiser Electro-Optics Vim1000HRpv Head-Mounted-Display (HMD) to track the head movement of the user. While the other Polhemus Fastrak sensor is attached to the VPL Dataglove to track the hand movement of the user. The Dataglove hand gestures are defined to rotate the drum, pick up, carry, and release the welding tools. The Dataglove hand gestures are also used to select button commands from the control panel. Texture mappings are attached to the buttons of the control panel to simulate the ISWE button selection. The texture mappings of all sides of the drum, buttons, and the control panel are attached to the polygons to improve the realism of the ISWE model. The MSFC/CAVE RMS hand controller HC-Hand consists of two 3-DOF devices. The left hand is used to control the X, Y, and Z coordinates of the navigator, while the right hand is used to control the Pitch, Yaw, and Roll of the navigator. The HC-Hand control button is used to switch among the navigation modes. The coarse/vernier switch is used to control the speed of the navigation. The two momentary switches are used to rotate the drum and the astronaut. The HC-Hand is connected to the RMSPC analog-to-digital device and the digital data are sent through the network to the VR system. This also provides the remote control capability of the VR system as well as the remote networked simulations. This HC-Hand can also be used in the VR environment for the networked battle field simulations by attaching each HC-Hand to an individual soldier. Since the data is sent through the network, it is not limited by the number of the serial ports available of the VR system. The 6-DOF Spaceball not only provides the X, Y, Z, Pitch, Yaw, Roll six degree of freedom, but also provides eight buttons keys for simulation tasks. Two of the button keys are used to increase and decrease the sensitivity of the sensors. One button key is used to switch among the object picking/moving/flying modes. One button key is used to zoom all the universe. While the other button key can be used to define tasks for specific VR applications. The mouse is used to navigate through the ISWE as well as the picking/moving/flying dynamic objects.

The tasks of the ISWE study includes:

1. To perform the viewing analysis of the ISWE model.
2. To navigate the astronaut along the Y-axis of rack-rail and to yaw to the left and right.



3. To rotate the drum of ISWE model.
4. To pick up the welding tools, move to the drum area, and perform welding process.
5. To perform the specific tasks by selecting the buttons from the control panel.
6. To view the safety of the work performed by the other astronaut.
7. To perform the orientation and position as well as welding process as the astronaut.

In the ISWE study, the movement of astronaut, foot stand slider, control panel, buttons, welding tools, and the hand should be done simultaneously. In this VR environment, the buttons, control panel and astronaut are attached to the foot stand slider. The hand is attached to the astronaut when the VR system is in the astronaut moving mode, and attached to the viewpoint when it is in the free navigation mode. The welding tools are attached to the hand when they are intersected by the index finger tip and a grab gesture is made. The welding tools are released when the release gesture is made. In the astronaut flying mode, the position and orientation of the navigator is set to the astronaut while the VR system remains in the flying astronaut mode. A stereo mode VR environment is also studied and developed by interleaving the two rendering images to each eye to achieve the 3D stereo vision effect. All the peripheral devices used in the above mentioned immersive VR environment can be used in the stereo mode VR system except the HMD. Instead, a pair of Crystaleyes shuttle glasses are used to view the stereo ISWE model. The advantage of stereo mode VR environment is that it can be viewed by several people simultaneously. It is very attractive in the viewing analysis review and training applications. It is also very valuable in the educational environment because it can be used by many students simultaneously with a relatively low cost. In the immersive VR environment, the VPL dataglove and HC-Hand should be used as the major sensors. While in the stereo mode VR environment, the 6-DOF Spaceball, VPL Dataglove, as well as the HC-Hand are served equally well to navigate through the universe and manipulate the dynamic objects.

### 3. CONCLUSIONS

The Summer Faculty Fellowship has been really challenging and interesting. A lot of difficult tasks have been studied and solved at great pleasure. It has been thrilling from time to time when great break-throughs were made. I am eager to take my research and experience back to Alabama A&M University Computer Information Science Department to share with fellow faculty, administrators, and students. The infrastructure of an integrated VR environment for ISWE built at MSFC/CAVE can be used as the teaching material of the Virtual Reality course at AAMU graduate school. It can also be used as the foundation of my three years research project from NASA/MSFC Equal Employment Office -- Development, Assessment, Validation and Evaluation of Human Anatomy Instruction (DAVE).

### 4. ACKNOWLEDGEMENT

I would like to express my great appreciations to my MSFC Colleague Joe Hale for his innovative ideas and guidance. I also like to thank George Hamilton and Geoffrey Beech for their advise and support in importing and translating the 3D CAD files of ISWE and MSG models into the VR environment. The financial support of the NASA/ASEE Summer Faculty Fellowship Program, Debbie Ott, Mike Freeman, Gerald Karr, and Frank Six are gratefully acknowledged.

### 5. REFERENCES

1. Hale, Joe and Wang, Peter "A user interface for an integrated Virtual Reality Environment", 34th Annual Southeast Conference. Tuskegee, Alabama April 17-19 1996 pp 328-329
2. Lindsey, Patricia F. "Development of Microgravity, Full Body, Functional Reach Envelope using 3-D computer Graphics model and Virtual Reality Technology", NASA contract Report NASA CR-196533

3. Phillips, James "Development of a low-cost Virtual Reality Workstation for traing and Education", NASA contract Report NASA CR-199830
4. Shiva, S.G. and Wang, Peter "A knowledge-based Software Reuse Environment for Program Development", The Twenty-sixth Southeastern Symposium on System Theory. Athens, Ohio March 20-22 1994 pp276-280
5. Watkins, Christopher and Marenka, Stephen "Virtual Reality Excursions with Programs in C", AP Professional, 1994



**1996**  
**NASA/ASEE SUMMER FACULTY FELLOWSHIP PROGRAM**

**MARSHALL SPACE FLIGHT CENTER**  
**THE UNIVERSITY OF ALABAMA**

**APPLYING PARALLEL PROCESSING TECHNIQUES TO**  
**A TETHER DYNAMICS SIMULATION**

Prepared By: B. Earl Wells, Ph.D.

Academic Rank: Assistant Professor

Institution and Department: The University of Alabama in Huntsville  
Department of Electrical and Computer Engineering

NASA/MSFC:

Office: Small Expendable Deployer Systems

Division: Earth and Space Science Projects

Branch: Science and Applications Projects

MSFC Colleagues: Jim Harrison  
Pat Doty  
Tommy Harris  
Frayne Smith



The focus of this research has been to determine the effectiveness of applying parallel processing techniques to a sizable real-world problem, the simulation of the dynamics associated with a tether which connects two objects in low earth orbit, and to explore the degree to which the parallelization process can be automated through the creation of new software tools. The goal has been to utilize this specific application problem as a base to develop more generally applicable techniques.

## The Tether Dynamics Problem

The basic tether deployment model, which served as a test-bed application for this research, is described in the NASA technical report outlined in reference [1] where it is assumed that two end bodies, each of point mass, are interconnected together via a nonconductive tether. It is also assumed that the tether is to be deployed by following a given deployment/control law and at least one of the end masses contains a finite amount of undeployed tether. The tether is assumed to be homogenous in composition, linearly elastic, and relatively thin, and the model also considers the longitudinal elasticity and bending stiffness.

## Software Description

A comprehensive serial simulation of the tether dynamics problem has been developed by John Glaese of Control Dynamics Corporation. Throughout this research this simulation was used as the "gold" standard by which the accuracy of parallel versions of this simulation were measured. A general overview of the derivative function calculation portion (i.e. main loop) of this software is shown below in Figure 1. Approximately 800, lines of source code from the Control Dynamics simulation were converted into a Pseudo C syntax to be used by the automatic parallelization software.

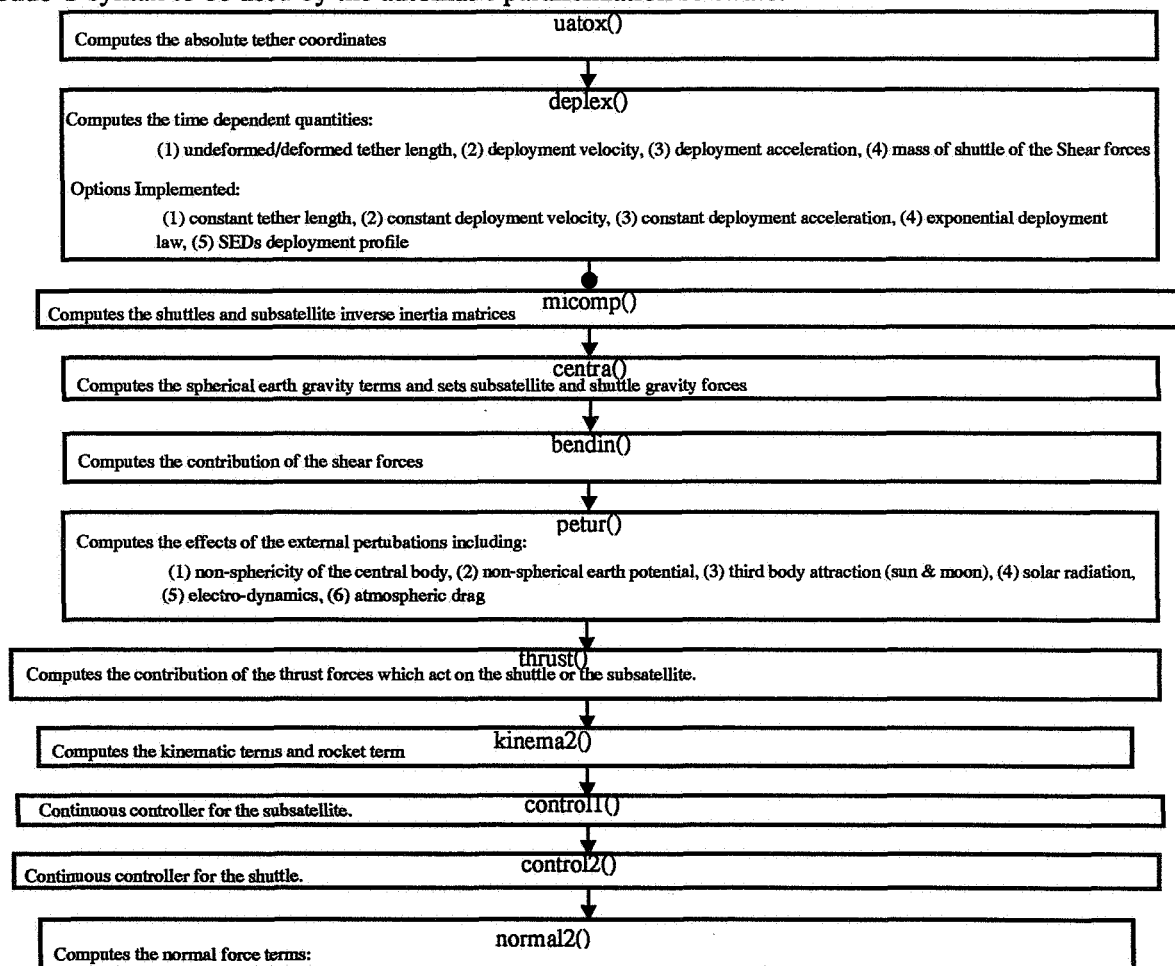


**Figure 1: Overview of the Main Loop of the Tether Dynamics Simulation**

## Automatic Parallelization

To facilitate the parallelization of this type of problem on arbitrarily-connected multicomputing environments, a software tool called the *Automated Partitioning and Mapping Engine*, APME, was created. It functions in conjunction with a task allocator to automatically create effi-

cient allocations encoded through the source-level files that it produces. The APME software requires that the user enter two application-dependent input files, and it produces two types of source-level output files as shown in Figure 2. The input files are called the *Hardware Topology File* which describes the topology and hardware characteristics of the system, and the *Dynamic System Description File* which describe the structure of the simulation in CSSL form [2]. The output files include a set of *System Configuration Files* and a number of *High-Level-Language Files*. In this research, the FORTRAN representation of the tether dynamics problem was transformed manually into the required CSSL form. The format of these files is described in some detail in reference [2] with additional constructs being added such as the *\$mapping* section which describes how the problem is to be spatially mapped to the hardware which is described in the hardware topology file. In addition to the automatic decomposition of the problem along spacial domains the APME software also allows the selection of a number of parallel integration algorithms. At this point in the research, the APME software is approximately 70% complete.

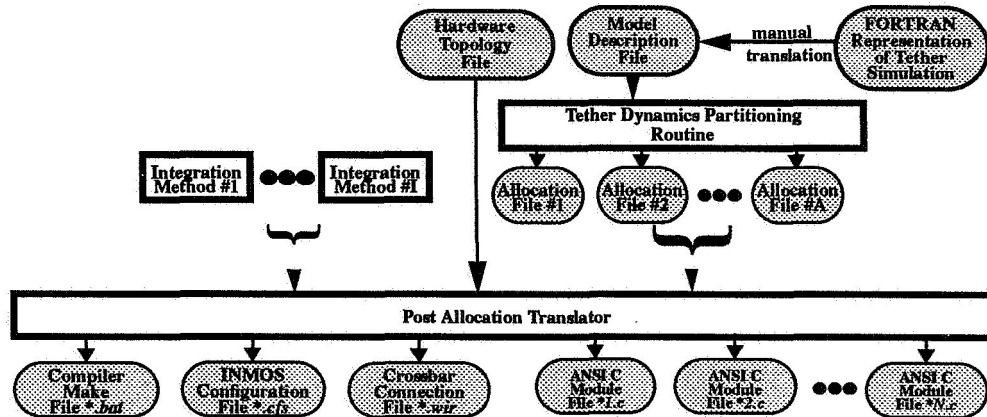


**Figure 2: Proposed Automated Partitioning and Mapping Tool**

#### Targeted Parallel Processing Environment

A small INMOS Transputer based system was used to determine the effectiveness of applying automatic parallelization to this general application domain. It served well in this capacity since it has many features that are present in other multicomputer architectures which have more powerful processors, while at the same time being a low-cost alternative to other commercially available parallel systems. Additionally, the Transputer system possesses a reconfigurable interconnection network which can be used to emulate a wide range of static topologies. This is accomplished, as shown in Figure 3, by superimposing the crossbar-connected links with the static links associated with the underlying fixed linear array topology present within the system. The base system had a total of ten T805 Transputers, with each Transputer having four bidirectional 20 Mb/s ports, two of which are used for the static connections and two of which are connected to the crossbar switch.

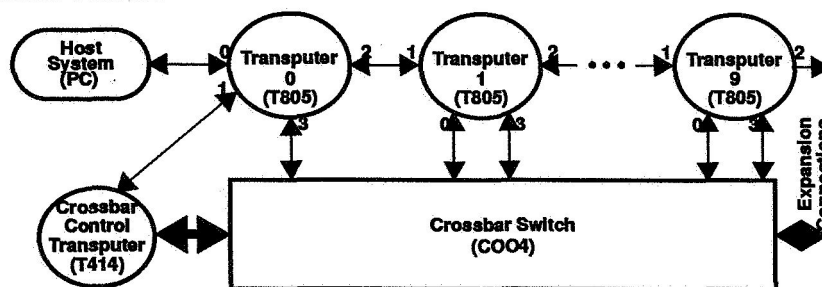
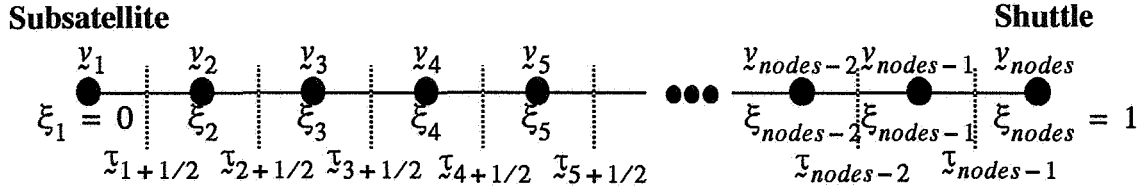


**Figure 3: Targeted Parallel Processing Environment**

#### Spatial Decomposition

The FORTRAN simulation of this model has been created by first transforming the equations of motion which describe the tether dynamics onto a new coordinate system which runs along the undeformed tether (it should be noted that transformations have been derived which map the underlying deformed tether model onto the more general deformed representation). This allows the set of partial differential equations to be converted into a set of ordinary differential equations by setting up a normalized coordinate system along the tether and discretizing at and exactly in between equally spaced (on the undeformed tether) nodal points. The resulting equations represent the individual nodal positions and velocities which given the position and velocity of one of the end bodies can be transformed to any viable coordinate system (see Figure 4).



Mapping Function:  $\text{processor number} = \text{int}\left(\frac{\text{node number} - 1}{n}\right) + 1$

**Figure 4: Spatial Decomposition of the Tether Dynamics Simulation**

The underlying implications from a parallel processing point of view is that the amount of computation grows in proportion to the number of nodal points (i.e. the algorithm is  $O(n)$  which is low-order polynomial) which in turn is somewhat proportional to the spacial resolution of the simulation. Additionally, the finite difference transformation results in a nearest and next-nearest neighbor communication pattern being present within the model if it is decomposed spacially along the undeformed tether; this maps well to a simple ring type topology which is highly desirable because of its low cost and high scalability.

Since the scope of the problem did not allow the modification of APME software to be completed by the end of the fellowship period, the parallel performance of this application was examined by profiling the APME-produced sequential simulation, and by evaluating the communication latency and bandwidth of the Transputer network. The following represents the results of this analysis under the following assumptions.

- 1) the mapping function of Figure 4 is used to place the nodal points on each Transputer,
- 2) the Crossbar Switch is statically configured into a virtual ring topology,
- 3) communication between processors is synchronous with no buffering of messages being allowed (blocking reads and blocking writes are the only communication mechanisms employed),
- 4) no single processor is allowed to simultaneously send and receive data to or from more than one other processor,
- 5) only simple store-and-forward routing of messages is supported,
- 6) cut through routing is not supported (if a communication must pass through an intermediate processor explicit communications must be scheduled on that processor to perform the echoing of the data through to the next processor along the communication path), and only ONE message can be sent through a link at a given time.

Table 1 highlights the results of this analysis for the arbitrarily chosen real-world case where it is assumed that a SEDS deployment scheme is employed, the model accounts for longitudinal deformations, the tether is inextensible, bending stiffness is neglected, nonsphericity is included, third body perturbations are neglected, atmospheric drag is included, diurnal and latitudinal effects are included and the radiation pressure is neglected. As shown in the second column of Table 1, during this analysis the time complexity for a portion of the simulation model was found to be linear with respect to the problem size but could not be parallelized without altering the algorithm. While it is believed that this section can be effectively parallelized, without significant loss of accuracy such investigations were reserved for future research.

In addition to characterizing the time complexity of the workload, the table shows the type and cost of each communication which is required when the mapping function of Figure 4 is implemented. Given the aforementioned sequential portion of the code no isoefficiency function [3] can exist, implying that the efficiency will steadily decrease as the number of processors increases, but significant speedups can still be obtained. Figure 5 shows the fixed workload, fixed time, and fixed memory speedups [3], where it can be observed that the speedup associated with a fixed size problem of 200 nodal points reaches a maximum of 11 for a value of 42 processors, and the fixed time and fixed memory speedups both approach a value of 20 as the number of processors is increased from 1 to 100. It should be noted that applying new algorithmic techniques to the aforementioned sequential portion would result in all three speedups monotonically increasing as the number of processors increases in a linear manner making this problem highly scalable. It should also be noted that there exists a region from 1 to 10 processors in which the speedups are highly linear and efficiencies approach 80%. This region can be exploited at this time without changing the algorithm.

Figure 5 also shows the effects of communication channel latency on overall speedup. If the latency is set to a value which is considered typical of many parallel processing systems then severe performance degradation will be observed. This strengthens the case for the development of low latency environments, even if it comes with the price of decrease communication bandwidth.

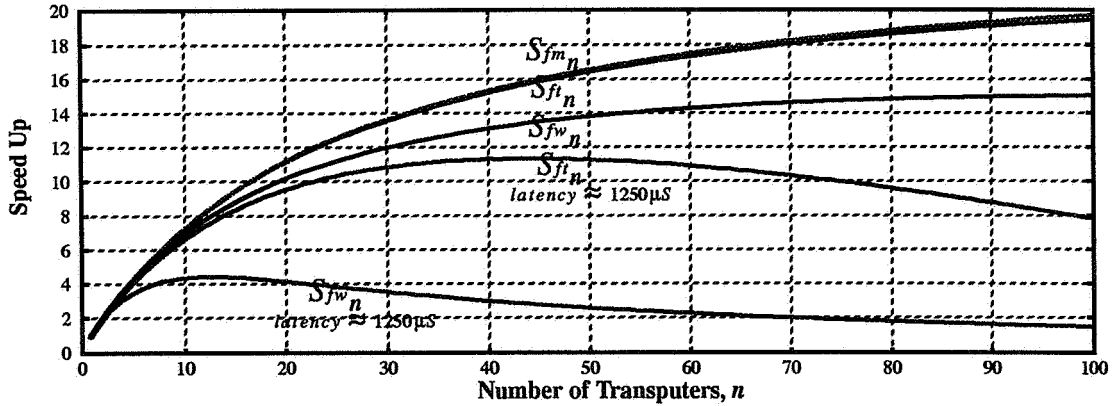


Table 1: work load and communication time parameters -- spacial decomposition

Subroutine Name	Linear Coefficients		Constant Term (C)	Type of Collaborative Communication	Communication Delay for T805-30 System (ring topology)
	Serial ( $K_1$ )	Parallelizable ( $K_2$ )			
uatox	66	67	130	heterogeneous one-to-all	$C_T(2) (n - 1)$
deplex	0	0	434	none	NA
micomp	0	0	230	none	NA
centra	0	158	128	none	NA
perturb	0	963	138	two, nearest neighbor	$2C_T(1)$
kinena2	0	130	60	four, nearest neighbor	$4C_T(1)$
control2	0	0	250	none	NA
normal2	0	127	79	four, nearest neighbor	$4C_T(1)$
uder	0	91	1552	homogeneous one-to-all	$C_T(4) \frac{(n + 1)}{2}$
Total	66	1536	3001		

workload  $\approx (K_1 + K_2) \text{ nodes} + C$  floating point operations

$C_T(V)$  = Transputer Communication Time =  $4.8V + 2.5$  mS



Fixed Work Load Speed Up

$$S_{fw_n} = \frac{T_1(\text{nodes})}{T_n(\text{nodes})}$$

where,

nodes = 200 tether nodal points (fixed).

Fixed Time Speed Up

$$S_{ft_n} = \frac{T_1(\text{nodes})}{T_n(\text{nodes})}$$

where,

nodes set such that  $T_1(200) \approx T_n(\text{nodes})$

Fixed Memory Speed Up

$$S_{fm_n} = \frac{T_1(\text{nodes})}{T_n(\text{nodes})}$$

where,

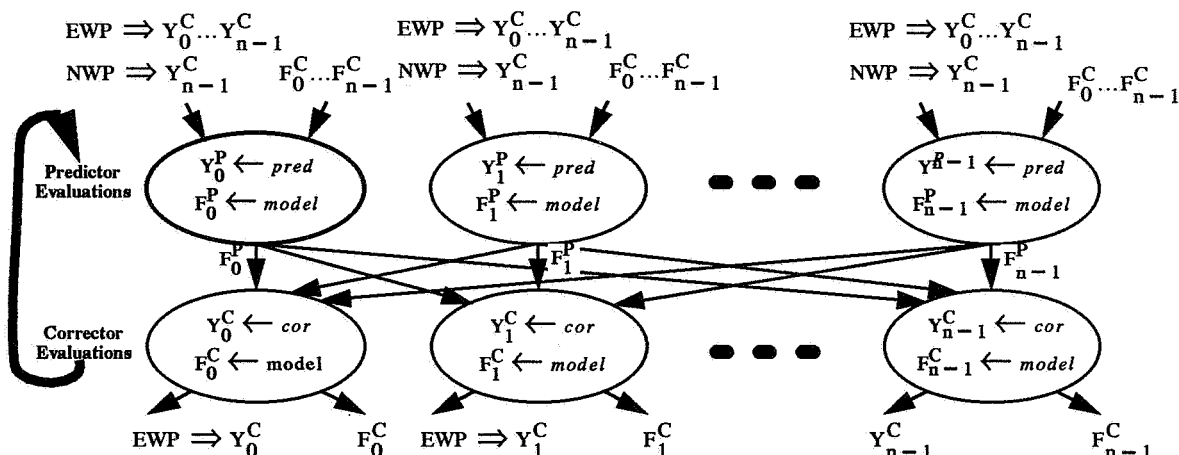
number of tether nodal points is proportional to n, (specifically, nodes = 200n)

Figure 5: Projected Speedups of Spacial Decomposition of Tether Simulation

### Parallel Integration Algorithm

In addition to spacially decomposing the problem the underlying algorithm of the simulation, integration, can itself be parallelized. For example, it has been determined by a number of researchers that it is possible to create parallel versions of the basic predictor/corrector algorithms. One such set of such algorithms is the so-called Block Implicit Methods outlined in reference [4]. This method divides the simulation into blocks of time, where each block contains a set of equally spaced solution points. Parallelism is obtained by permitting the equations for each solution point within a block to be concurrently processed. With parallel block predictor-corrector algorithms (see Figure 6), each solution point results from the exe-

cution of one predictor and one corrector equation where all of the predictor equations associated with the solution points for a given block of time can be processed concurrently.



**Figure 6: Structure of Parallel Block Predictor/Corrector Algorithm**

As shown in Figure 7, the effects of applying the Null Weight Predictor/Corrector Algorithm to this problem shows very promising results for the case of 1 to 10 processors. It is important to note that the parallel version of the algorithm has similar accuracy characteristics when compared to its serial counterpart but has inferior stability. This decreased stability limits such algorithms applicability to implementations with 10 or few processors. It is possible to utilize parallel integration algorithms in combination with spacial decomposition techniques to have a multiplicative effect on overall performance. This is an area for future research.

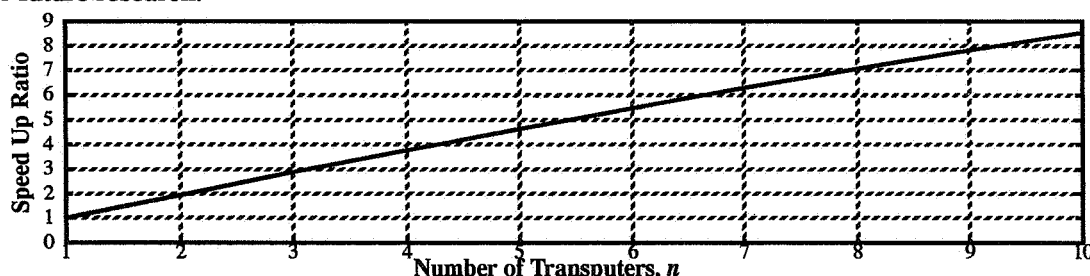


**Figure 7: Projected Speed Up for Parallel NWP Block Predictor Corrector Algorithm**

## Conclusions

This research has shown that effective parallel representations can be obtained for sizable real-world problems such as this tether dynamics simulation using either spacial data domain decomposition techniques and/or parallel algorithmic techniques. This is important since it is expected that the simulation needs for these types of problems will continue to expand much faster than the raw computing power of our sequential computing resources as we explore *much* more complicated scenarios. Future research should be directed to develop new algorithmic techniques (both sequential and parallel), improve and develop new automated software tools such as the APME, and develop simulation paradigms which utilize existing supercomputing facilities and networked hardware resources such as PC/Workstation clusters (with the possible addition of low-latency communication hardware facilities).

## References

1. P. Kohler, W. Maag, R. Wehrli, "Dynamics of a System of Two Satellites Connected by a Deployable and Extensible Tether of Finite Mass", NASA Technical Report, October 1978.
2. B. Earl Wells, "A Multicomputer Software Interface for Parallel Dynamic System Simulation", *Simulation Journal of the Society for Computer Simulation*, Vol. 65, No. 3, September 1995, pp. 191-205.
3. X. H. Sun and L. M. Ni, "Scalable Problems and Memory-Bound Speedup", *Journal of Parallel and Distributed Computing*, 1993.
4. L. G. Birta and O. Abou-Rabia, "Parallel Block Predictor-Corrector Methods for ODE's", *IEEE Transactions on Computers*, Vol. C-36, No. 3, March 1987, pp. 299-311.



**1996  
NASA/ASEE SUMMER FACULTY FELLOWSHIP PROGRAM**

**MARSHALL SPACE FLIGHT CENTER  
THE UNIVERSITY OF ALABAMA**

**VISUALIZATION OF HIGH LATITUDE ION UPFLOW IN SUPPORT  
OF THE IMAGE MISSION**

Prepared By:	Gordon R. Wilson
Academic Rank:	Assistant Research Professor
Institution and Department:	The University of Alabama in Huntsville Department of Physics
NASA/MSFC:	
Laboratory:	Space Science Laboratory
Division:	Space Physics Division
Branch	Space Plasma Physics Branch
MSFC Colleague:	Thomas E. Moore, Ph.D.



## Introduction

The study of the magnetosphere is a 400 year old science that began with the publication by Gilbert, in 1600, of his hypotheses that the Earth was a giant magnet. Since then we have learned many things about the magnetosphere, particularly in the last 40 years of the space age, but we still have many unanswered questions. In spite of the many thousands of observations of this system we still lack a global understanding of how it works. This is due to its large size and tenuous nature that mean that any measurement made of the fields or particles involved only give one a knowledge of the local conditions at a given time. To gain a global perspective through such observations would require the simultaneous operation of thousands of satellites spread throughout the magnetospheric system in addition to observations made on the ground. Such a program would be impractical at least from financial considerations. What is needed for the advancement of magnetospheric physics is to develop the same capabilities that astrophysicists, solar physicists and meteorologists have been using for years --- the ability to stand back from the object under study and see it in its entirety.

The challenge for doing this for the magnetosphere is that the particle densities are very low and the material is, for the most part, not luminous. In the last 25 years several ideas have been proposed that would allow at least the imaging of certain portions of the magnetosphere. These include imaging of the plasmasphere through the resonant scattering of solar 304 Å from  $\text{He}^+$  ions, imaging of various hot plasma populations (i.e. the ring current, plasmasheet, upflowing ionospheric ions, etc.) from the neutral atoms that result when ions of these populations charge exchange with the hydrogen geocorona, and imaging the aurora at various wavelengths in the far ultraviolet. In addition a novel technique for probing various boundaries in the magnetosphere by bouncing low frequency radio waves off of them has been extensively studied. Such a technique is analogous to the way the under water world can be probed with sonar.

About five years ago NASA convened a science working group to study the possibility of flying a magnetospheric imaging mission. This resulted in a number of proposals for such a mission, one of which was selected to be the first MIDEX mission, to be launched in early 2000. The mission is called IMAGE (Imager for Magnetopause to Aurora Global Exploration) and its P.I. is J. Burch at SwRI. The IMAGE spacecraft will carry imagers to view the plasmasphere, aurora, ring current, inner plasmasheet, and upflowing ionospheric ions as well as a radio sounder to probe the location, shape and dynamics of the magnetopause, plasmopause, etc. Between its selection last April and the non advocacy mission review, which takes place next spring, the IMAGE teams needs to further refine the design of the mission and its instruments. The theory and modeling (T&M) subgroup of this team has the task of demonstrating what kind of images the instruments on IMAGE will see as well as showing that useful scientific information can be extracted from such images.

As a central element to the efforts of the T&M subgroup we have decided to simulate and create synthetic images for the magnetic cloud event of October, 1995. In

this event a large cloud, with high plasma densities and strong magnetic fields, ejected from the sun collided with the earth's magnetosphere triggering a three day period of intense magnetic storms and substorms. This event was observed from a number of different spacecraft and on the ground so we have a good data set to work with. In our work we will place the IMAGE spacecraft in the magnetosphere on its proposed orbit, with its proposed instruments, to see what it would see had it been there. Existing models of the plasmasphere, ring current and magnetopause will be run for this event to give the structures for the imaging instruments. There are several models which are lacking and which need to be developed. These include a model for the cusp, the inner plasmasheet and the upflowing ions. My task this summer was to develop the upflowing ion model and use it to create synthetic images.

## The Model

$O^+$  and  $H^+$  ions in the ionosphere typically have low energies, often less than one eV. The LENA (Low Energy Neutral Atom) imager will have a low energy cutoff of 10 eV and will not be able to see such ions unless they are energized up into the range of 10--300 eV. This happens frequently in the auroral zone and cusp regions in the ionosphere where energy, in the form of precipitating energetic electrons, ions and currents, is deposited by various processes in the magnetosphere. The amount of ions flowing out is dependent on the amount of energy flowing in and both go up as magnetic activity increases. In the model that I developed the first task was to define the source function.

For this function I assume that all energized ionospheric ions are launched from an altitude of 1000 km. At that altitude the velocity distribution of these ions is assumed to be bi-Maxwellian with a perpendicular temperature 10 time larger than the parallel temperature. This is equivalent to assuming that all of the ions are energized by waves (ion cyclotron or lower hybrid) whose  $k$  vectors are nearly perpendicular to  $B$ . Next I assume that the upward ion flux in the auroral zone and polar cap is proportional to the downward energy flux of the precipitating auroral electrons. The pattern for this flux was taken from the model of Hardy et al. (1987). In the auroral zone at the 1000 km boundary, I assume that the upflowing ions have a perpendicular temperature of 300 eV. In the polar cap this value is 50 eV and in the cleft ion fountain the value used is 10 eV. The total ion flux from the auroral zone and polar cap is taken to be that given by the expressions obtained by Yau et al. (1988) based on 6 years of EICS data from DE 1. These expressions are

$$F(O^+) = 10^{25} \exp[0.01 (F_{10.7}-100)] \exp(0.5 Kp) \text{ ions/s}$$

$$F(H^+) = 2.5 \times 10^{25} \exp[-0.0027 (F_{10.7}-100)] \exp(0.23 Kp) \text{ ions/s}$$

where  $Kp$  is an index which measures magnetic activity and  $F_{10.7}$  is an index which measures the EUV output of the sun. For the cleft ion fountain the total  $O^+$  flux was assumed to have a constant value of  $10^{25}$  ions/s and the  $H^+$  flux had a value of  $2.5 \times$

$10^{24}$  ions/s. The location and size of the cleft ion fountain was taken from the De 1 observations as reported by Giles et al. (1994) and Pollock et al. (1990).

Once ions leave the lower boundary at 1000 km they flow upward along the magnetic field lines and drift across these field lines. Throughout the region which I modeled (above  $50^\circ$  magnetic latitude and out to a geocentric distance of  $5 R_E$ ) I assumed that the magnetic field was dipolar. I also assumed that the electric field was only perpendicular to the magnetic field. As a result ions will drift across the magnetic field due to the curvature, gradient and  $\mathbf{E} \times \mathbf{B}$  drifts, all of which were included in the particle equations of motion. The equations of motion used in the model were the guiding center equations as developed by Delcourt et al. (1988). Since I assume that  $\mathbf{B}$  field lines are equal potentials (no  $\mathbf{E}$  parallel) the electric field throughout the volume of interest is defined by the electric potential in the ionosphere. In the current version of the model the Volland (1978) model for this potential is used. Later versions will be updated to the Heppnard Maynard model used in the Rice convection model.

The code which implements this model does the following. The ionosphere at 1000 km is subdivided into about 1000 small regions within which the upflux of  $H^+$  and  $O^+$  ions is assumed constant. From each of these regions 20 ions, whose initial energies and pitch angles are chosen from the assumed velocity distribution, are launched and followed until they leave the region. At each step along the way their energy and pitch angle are found and a 5 dimensional array, which contains the ion flux as a function of position, pitch angle and energy, is updated. The process of updating this array is continued until all particles from all regions have been launched and tracked through the simulation region. Since the particles are not all followed simultaneously, or on the same time step, the solution found is a steady state solution.

Once the five dimensional ion flux function has been found for both  $H^+$  and  $O^+$  it is converted into an ENA flux function for neutral H and O. The reactions which produce this results are



In these reactions there is very little energy exchange between the ion and the hydrogen atom so that the velocity distribution of the ions is directly translated into the velocity distribution of the neutral atoms. The neutral hydrogen with which the ions react is part of the earth's geocorona. The production rate of the energetic neutrals will therefore decrease as one moves away from the earth because of the decreasing density of the hydrogen. The model for this density function used in this work is that of Rairden et al. (1986).

Once the ENA flux function is available it is possible to create images of this flux by using a line-of-sight integration code since the medium is very tenuous and one can see



all the way through it. The code used was one developed by D. L. Gallagher here at MSFC. To run the code one gives it a luminosity flux function, in the form of a subroutine, the position of the spacecraft, its viewing direction and characteristics of the camera such as angular resolution, effective area and field of view. The code returns a sky map of the flux into the instrument for each pixel bin.

### Images of Upflowing Ions

Figure 1 is a sequence of images of the outflowing  $H^+$  ions whose energies lie between 128 eV and 300 eV (high energy channel of the LENA instrument). The numbers with each image are the times, in UT, when the image was made. These times correspond to an interval near the most intense part of the magnetic storm triggered by the October 1995 magnetic cloud event when the IMAGE spacecraft is approaching perigee from the northern hemisphere. The intensity scale is an inverted gray scale where black represents the most intense fluxes and white the least intense. The black circle in each figure is an outline of the earth while the small plus sign indicates the direction toward the north magnetic pole.

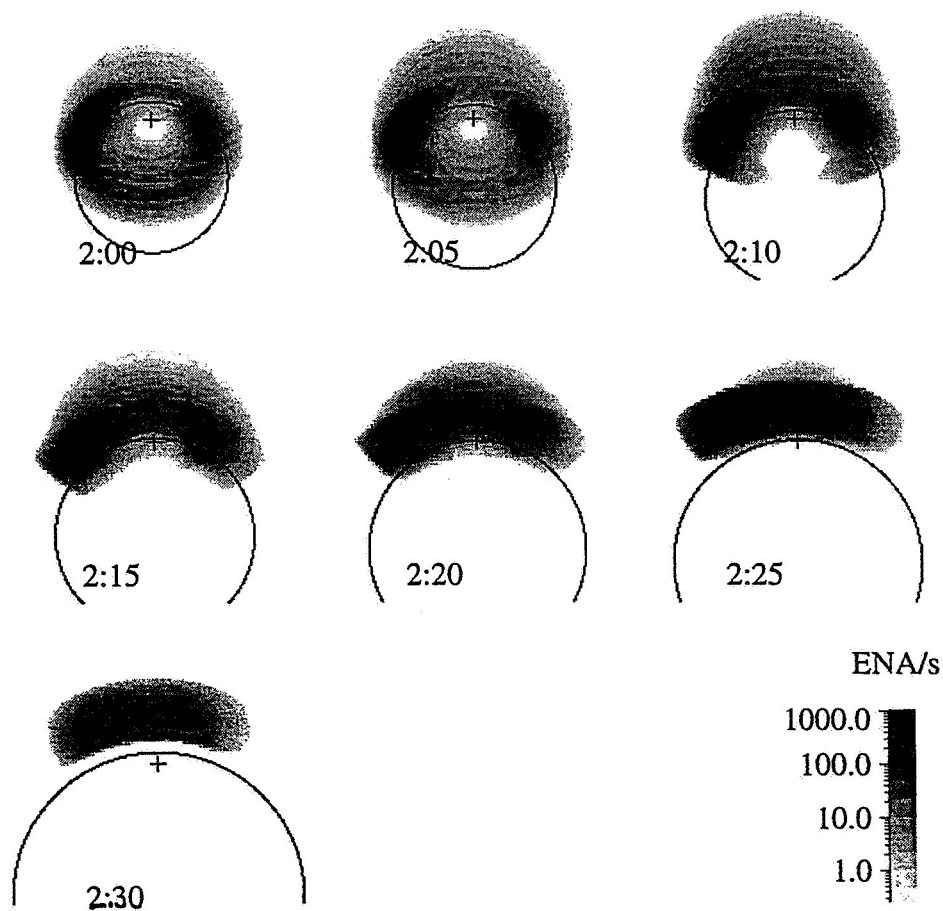


Figure 1. A sequence of  $H^+$  ENA images from a time period during the most intense portion of the magnetic storm.

For this time interval the  $K_p$  is about 7 and  $F_{10.7}$  is about 80. The  $H^+$  flux from the auroral zone and polar cap is  $1.3 \times 10^{26}$  ions/s and from the cleft ion fountain is  $2.5 \times 10^{24}$  ions/s. The corresponding  $O^+$  fluxes are  $2.7 \times 10^{26}$  ions/s and  $10^{25}$  ions/s respectively. Although the auroral zone fluxes dominate the cleft ion fountain it is possible to see this source in the lowest energy channel (10-23 eV).

One of the things that the sequence of images in figure 1 demonstrates is that during intervals when the IMAGE spacecraft is passing close to the earth and the direction from which it is viewing the upflowing ions is changing rapidly it may be possible to use tomographic techniques to reconstruct the ion flux function from the images. In a single image the pitch angle distribution of the ions at a given point on a given field line is sampled at only one pitch angle. This same field line is also sampled at other pitch angles at other locations. (The pitch angle sampled is determined by the angle between the look direction and the magnetic field.) It may be possible to fill in the total pitch angle distribution at all points along the field line by adiabatically mapping the observed flux at one point to other points along the field line. If only one field line were emitting ENA then a complete reconstruction of the pitch angle distribution along the whole field line would be possible with a single image. Because the counts in a single pixel would, in general, not come from a single field line a sequence of images, taken from different vantage points, would be needed as a minimum to sort out what comes from a given field line.

It is clear that much work with these images needs to be done.

## References

- Delcourt, et al., Influence of the interplanetary magnetic field orientation on polar cap ion trajectories: Energy gain and drift effects, *J. Geophys. Res.*, **93**, 7565, 1988.
- Hardy, et al., Statistical and functional representation of the pattern of auroral energy flux, number flux, and conductivity, *J. Geophys. Res.*, **92**, 12275, 1987.
- Giles, et al., Statistical survey of pitch angle distributions in core (0-50 eV) ions from Dynamics Explorer 1: Outflow in the auroral zone, polar cap, and cusp, *J. Geophys. Res.*, **99**, 17483, 1994.
- Pollock, et al., A survey of upwelling ion event characteristics, *J. Geophys. Res.*, **95**, 18969, 1990.
- Rairden, et al., Geocoronal imaging with Dynamics Explorer, *J. Geophys. Res.*, **91**, 13613, 1986.
- Volland, H. A model of the magnetospheric electric convection field, *J. Geophys. Res.*, **83**, 2695, 1978.
- Yau, et al., Quantitative Parametrization of Energetic Ionospheric Ion Outflow, in *Modeling Magnetospheric Plasma*, eds. T. E. Moore and J. H. Waite, Jr., p. 211, Geophys. Mono. #44, AGU, Washington, DC, 1988.



1996

NASA/ASEE SUMMER FACULTY FELLOWSHIP PROGRAM

MARSHALL SPACEFLIGHT CENTER  
THE UNIVERSITY OF ALABAMA

SOLIDIFICATION INTERFACE SHAPE AND LOCATION  
DURING PROCESSING IN HIGH GRADIENT  
FURNACE WITH QUENCH

Prepared by:	Keith A. Woodbury
Academic Rank:	Associate Professor
Institution and Department:	The University of Alabama Mechanical Engineering Department
NASA/MSFC:	
Laboratory:	Structures/Dynamics
Division:	Thermal and Life Support
Branch:	Environmental Control and Life Support
MSFC Colleague:	William C. Patterson



## INTRODUCTION

High Gradient Furnace with Quench (HGFQ) is being developed to facilitate metals processing experiments aboard the International Space Station. The general furnace schematic is depicted in Fig. 1. The sample is centered in an annular furnace and is held fixed during processing. The furnace itself is made to translate over the sample. Once in process, heat will flow through the sample from the Heater Zone to the Chill Zone. If operating conditions are correct, the solidification interface will stand in the gradient zone. Objectives of the HGFQ process are to provide a high gradient for the solidification with the solidification interface properly positioned in the gradient zone.

At the recent RDR for HGFQ, one of the panelists raised the question about the suitability of HGFQ for potential future PIs. Specifically, it was stated by the design team at RDR that the present HGFQ design would provide a radius of curvature of the solidification interface of at least one sample diameter. The RDR panel argued that this was too small, and that most investigators would need a radius of curvature larger than this.

The requirements established by the current PIs are shown in Table 1. Note that these requirements do not contain any specification about the interface shape. However, these requirements do define the envelope of operational parameters for HGFQ.

The objectives of the present investigation are to 1) determine a suitable means of quantifying the interface shape, and 2) investigate the interface shape and how it is affected by processing parameters. The processing parameters to be considered are 1) sample material, 2) sample diameter, and 3) gradient zone length.

## COMPUTATIONAL METHODS

The computer package FIDAP was used to investigate the process. FIDAP is a general purpose finite element analysis program which is especially applicable to heat transfer problems involving fluid flow. The current investigation does not make use of FIDAP's fluid flow analysis methodology, but in future the convection in the sample during ground-based testing could be simulated by adding this feature to the present model.

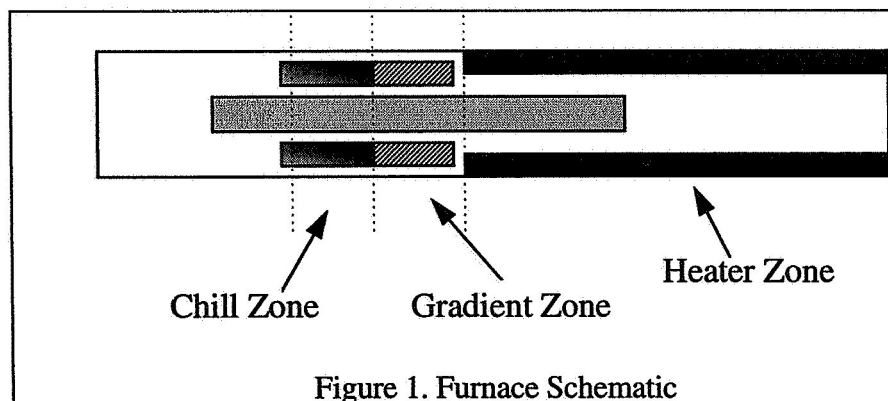


TABLE 1. PI Requirements for HGFQ

PI	Material	Diameter	Hot Temp.	Gradient	$V_{\text{translation}}$
Stefanescu <sup>1</sup>	Aluminum?	6-10mm 10 mm	700-800 C < 900 C	80-100 C/cm 70-100 C/cm	0.1- 50 $\mu\text{m/s}$ 0.5-150 $\mu\text{m/s}$
Andrews <sup>2</sup>	Al-Indium	10 mm	1000-1100C	80-100 C/cm	1.0-10 $\mu\text{m/s}$
Poirier <sup>3</sup>	Pb-23%Sn	6-10 mm	unspecified	50 C/cm	2-200 $\mu\text{m/s}$
Poirier <sup>4</sup>	Al-15%Cu	6-10 mm	unspecified	140 C/cm	12-200 $\mu\text{m/s}$
Trivedi <sup>5</sup>	Al-4%Cu	6-10 mm	unspecified	40-140 C/cm	1-48 $\mu\text{m/s}$
Trivedi <sup>5</sup>	Al-15%Cu	6-10 mm	unspecified	140 C/cm	1-48 $\mu\text{m/s}$

<sup>1</sup> From RDR - values listed appeared in different talk segments

<sup>2</sup> From RDR

<sup>3</sup> Letter/fax from David Poirier to Dorothy Hubbard dated June 21, 1996

<sup>4</sup> Letter/fax from David Poirier to Dorothy Hubbard dated June 27, 1996

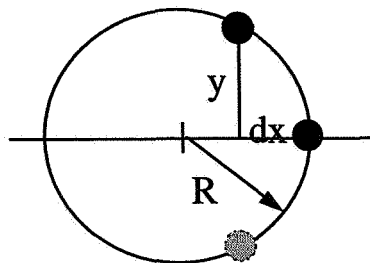
<sup>5</sup> Letter/fax from Rohit Trivedi to Dorothy Hubbard dated July 3, 1996

The computational approach employed is to fix the sample at a location and compute the steady-state temperature distribution in the sample and the furnace. After the temperature field is obtained, the solidification interface is identified by the temperature contour corresponding to the phase change temperature.

The steady-state mode is believed to closely approximate the temperature field during "slow" processing of the sample. Obviously, at higher translation velocities the nonstationary effects will become important.

## RADIUS OF FLATNESS

A suitable measure of the shape is needed in order to compare results from different cases. The most intuitive might seem to be the radius of curvature, obtained by passing the equation of a circle through 3 consecutive points. However, this measure of curvature can result in unrealistic implications of flatness, particularly where an isotherm curves at the wall. A better idea is the radius of flatness (RoF) which is defined to be the radius of a circle passing through the point on the centerline, any point off the centerline, and its mirror image on the other side of the centerline. Calculation of the radius of flatness is accomplished via:



$$R = (y^2 + dx^2)/2dx$$

Calculation of the RoF will result in a distribution of flatness across the thickness. This distribution is depicted in Table 2. for a typical case. The RMS average of these is computed and used to quantify the shape of the interface.

TABLE 2. Radius of Curvature and Radius of Flatness

R	local RoC	diams	local RoF	diams	global RoF	diams
0.0000e+00	3.64e-02	3.7	3.64e-02	3.7	3.64e-02	3.7
6.1940e-04	5.27e-02	5.3	1.53e-02	1.5	4.30e-02	4.3
1.2388e-03	8.99e-02	9.1	1.14e-02	1.2	4.98e-02	5.0
1.8581e-03	2.94e+00	297.1	1.15e-02	1.2	5.98e-02	6.0
2.4775e-03	2.51e-01	25.3	1.27e-02	1.3	7.21e-02	7.3
3.0969e-03	1.38e-02	1.4	4.48e-03	0.5	6.31e-02	6.4
3.7162e-03	5.23e-03	0.5	1.68e-03	0.2	4.13e-02	4.2
4.3356e-03	1.20e-02	1.2	1.33e-03	0.1	3.24e-02	3.3
RMS->	1.05e+00	105.5	1.58e-02	1.6	5.14e-02	5.2
Avg->	4.2569e-01	43.0	1.1839e-02	1.2	4.9746e-02	5.0

## RESULTS

The baseline configuration for calculation is as follows:

Steady-State Analysis  
 25% Processed Sample  
 Crucible (no gap or cartridge)  
 Argon atmosphere  
 PAN coupling to chill block  
 900 W/m<sup>2</sup> -C cooling on back of chill block  
 1373 K Hot Zone Setpoint  
 (1123 K for Stefanescu and Pb 23%Sn)

The results for the baseline calculation are seen in Table 3. The smallest curvature results for the case of Stefanescu, and that is because the solidification occurs outside the gradient zone. For any of the alloy systems, the radius of flatness is much larger.

Table 4 shows the results of varying the sample diameter for the Al 4.5%Cu system. Note that shrinking the diameter increases the axial gradient, but has an adverse effect on the interface curvature.



Table 5 shows the effect of an increased gradient zone length on the Al 4.5%Cu alloy. For the 1100 C setpoint, the gradient is reduced, and the RoF is in fact increased slightly. For the 850 C setpoint, the RoF is increased slightly, and the gradient is increased slightly as well.

## CONCLUSIONS

Radius of Flatness values for the liquidus isotherm of different aluminum alloys processed in HGFQ range from 3.1 to 11.1 sample diameters under baseline conditions. Decreasing sample diameter does not appear to be a means of increasing RoF. Increasing the gradient zone length appears to provide a means for increasing RoF.

TABLE 3. Results for Baseline Case

Material	PIs	Location (cm)	Gradient C/cm	RoF Liq	RoF Sol
Al	An	10.1	122	3.4	--
Al	St <sup>1</sup>	15.1	33	3.1	--
Al 4.5%Cu	Po/Tr	9.71	100	11.1	64.3
Al 15%Cu	Po/Tr	9.49	110	6.1	1086
Pb 23%Sn	Po <sup>1</sup>	8.34	120	305	5.3*

1 - Setpoint 1123 K

\* -approximate result since mesh was > 300  $\mu$ m

Note: Gradient zone is from 7.985 cm to 10.985 cm

TABLE 4. Results for Smaller Diameter - Al 4.5%Cu

Diameter	Hot Zone (C)	Chill Block (C)	Location (Liq) (cm)	Gradient C/cm	RoF Liq (diams)	RoF Sol (diams)
10 mm	1100	68	9.71	100	11.1	(-)64.3
10 mm	850	55	13.5	33	4.5*	11.9*
6mm	1100	65	9.94	102	6.8	405
6mm	850	52	13.4	36	4.1*	11.1*

\* -approximate result since mesh was > 300  $\mu$ m

Note: Gradient zone is from 7.985 cm to 10.985 cm

TABLE 5. Effect of Extended Gradient Zone

Length	Hot Zone (C)	Chill Block (C)	Location (Liq) (cm)	Gradient C/cm	RoF Liq (diams)	RoF Sol (diams)
3 cm	1100	68	9.71	100	11.1	(-)64.3
3 cm	850	55	13.5	33	4.5*	11.9*
5 cm	1100	n/a	10.8	88	12.1*	517*
5 cm	850	65	14.2	42	5.5*	28.8

\* -approximate result since mesh was > 300  $\mu$ m

Note: Gradient zone starts at 7.985 cm

1996

NASA/ASEE SUMMER FACULTY FELLOWSHIP PROGRAM

MARSHALL SPACE FLIGHT CENTER  
THE UNIVERSITY OF ALABAMA

RECEPTOR EXPRESSION IN RAT SKELETAL MUSCLE CELL CULTURES

Prepared by: Ronald B. Young, Ph.D.

Academic Rank: Professor

Institution and Department: University of Alabama in Huntsville  
Department of Biological Sciences

NASA/MSFC:

Laboratory: Space Sciences Laboratory  
Division: Microgravity Science and  
Applications  
Branch: Biophysics

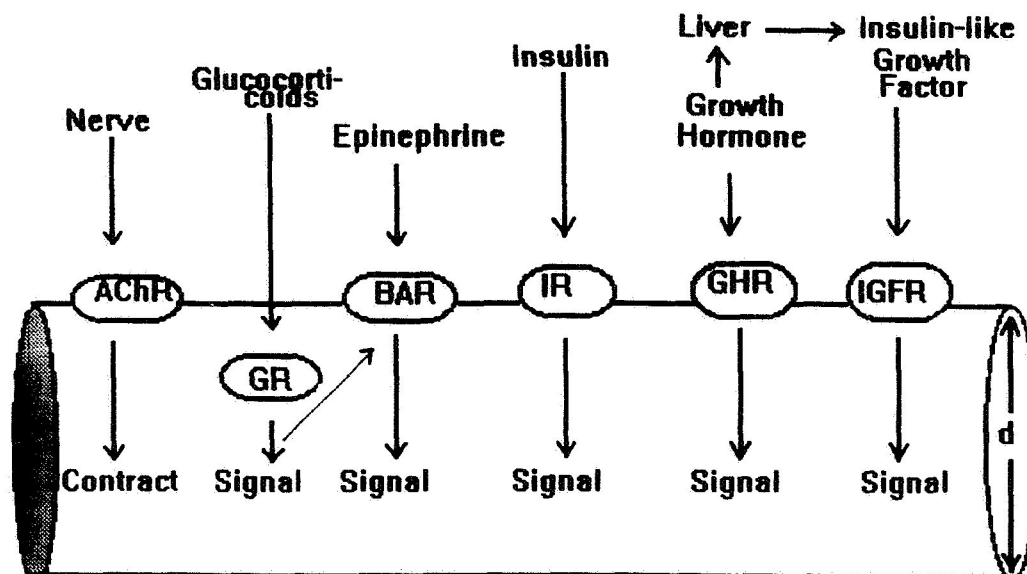
MSFC Colleague: Robert Snyder, Ph.D.



## INTRODUCTION

One of the most persistent problems with long-term space flight is atrophy of skeletal muscles. Skeletal muscle is unique as a tissue in the body in that its ability to undergo atrophy or hypertrophy is controlled exclusively by cues from the extracellular environment. The mechanism of communication between muscle cells and their environment is through a group of membrane-bound and soluble receptors, each of which carries out unique, but often interrelated, functions. The primary receptors include acetyl choline receptors, beta-adrenergic receptors, glucocorticoid receptors, insulin receptors, growth hormone (i.e., somatotropin) receptors, insulin-like growth factor receptors, and steroid receptors.

This project has been initiated to develop an integrated approach toward muscle atrophy and hypertrophy that takes into account information on the populations of the entire group of receptors (and their respective hormone concentrations), and it is hypothesized that this information can form the basis for a predictive computer model for muscle atrophy and hypertrophy. The conceptual basis for this project is illustrated in the figure below. The individual receptors are shown as membrane-bound, with the exception of the glucocorticoid receptor which is a soluble intracellular receptor. Each of these receptors has an extracellular signalling component (e.g., innervation, glucocorticoids, epinephrine, etc.), and following the interaction of the extracellular component with the receptor itself, an intracellular signal is generated. Each of these intracellular signals is unique in its own way; however, they are often interrelated.



MODEL FOR MUSCLE ATROPHY/HYPERTROPHY

In summary, the presence of an active signal within a muscle cell depends on a number of levels, each of which is a potential site for regulation. These levels include the concentration or pulse frequency of the extracellular hormone, the number of receptors either on the surface or within the interior of the cells, whether or not the receptor-ligand interaction is coupled to the appropriate intracellular signal, and the extent to which individual signalling pathways interact with each other. The fact that interaction among pathways takes place is often referred to as receptor "cross talk". An example of the fact that receptors do not function independently of each other is as follows. An increase in muscle contraction via acetylcholine receptors and an increase in concentration of beta-adrenergic agonists (such as epinephrine) tend to lead to muscle hypertrophy, whereas an increase in glucocorticoid concentrations tend to lead to muscle atrophy. However, these are not independent events. A prolonged increase in contraction also results in a higher number of beta-adrenergic receptors and a lower number of glucocorticoid receptors. In addition, a prolonged decrease in contraction (such as that which occurs during weightlessness) results in a decreased number of beta-adrenergic receptors and an increased number of glucocorticoid receptors. Thus, not only is the number of receptors affected, but their capability to produce a signal is affected as well.

## Materials and Methods

**Rat Muscle Cell Cultures.** Skeletal muscle tissue was excised from the hind limbs of newborn rats and placed in ice cold culture medium. The culture medium consisted of Dulbecco's Modified Eagle's Medium (DMEM) with L-glutamine and 1000 mg glucose/L (catalog #D5523, Sigma Chemical Co., St. Louis, MO), sodium bicarbonate buffer (3.7 g/L) and 13% horse serum (Gibco BRL Life Technologies, Grand Island, NY). Fungizone (250 µg/L; GIBCO BRL), Penicillin (100,000 U/L), and Gentamicin (20 µg/ml) were also added and the pH was adjusted to 6.8.

Working under sterile conditions, the muscle tissue was placed in warm phosphate buffered saline (PBS). After rinsing the tissue in PBS, it was minced with a scalpel. Muscle tissue was then placed in 50 ml conical tubes at approximately 10 g/tube, and 25 ml of a 2 mg/ml pronase enzyme solution in PBS (Catalog No. P6911, Sigma Chemical Co., St. Louis MO). The digestion procedure was carried out at 37°C in a rotary shaker at 175 rpm for approximately 45 min. The suspension was centrifuged at 1500 x g for 6 min, the protease solution was discarded, and myoblasts were harvested from the pellet by differential centrifugation. Briefly, PBS was added to the pellet to give a final volume of 30 ml, and the pellet was resuspended at top speed for 30 sec on a vortex mixer. The suspension was centrifuged at 400 x g for 3 min, and the supernatants were collected and saved. These steps were repeated two more times with the digested muscle pellet. The filtrate was then

centrifuged at 1500 x g for 6 min to collect the myoblasts. Cells were resuspended in culture medium. The cells were then plated in matrigel-coated 6 cm tissue culture dishes at a density of  $1.8 \times 10^5$  cells/cm<sup>2</sup>. On the day fusion was first observed,  $10^{-6}$  M fluorodeoxyuridine was also added to inhibit DNA synthesis and thus overgrowth by fibroblasts.

**Experimental Design.** The purpose of this project is to measure the populations of beta-adrenergic receptors, glucocorticoid receptors, insulin receptors, insulin-like growth factor receptors and growth hormone receptors. To make these measurements, two different general approaches were taken. The beta-adrenergic receptor population was measured directly as described below, and culture samples for the others were collected and frozen for future analysis. In all, six experiments were carried out and samples collected. Since twenty-four culture wells are needed for each of the five receptors, a total of 720 samples were collected during the summer (i.e., 5 receptors x 6 experiments x 24 samples).

**Beta-adrenergic Receptor Measurement.** Cells in multiwell dishes were rinsed and incubated at room temperature for 15 min in buffer containing 0.1-3 nM (-)-[<sup>3</sup>H]CGP-12177 (40-50 Ci/mmol) to determine total binding to beta-adrenergic receptors. Nonspecific binding was determined by measuring the amount of (-)-[<sup>3</sup>H]CGP-12177 bound in the presence of  $10^{-6}$  M (+)-propranolol. Myotubes from the rat skeletal muscle cell line L<sub>6</sub> were used as a positive control. These L<sub>6</sub> cells are grown in the same culture medium and exhibit a large population of beta-adrenergic receptors. The cell number in replicate cultures was determined by measuring the DNA content so the number of receptors per cell could be calculated. To determine the K<sub>d</sub> and B<sub>max</sub>, the least squares nonlinear curve fitting technique of the LIGAND computer program was used.

**Sample Collection Protocol.** For glucocorticoid receptor analysis, cultures were rinsed three times with cold phosphate buffered saline (PBS), and then homogenized 10 times with a tightly fitting Dounce homogenizer. Samples were either frozen directly at -70 C, or were centrifuged at 50,000 x g for 1 hr immediately prior to receptor analysis. Total binding was determined with 0-50 nM [<sup>3</sup>H]dexamethasone, and nonspecific binding was determined with 0-50 nM [<sup>3</sup>H]dexamethasone in the presence of 20  $\mu$ M nonradioactive dexamethasone.

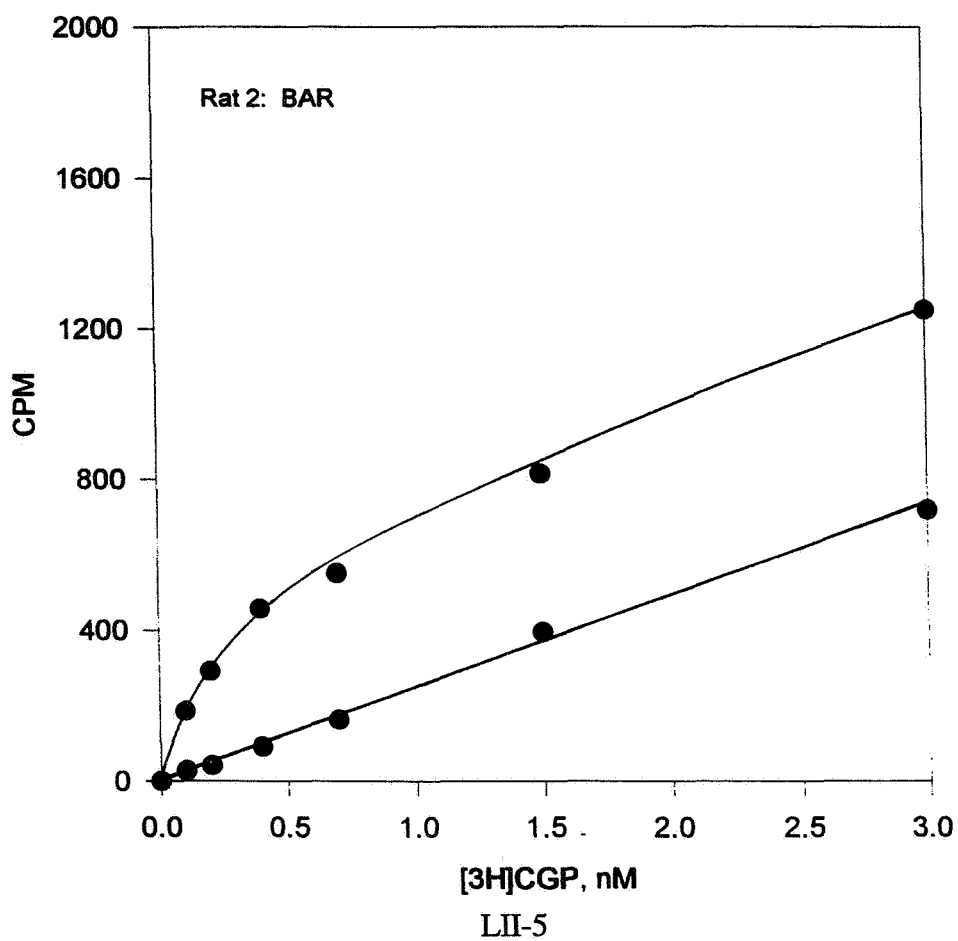
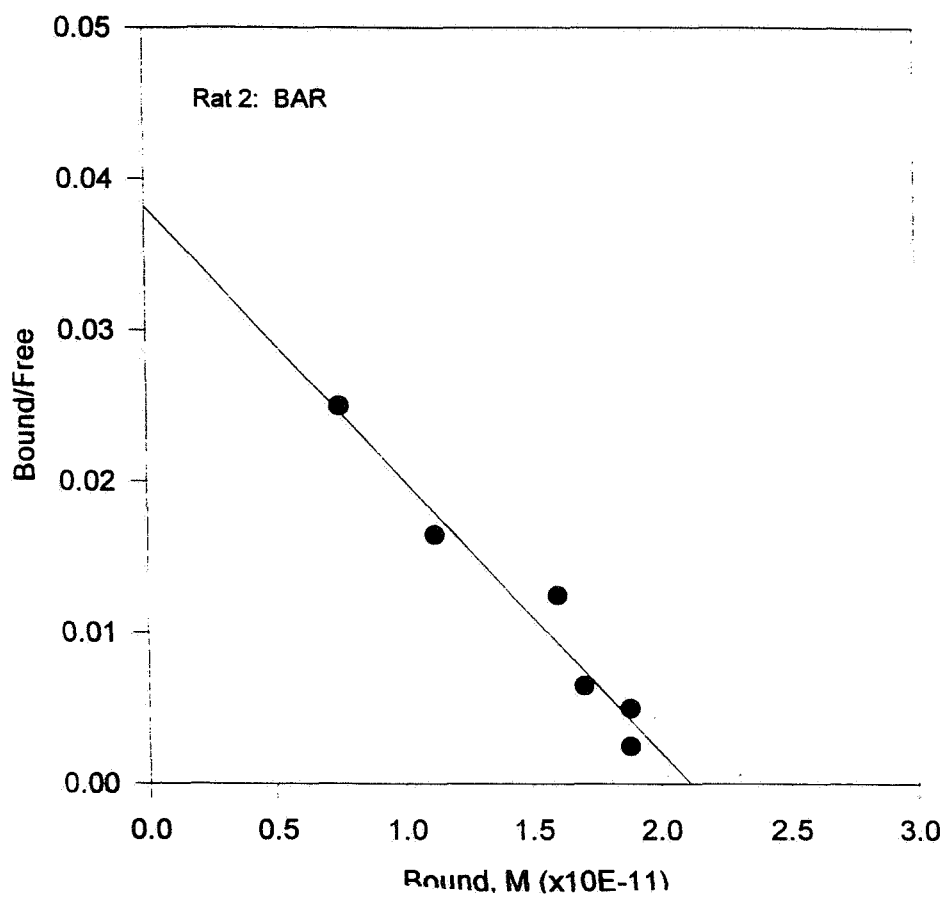
Cultures for insulin, IGF and growth hormone receptor measurements were rinsed three times with cold PBS, and scraped from the dishes into 2 mM EDTA, 1 mM HEPES, 0.3 mM PMSF, pH 7.4. Cells were collected by centrifugation at 24,000xg for 15 min, the cell pellet was resuspended in isotonic saline, and cells were homogenized 10 times with a loose fitting Dounce homogenizer. Samples were frozen at -70 C.

## Results

Beta-adrenergic receptor population was quantified in rat primary cell cultures as described above. The receptor population was estimated to be  $10.2 \pm 1.2$  million receptors per muscle cell. The  $K_d$  (i.e., the binding constant) was  $0.47 \pm 0.06$  nM. An example of a saturation curve is shown at the top of the next page, and the transformation of these data to a Scatchard plot to determine receptor number is shown at the bottom of the next page. While the  $K_d$  is quite consistent with published values, it is difficult to compare the receptor population with published information. First, extensive literature searches have indicated that this receptor population has not previously been analyzed in muscle cell cultures. Second, values have been published for several other cell types (including heart cells, adipose cells and connective tissue cells), and the population ranges from approximately 5-15 million receptors per cell. Thus, the observed number of receptors is physiologically realistic.

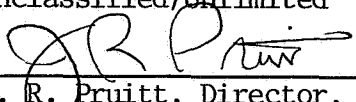
In addition to the above results, two other lines of investigation were initiated during the summer, one of which was productive and the other was not. In anticipation of studying muscle atrophy and hypertrophy using a rotating wall bioreactor in the future, an attempt was made to grow an established muscle cell line under the same conditions as the rat primary cultures. Use of a cell line would be more adaptable and easier for shuttle flights than primary cultures. Unfortunately, these  $C_2C_{12}$  cells differentiated poorly and did not exhibit most of the characteristics of muscle cells. It was initially planned to compare the receptor populations between the cell line and the primary cultures; however, the decision was made to exclude the  $C_2C_{12}$  cell because of their poor quality. The second line of investigation was to attempt to grow primary cultures of muscle on micro-carrier beads in suspension. This was successful, with tissue differentiation and aggregation evident. Once a rotating bioreactor is available, experiments can be initiated to examine growth of cells on microcarrier beads under conditions that will simulate microgravity; furthermore, conditions can be established to analyze muscle cell receptor populations under conditions that will mimic either muscle atrophy or muscle hypertrophy.

This project was initiated to develop an integrated approach toward muscle atrophy and hypertrophy that takes into account information on the populations of the entire group of receptors (and their respective hormone concentrations), and it is hypothesized that this information can eventually form the basis for a predictive computer model for muscle atrophy and hypertrophy. This would be an extremely helpful approach in understanding the potential responses during tissue modeling experiments because the complex interactive effects from changing a single parameter could be predicted. We have made a few small steps in this new direction. At least we are certain of the two following things: 1) That receptors can be measured in muscle cells, and 2) that muscle cells will grow on microcarrier beads.





Public reporting burden for this collection of information is estimated to average 1 hour per response, including the time for reviewing instructions, searching existing data sources, gathering and maintaining the data needed, and completing and reviewing the collection of information. Send comments regarding this burden estimate or any other aspect of this collection of information, including suggestions for reducing this burden, to Washington Headquarters Services, Directorate for Information Operations and Reports, 1215 Jefferson Davis Highway, Suite 1204, Arlington, Va 22202-4302, and to the Office of Management and Budget, Paperwork Reduction Project (0704-0188), Washington, DC 20503.

1. AGENCY USE ONLY (Leave Blank)		2. REPORT DATE October 1996		3. REPORT TYPE AND DATES COVERED Contractor Report (Final Report)	
4. TITLE AND SUBTITLE Research Reports- 1996 NASA/ASEE Summer Faculty Fellowship Program				5. FUNDING NUMBERS NGT8-52819	
6. AUTHOR(S) M. Freeman, R. Chappell, F. Six, G. Karr, Editors					
7. PERFORMING ORGANIZATION NAME(S) AND ADDRESS(ES) The University of Alabama, Tuscaloosa, Alabama, and The University of Alabama in Huntsville				8. PERFORMING ORGANIZATION REPORT NUMBERS	
9. SPONSORING/MONITORING AGENCY NAME(S) AND ADDRESS(ES) National Aeronautics and Space Administration Marshall Space Flight Center, AL 35812				10. SPONSORING/MONITORING AGENCY REPORT NUMBER NASA CR- 205205	
11. SUPPLEMENTARY NOTES					
12a. DISTRIBUTION/AVAILABILITY STATEMENT Unclassified/Unlimited  J. R. Pruitt, Director, Education Programs Office				12b. DISTRIBUTION CODE	
13. ABSTRACT (Maximum 200 words) For the 32nd consecutive year, a NASA/ASEE Summer Faculty Fellowship Program was conducted at the Marshall Space Flight Center (MSFC). The program was conducted by the University of Alabama and MSFC during the period May 28, 1996 through August 2, 1996. Operated under the auspices of the American Society for Engineering Education, the MSFC program, as well as those at other NASA centers, was sponsored by the Higher Education Branch, Education Division, NASA Headquarters, Washington, D.C. The basic objectives of the programs, which are in the 33rd year of operation nationally, are (1) to further the professional knowledge of qualified engineering and science faculty members; (2) to stimulate an exchange of ideas between participants and NASA; (3) to enrich and refresh the research and teaching activities of the participants' institutions; and (4) to contribute to the research objectives of the NASA centers. The Faculty Fellows spent 10 weeks at MSFC engaged in a research project compatible with their interests and background and worked in collaboration with a NASA/MSFC colleague. This document is a compilation of Fellows' reports on their research during the summer of 1996. The University of Alabama presents the Co-Directors' report on the administrative operations of the program. Further information can be obtained by contacting any of the editors.					
14. SUBJECT TERMS Astrionics; structures and dynamics; materials and processes; systems analysis and integration; propulsion; space sciences; mission operations; information systems; advanced spacecraft and payload systems; preliminary design; and technology transfer.				15. NUMBER OF PAGES 404	
				16. PRICE CODE A18	
17. SECURITY CLASSIFICATION Unclassified	18. SECURITY CLASSIFICATION OF THIS PAGE Unclassified	19. SECURITY CLASSIFICATION OF ABSTRACT Unclassified	20. LIMITATION OF ABSTRACT Unlimited		

National Aeronautics and  
Space Administration  
Code JTT  
Washington, DC  
20546-0001

*Official Business*  
*Penalty for Private Use, \$300*

*Postmaster: If Undeliverable (Section 158 Postal Manual), Do Not Return*

---